

# Arbeitsbericht NAB 14-87

**Development and evolution of the  
Excavation Damaged Zone (EDZ) in the  
Opalinus Clay – A synopsis of the state  
of knowledge from Mont Terri**

December 2014

G.W. Lanyon, D. Martin,  
S. Giger, P. Marschall

Nationale Genossenschaft  
für die Lagerung  
radioaktiver Abfälle

Hardstrasse 73  
CH-5430 Wettingen  
Telefon 056-437 11 11

[www.nagra.ch](http://www.nagra.ch)



# Arbeitsbericht NAB 14-87

## Development and evolution of the Excavation Damaged Zone (EDZ) in the Opalinus Clay – A synopsis of the state of knowledge from Mont Terri

December 2014

G.W. Lanyon<sup>1</sup>, D. Martin<sup>2</sup>,  
S. Giger<sup>3</sup>, P. Marschall<sup>3</sup>

<sup>1</sup> Fracture Systems Ltd., St. Yves, Cornwall, UK

<sup>2</sup> Derek Martin Consulting, Edmonton, Alberta, CA

<sup>3</sup> Nagra, Wettingen, Switzerland

### KEYWORDS

Opalinus Clay, Excavation Damaged Zone, EDZ, stress, deformation, stability, creep, lining, engineering feasibility, long-term safety

Nationale Genossenschaft  
für die Lagerung  
radioaktiver Abfälle

Hardstrasse 73  
CH-5430 Wettingen  
Telefon 056-437 11 11

[www.nagra.ch](http://www.nagra.ch)

Nagra Working Reports concern work in progress that may have had limited review. They are intended to provide rapid dissemination of information.

"Copyright © 2014 by Nagra, Wettingen (Switzerland) / All rights reserved.

All parts of this work are protected by copyright. Any utilisation outwith the remit of the copyright law is unlawful and liable to prosecution. This applies in particular to translations, storage and processing in electronic systems and programs, microfilms, reproductions, etc."

## **Zusammenfassung**

Beim Bau und Betrieb eines geologischen Tiefenlagers entwickelt sich im Umfeld der Untertagebauwerke eine Auflockerungszone. Im Rahmen der Risikoanalyse zur bautechnischen Machbarkeit eines geologischen Tiefenlagers werden die bautechnischen Anforderungen bezüglich der Tragsicherheit und Gebrauchstauglichkeit der Untertagebauwerke anhand von Entwurfskriterien formuliert, die sich vor allem auf die Form und Ausdehnung der Auflockerungszone beziehen.

Darüber hinaus stellt die Auflockerungszone nach Lagerverschluss einen möglichen Freisetzungspfad für Radionuklide dar und ist somit im Rahmen der Langzeit-Sicherheitsanalysen zu berücksichtigen. Die Wirksamkeit dieses Freisetzungspfads hängt ebenfalls von der Form und der räumlichen Erstreckung der Auflockerungszone ab und von der Art der Gebirgsauflockerung. In überkonsolidierten Tonformationen zeigen sowohl empirische Befunde als auch experimentelle Untersuchungen ausnahmslos, dass die Auflockerungszone aus diskreten, exkavationsbedingten Trennflächensystemen besteht.

Im vorliegenden Bericht werden empirische und experimentelle Befunde zur Entstehung und Entwicklung der Auflockerungszone in tonreichen Formationen zusammengetragen und interpretiert. Die geowissenschaftlichen Grundlagen stammen vorwiegend aus dem Forschungs- und Entwicklungsprogramm des Felslabors Mont Terri sowie aus anderen Felslabors in Tonformationen. Sie dienen zur Überprüfung der Gültigkeit der bautechnischen Entwurfskriterien und sicherheitstechnischen Anforderungen zur Auflockerungszone im Rahmen der Etappe 2 des Sachplanverfahrens und zur Bewertung der Übertragbarkeit der Erkenntnisse auf die Verhältnisse in den vorgeschlagenen Standortgebieten der Nordschweiz.



## Table of Contents

Zusammenfassung.....	I
Table of Contents .....	III
List of Tables.....	V
List of Figures .....	VII
<b>1 Introduction .....</b>	<b>1</b>
1.1 Background and scope .....	1
1.2 Objectives .....	2
1.3 Report outline .....	2
<b>2 The EDZ - features, phenomena and processes .....</b>	<b>3</b>
2.1 Definition of disturbed and damaged zone .....	3
2.2 Current state of knowledge.....	4
2.2.1 Basic considerations .....	4
2.2.2 Indurated clays.....	5
2.2.3 Experience from the Meuse/Haute Marne URL .....	6
2.3 EDZ characterization .....	8
2.3.1 Structural characterization .....	8
2.3.2 Geomechanical characterization.....	9
2.3.3 Hydraulic characterization.....	9
2.3.4 Complementary evidence .....	10
<b>3 Mont Terri Site .....</b>	<b>11</b>
3.1 Opalinus Clay .....	11
3.2 Mont Terri URL.....	11
3.3 Stress field at the URL.....	14
3.4 Synopsis of achievements from previous EDZ studies at Mont Terri .....	14
3.4.1 Conceptual models for EDZ related features, phenomena and processes .....	15
3.4.2 Influence of support and orientation .....	18
<b>4 EDZ-related experimental database from Mont Terri.....</b>	<b>19</b>
4.1 EZ-A Niche.....	20
4.1.1 Location and local geological setting .....	20
4.1.2 Excavation procedures and support measures .....	22
4.1.3 Excavation response .....	24
4.1.4 Long-term response .....	28
4.1.5 Summary of EZ-A results.....	28
4.2 Gallery 04 .....	31
4.2.1 Location and local geological setting .....	31
4.2.2 Excavation .....	31

4.2.3	Excavation response .....	35
4.2.4	Long-term monitoring .....	38
4.2.5	Summary of results .....	41
4.3	EZ-B Niche .....	43
4.3.1	Location and local geological setting .....	43
4.3.2	Excavation .....	43
4.3.3	Excavation response .....	43
4.3.4	Long-term response .....	45
4.3.5	Summary of results .....	45
4.4	HG-A Microtunnel .....	50
4.4.1	Location and local geological setting .....	50
4.4.2	Excavation .....	51
4.4.3	Excavation response .....	53
4.4.4	Long-term response .....	59
4.4.5	Summary of results .....	63
4.5	Gallery 08 .....	65
4.5.1	Location and local geological setting .....	65
4.5.2	Excavation .....	66
4.5.3	Excavation response .....	66
4.5.4	Long-term response .....	69
4.5.5	Summary of results .....	73
4.6	Mine-By Experiment .....	77
4.6.1	Location and local geological setting .....	77
4.6.2	Excavation .....	78
4.6.3	Excavation response .....	79
4.6.4	Long-term response .....	83
4.6.5	Summary of results .....	84
4.7	FE Gallery .....	87
4.7.1	Location and local geological setting .....	88
4.7.2	Excavation .....	89
4.7.3	Excavation response .....	91
4.7.4	Long-term response .....	102
4.7.5	Summary of results .....	103
4.8	Other relevant experience from Mont Terri .....	104
<b>5</b>	<b>The EDZ in the Opalinus Clay – derivation of a generalised conceptual framework</b> .....	<b>109</b>
5.1	Overview .....	109
5.2	Results of EDZ-related data analyses at Mont Terri .....	109
5.2.1	Identification and classification of excavation-induced features .....	109
5.2.2	EDZ related phenomena and processes .....	115
5.2.3	Further processes and phenomena during operations period .....	127
5.2.4	Synopsis of empirical and experimental evidence from Mont Terri .....	130

5.3	Conceptual framework for modelling the excavation response.....	131
5.3.1	Conceptualization of the rock fabric.....	131
5.3.2	Conceptualization of deformation behaviour .....	134
5.3.3	Effective stress framework .....	138
<b>6</b>	<b>Transferability approach</b> .....	<b>141</b>
6.1	Motivation and expected deliverables .....	141
6.2	Geological setting in the siting regions.....	142
6.2.1	Depth distribution and tectonic regime in Northern Switzerland .....	142
6.2.2	Stress conditions in the siting regions.....	144
6.2.3	Rock properties and rock models .....	147
6.3	Description of the transferability approach .....	152
6.3.1	Rationale.....	152
6.3.2	Applied modelling tools .....	156
6.3.3	Modelling approach.....	158
6.4	Results of the sensitivity analyses .....	162
6.4.1	Size and shape of the yield zone.....	162
6.4.2	Nomograms representing the baseline configuration .....	165
6.4.3	Effect of the stress magnitudes (RSR_max, RSR_min) .....	169
6.4.4	Effect of bedding plane stiffness .....	171
6.5	Summary.....	175
<b>7</b>	<b>Acknowledgements</b> .....	<b>177</b>
<b>8</b>	<b>References</b> .....	<b>179</b>

## List of Tables

Tab. 2-1:	Extent of fracture types around tunnels oriented parallel to $\sigma_h$ and $\sigma_H$ . Extent given in excavation radii $a$ (from Armand et al. 2014).....	6
Tab. 3-1:	Geotechnical reference parameters of the Opalinus Clay at the Mont Terri underground laboratory from Bock (2000).....	13
Tab. 3-2:	Latest estimates of rock strength from Giger & Marschall (2014).....	13
Tab. 3-3:	Stress tensor for Mont Terri Rock Laboratory (from Martin & Lanyon 2003a, Bossart & Wermeille 2003 and Corkum & Martin 2007).....	14
Tab. 4-1:	Excavation schedule for EZ-A Niche. ....	23
Tab. 4-2:	Convergence measurements in EZ-A Niche.....	26
Tab. 4-3:	Location and depth of borehole extensometers in EZ-A Niche.....	26
Tab. 4-4:	Convergence and diametral strain in EZ-A Niche and Extension. ....	29
Tab. 4-5:	Summary of observations for EZ-A Niche excavation.....	30
Tab. 4-6:	Excavation schedule for Gallery 04 and adjacent niches.....	33

Tab. 4-7:	Convergences measured during construction of Gallery 04 and adjacent niches. ....	36
Tab. 4-8:	Diametral strains for Gallery 04 at 100 days after excavation and most recent data. ....	42
Tab. 4-9:	Summary of observations for Gallery 04 excavation. ....	42
Tab. 4-10:	Monitoring boreholes around EZ-B Niche. ....	43
Tab. 4-11:	Summary of maximum displacement magnitude in mm for the different sections of the EZ-B Niche excavation. ....	45
Tab. 4-12:	Summary of observations for EZ-B Niche excavation. ....	49
Tab. 4-13:	HG-A excavation timetable. ....	51
Tab. 4-14:	HG-A excavation monitoring instrumentation. ....	52
Tab. 4-15:	Monitoring and packer intervals B-A02 and B-A03 TM coordinates. ....	55
Tab. 4-16:	Deflectometer and clinochain element locations as tunnel meterage (TM) and radial distance from centre line. ....	57
Tab. 4-17:	Summary of observations for HG-A Microtunnel excavation. ....	64
Tab. 4-18:	Overall schedule of Gallery 08 excavation. ....	66
Tab. 4-19:	Convergence profiles monitoring of excavation of Gallery 08 and summary of observations. ....	67
Tab. 4-20:	Convergence profiles monitoring of excavation of Gallery 08. ....	69
Tab. 4-21:	Summary of convergence data from Gallery 08. ....	74
Tab. 4-22:	Summary of observations for Gallery 08 excavation. ....	77
Tab. 4-23:	Monitoring instruments for the Mine-By Experiment. ....	79
Tab. 4-24:	Measured convergence (mm) in Mine-By Niche (taken from Martin et al. 2014b) ....	80
Tab. 4-25:	Best estimate of near field effective hydraulic conductivity (m/s) from hydrotesting campaigns in BMB-15 and BMB-16 (Achtziger et al. 2011). ....	82
Tab. 4-26:	Initial interval pressure (kPa) from hydrotesting campaigns in BMB-15 and BMB-16. ....	82
Tab. 4-27:	Summary of observations for MB Niche excavation. ....	87
Tab. 4-28:	Support used in excavation of FE Gallery. ....	90
Tab. 4-29:	Convergence sections in FE Gallery. ....	96
Tab. 4-30:	Measured convergences in FE Gallery approximately one month after excavation. ....	98
Tab. 4-31:	Measured strain normalised to gallery radius. ....	99
Tab. 4-32:	Extensometer sections in FE Gallery. ....	99
Tab. 4-33:	Summary of observations for FE Tunnel excavation. ....	104
Tab. 5-1:	Excavation support for different excavation orientations. ....	111
Tab. 5-2:	Inventory of EDZ-related structural features for excavations normal to bedding strike. ....	112

Tab. 5-3:	Inventory of EDZ-related structural features for excavations parallel to bedding strike. ....	113
Tab. 5-4:	Long-term monitoring convergence profiles at Mont Terri.....	116
Tab. 5-5:	Largest long-term slope (mm/ln(day)) for each convergence profile. Trend lines for slopes larger than 5 mm/ln(day) shown in <b>bold</b> in Fig. 5-6. ....	122
Tab. 5-6:	Short-term (100 days) diametral strain from selected convergence arrays for excavations heading 150° normal to bedding strike. ....	124
Tab. 5-7:	Long-term (most recent data 08/08/13) diametral strain from selected convergence arrays for excavations heading 150° normal to bedding strike.....	124
Tab. 5-8:	Short-term (100 days) diametral strain from selected convergence arrays for excavations heading 240° along to bedding strike. ....	124
Tab. 5-9:	Long-term (most recent data 08/08/13) diametral strain from selected convergence arrays for excavations heading 150° normal to bedding strike.....	125
Tab. 5-10:	Reference values of the anisotropic Young's modulus and Poisson's ratio (after Giger & Marschall 2014). ....	136
Tab. 6-1:	Overburden depth of the Opalinus Clay in the siting regions of Northern Switzerland (after Nagra 2010). ....	142
Tab. 6-2:	Reference principal total normal stress values as a function of depth. ....	146
Tab. 6-3:	Reference values of undrained shear strength $S_{u,GMi}$ , representing the rock models GM1-GM6. ....	150
Tab. 6-4:	Approximate relationship between strain and the degree of difficulty associated with tunnelling through squeezing rock. Note that this curve is for tunnels with no support (from Hoek & Marinos 2000).....	153
Tab. 6-5:	Compilation of convergence data in Opalinus Clay at Mont Terri and underground structures with similar argillaceous rocks. ....	155
Tab. 6-6:	Overview of input parameters for for the development of the nomograms.....	162
Tab. 6-7:	Summary of geometry of the yield zone (W, H in metres) and the associated average diametral strain, (see Fig. 6-14 for definitions). ....	164
Tab. 6-8:	Water contents used to derive undrained shear strengths for nomograms.....	167
Tab. 6-9:	Equivalent elastic moduli of the corresponding transverse isotropic homogeneous continuum.....	172

## List of Figures

Fig. 2-1:	Schematic illustrating definitions of EdZ and EDZ (Alheid et al. 2007). ....	3
Fig. 2-2:	Induced fracture networks at the main level of Meuse/Haute Marne URL for drifts.....	7
Fig. 2-3:	EDZ extent from Schuster et al. (2002): (a) in boreholes BED-C4-C8; (b) in boreholes BED-B18-B26 around the ED-B tunnel section. Purple bar indicates extent of damage.....	8

Fig. 3-1:	Map of Mont Terri Underground Rock Laboratory showing excavations, main facies and fault.....	12
Fig. 3-2:	Conceptual models of EDZ from Nussbaum et al. (2011).....	15
Fig. 3-3:	Conceptual model of EDZ for the EDB drifts excavated in $\sigma_H$ direction (bedding-strike normal) from Martin & Lanyon (2003a).....	16
Fig. 3-4:	Structural models of EDZ for the HG-A microtunnel excavated in $\sigma_h$ direction (along bedding strike) from Marschall et al. (2006).....	17
Fig. 4-1:	Locations of excavations considered in this chapter. ....	19
Fig. 4-2:	Structural mapping of the excavation face of EZ-A Niche at TM20.....	21
Fig. 4-3:	Structural mapping of (a) the first part of EZ-A Niche; (b) the EZ-A Niche Extension. ....	22
Fig. 4-4:	Planned excavation geometry for EZ-A Niche.....	23
Fig. 4-5:	Photographs illustrating the development of the rockfall in the EZ-A Niche 11-12/09/03 (taken from Nussbaum et al. 2004). ....	24
Fig. 4-6:	As-built profiles of the EZ-A Niche showing the region of collapse. ....	25
Fig. 4-7:	Locations of (a) convergence arrays in Gallery 04 and EZ-A Niche; (b) extensometer profile at EZ-A Niche TM12. ....	26
Fig. 4-8:	Measured convergences in the new profile at TM12 of EZ-A Niche.....	27
Fig. 4-9:	Short-term measured convergences EZ-A Niche Extension TM6. ....	27
Fig. 4-10:	Measured long-term convergences of EZ-A Niche Extension TM6 (Profile 4).....	28
Fig. 4-11:	Structural mapping of (a) Gallery 98 wall at start of EZ-A Niche and (b) Slot in floor of EZ-A Niche Extension (TM6.3).....	30
Fig. 4-12:	Structural mapping of the Gallery 04 access tunnel (for orientation see Fig. 4-1).....	32
Fig. 4-13:	Planned excavation shape for Gallery 04. ....	33
Fig. 4-14:	(a) Installation of GFK anchor at the EZ-B Start Niche and (b) view of the end of the GA04 access tunnel showing the anchors.....	34
Fig. 4-15:	Measured convergences in Profiles 1-3 during construction of Gallery 04 access tunnel. (a) Start Niche; (b) GM40; (c) GM68. Green vertical lines show approximate day when excavation face has passed beyond the measurement profile (1 <sup>st</sup> line 1 diameter, 2 <sup>nd</sup> line 2 diameters, etc.). ....	37
Fig. 4-16:	Measured long-term convergences in Gallery 04. Green lines show face advance in diameters and red lines show related excavation events. ....	38
Fig. 4-17:	Structural mapping of Start Niche face at (a) GM17 (ERT Ring 3) and (b) GM21. Bedding-parallel structures are oriented at 150/45°.....	39
Fig. 4-18:	Evolution of the average resistivity with time from 2004 July to 2008 April. Tunnel heading is 250°, SSE to left and ENE on the right side of diagrams.....	40
Fig. 4-19:	Reconstructed resistivities around Rings 1, 2 and 3 from July and December 2004 and April 2008. ....	40

Fig. 4-20:	Structural mapping of SB Niche: (a) east wall; (b) west wall; (c) invert; (d) DR Niche ENE wall .....	41
Fig. 4-21:	Pore pressures and atmospheric pressure (from nearby niche) from the EZ-B Niche.....	44
Fig. 4-22:	Long-term convergence measured in EZ-B Niche. ....	45
Fig. 4-23:	Structural mapping of EZ-B Niche walls. Note dense network of EDZ fractures in sidewall of Gallery 04 from (Yong 2008). ....	46
Fig. 4-24:	Extent of fractured (red marker) and perturbed zone around EZ-B Niche from (Yong 2008). ....	47
Fig. 4-25:	Integrated analysis of BEZ-B3 drilled prior to excavation of EZ-B Niche. Intersections of mapped bedding-parallel shears with BEZ-B3 (blue spheres) and the advancing niche face are shown in the longitudinal-section (top). Lower plots show modelled stress ratios, DOPTV imaging, and seismic parameters derived from logging (from Yong 2008). ....	48
Fig. 4-26:	Mapping of front wall of HG-A Niche showing relationship between bedding-parallel faulting and microtunnel.....	50
Fig. 4-27:	Schematic drawing of the microtunnel and the site instrumentation.....	53
Fig. 4-28:	Laser scans of un-lined portion of the microtunnel TM6-TM13.....	54
Fig. 4-29:	View towards end of microtunnel showing development of breakout zones at a) TM0-TM3 and b)TM6-TM9. ....	54
Fig. 4-30:	Structural mapping of microtunnel TM6-TM13 (a) March 2005; (b) February 2006 (Nussbaum et al. 2005a, b; Nussbaum & Bossart 2006).....	55
Fig. 4-31:	Response during microtunnel excavation in BA02 and BA03: (a) piezometer interval pressure; (b) packer pressure. ....	56
Fig. 4-32:	Response during microtunnel excavation in B-A04, B-A05, B-A06 and B-A07. (a) deflectometers,(b) clinochains.....	58
Fig. 4-33:	Response during microtunnel excavation in B-A02 and B-A03. (a) piezometer interval pressure, (b) packer pressure. ....	60
Fig. 4-34:	Response after HG-A microtunnel excavation in horizontal and vertical extensometers. ....	61
Fig. 4-35:	Response after microtunnel excavation in strain gauge array within HG-A microtunnel.....	61
Fig. 4-36:	Response after HG-A microtunnel excavation in boreholes B-A04, B-A05, B-A06 and B-A07: (a) deflectometers, (b) clinochains.....	62
Fig. 4-37:	Response after HG-A microtunnel excavation in borehole stressmeter (triple strain gauges).....	63
Fig. 4-38:	The main fault in the side wall and invert of Gallery 08. ....	65
Fig. 4-39:	Measured short-term (100 days) convergences in Gallery 08. ....	68
Fig. 4-40:	Measured short-term convergences in Gallery 08: (a) DR-A Niche (Niche 1) and (b) TT Niche (Niche 4). ....	68
Fig. 4-41:	Long-term measured convergences in Gallery 08. ....	70

Fig. 4-42:	Long-term measured convergences in Gallery 08: (a) DR-A Niche (Niche 1) and (b) TT Niche (Niche 4). .....	70
Fig. 4-43:	Geodetic measurement sections and point locations. ....	71
Fig. 4-44:	Survey marks in different galleries of the laboratory with the selected fix-points. ....	72
Fig. 4-45:	Uplifts in Gallery 08 from September 2007 to January 2009. ....	72
Fig. 4-46:	Geological map of the invert between GM 70 and GM 85 (from Nussbaum et al. 2010). Note the very low frequency of pre-existing tectonic faults (in red) and by contrast the well-developed EDZ fracture network (in grey). ....	75
Fig. 4-47:	Geological and structural map of DR-A Niche. ....	76
Fig. 4-48:	Geometry of Mine-By Niche and associated support (anchors and shotcrete). ....	78
Fig. 4-49:	Excavation sequence and support installation. ....	79
Fig. 4-50:	Best estimate interval conductivity (m/s) versus radial distance from tunnel axis for the three hydrotesting campaigns in BMB-15 and BMB-16. ....	83
Fig. 4-51:	Long-term measured convergences in Mine-By Niche. ....	84
Fig. 4-52:	Location of sensors and resin injection boreholes around Mine-By Niche. ....	85
Fig. 4-53:	The peak yield stress state (in situ) at the location of piezometers when the piezometers showed the rapid pore-pressure drop. ....	86
Fig. 4-54:	Visualization of FE Experiment. ....	87
Fig. 4-55:	Face mapping from FE Gallery at GM26.5 (left) and at GM43.5 (right). ....	89
Fig. 4-56:	Initial excavation of FE Gallery from FE-A Niche. ....	89
Fig. 4-57:	Visualization of FE far-field monitoring borehole array. ....	91
Fig. 4-58:	Location in plane normal to excavation of piezometer interval and packer midpoints around FE Gallery. ....	92
Fig. 4-59:	Pore pressure response to FE Gallery excavation in monitoring borehole array. ....	93
Fig. 4-60:	Delta pore pressure as a function of distance ahead of the FE Gallery excavation face. ....	94
Fig. 4-61:	FE Gallery far-field piezometer and packer response. Peak change in pressure (DP) and location relative to the face when it occurred. ....	95
Fig. 4-62:	Geometry of FE Gallery convergence sections and extensometer sections. ....	96
Fig. 4-63:	FE Gallery Convergence measurements versus distance behind excavation face for P1-P7. ....	97
Fig. 4-64:	Geological mapping of excavation face of FE Gallery at approximate locations of convergence sections (from Jaeggi, Lisjak et al. 2012). ....	98
Fig. 4-65:	Measured strains versus days after excavation for extensometers at E1 and E2 sections of FE Gallery. ....	100
Fig. 4-66:	Strain profiles in tunnel wall at (a) E1 (GM 14.6 shotcrete only) and (b) E2 (GM 43.1 arches only) on 06/08/12. ....	101

Fig. 4-67:	Comparison of convergence and extensometer response, parallel to bedding (left) and normal to bedding (right) for FE Gallery.....	102
Fig. 4-68:	Linear and log-linear plots of total convergence measured at FE Gallery: (a), (b) C4 (GM 27.6 shotcrete only) and (c), (d) C7 (GM 44.2 – steel arches only) sections.....	102
Fig. 4-69:	Fracture counts in 0.5 m borehole intervals from around the EZ-B Niche and previous sub-parallel excavations (from Yong 2008).....	105
Fig. 4-70:	Breakout observations from Wermeille & Bossart (1999). .....	106
Fig. 4-71:	Vertical sections of the overcore at two depths, showing details of failure mechanisms. ....	107
Fig. 4-72:	BDZ status during long-term hydrotesting (left) and after collapse (right).....	108
Fig. 5-1:	Conceptual model of the EDZ fracture network for excavations normal to bedding strike at Mont Terri.....	112
Fig. 5-2:	Conceptual model of the EDZ fracture network for excavations parallel to bedding strike (MB Niche, FE Gallery) at Mont Terri:.....	114
Fig. 5-3:	Dimensions of EDZ envelope and pore pressure disturbed zone. ....	114
Fig. 5-4:	Locations of convergence profiles at Mont Terri (excludes FE Gallery). ....	117
Fig. 5-5:	Diametral strain against tunnel heading.....	118
Fig. 5-6:	Convergence versus time since excavation (log scale). Fitted maximum log-linear long-term slope shown as red line. ....	120
Fig. 5-7:	Location of long-term convergence profiles (excludes FE Gallery). ....	123
Fig. 5-8:	Piezometer pressure (after excavation) as a function of normalised radial distance from the excavation axis.....	126
Fig. 5-9:	Radial convergence normalised to maximum convergence. The data is compiled from all the instruments and only provides a trend.....	126
Fig. 5-10:	EDZ-related phenomena in the Opalinus Clay during the operations phase of the Mont Terri URL.....	127
Fig. 5-11:	Cyclic deformation experiment in the EZ-B Niche (Möri et al. 2012).....	128
Fig. 5-12:	Sample core from EZ-A boreholes.....	129
Fig. 5-13:	Geochemical processes near the microtunnel wall from Mayor & Velasco (2008).....	130
Fig. 5-14:	Heterogeneity and anisotropy in the Opalinus Clay at Mont Terri:.....	132
Fig. 5-15:	Complementary examples for the abstraction of the rock fabric of the Opalinus Clay at the tunnel scale.....	134
Fig. 5-16:	Complementary stiffness models of a fractured rock mass. ....	137
Fig. 5-17:	Strength anisotropy caused by bedding and / or sub-parallel fractures. ....	138
Fig. 6-1:	Tectonic units of the proposed geological siting regions in Northern Switzerland. ....	143
Fig. 6-2:	Schematic cross sections through the Mont Terri underground lab and the area of geological siting regions in Northern Switzerland.....	145

Fig. 6-3:	Overview of stress data in Northern Switzerland. ....	146
Fig. 6-4:	Depth trend of stress scenarios for Opalinus Clay in Northern Switzerland. ....	147
Fig. 6-5:	Relationship between undrained shear strength and water content of the Opalinus Clay. ....	148
Fig. 6-6:	Schematic destructuring of intact, anisotropic Opalinus Clay rock mass. ....	149
Fig. 6-7:	Undrained shear strength ( $S_u$ ), derived for the different rock models GM1 – GM6. ....	151
Fig. 6-8:	Numerically predicted squeezing convergence normalised to the tunnel diameter versus rock mass strength normalised by the far field maximum stress. ....	152
Fig. 6-9:	EDZ indicators related to long-term safety: .....	154
Fig. 6-10:	Measured diametral convergence strain in tunnels at Mont Terri versus Squeezing Index. ....	156
Fig. 6-11:	Model analyses addressing the impact of anisotropic stiffness on the size and extent of the EDZ around a circular cavity. ....	157
Fig. 6-12:	Transferability approach: workflow for the elaboration of the nomograms for the assessment of maximum repository depth. ....	159
Fig. 6-13:	Phase <sup>2</sup> Model with bedding represented by a variable joint network. ....	160
Fig. 6-14:	Relationship between undrained shear strength and tunnel strain established using Phase <sup>2</sup> for the Mont Terri Mine-By tunnel. ....	161
Fig. 6-15:	Definitions used for the geometry of the yield zone (W and H) and the associated diametral strain ( $D_e = 2 \cdot U_r / D$ %). ....	163
Fig. 6-16:	Examples of the geometry of the yield zone for baseline simulations with various undrained shear strengths. ....	163
Fig. 6-17:	Various relationships between the extent of yielding measured around the tunnel in the Phase <sup>2</sup> models, and the undrained shear strength and tunnel strain. ....	165
Fig. 6-18:	Nomogram of diametral tunnel strains in [%] for repository depths of 500 m, 700 m and 900 m using the reference stress scenario RSR_ref. ....	166
Fig. 6-19:	Nomograms of the diametral tunnel strains in [%] for various repository depths. ....	168
Fig. 6-20:	Comparison of the diametral tunnel strain from the reference stress case (RSR_ref) with the RSR_max and RSR_min cases, respectively. ....	170
Fig. 6-21:	Comparison of the diametral strain at a depth of 700 m with the normal stiffness of the bedding increased from 8000 MPa/m to 800000 MPa/m. ....	171
Fig. 6-22:	Effect of shear stiffness on diametral tunnel strain, for a depth of 700 m. ....	173
Fig. 6-23:	Effect of shear stiffness on diametral tunnel strain, for a depth of 700 m. ....	174

# **1 Introduction**

## **1.1 Background and scope**

The selection of sites for repositories for the disposal of radioactive waste in Switzerland is defined in the Sectoral Plan for Deep Geological Repositories ("SGT", SFOE 2008). The Swiss disposal concept envisages a separate repository for low- and intermediate-level waste (L/ILW) and another for high-level waste (HLW) – or, as a possibility, both together in a combined repository.

In Stage 1 of the Sectoral Plan several potential geological siting areas for the disposal of L/ILW and several potential geological siting areas for the disposal of HLW were selected. It is the objective of Stage 2 to select at least two sites for each repository type, followed by the selection of a single site for each repository type and the preparation of the application for the general license in Stage 3. As a decision basis for the second stage of the site-selection process, provisional safety analyses are to be elaborated together with further documents on construction feasibility and on the geological data. The technical documentation of the state of knowledge provides input for the qualitative and quantitative comparison of construction feasibility and long-term safety of the proposed repository settings in the candidate siting regions.

In SGT-Stage 2 construction feasibility has been the subject of elaborate repository design studies. A key aspect has been the assessment of the maximum allowable repository depth, while permitting adequate safety margins with regard to the ability to construct and service the underground facilities in the proposed siting regions. The evaluations have been based on geomechanical scoping calculations with a suite of numerical modelling tools (Nagra 2014a) commonly used in engineering practice to analyse the stability of the underground structures. The present report feeds in those engineering studies, in that it provides a framework for validating the geomechanical modelling approaches.

In the context of the provisional safety analyses the authorities have requested a balanced evaluation of the impact of repository-induced effects on long-term safety, including the role of the excavation damaged zone (EDZ) around the backfilled underground structures. Emphasis is on the hydraulic significance of the EDZ as a viable release path for radionuclides. Alcolea et al. (2014) evaluate the evolution of hydraulic conductance of the EDZ after backfilling and sealing of the underground structures, assuming that Opalinus Clay is the host rock. The authors are referring to phenomenological studies on EDZ self-sealing, EDZ related databases and in-situ validation experiments from the Mont Terri URL which have been detailed in the present report.

## 1.2 Objectives

This report presents a compilation of excavation and EDZ characterization experience from the Mont Terri Underground Rock Laboratory (URL). The aim is to summarize experience from excavation and develop a revised conceptual model of the creation and evolution of the EDZ around excavations at Mont Terri, in particular in excavations parallel to bedding. Previous work on the EDZ (Martin & Lanyon 2003) focused on the EDZ around the ED-B tunnel normal to bedding strike, but bedding-parallel excavations are likely to be relevant to the situation in a future deep repository. Further evidence is collected on the development of the EDZ in response to tunnel ventilation and on self-sealing processes, associated with the resaturation of the EDZ fracture network. The tectonic and stress situation at Mont Terri is not directly comparable to those expected in the siting regions due to the anticline-related faulting and stress anisotropy, although understanding of the fundamental failure and self-sealing mechanisms and controls will be of relevance.

The emphasis in the report is on providing:

- A synopsis of current understanding of the EDZ in clay-rich rocks;
- An overview of relevant data sources from Mont Terri;
- An analysis of EDZ observations from Mont Terri, aimed at identifying relevant phenomena and processes related to the creation and evolution of the EDZ,
- A transferability approach for using results from Mont Terri in the context of a deep geological repository.

## 1.3 Report outline

Chapter 2 gives an overview of current understanding of the EDZ in clay-rich rocks.

Chapter 3 provides background on the Mont Terri URL together with a brief summary of previous work on the EDZ at Mont Terri.

Chapter 4 presents observations of excavation response and EDZ from 2004 onwards (excavation of Gallery 04, Gallery 08, FE Gallery and associated niches).

Chapter 5 presents a synthesis of the observations and presents revised concepts for the EDZ.

Chapter 6 presents the transferability approach and expected relationships between rock mass properties and EDZ characteristics.

## 2 The EDZ - features, phenomena and processes

Excavation damaged and disturbed zones have been studied in a range of rocks since the 1980s (Wilson et al. 1983). In the context of Nagra's waste disposal programme, a conceptualization of the EDZ for a L/ILW repository in the Helvetic Marls was elaborated as part of the Geosynthesis Wellenberg (Nagra 1997). In the framework of the project "Entsorgungsnachweis", a comprehensive appraisal was dedicated to the creation and evolution of the EDZ for a SF(Spent Fuel)/HLW repository in the Opalinus Clay formation at a repository depth of 650 m (Nagra 2002). In the EURATOM Integrated Project "NFPRO", Nagra contributed to a state-of-the-art report on the creation and evolution of the EDZ (Alheid et al. 2007) comprising a summary of experience from investigations in hard rocks, rock salt and clay formations. The overall achievements of the "NFPRO" research programme were summarized in the Final Synthesis Report (Aranyossy et al. 2008). More recently, a review of studies on the EDZ around excavations in sedimentary rock was presented by Lanyon (2011). This chapter is largely taken from the aforementioned reports to provide some background to the discussion of the EDZ around excavations in the Opalinus Clay at Mont Terri.

### 2.1 Definition of disturbed and damaged zone

The creation of any underground opening creates a zone of disturbed rock around it. Within this disturbed zone there may exist a zone of damaged rock. In the past, various definitions of the disturbed and damaged zones have been used. This report uses the definitions of the Damaged and Disturbed Zone proposed by Tsang et al. (2005):

- The Excavation Disturbed Zone (EdZ) is a zone with hydromechanical and geochemical modifications, without major changes in flow and transport properties.
- The Excavation Damaged Zone (EDZ) is a zone with hydromechanical and geochemical modifications inducing significant changes in flow and transport properties. These changes can, for example, include one or more orders of magnitude increase in flow permeability.

Within the EdZ, state variables such as stress, water pressure, temperature, saturation, chemical composition of the pore water and related properties such as sonic velocity may be altered by the presence of the opening, but these changes are either temporary (e.g. saturation) or do not have a major influence on flow and transport properties (e.g. small changes in porosity due to changes in effective stresses).

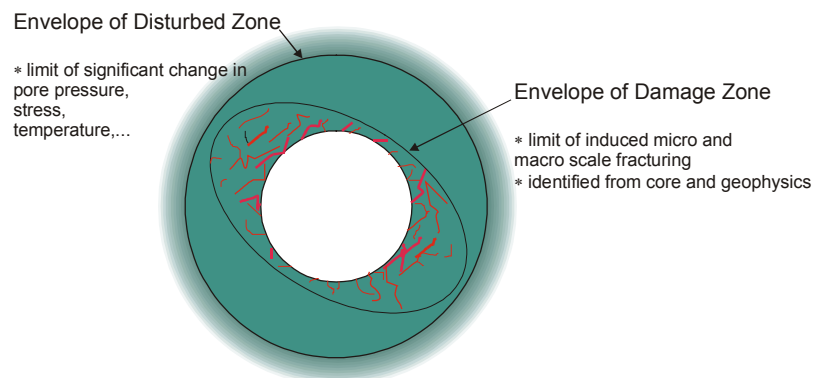


Fig. 2-1: Schematic illustrating definitions of EdZ and EDZ (Alheid et al. 2007).

These zones should be treated as "envelopes" encompassing those regions where property changes may occur, but also potentially including regions of unaltered rock properties (just as unaltered rock lenses may occur within a fault damage zone). The definitions are illustrated in Fig. 2-1.

## **2.2 Current state of knowledge**

### **2.2.1 Basic considerations**

The excavation of the underground facilities, the emplacement of wastes and the closure operations in different parts of the repository will induce perturbations of state variables (stress, water pressure, temperature, saturation, chemical composition of the pore water) in the host rock around the underground structures. These perturbations are induced by various coupled thermo-hydro-mechanical and –chemical phenomena (THM-C).

Alheid et al. (2007) compile the observations from experiments in various Underground Research Laboratories (URLs), together with laboratory experiments on rock samples and various numerical modelling activities. Valuable insight is gained into the deformation behaviour of the rock during construction of the cavities, associated with micro-cracking, fracturing and tunnel convergence in the vicinity of works, together with a progressive loading of the works structures, particularly on the lining structures. Further studies, dedicated to the chemical behaviour of the lining structures showed a strong interaction with mechanical behaviour, in particular through the corrosion of metallic components, the hydrolysis and carbonation of cement, and through the alkaline alteration and oxidation of interfaces and fractures filling within the host rock.

The nature and the magnitude of these phenomena evolve according to the disposal system life phases. They depend largely on industrial and natural processes. The main processes and phenomena related to the different phases of the repository lifecycle were summarized by Alheid et al. (2007):

- Excavation phase - a mechanical (un)loading generates an immediate mechanical response and initiates hydromechanical effects within the host rock.
- Operation phase (facilities opened to air circulation)–a hydric loading associated with ventilation (drainage and/or desaturation processes) initiates an unsaturated zone in the host rock; a thermal loading associated with the emplacement of exothermic waste canisters triggers thermo-hydromechanical effects in the host rock;
- Backfilling and sealing of emplacement rooms during operation phase – the change in ventilation conditions gives rise to an amplification of heating effects and coupled THM phenomena;
- Repository closure phase - the progressive resaturation of the host rock around the repository and saturation of the underground facilities induces chemical loadings able to amplify the interaction between chemical and mechanical processes.

### 2.2.2 Indurated clays

Indurated clays such as clay shales and claystones form a class of rock between soft rocks and hard clays. The strength of these rocks is relatively low but tunneling is still feasible even with standard methods and low to medium support measures. The permeability is very low and even existing natural fractures do not show increased permeability as long as a significant normal stress is acting on fracture surfaces.

The stability of excavations in hard rocks (e.g. Martin et al. 2001) can be considered under three classes:

- Structurally controlled failure;
- Stress-controlled failure;
- A combination of structure- and stress-controlled failure.

As compared to hard rocks, additional processes related to wetting can lead to failure:

- Swelling, weakening and softening (see Steiner 1993, 1996 and Einstein 1996, 2002);
- Shrinkage during drying and loss of strength due to repeated wetting/drying cycles (see Rejeb & Cabrera 2007).

Structurally-controlled wedge-type failures can be managed by maintenance of a compressive regime (Diederichs & Kaiser 1999) and identification of relevant discontinuity sets, although problems may occur at excavation intersections or regions with unexpected discontinuity orientations. The focus for the EDZ around repository tunnels is therefore on stress-controlled failure and combinations of stress/structure failure modes. The application of such a failure classification scheme to clay-rich rocks is complicated by compaction processes, bedding anisotropy and the influence of wetting.

The geometry of the EDZ in indurated clays is not only controlled by the primary stress tensor, rock anisotropy (stiffness and strength) and the heterogeneity of the rock mass (facies variability and tectonic features), but also by the excavation technique, tunnel geometry, tunnel support and ground interaction. During the construction phase the rock response is controlled by the creation of the new free surfaces. Part of the deformation already takes place in front of the tunnel face; it continues during excavation and even when the face advances beyond the point of observation. The latter is due to the loss of the support function of the tunnel face. In addition, the stress re-distribution and the associated changes in effective mean stress in the vicinity of the tunnel may locally cause squeezing and consolidation. This hydromechanically coupled process is strongly time-dependent due to the low hydraulic conductivity of the rock. The associated deformations are difficult to separate from other time-dependent deformations such as brittle creep which results from cataclastic failure processes.

Full scale investigations on EDZ development in indurated clays are limited, so far, to the underground laboratories at Mont Terri (Switzerland), Tournemire (France) and the Meuse/Haute Marne site (France). Experience from the Meuse/Haute Marne site is of special interest due to the lithostratigraphic similarities between the Callovo-Oxfordian and the Opalinus Clay formation.

### 2.2.3 Experience from the Meuse/Haute Marne URL

The maximum extent of fracture zones in different EDZ investigations at the Meuse/Haute Marne URL near Bure (Armand et al. 2013, 2014) have resulted in a well-developed model of EDZ fracture geometry controlled by the tunnel orientation relative to maximum horizontal stress. "Excavations exhibit extensional (mode I) and shear (mode II) fractures. Spalling is not the prevailing mechanism of failure due to the high mean stress compared to the Callovo-Oxfordian claystone strength. Shear failure seems to occur first from the excavation front face. Shear bands have been observed by the resin impregnation method at smaller scale confirming the shear failure mechanism." Armand et al. (2013,2014) showed that the fracture pattern and extent depend on the drift orientation versus the state of in situ stress. At the Meuse/Haute Marne URL the maximum principal stress  $\sigma_H$  is horizontal and approximately 1.3 times the vertical and minimum horizontal principal stresses  $\sigma_v$  and  $\sigma_h$  which are roughly equal (Wileveau et al. 2007).

The maximum extent of fracture zones in different drifts can be summarized as follows:

- Drifts parallel to  $\sigma_H$ : the extensional and shear fractures are observed within 0.8 and 2 radii from the wall, respectively. In the floor and ceiling, shear and extensional fracture zones are both present up to 0.3 radii.
- Drifts parallel to  $\sigma_h$ : the extensional and shear fractures are observed up to 1 and 2 radii respectively, in the floor and the ceiling. At the wall, shear and extensional fracture zones are both present up to 0.4 radii.

Fig. 2-2 illustrates the models of the EDZ fracture network for drifts parallel to the two horizontal principal stresses and Tab. 2-1 gives the extent of the different types of fracture zones. The region with extensional fractures (unloading - mode I) exhibits the highest hydraulic conductivity up to  $10^{-10}$  m/s. This high value is due to the fracture transmissivity and not the permeability of the rock matrix. Farther from the wall, the shear fractures exhibit low transmissivity, which does not significantly alter the average hydraulic conductivity.

Tab. 2-1: Extent of fracture types around tunnels oriented parallel to  $\sigma_h$  and  $\sigma_H$ . Extent given in excavation radii  $a$  (from Armand et al. 2014).

	Location	Extensional fracture extent (a)			Shear fracture extent (a)		
		Min	Mean	Max	Min	Mean	Max
$\sigma_h$ parallel	Ceiling	0.4	0.6	0.8	1.0	1.2	1.6
	Wall	0.2	0.2	0.4	-	-	-
	Floor	0.4	0.8	1.0	1.6	1.6	2.2
$\sigma_H$ parallel	Ceiling		0.2	0.3	-	-	-
	Wall	0.02	0.4	0.8	1.4	1.6	2.0
	Floor		0.2	0.3	-	-	-

extent not greater than network of extensional fractures.

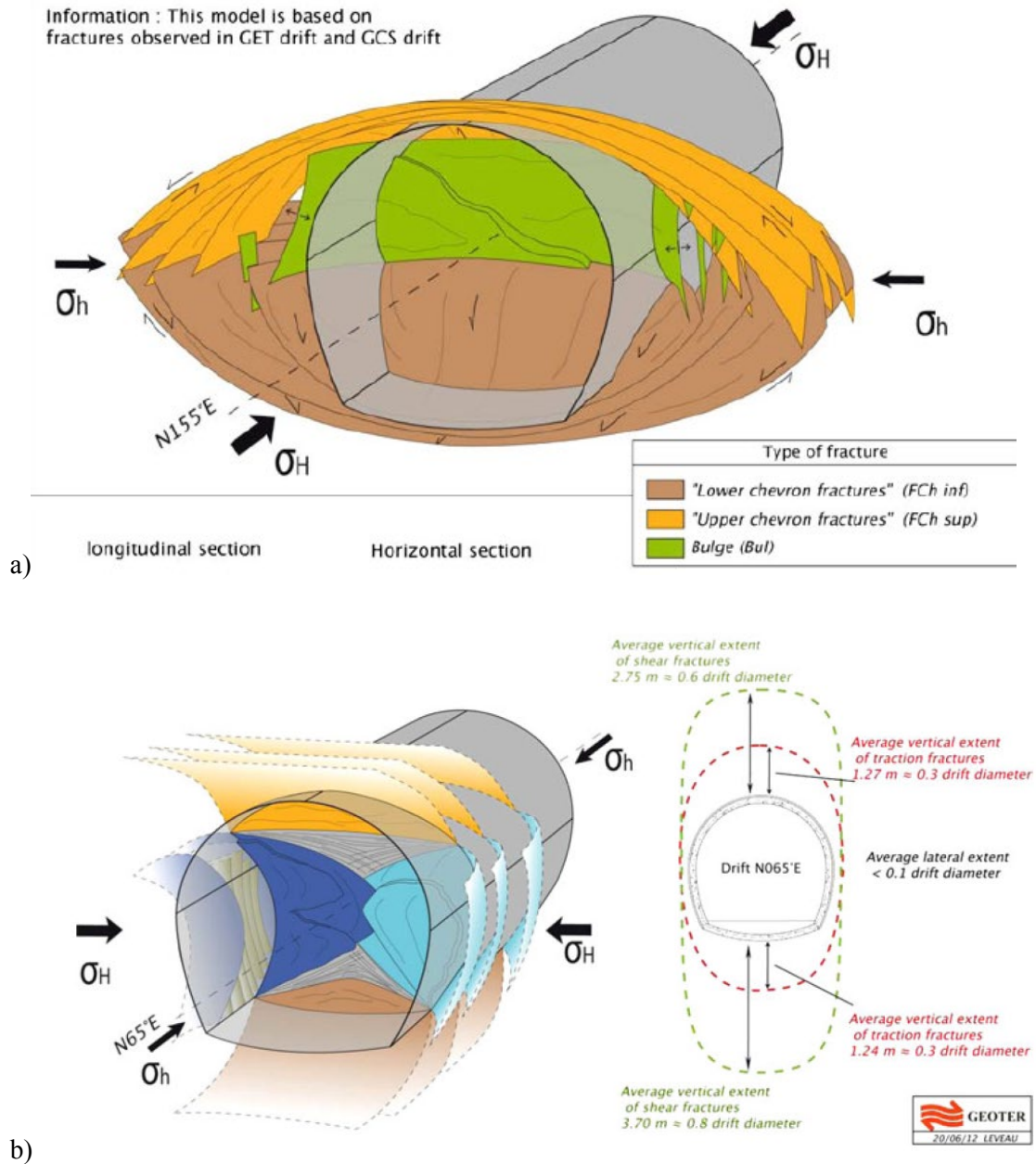


Fig. 2-2: Induced fracture networks at the main level of Meuse/Haute Marne URL for drifts  
a) parallel; b) perpendicular to the horizontal major stress (from Armand et al. 2014)

The observations from the Meuse/Haute Marne URL are not directly applicable to Mont Terri due to: the lower stress anisotropy; different bedding orientation; lack of pre-existing tectonic features, less pronounced material anisotropy and higher rock strength. However the key failure mechanisms in the EDZ at the Meuse/Haute Marne URL are:

- Extensional fracture generation around the tunnel nearfield – creating a connected fracture network close to the tunnel surface.
- Shear failure initiated ahead of the face and extending out in a curved trajectory into the roof, floor and side-walls.

It is likely that these mechanisms will be important at Mont Terri although their action will be complicated by the greater material and stress anisotropy.

## 2.3 EDZ characterization

### 2.3.1 Structural characterization

The extent and form of the EDZ is typically characterized using both geological and geophysical methods. Geological investigations include structural mapping of excavation surfaces (tunnel walls, niches and "windows") and core mapping of boreholes drilled from the excavation (most commonly radial boreholes). It is necessary to discriminate between natural (tectonic) fractures and faults, EDZ-related features and artificially induced fractures due to drilling and core handling.

A method for core mapping developed at Mont Terri involves resin injection into a pilot hole followed by subsequent overcoring (Bossart et al. 2002, 2004; Armand et al. 2007). The resin injection method allows identification of open (resin-impregnated) fractures within the EDZ and can give information on reactivation of pre-existing features, connectivity and structural relationships. A variation of this method has been used to investigate the damaged zone around boreholes. Larger scale sampling of the EDZ can be performed via slotting (Emsley et al. 1997; Mellanen et al. 2008) or block extraction.

Geophysical characterization methods include seismics/ultrasonics, geoelectrical and radar. Ultrasonic interval velocity measurements have been widely used at Mont Terri (Schuster et al. 2001, 2002; Contrucci et al. 2007) to determine the extent of the disturbed and damaged zones. In the Opalinus Clay at Mont Terri, interpretation is complicated by the rock mass anisotropy and a potential borehole damage zone (BDZ). Fig. 2-3 illustrates EDZ extent around Gallery 98 at Mont Terri according to relevant criteria. Schuster and Alheid (2007) and Shao et al. (2008) describe investigations at the Meuse/Haute Marne URL. The ultrasonic measurements may in addition be integrated with tomographic (Nicollin et al. 2008) or cross-hole surveys.

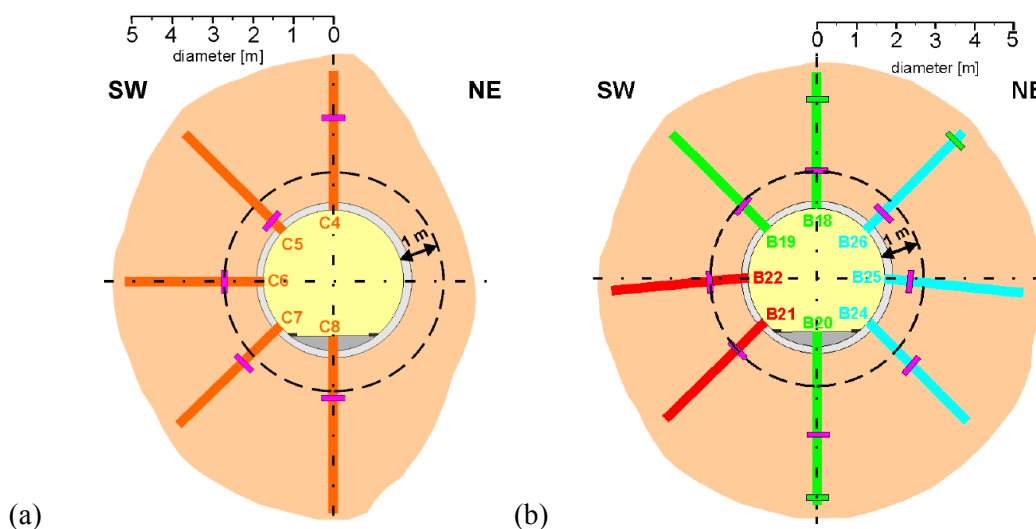


Fig. 2-3: EDZ extent from Schuster et al. (2002): (a) in boreholes BED-C4-C8; (b) in boreholes BED-B18-B26 around the ED-B tunnel section. Purple bar indicates extent of damage.

Geoelectrical methods have also been used at Mont Terri (Nicollin et al. 2010; Lesparre et al. 2013). although the presence of an unsaturated zone around the excavation can significantly influence the response and needs to be accounted for in any discrimination between the EdZ and EDZ.

### **2.3.2 Geomechanical characterization**

Geomechanical methods of in situ characterization of the EdZ and EDZ typically relate to the long-term monitoring of deformation at the tunnel surface (convergence), or in the rock (extensometers), or of stress via load cells (usually at the liner/rock interface).

Different forms of borehole deformation sensors include:

- Chain inclinometers to measure changes in borehole inclination;
- Extensometer chains to measure relative deformation along a borehole;
- Mineable extensometers to monitor ahead of the advancing excavation face.

In a "Mine-By" experiment, extensometers are emplaced in boreholes prior to excavation and monitor the response as the excavation face advances. Ideally the "head" of any extensometer chain should be located sufficiently far from the excavation to be outside the region of significant deformation.

Convergence measurements involve the installation of fixed targets (pins) on the excavation surface and periodic measurement of the relative motion. Measurements can be of either radial or total movement.

### **2.3.3 Hydraulic characterization**

Monitoring of pore pressures during excavation can identify stress changes and yielding/fracturing. In low permeability rocks changes in stress result in volumetric strains and pore pressure changes that cannot be quickly dissipated. The magnitude and sign (compression/dilation) can be used to characterize the response to excavation (see Martin and Lanyon 2003a). Where piezometers are located within the plastic/yield zone the creation of fractures or microcracking, leading to enhanced permeability can result in rapid depressurization close to the advancing tunnel face.

Hydrotesting can be used to identify the extent of any changes in permeability due to fracturing or microcracking. Tests can be made before and after excavation to identify changes in properties (Emsley et al. 1997). Alternatively where no prior test is possible (e.g. radial boreholes drilled from the excavation) it is necessary either to have a robust understanding of the undisturbed permeability or to perform tests sufficiently far from the excavation to identify undisturbed conditions.

Pneumatic testing offers an alternative to hydrotesting in partially saturated rocks (Matray et al. 2007). Measurements of saturation can also be made from core or by Time Domain Reflectometers (TDRs) or other sensors.

### **2.3.4 Complementary evidence**

Other complementary evidence can come from geochemical signatures in the tunnel near field. At Mont Terri gypsum spots on fracture surfaces (Bossart et al. 2002, 2004) have been used to identify the extent of connected air-filled EDZ fracture network. Vinsot et al. (2014) present evidence of mineralogical changes associated with the oxidation front around excavations at the Meuse/Haute Marne URL. Oxidised features were found on excavation-induced fractures up to 1.8 m from the tunnel wall. The distance from the tunnel wall was found to depend on the morphology of the EDZ fracture system.

Evidence of the development of similar oxidation fronts around excavations in clay-rich rocks has been found in the Toarcien marls at Tournemire (Matray et al. 2007) and in the Boom Clay at Mol (De Craen et al. 2008).

### 3 Mont Terri Site

Chapter 3 gives an introduction of the geological site conditions at the Mont Terri Underground Rock Laboratory (URL). This includes a general overview of the underground structures and a brief description of the main sedimentary and tectonic features of the Opalinus Clay on the site scale. In addition, a summary of the geotechnical reference parameters is given. Furthermore, the complex tectonic and stress situation at Mont Terri, which is governed by the anticline-related faulting and stress anisotropy, is discussed. Finally, the achievements of previous EDZ-related studies are summarized.

#### 3.1 Opalinus Clay

The Opalinus Clay in Northern Switzerland has been identified as a potential host rock formation for the disposal of radioactive waste (Nagra 2002). The formation is part of a thick Mesozoic - Tertiary sedimentary sequence which was deposited 180 Ma ago in a shallow marine environment. The Opalinus Clay at Mont Terri can be divided into three main facies (Nussbaum et al. 2011):

- A shaly facies in the lower part of the formation (argillaceous and marly shales with micas and nodular, bioturbated layers of marl or with mm-thick layers of sandstones),
- A sandy facies in the middle and upper part of the formation (marly shales with layers of sandstones and bioturbated limestones or with lenses of grey, sandy limestones and mm-thick layers of white sandstones with pyrite) and
- A thin carbonate-rich, sandy facies in the middle of the formation (calcareous sandstones intercalated with bioturbated limestone beds, the latter showing a high detrital quartz content).

#### 3.2 Mont Terri URL

The Mont Terri URL was established in 1996 and is located in the Jura Mountains in northwest Switzerland (Thury & Bossart 1999). It is located at a depth of 300 m and is accessed from the Security Tunnel of the A16 motorway tunnel. The layout of the rock laboratory is shown in Fig. 3-1. The rock laboratory has been developed over time with new galleries being excavated in 1998, 2004 and 2008. Experiments are typically located in niches off the galleries. The research galleries have a total length of about 500 m.

The rock laboratory is located entirely in the Opalinus Clay formation, which has an apparent thickness of 160 m and a true thickness of 90 m (Nussbaum et al. 2011). The URL is located in the south-eastern limb of the Mont Terri anticline and bedding dips to the SSE. Dip angles increase from 30° to 50° between the upper and lower boundaries of the Opalinus Clay. Nussbaum et al. (2011) identify three different fault systems at Mont Terri:

- SSE dipping fault system: fault planes sub-parallel to bedding.
- Low angle SW-dipping and flat-lying fault system: gently SW-dipping fault planes with dip angles ranging from 10° to 40° and flat-lying (sub-horizontal) fault planes with dip angles ranging from 0° to 15°. These two fault systems are considered together due to their similar geometric features.
- N- to NNE-striking fault system: N-S-striking fault planes dip moderately with angles varying between 20° and 60°.

An extensive fault zone "Main Fault" is present in the shaly facies intersecting the Motorway Tunnel, Safety Gallery, Gallery 98 and Gallery 08. Main Fault is approximately 1 m thick dipping at 55-60° to the SSE. Bedding plane dips change from about 30° in the northern part of the laboratory to 50° in the southern part, across Main Fault.

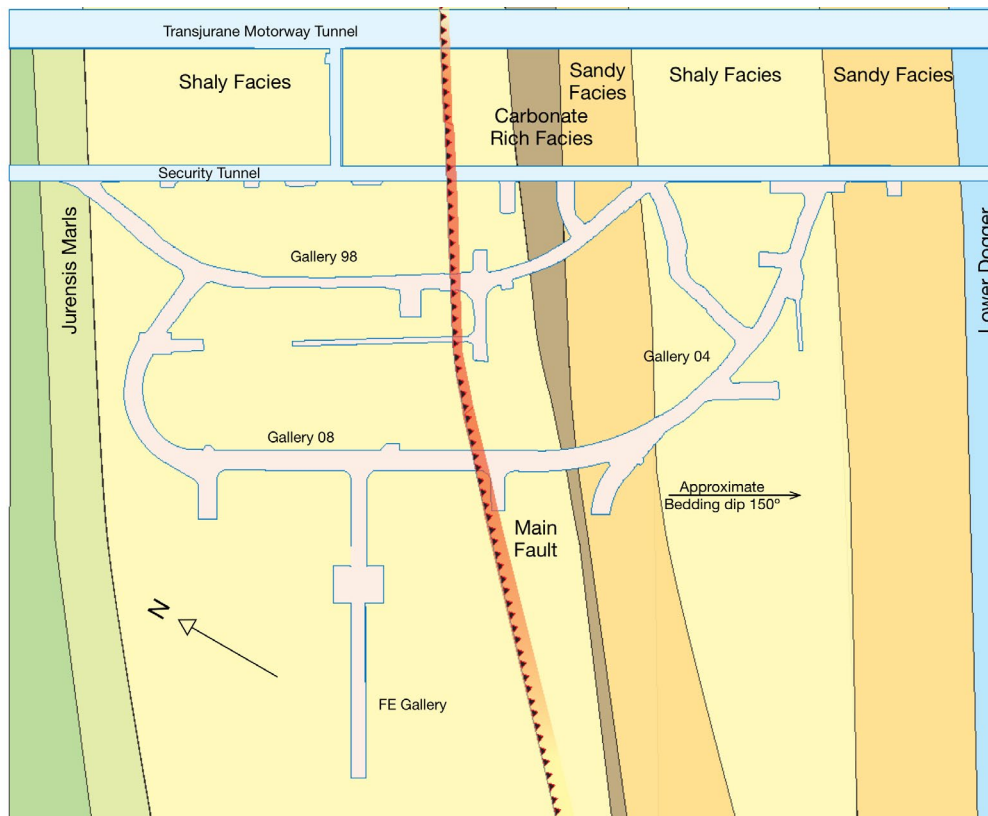


Fig. 3-1: Map of Mont Terri Underground Rock Laboratory showing excavations, main facies and fault.

At Mont Terri the Opalinus Clay formation reached a maximum depth of about 1000 m and can be classified as a slightly overconsolidated rock; the estimated overconsolidation ratio varying between 2.5 and 3.5 (estimates derived from both laboratory tests and burial history). Quantitative laboratory analyses of core samples from Mont Terri showed a total mass fraction of clay minerals of 47 – 60%, a quartz content of 14 – 30% and 16 – 22% carbonates. The fraction of swelling clay minerals of 23 – 27% (illite, illite / smectite mixed layers) is of particular relevance for the consolidation behaviour of the rock. Further minerals are siderite, pyrite and feldspar (Pearson et al. 2003).

Intact Opalinus Clay at Mont Terri exhibits a very low hydraulic conductivity, with a mean hydraulic conductivity of  $2 \times 10^{-13}$  m/s, and a moderate spatial variability, which is less than an order of magnitude (Marschall et al. 2004). Microscopic observation of the fabric of the Opalinus Clay at Mont Terri suggests that there may be a significant core-scale hydraulic anisotropy. The ratio between bedding-parallel and bedding-normal permeability is thought to lie between 1 and 10. The very fine pore network is saturated with a Na-Cl-SO<sub>4</sub> connate pore water of marine origin with a mean content of dissolved solids of about 12 g/l. Even though the

rock is fractured, a distinct fracture transmissivity has not been observed, suggesting that the fractures are generally tight for the given stress conditions.

Rock mechanical characterization of the Opalinus Clay is challenging due to its ultra-low permeability, overconsolidation and distinct bedding. Typical values for key geotechnical parameters are shown in Tab. 3-1 (Bock 2000).

Tab. 3-1: Geotechnical reference parameters of the Opalinus Clay at the Mont Terri underground laboratory from Bock (2000).

Parameter	Value	Remarks
Bulk density [ $\text{Mg/m}^3$ ]	2.45	water saturated
Grain density [ $\text{Mg/m}^3$ ]	2.71	
Porosity [%]	13.7	range: 10 – 16%
Water content [% wt]	6.1	range: 6 – 7%
Young's modulus [GPa]	10 4	parallel to bedding normal to bedding
Shear modulus	1.2	
Poisson's ratio [-]	0.27	
Uniaxial compressive strength [MPa]	10 16	parallel to bedding normal to bedding
Tensile strength [MPa]	2 1	parallel to bedding normal to bedding
P-wave velocity [m/s]	3410 2620	parallel to bedding normal to bedding
S-wave velocity [m/s]	1960 1510	parallel to bedding normal to bedding
Fracture toughness $K_{IC}$ [ $\text{MN/m}^{1.5}$ ]	0.53 0.12	parallel to bedding normal to bedding

The most recent estimates for rock strength are given in Tab. 3-2 and are taken from Giger & Marschall (2014).

Tab. 3-2: Latest estimates of rock strength from Giger & Marschall (2014).

Parameter	Best estimate	Range	Remarks
Uniaxial compressive strength [MPa]	17	12-24	parallel to bedding normal to bedding
	8	7-13	inclined bedding, relevant for caverns parallel to $\sigma_h$

### 3.3 Stress field at the URL

Martin & Lanyon (2003a, b) and Bossart & Wermeille (2003) report results from several stress measurement campaigns at the Mont Terri Rock Laboratory including the results of a previous data compilation by Wermeille & Bossart (1999). Martin & Lanyon (2003a) suggest that the stress tensor given in Tab. 3-3 is representative of the stress state at the laboratory although the greatest uncertainty is in the estimate of  $\sigma_3$ . In particular the low value of 0.6 (derived from the analysis of an undercore experiment) is below the best estimate of pore pressure at the laboratory (Marschall et al. 2004).

Tab. 3-3: Stress tensor for Mont Terri Rock Laboratory (from Martin & Lanyon 2003a, Bossart & Wermeille 2003 and Corkum & Martin 2007).

Martin & Lanyon (2003a)					
	Orientation	Trend (°)	Plunge (°)	Magnitude Estimate	Range (MPa)
$\sigma_1$	Vertical	210	70	6.5	6-7
$\sigma_2$	NW-SE	320	10	4.0	4-5
$\sigma_3$	NE-SW	50	15	0.6	0.6-2
Bossart & Wermeille (2003)					
$\sigma_1$		210	70	6.5	6-7
$\sigma_2$		320	10	4.4	4-5
$\sigma_3$		50	20	2.2	2-3
Corkum & Martin (2007)					
$\sigma_1$	Vertical	210	70	6.5	6-7
$\sigma_2$	NW-SE	320	7	4.0	4-5
$\sigma_3$	NE-SW	52	18	2.2	2-3

Recent studies by Corkum & Martin (2006) and Corkum & Martin (2007) led to a revised estimate of  $\sigma_3$  magnitude as shown in Tab. 3-3. Note that there are minor orientation differences<sup>1</sup>. The recommended full tensor for the Mont Terri rock laboratory is that from Corkum & Martin (2007).

More recent studies (Enachescu 2011) have involved stress measurements in the surrounding lithologies at Mont Terri to avoid problems of measurement in the anisotropic moisture-sensitive Opalinus Clay (see Martin & Lanyon 2003b for a discussion of the difficulties of measurements in the Opalinus Clay).

### 3.4 Synopsis of achievements from previous EDZ studies at Mont Terri

Previous studies of the EDZ at Mont Terri (Blümling et al. 2007; Bossart et al. 2002, 2004; Martin & Lanyon 2003a; Nussbaum et al. 2011) have suggested conceptual models for the EDZ around excavations.

<sup>1</sup> Note: Table 1 and Figure 6 of some copies of Corkum & Martin (2007) are in error. The values given in Tab. 3-3 are correct.

### 3.4.1 Conceptual models for EDZ related features, phenomena and processes

Nussbaum et al. (2011) present a refinement of the earlier models from Bossart et al. (2002, 2004) as shown in Fig. 3-2. The model (Fig. 3-2a) idealises the EDZ as an inner shell of thickness 1 m with a network of interconnected (air-filled) fractures with transmissivities ranging from  $10^{-9}$  to  $10^{-5}$  m<sup>2</sup>/s (highest transmissivity within 0.4 m of the tunnel wall). An outer 1 m-thick shell contains isolated, partly saturated fractures of lower transmissivity ( $10^{-12}$  to  $10^{-9}$  m<sup>2</sup>/s). The three-dimensional arrangement of the EDZ fractures is influenced by the bedding plane anisotropy, especially in the roof and floor of the excavation. The orientation of some extensional fractures in the sidewalls of Gallery 08 suggests that these were formed in response to stress redistribution ahead of the face.

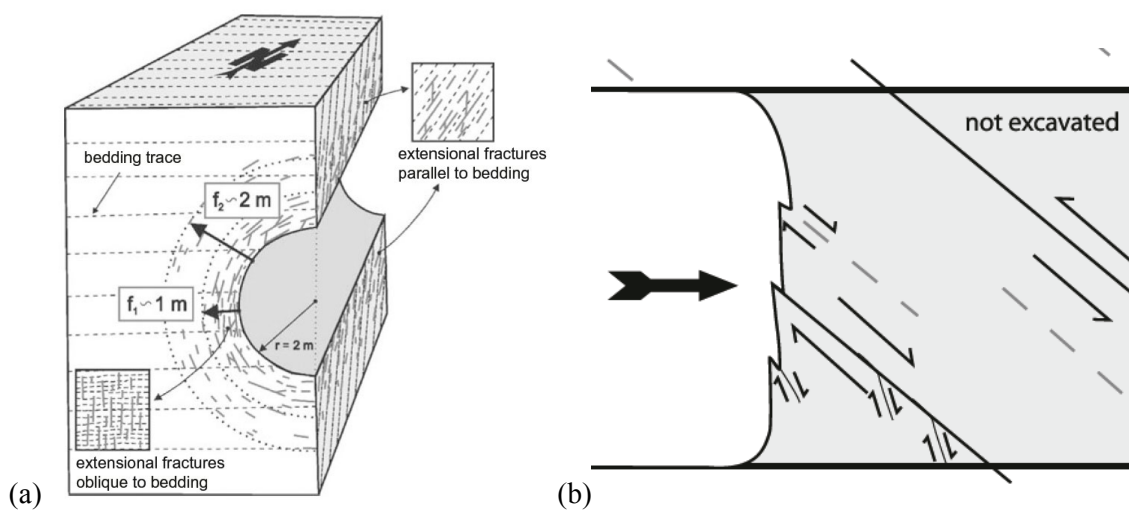


Fig. 3-2: Conceptual models of EDZ from Nussbaum et al. (2011).

(a) radial distribution of fracturing around tunnel; (b) mechanism for development of shear planes ahead of the face.

In addition to the extensional features shown in Fig. 3-2a, EDZ shear fractures identified in the tunnel face of Gallery 08 are interpreted as being formed during the reactivation of bedding-parallel structures ahead of the face (see Fig. 3-2b). These fractures strike parallel to the gallery face and are inclined to bedding at 20-40°. The system of pre-existing bedding planes, sub-parallel fault planes and EDZ shear fractures are activated in normal faulting mode and show geometries similar to strike-slip fault systems (Kim et al. 2004).

Martin & Lanyon (2003a) developed a conceptual model of the EDZ around the ED-B section of Gallery 98 incorporating a revised stress tensor and previous work from Bossart et al. (2002). Extensional fractures formed in the excavation side-walls while the EDZ in the roof and floor was related to a region of potential bedding-slip and subsequent kink/buckling failures (see Fig. 3-3). The low permeability of the Opalinus Clay also resulted in significant pore pressure disturbance (both positive and negative) which influenced the time-dependent development of the EDZ. Blümling et al. (2007) show a slightly revised version of the model of Martin & Lanyon (2003a), incorporating the observed buckling failure and through-going shears associated with bedding slip.

EDZ investigations around the HG-A microtunnel (see Chapter 4.3) resulted in the development of a structural model (Fig. 3-4) for the EDZ around the bedding-strike parallel microtunnel. The influence of pre-existing tectonic features was identified as an important control on fracture development while the interaction of stress and structural (orientation to bedding) controls were also considered.

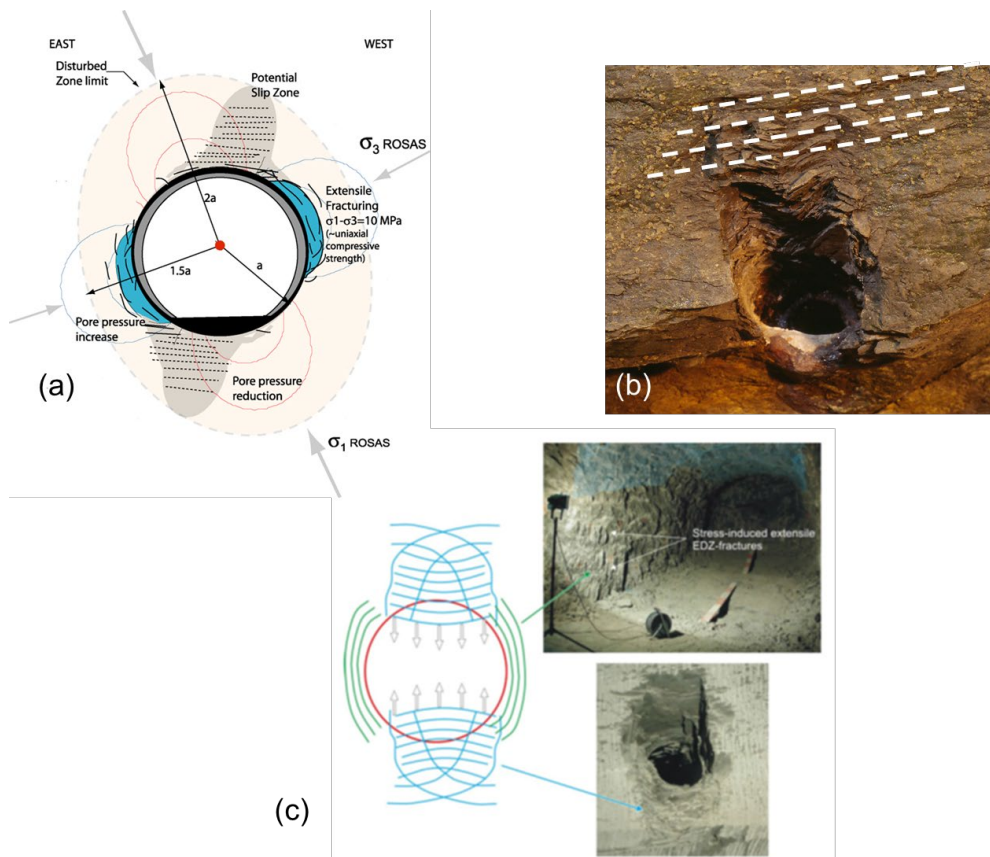


Fig. 3-3: Conceptual model of EDZ for the EDB drifts excavated in  $\sigma_H$  direction (bedding-strike normal) from Martin & Lanyon (2003a).  
 (a) Schematic sketch; (b) photograph of damage zone around borehole showing buckling failure and relationship to bedding (white lines); (c) revised sketch from Blümling et al. (2007).

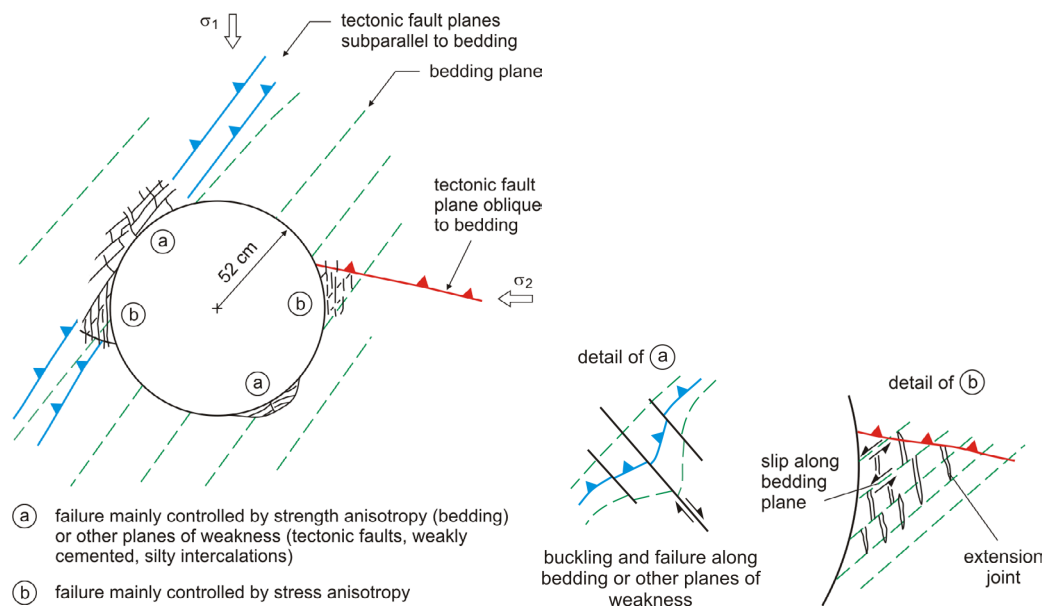


Fig. 3-4: Structural models of EDZ for the HG-A microtunnel excavated in  $\sigma_h$  direction (along bedding strike) from Marschall et al. (2006).

The various models discussed above should be viewed as complementary rather than alternative each placing different emphases on various aspects of the EDZ and excavation orientation. A composite model would include the following mechanisms:

- *Extensional fracturing* - Extensional fracturing has been commonly observed at Mont Terri (Bossart et al. 2002, 2004; Martin & Lanyon 2003a; Nussbaum et al. 2011). Nussbaum et al. (2011) suggest that such fractures form an interconnected network within 1 m of the tunnel wall but tend to be isolated structures beyond this.
- *Bedding and bedding-parallel slip* - Anisotropy and small-scale heterogeneity may induce bedding-parallel slip structures creating chimney-like formations (Martin & Lanyon 2003a).
- *Buckling and kink failures* - Commonly associated with zones of bedding slip are buckling zones characterized by multiple through-going shears. These zones have been imaged around boreholes (Blümling et al. 2007; Vietor et al. 2006).
- *Shear fractures* - Nussbaum et al. (2011) identify a set of shear fractures formed parallel to the excavation face and systematically inclined to bedding. They suggest that these shears form in response to deformation ahead of the face along bedding-parallel structures as normal faults.
- *Reactivation of tectonic features* - Pre-existing tectonic fractures may also be reactivated (typically in shear) by similar processes to those responsible for the EDZ fractures. Such features may also limit the extent of EDZ fracturing as suggested by Marschall et al. (2006) and Yong et al. (2008).

In addition to these "mechanical" processes the effect of humidity or wetting can result in significant weakening of the rock. Similarly the creation of unsaturated zones resulting in significant suction can, at least temporarily, stiffen/strengthen the rock.

### **3.4.2 Influence of support and orientation**

Prior to excavation of the EZ-A Niche there was only limited experience of different tunnel orientations or support (see Nussbaum 2004). The 10 m long EB Niche with a diameter of 3.60 m, excavated towards SSE, was not lined and was stable during the whole installation period of about 2 months, while the MI Niche excavated in WSW direction (parallel to the EZ-A niche) suffered one large breakout of about 5 m<sup>3</sup> in the northern wall due to tectonic fractures. This was thought to relate to the higher deviatoric stress in this direction although other niches in this orientation (FM-C, SHGN, C) were stable.

Most excavations were not immediately lined with shotcrete and remained open for several days. This was the case during the excavation of the new gallery in 1997/98, where more than 200 m of galleries were excavated. During the excavation period only small breakouts (< 1 m<sup>3</sup>) were observed (typically in the roof).

## 4 EDZ-related experimental database from Mont Terri

Chapter 4 reviews relevant information from EDZ-related experiments at the Mont Terri URL during the last 10 years, comprising important geological and tectonic features of the considered experimental sites, the excavation history and the available hydromechanical data of the rock in response to the excavation process. Martin & Lanyon (2003a) present results from Mont Terri EDZ investigations focusing on the ED-B experiment in Gallery 98 but also drawing on experience from other investigations. Typically the excavations considered were not oriented along bedding strike and the database and conceptual model presented in Martin & Lanyon (2003a) did not explicitly consider this direction. This chapter presents information from excavations and experiments related to Gallery 04 and Gallery 08 and the associated experimental niches. This represents a significant increase to the number of observations recorded in the experimental database.

Of particular interest are the excavations parallel to bedding strike (EZ-A, HG-A, MB Niche, FE tunnel). This orientation relative to bedding partly mimics that expected in horizontal repository tunnels where bedding will be flat-lying. These excavations are sub-parallel to the minimum stress resulting in less severe stress anisotropy than ED-B but show the influence of material anisotropy.

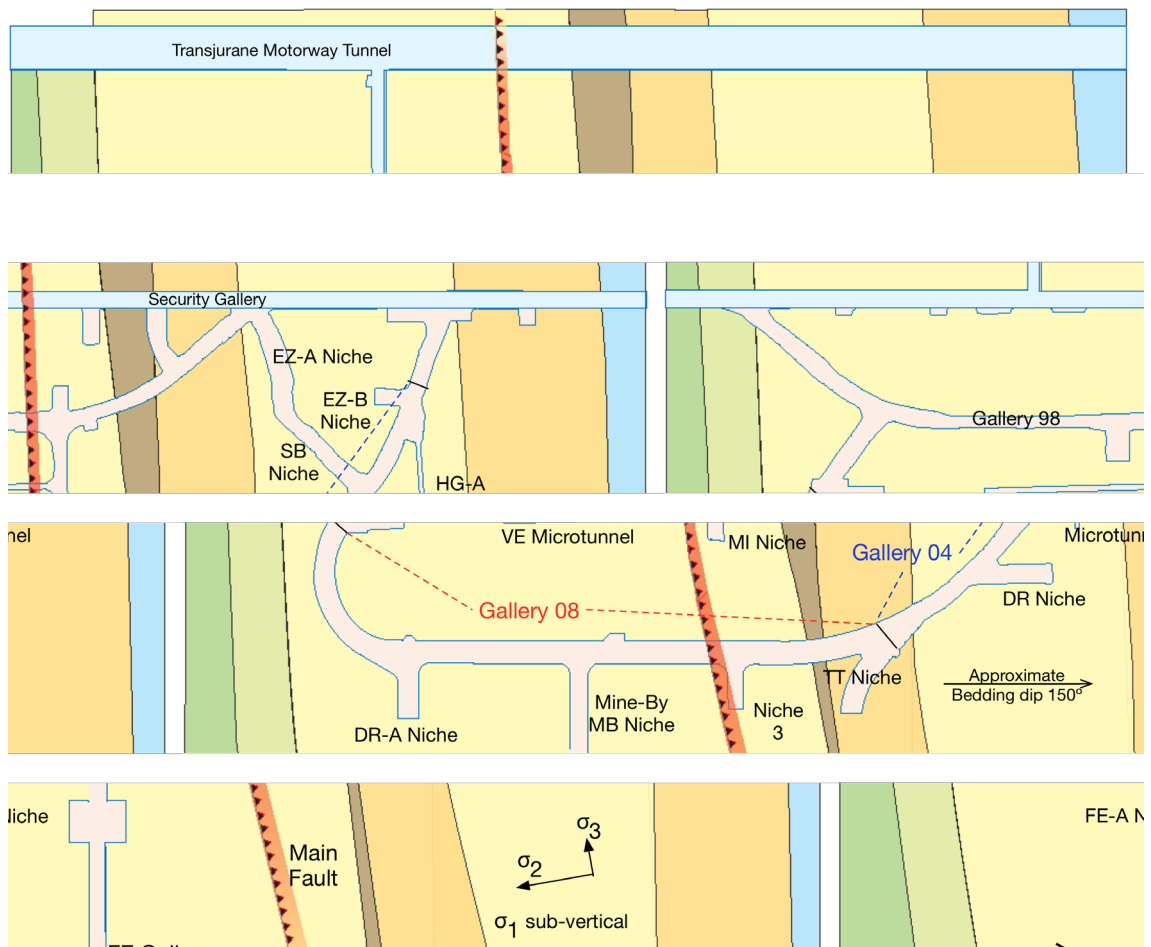


Fig. 4-1: Locations of excavations considered in this chapter.

The excavations considered in this chapter are shown in Fig. 4-1. The description of the EDZ related in-situ experiments is outlined in a standardized manner as follows:

- Location of the experimental site and local geological setting;
- Excavation procedures and support measures;
- Short-term response of the rock on the excavation process;
- Long-term response of the rock, including the impact of operations;
- Summary of results.

Locations within the excavations are described by Tunnel Metre (TM) or Gallery Metre (GM for Gallery 04, Gallery 08 and FE Gallery). Where multiple excavations are discussed TM is used.

## **4.1 EZ-A Niche**

### **4.1.1 Location and local geological setting**

The EZ-A Niche lies within the shaly facies. The start of the niche and its junction with Gallery 98 is close to the boundary of the sandy facies to the northwest (see Fig. 4-1).

Two sets of fault planes were identified in the EZ-A Niche and Gallery 04 Start Niche. The dominant set is oriented sub-parallel to bedding (typically 140-150/45-50°) dipping to the SE. Fault planes of the dominant system dip somewhat more strongly: 50-65°. The minor set dips at low angle to the SW 200-220/10-20° and is characterized by calcite fill. This fault system is often cut and folded by the dominant system. The presence of the minor fault system was identified for the first time during excavation of the EZ-A Niche. The original niche heading was 234°. The resulting fault-plane geometry in relation to the excavation is clearly seen in the structural mapping of the tunnel face at TM20 in Fig. 4-2 and along the niche in Fig. 4-3.

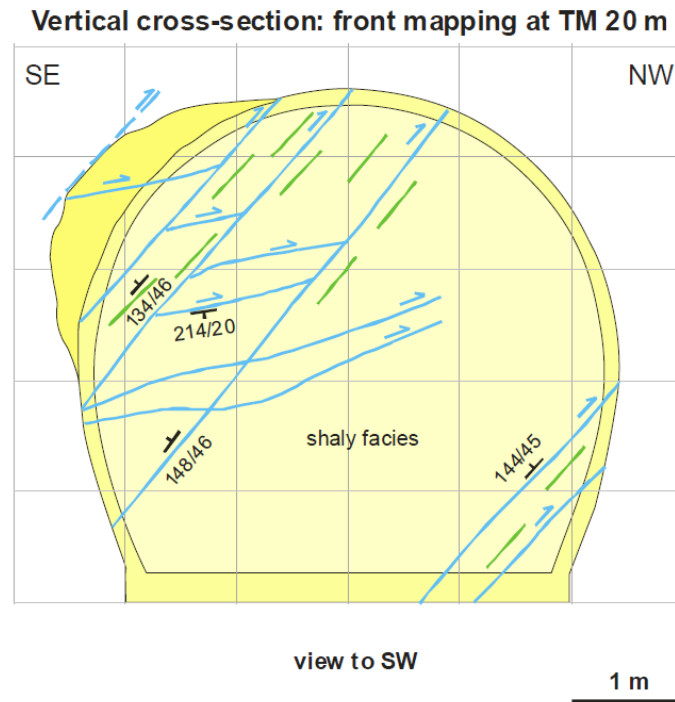


Fig. 4-2: Structural mapping of the excavation face of EZ-A Niche at TM20.

The adverse geometry created by the faulting resulted in a significant rockfall requiring remediation work and a change in the niche orientation to 195°. Structural mapping of the niche to TM23 and the niche extension are shown in Fig. 4-3.

A complex stress state is likely to exist around the start of the EZ-A Niche close to the junction of the Security Tunnel. Away from the influence of these excavations, however, the first part of the niche is roughly aligned with the minimum stress direction, with the intermediate stress direction normal to the side-walls. This results in a lower anisotropy than other tunnel directions, but greater influence of the material (bedding) and structural (fault system) anisotropy. The change of heading after the rockfall is likely to have reduced the effect of this adverse geometry.

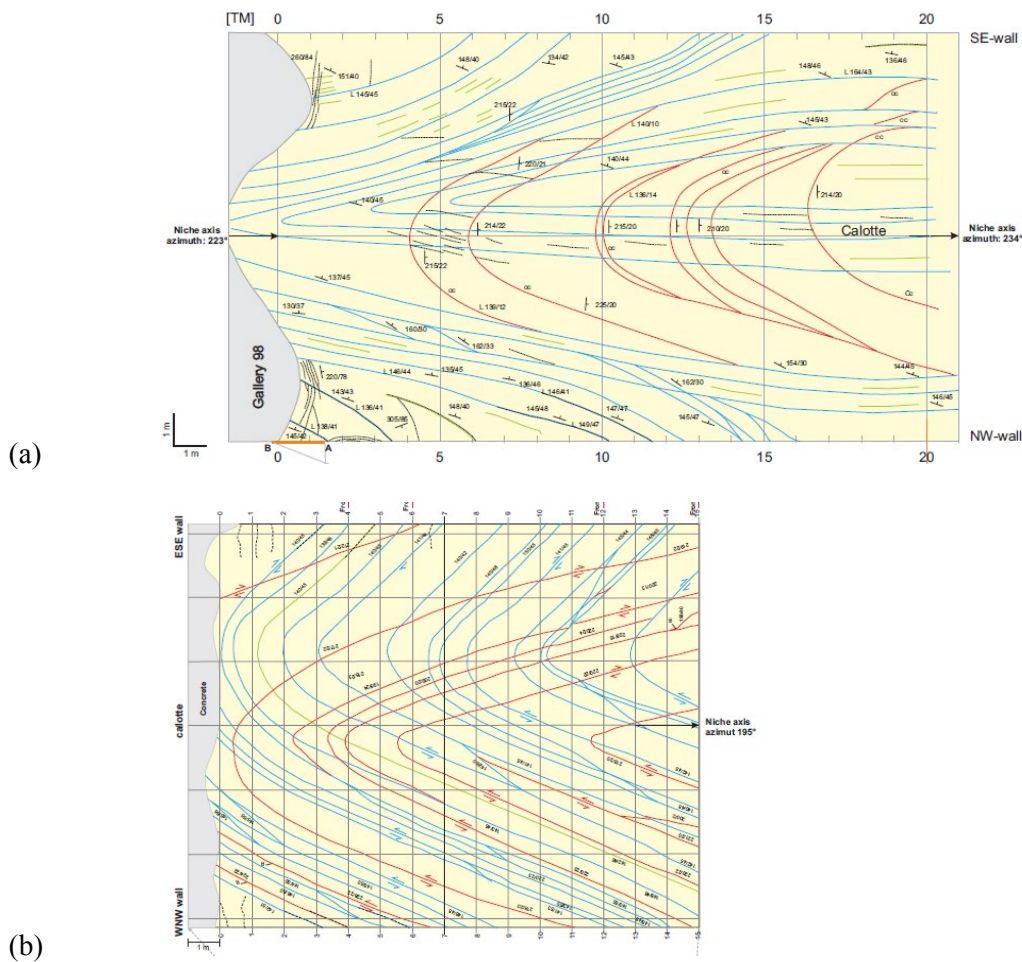


Fig. 4-3: Structural mapping of (a) the first part of EZ-A Niche; (b) the EZ-A Niche Extension.

#### 4.1.2 Excavation procedures and support measures

The initial EZ-A Niche heading was  $234^\circ$  which was followed until the collapse when the excavation front was at TM23. After this, the heading was changed to  $195^\circ$  to completion at TM30 to achieve a more stable situation. The planned excavation cross-section for the EZ-A Niche is shown in Fig. 4-4. The cross-section is a rounded horse-shoe with an upper inner diameter of 5 m and height of 4.6 m (4 m wide invert). The rock wall diameter is 5.3 m (horizontal) and 5 m (vertical). An approximate schedule of the excavation for the EZ-A Niche is given in Tab. 4-1.

The EZ-A Niche was excavated using a roadheader in two steps. Experimental requirements included smooth rock surfaces (no shotcrete) and the avoidance of the use of steel anchorages between TM10 and TM30 to facilitate geophysical surveys. Anchorages were placed at the niche entrance and the entrance columns were reinforced with shotcrete. The original plan called for weekly application of shotcrete. After minor breakouts were encountered geological mapping was reduced and the steel fibre-reinforced shotcrete was applied at least twice a week. The concept of unlined surfaces was also rejected and it was planned to cut openings with a saw after excavation.

A major rockfall occurred on 11/09/03 which required significant remedial actions and a change of tunnel heading and support.

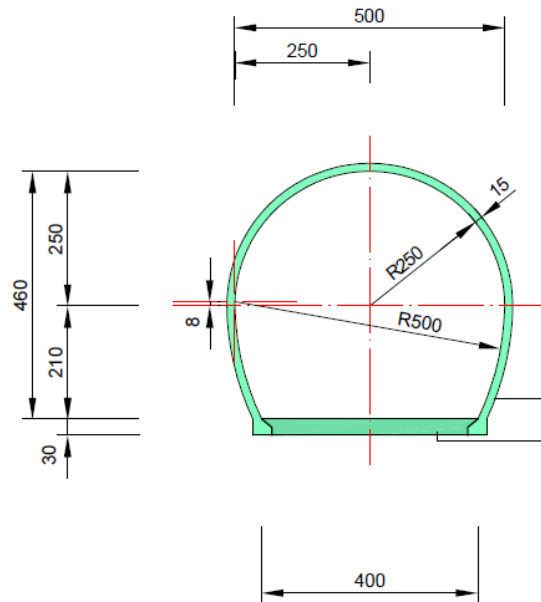


Fig. 4-4: Planned excavation geometry for EZ-A Niche.

Tab. 4-1: Excavation schedule for EZ-A Niche.

Start	End	Event
12/08/03	11/09/03	Excavation of 1st part of EZ-A Niche (TM23)
11/09/03		Partial collapse
12/09/03	14/09/03	Reinforcement of security tunnel
15/09/03	16/10/03	Renovation of EZ-A Niche
17/10/03	01/11/03	Excavation of invert
14/01/04	09/02/04	Excavation of 2nd part of EZ-A Niche including first shotcreting and lining with steel arches and anchorages
09/02/04	12/02/04	Installation of 2 steel arches
16/02/04	20/02/04	Excavation of invert and construction of liner
24/02/04		Completion of concreting

### **EZ-A Niche (extension)**

Following the renovation of the first part of the niche, the direction of the remainder of the niche was altered to reduce the frequency of tectonic features and it was decided that daily excavation steps were immediately covered by a 15 cm thick shotcrete layer, reinforced with steel fibres to the rock floor.

### 4.1.3 Excavation response

#### Excavation of EZ-A Niche

Prior to 11/09/03 minor breakouts were observed and had resulted to changes in the excavation support as discussed previously. On 11/09/03 at 11:30 small cracks started to develop in the shotcrete on the southern wall between TM8 and 12 (see Fig. 4-5). Over the next hour crack width increased steadily and new cracks formed with cracks appearing in the northern wall. The last convergence measurement prior to rock fall on 11/09/03 showed increasing deformations. The site was closed and heavy equipment evacuated at 13:45. Heavy rock breakouts started at 14:30 from the southern wall and by 17:00 about 25 m<sup>3</sup> had broken out from the southern wall between TM6 and 18. The northern wall was stable but showing increased cracking.



Fig. 4-5: Photographs illustrating the development of the rockfall in the EZ-A Niche 11-12/09/03 (taken from Nussbaum et al. 2004).

During 12/09/03 further breakouts occurred (breakout volume in the morning ~ 50 m<sup>3</sup>). Cracks started to develop in the shotcrete at the entrance and the whole of the EZ-A Niche from TM2-TM20 was affected. The entrance was reinforced with anchors but these did not stop the increasing deformation in the Security Gallery. This led to the decision to stabilize the first 5 m of the EZ-A Niche. On 13/09/03 the breakout volume was estimated at 100 m<sup>3</sup> and the first 5 m of the EZ-A Niche was reinforced with 20 cm of shotcrete stabilizing the deformations around the tunnel entrance.

In order to ensure the stability of the security tunnel it was necessary to perform a fast renovation of the EZ-A Niche over the next month. This included:

- Steel fibre-reinforced shotcrete of minimum 20 cm thickness over the complete length of the niche.

- Approximately 40 3 m-long anchorages in the upper walls and ceiling.

Finally the invert was excavated in October 2003. The final excavation profiles are shown in Fig. 4-6. The extent of the overbreak (2-3 m) in the SE of the ceiling is clearly seen.

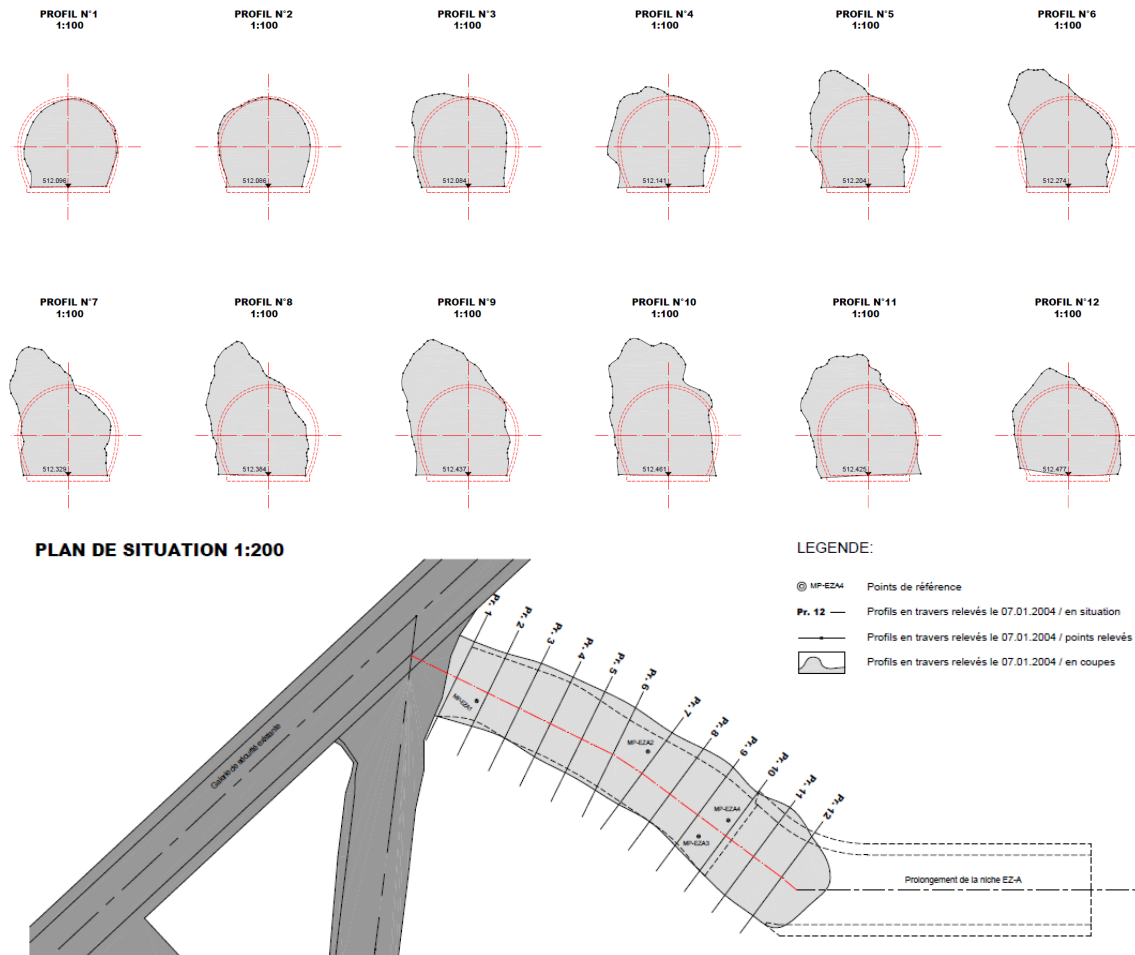


Fig. 4-6: As-built profiles of the EZ-A Niche showing the region of collapse.

A convergence profile had been installed at TM0 (entrance to niche). This profile was damaged during the rockfall and reinstalled on 18/09/03. An extensometer profile was installed at TM12 on 01/09/03. The surface extensometer was supplemented by two downhole extensometers in BEZ-A25 (parallel to bedding) and BEZ-A26 (normal to bedding). A third convergence profile was subsequently installed at TM6 in the EZ-A Niche Extension (equivalent TM30 in EZ-A Niche). The convergence profile and extensometer locations are summarised in Tab. 4-2 and 4-3 and shown in Fig. 4-7.

Convergence measurements at TM0 showed an initial increase followed by stabilization and then a rapid acceleration immediately prior to the rockfall with a maximum of 58 mm (1.2% diametral strain) measured in the 1-3 chord (horizontal). Convergence at TM12 (see Fig. 4-8) showed a similar pattern with a rapid jump on 11/09/03 to 70 mm (1.4% strain). Much smaller displacements were observed in the downhole extensometers indicating deformation occurring beyond the end of the borehole (~ 3 m) with possible detachment of a large rock-block.

The short-term (to 100 days after excavation) convergence measured in the EZ-A Niche extension at TM6 are shown in Fig. 4-8.

Tab. 4-2: Convergence measurements in EZ-A Niche.

Location	Type	Installation	Maximum convergence measured
EZ-A TM0	Invar wires		Destroyed during rock fall
EZ-A TM12	Surface extensometer +BEZ-A25,26	01/09/03	Destroyed during rock fall
	4-pad extensometer +BEZ-A29,30	11/03/04	Replacement boreholes drilled into ceiling rock fall zone
Niche extension TM6	Extensometer	04/02/04	Approx.EZ-ATM30

Tab. 4-3: Location and depth of borehole extensometers in EZ-A Niche.

Borehole	Extensometer	Depth	Borehole	Extensometer	Depth
BEZ A-21	EZ-A_21_1	-3.05	BEZ A-25/26/29/30 Anchor depths same for all boreholes.	EZ-A_25_1	-2.5
	EZ-A_21_2	-1.35		EZ-A_25_2	-1.2
	EZ-A_21_3	-0.85		EZ-A_25_3	-0.8
	EZ-A_21_4	-0.60		EZ-A_25_4	-0.4

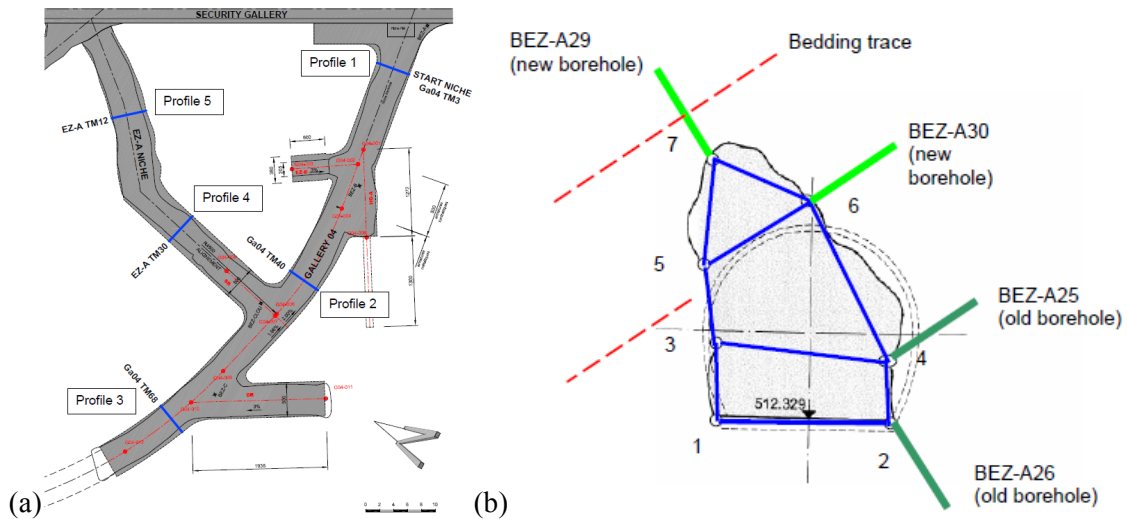


Fig. 4-7: Locations of (a) convergence arrays in Gallery 04 and EZ-A Niche; (b) extensometer profile at EZ-A Niche TM12.

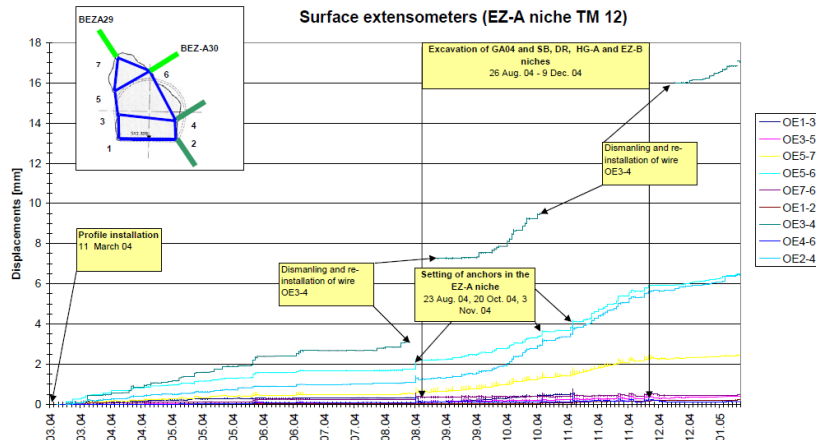


Fig. 4-8: Measured convergences in the new profile at TM12 of EZ-A Niche.

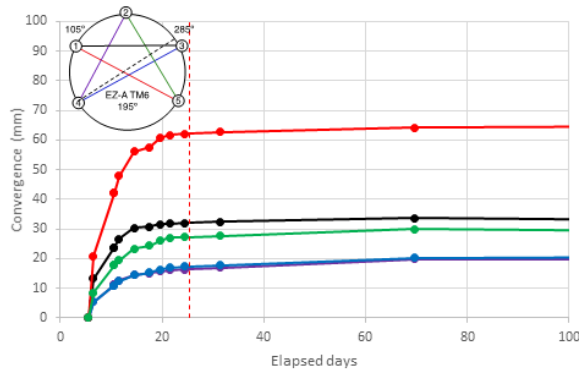


Fig. 4-9: Short-term measured convergences EZ-A Niche Extension TM6.

### 4.1.4 Long-term response

Fig. 4-10 shows the measured convergence at TM6 in the EZ-A Niche extension. Convergence stabilized after the end of excavation but then increased with the excavation of Gallery 04 (~ 210 – 270 days). Chord 5-1 registered the greatest convergence which developed in the immediate period after excavation prior to lining. After this period all chords showed roughly the same behaviour. In late time (500-3500 days) all chords showed an approximately linear increase with log time.

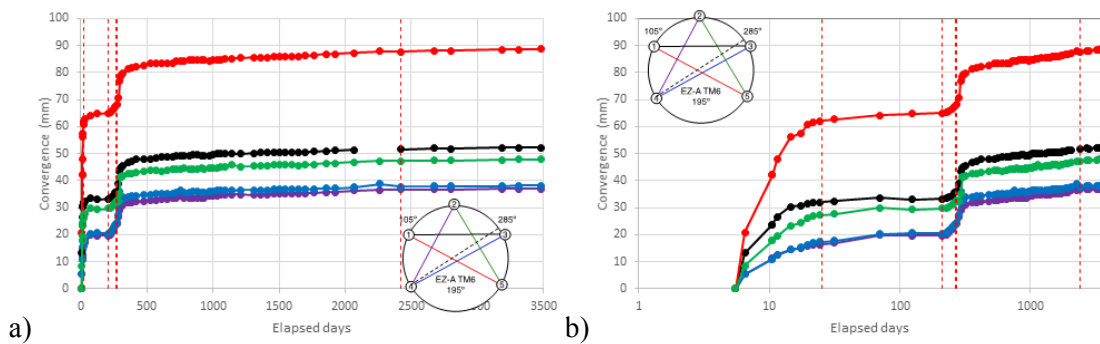


Fig. 4-10: Measured long-term convergences of EZ-A Niche Extension TM6 (Profile 4).

### 4.1.5 Summary of EZ-A results

#### Understanding of failure mechanisms

Post-mortem analysis of the rockfall in the EZ-A Niche (Nussbaum 2004) suggested a structurally controlled failure due to the presence of a high density of flat lying joints belonging to a set that had not been previously explicitly identified in the URL. The collapse in the EZ-A tunnel illustrates structurally controlled failure associated with unfavourably oriented planes of weakness that led to significant caving into the tunnel. In this case the tunnel heading was such that the tunnel surface was sub-parallel to both bedding and a second low-angle fault system (see Fig. 4-2 and Fig. 4-3). This resulted in detachment of rock blocks and significant rock fall.

### Diametral strains

Tab. 4-4 summarizes the observed convergence in the EZ-A Niche and EZ-A Niche Extension. The rapid increase of measured convergences prior to the rockfall were a strong indicator of the likelihood of collapse. The extensometer data suggest that much of the deformation was occurring beyond 3 m (over 1 radius) of the tunnel wall.

Tab. 4-4: Convergence and diametral strain in EZ-A Niche and Extension.

Location		Convergence and diametral strain
EZ-A Niche	TM0	> 58 mm (1.2%) immediately prior to failure and damage
		< 5 mm after reinstallation 18/09/03
EZ-A Niche	TM12	~ 70 mm (1.4%) immediately prior to failure and damage BEZA-25 < 3 mm prior to failure BEZA-26 < 6 mm prior to failure
		After reinstallation of surface extensometer < 3 mm Downhole < 0.5 mm
EZ-A Niche extension	TM6	0 – 100 days: 20 – 64 mm (0.4-1.3%) 08/08/13: 37 – 89 mm (0.7 – 1.8%)

### EDZ extent

The collapse demonstrates the possibility of extensive failure if support fails with an overbreak extending over an excavation radius. In contrast locally structural mapping in the side-wall of Gallery 98 showed a maximum EDZ depth of 0.6 m (Fig. 4-11a). Mapping of the slot in the floor of the EZ-A Niche Extension showed a network of induced structures to about 0.5 m with some structures extending to about 0.8 m below the floor (Fig. 4-11b). The influence of pre-existing and reactivated bedding/fault structures on the EDZ network is seen at both locations (see discussion of EZ-B Niche). EDZ fractures are compartmentalized by the pre-existing bedding-parallel faults.

**Monitoring of pore pressure during excavation**

No pressure monitoring boreholes were located sufficiently close to the excavations to identify strong responses to excavation. Monitoring in distant boreholes showed largely seasonal effects.

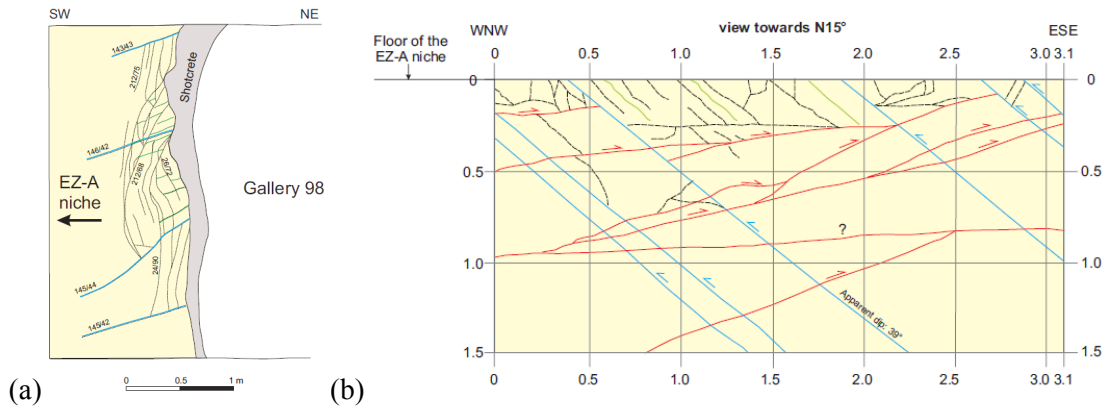


Fig. 4-11: Structural mapping of (a) Gallery 98 wall at start of EZ-A Niche and (b) Slot in floor of EZ-A Niche Extension (TM6.3).

Tab. 4-5: Summary of observations for EZ-A Niche excavation.

	Summary	Comment
Cross-section	Circular cross-section with flattened invert diameter 5 m	Significant overbreak after rockfall see Fig. 4-6
Orientation	Original heading 234°. Revised for Niche extension 195°	See Fig. 4-3
Geology	Shaly facies (near margin of sandy facies) with closely spaced bedding-parallel faults (140-150/45-50°) and a subordinate low-angle fault set (200-220/10-20°).	
Method	Roadheader: in two steps - calotte and invert	
Support	Originally only minimal support planned for geophysics but subsequently steel fibre reinforced shotcrete and significant numbers of anchors installed.	
EDZ	Large overbreak suggests significant EDZ extent. EDZ fracture network in Gallery 98 sidewall and floor of Niche Extension < 1 m thick.	Pre-existing bedding-parallel faults compartmentalize EDZ fracture network in the side-walls and floor.
Diametral Strain	> 60 mm immediately prior to failure. Niche Extension TM6 0-100 days: 0.4-1.3% Most recent data: 0.7-1.8%	
Pore pressure monitoring	No near field pressure monitoring	

## 4.2 Gallery 04

### 4.2.1 Location and local geological setting

Gallery 04 comprises the access tunnel and adjacent niches: SB Niche, DR Niche, HG-A Niche and EZ-B Start Niche. Gallery 04 and its adjacent niches lie within the shaly facies from GM4 to GM79. Locally the shaly facies are composed of numerous lenses of two types: 1) lenses with white/grey sandy limestones and 2) brownish oxidised lenses made of siderite.

Small-scale mapping of Gallery 04 and adjacent niches identified three different fault systems, listed below in order of importance and frequency:

- SSE-dipping fault planes, sub-parallel to bedding planes;
- low angle to flat lying S- to SW-dipping fault planes;
- W- to WNW-dipping fault planes, sinistral transpressive strike-slip faults.

A tectonically disturbed zone was encountered in the Gallery 04 access tunnel between GM65 and GM75. A narrow NNE-SSW striking fault zone was found between GM61-GM66 made up of W-WNW dipping fault planes which can be correlated with similar oriented faults mapped near the C Niche during the mapping of Gallery 98. Fig. 4-12 shows the structural map of Gallery 04.

### 4.2.2 Excavation

The excavation of Gallery 04 (GA04) was performed in three steps (tab. 4-6). The excavation of the Start Niche was performed as a full-face single step in 25 days, while the remaining excavation was in two steps: excavation of the calotte (top heading) followed by excavation of the invert (a 1 m bench). Excavation of the calotte proceeded at about 2 m/day followed by installation of anchors and application of a 5 cm layer of shotcrete as head protector. Excavation of the invert was performed in two further steps. The planned profile and support is shown in Fig. 4-13.

The SB Niche was excavated using roadheader and pneumatic hammer (rear part). The use of the pneumatic hammer was because of limited access for the roadheader and to speed excavation (excavation of the DR Niche was performed in parallel). The DR Niche was excavated exclusively with roadheader at twice the rate of GA04 because of the use of two working teams (06:00-22:00). The HG-A Niche and EZ-B Start Niche were excavated with roadheader and pneumatic hammer (again for reasons of speed and limited access).

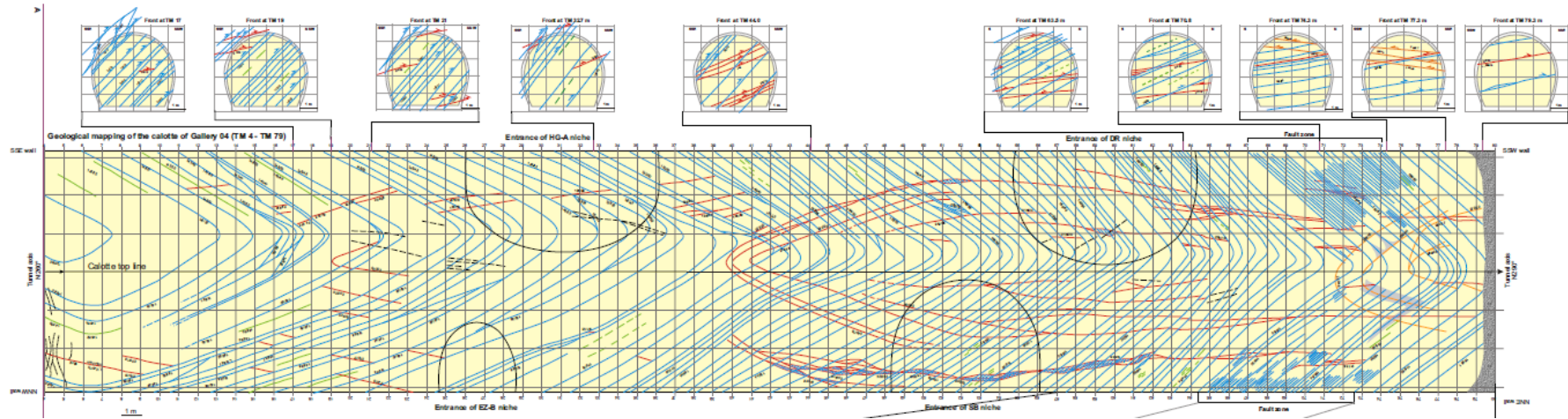


Fig. 4-12: Structural mapping of the Gallery 04 access tunnel (for orientation see Fig. 4-1).

Tab. 4-6: Excavation schedule for Gallery 04 and adjacent niches.

Start	End	Event
March 04	May 04	Excavation of Start Niche 20 m.
25/08/04	21/10/04	Excavation of GA04 Top heading (calotte)
28/10/04	04/11/04	Excavation of bench GM20 to GM55
25/11/04	30/11/04	Excavation of bench GM20 to GM55
05/11/04	16/11/04	Excavation of SB Niche
15/11/04	24/11/04	Excavation of DR Niche calotte (roadheader)
29/11/04	30/11/04	Excavation of DR Niche invert (roadheader)
02/12/04	02/12/04	Concreting of DR Niche invert
06/12/04	10/12/04	Excavation of HG-A Niche and EZ-B Start Niche (roadheader and pneumatic hammer)

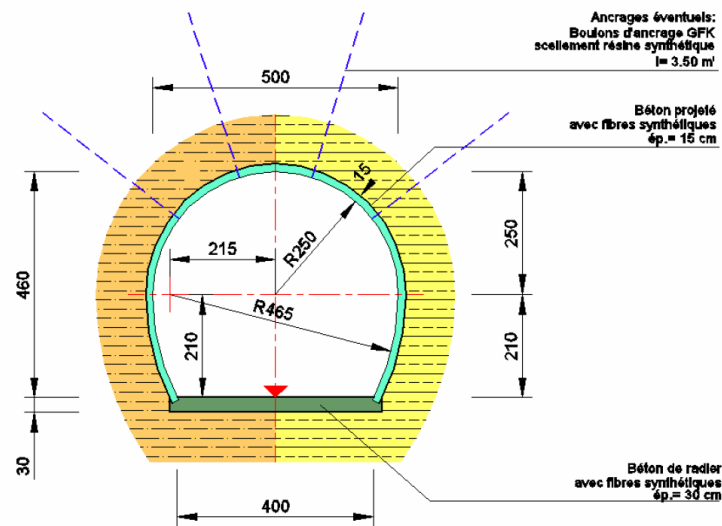


Fig. 4-13: Planned excavation shape for Gallery 04.

After excavation of the calotte, anchor emplacement points were chosen and installed in the following steps:

- Drilling a hole with a Jumbo.
- Introduction of two-compound synthetic resin into the hole.
- Installation of rod inside the hole with a rotational motion to mix the resin.
- Installation of anchor plate and head on the rod and hand-tightening.

Anchor locations were selected by the engineer according to the local geology (bedding/fault orientation), tunnel orientation and rock condition. At the start of GA04 access tunnel anchors were mostly placed on the southern wall where the tunnel surface is parallel to bedding. As excavation continued it was necessary to change the location due to change in relative orienta-

tion and the presence of a tectonically disturbed zone between GM65 and GM75. Two types of anchor were used: steel and glass-fibre (GFK). GFK anchors were used up to GM30 in the access tunnel (see Fig. 4-14) and in the HGA and EZ-B Start Niches to avoid disturbances to the geo-electric surveys of the EZ-G experiment. They were also used at the entrances of the DR and SB Niches to facilitate subsequent excavation.



(a)

(b)

Fig. 4-14: (a) Installation of GFK anchor at the EZ-B Start Niche and (b) view of the end of the GA04 access tunnel showing the anchors.

On 17/09/04 fifteen anchors were installed in the Start Niche after large cracks had developed in the shotcrete. Before the excavation of the invert, anchors had also been installed on both side of the access tunnel at the bottom to ensure the stability of the vault during the second step of excavation and installation of lining, as relatively high convergences had been observed. Shotcrete in the Gallery 04 access tunnel and adjacent niches had been applied in two steps (with the exception of the EZ-B Niche where it was applied in a single step):

- A first layer of 5 cm thick shotcrete was applied almost every day in the calotte after the excavation work.
- Every day after excavation of the invert, shotcreting of the lower parts of the walls and of the calotte (second layer) was performed to ensure stability of the calotte. The goal was to avoid that the latter was "suspended" in the air. After this second shotcreting step, the final thickness of shotcrete was about 15 cm.

The shotcrete was reinforced with plastic fibres ( $6 \text{ kg/m}^3$ ) from tunnel meter 0 to tunnel meter 29.4 and in the HG-A Niche and EZ-B Start Niche. Elsewhere, it was reinforced with steel fibres ( $30 \text{ kg/m}^3$ ). The compression strength of shotcrete was  $35 \text{ N/mm}^2$  with plastic and steel fibres.

### **Local lining**

In cases where small breakouts occurred, especially in the access tunnel of Gallery 04 on the southern wall, steel meshes were installed, supported by steel anchors, prior to shotcreting. The excavation fronts in the tunnel access of Gallery 04 and DR Niche were not shotcreted to allow inspection by visitors. Stress concentrations developed on the lining close to these fronts, and it was necessary to install steel arches to reinforce the lining. Three GFK anchors were placed in the front of the DR Niche since the front is sub-parallel to bedding and there is a sizeable fault parallel to it.

In the SB Niche a steel mesh (K188) and 35 steel anchors were placed to ensure the stability of the vault before shotcreting the central part of the niche, as the orientation of the niche is not favourable in relation to bedding and tectonic faults.

### **4.2.3 Excavation response**

Deformation measurements were made before and after excavation. The main aim was to ensure the safety of the excavation. Three new convergence profiles were installed at Gallery 04: GM3, GM40 and GM68. The two convergence arrays in the EZ-A Niche installed prior to the excavation of the main part of Gallery 04 were monitored periodically during the excavation.

Deformations were also monitored in the MI Niche (approximately 50 m from the end of Gallery 04) after shotcrete detachments were observed during the excavation. Measurements were made of the crack-width of six gypsum seals (MI1-6). The maximum opening between 08/10/04 and 25/01/05 was 25 mm.

Inclination and displacement were measured in BHE-D5 and BHE-D6 drilled from the MI Niche to measure deformation associated with the HE-D experiment heating phases. BHE-D5 contains a clinometer while BHE-D6 contains five extensometers connected via carbon extension cables to fixation points (packers) in the borehole and measuring the displacement of the packers relative to the borehole mouth. Both systems showed a response to excavation with a change in displacement  $\sim 15$  mm during the excavation period. Long-term monitoring of pore pressures associated with the HE-D, PP, OP, GS and ED-B experiments during excavation showed mainly the influence of seasonal variations rather than any pressure redistribution due to excavation.

The measured convergences in Gallery 04 are shown in Fig. 4-15.

Tab. 4-7 lists the maximum observed convergences in the five monitoring arrays. At GM3 the greater part of the measured convergence was associated with construction of the Start Niche with a maximum convergence (normal to bedding) of  $\sim 55$  mm at the end of excavation. Convergences then largely stabilized until construction of Gallery 04 access tunnel in September 2004 which typically resulted in a further convergence of 5-10 mm.

The profile at GM40 was installed when the face was at GM41.5 some three days after the heading face reached the installation point. The convergence profiles showed ongoing deformation as excavation of the calotte progressed and subsequently responded to excavation of the invert and some of the niches. The maximum convergence was 47 mm. It is likely that setting lateral anchors between GM20 and GM55 (anchor spacing 1.5 m) resulted in a reduction in the tunnel convergence.

The profile at GM68 was installed after completion of the excavation GM79.4, approximately 15 days after the heading reached the installation point. The maximum measured convergence was 26 mm (normal to bedding). The data showed responses to the excavation of the DR Niche. Deformation responses of 10-15 mm were also seen in the two profiles in the EZ-A Niche as shown in Fig. 4-8.

Tab. 4-7: Convergences measured during construction of Gallery 04 and adjacent niches.

Profile	Type	Location	Installation	Maximum convergence measured
1	Invar wires	GA04 GM3	3 days after start of Start Niche	65 mm normal to bedding (to 10/12/04) Mostly due to excavation of Start Niche. Estimated < 10 mm due to Gallery 04
2	Invar wires	GA04 GM40	13/09/04 1.5 m behind front	47 mm normal to bedding (to 10/12/04) At least additional 5 mm in period between excavation and zero reading.
3	Invar wires	GA04 GM68	22/10/04 after GA04 completion (GM79.4)	26 mm normal to bedding (to 10/12/04) Additional a few mm should be added
4	Invar wires	EZ-A TM30	04/02/04 prior to completion of EZ-A Niche	80 mm normal to bedding (to 10/12/04) Only 16 mm due to excavation of GA04
5	Extensometer	EZ-A TM12	11/03/04	Maximum measured deformation 7 mm (25/01/05)

In addition to the measured convergences, accelerated displacements ~ 15 – 20 mm were measured in BHE-D65 and BHE-D6, although the period during which these measurements were taken coincided with the heating phase II in borehole BHE-D0. Also, crack development was observed in the rear part of the EZ-A Niche during excavation of the SB Niche which required renovation of the shotcrete in this area.

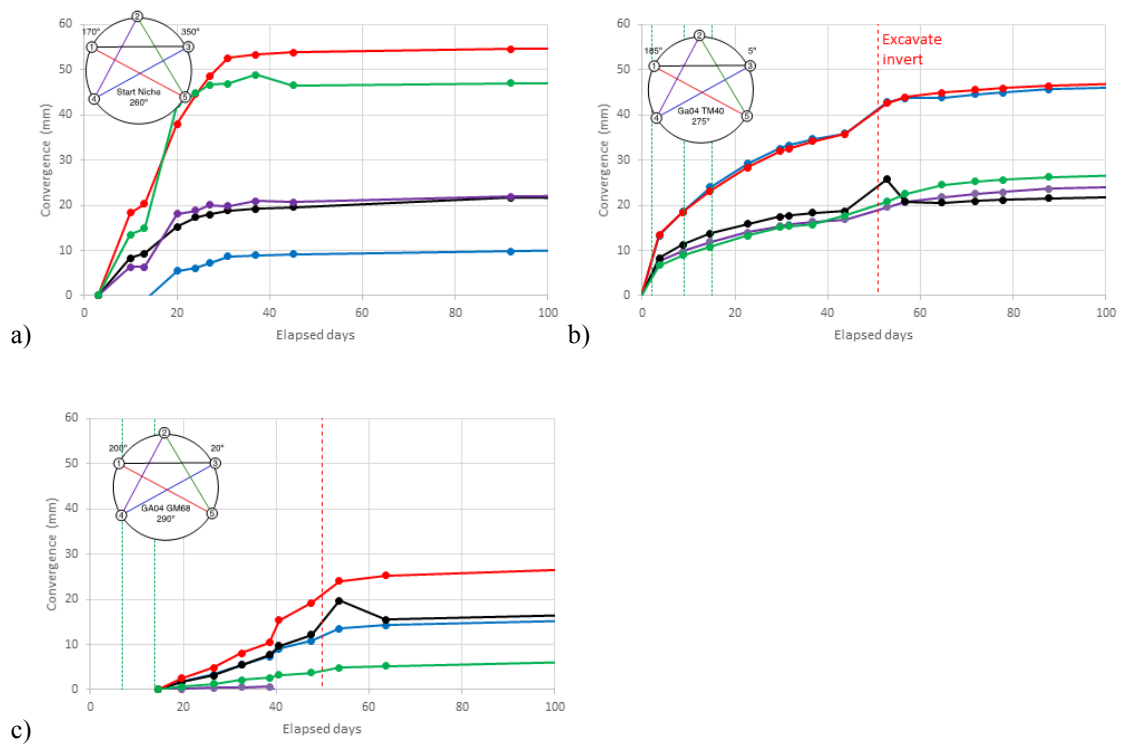


Fig. 4-15: Measured convergences in Profiles 1-3 during construction of Gallery 04 access tunnel. (a) Start Niche; (b) GM40; (c) GM68. Green vertical lines show approximate day when excavation face has passed beyond the measurement profile (1<sup>st</sup> line 1 diameter, 2<sup>nd</sup> line 2 diameters, etc.).

### 4.2.4 Long-term monitoring

Fig. 4-16 shows the measured long-term convergences in Gallery 04. Convergence stabilizes after the end of excavation. After this period all chords show roughly the same behaviour: at late time (500 – 3500 days) all chords show a roughly linear increase with log time. The array at GM68 shows a small increase with the excavation of the end of Gallery 08 (~ 1500 days).

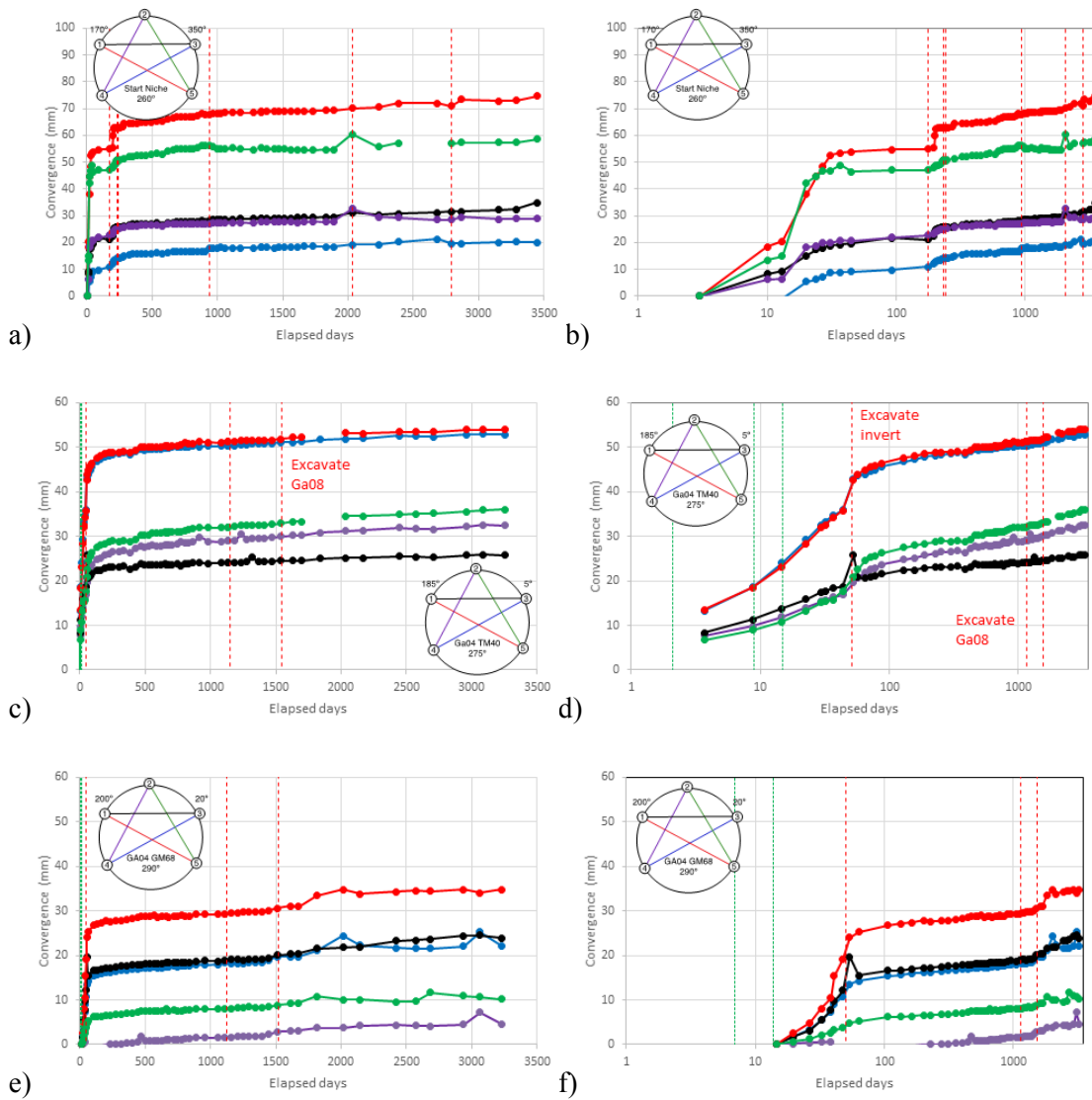


Fig. 4-16: Measured long-term convergences in Gallery 04. Green lines show face advance in diameters and red lines show related excavation events.

Lesparre et al. (2013) present results from monitoring the resistivity of the EDZ around a short section of Gallery 04 over a 4 year period (July 2004 – April 2008). They performed electrical resistivity tomography (ERT) over a 4 m section of the Gallery 04 Start Niche (GM17-21) oriented at  $250^\circ$  (roughly sub-parallel to bedding strike; see Fig. 4-17). The survey period covered the start of excavation of the main part of Gallery 04, excavation of the EZ-B and HG-A Niches and a three year "undisturbed" period from January 2005 prior to the start of Gallery 08 excavation. Three 2D profiles were measured at 1 m (Ring 1), 1.5 m (Ring 2) and 4 m (Ring 3) from the end of the Start Niche.

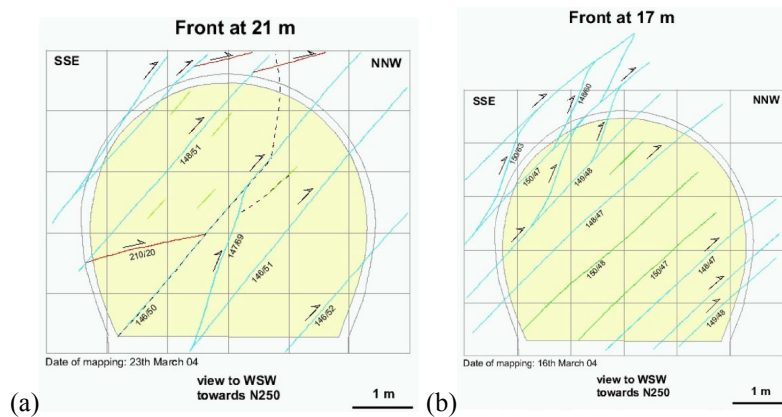


Fig. 4-17: Structural mapping of Start Niche face at (a) GM17 (ERT Ring 3) and (b) GM21. Bedding-parallel structures are oriented at  $150/45^\circ$ .

Fig. 4-18 shows the interpreted average resistivity evolution. The overall spatial geometry and extent of the resistivity anomalies appear to be consistent with the model of the EDZ geometry for HG-A from Marschall et al. (2006). Early changes between July and December 2004 are probably related to the excavation of Gallery 04 and associated niches, while the subsequent changes are due to time-dependent evolution of the EDZ. Variability between rings was observed. At Ring 3 a resistivity anomaly was correlated to locally increased fracturing, while the increased resistivity between 10-2 o'clock in Ring 2 was linked to the restart of Gallery 04 excavation and shotcrete damage requiring reinforcement. Variability between the rings persisted over the monitoring period (Fig. 4-19).

The surveys suggested initial short-time changes due to excavation over the first 6 months followed by a slower evolution (although survey frequency also decreased during this period). Observed changes over the long term are difficult to interpret and reflect local differences and multiple phenomena (seasonal variations and EDZ evolution).

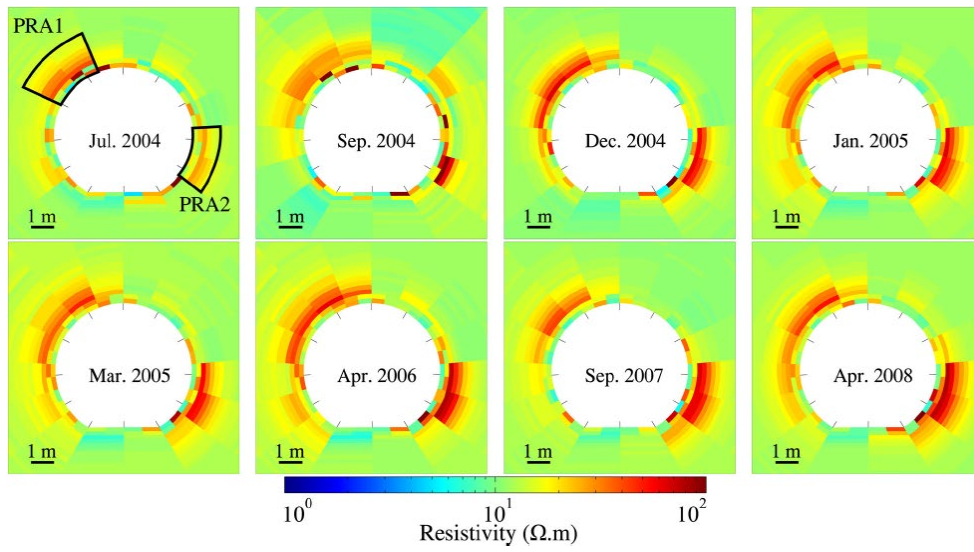


Fig. 4-18: Evolution of the average resistivity with time from 2004 July to 2008 April. Tunnel heading is 250°, SSE to left and ENE on the right side of diagrams.

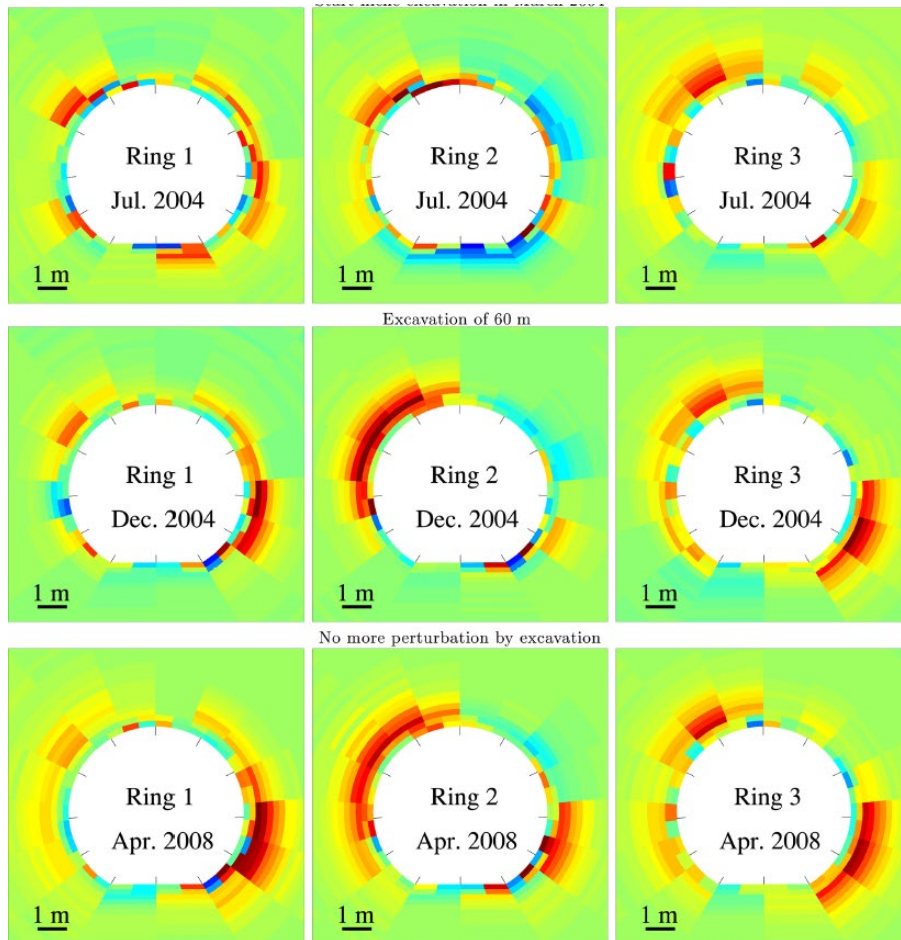


Fig. 4-19: Reconstructed resistivities around Rings 1, 2 and 3 from July and December 2004 and April 2008.

### 4.2.5 Summary of results

#### EDZ extent

Mapping in the SB Niche and DR Niches showed EDZ fracturing within the first metre of the Gallery 04 side-walls (Fig. 4-20). Fractures were typically in connected clusters with increased density near the tunnel wall. In the SB Niche, clusters were typically truncated by bedding plane-parallel faults. In the invert of the SB Niche, EDZ fractures were visible as it approached the previously excavated EZ-A Niche extension. Resistivity mapping showed 1-2 m thick zones of altered resistivity around the excavation.

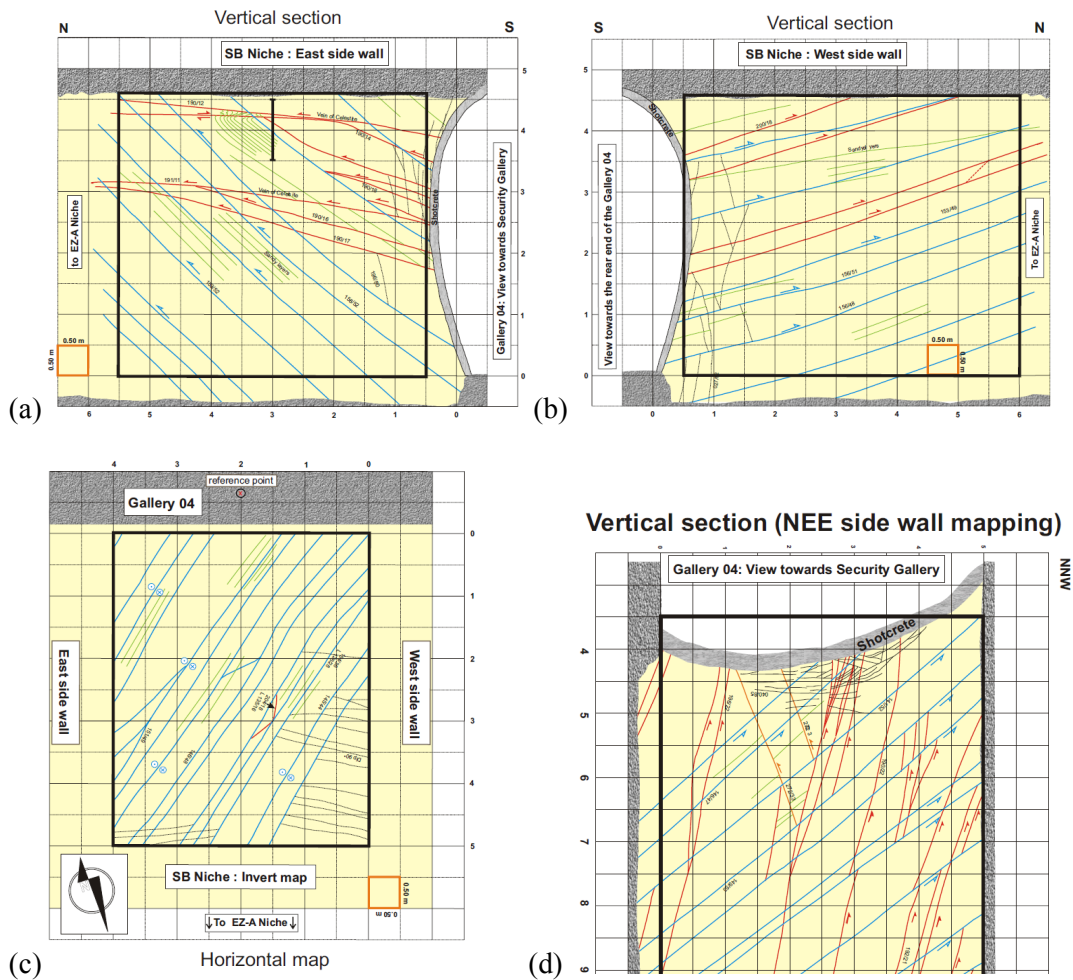


Fig. 4-20: Structural mapping of SB Niche: (a) east wall; (b) west wall; (c) invert; (d) DR Niche ENE wall .

## Understanding of failure mechanisms

Observations of the EDZ during the excavation of Gallery 04 and associated niches were largely consistent with previous experience at the URL.

## Diametral strains

The minimum and maximum diametral strains for the 3 profiles are listed in Tab. 4-8. Typically, strains stabilized soon after excavation (taken here as 100 days) and then developed more slowly showing long-term deformations.

Tab. 4-8: Diametral strains for Gallery 04 at 100 days after excavation and most recent data.

	GM30	GM40	GM68
Strain at 100 days after excavation		0.4 – 0.9%	0 – 0.5%
Most recent data (on 09/08/13 ~ 3250 days)	0.2 – 0.3%	0.5 – 1.1%	0.1 – 0.7%

## Pore pressure monitoring

No near field pressure monitoring boreholes were located sufficiently close to identify clear excavation responses. Monitoring in distant boreholes showed largely seasonal effects.

Tab. 4-9: Summary of observations for Gallery 04 excavation.

	Summary	Comment
Cross-section	Rounded horseshoe wall horizontal diameter 5 m. Height 4.6 m. Start Niche 20 m long. Total length 80 m.	Dimensions at rock wall horizontal 5.3 m diameter, 5 m high.
Orientation	Gallery heads 260° for first 30 m but bends round to North with final heading 300°.	
Geology	Shaly facies with tectonically disturbed zone GM65-GM75 and NNE-SSW striking fault zone GM61-GM66.	
Method	Roadheader	Niches used roadheader and pneumatic hammer
Support	3 m- long 25 mm diameter anchors 15 cm fibre-reinforced shotcrete 30 cm concrete floor	See Nussbaum, Bossart et al. (2005)
EDZ	Connected EDZ network within 1 m of the sidewalls. EDZ fractures often truncated by bedding-parallel faults.	
Diametral Strain	0-100 days: 0-0.9% Most recent data: 0.1-1.1%	
Pore pressure monitoring	No near field pressure monitoring	

### 4.3 EZ-B Niche

#### 4.3.1 Location and local geological setting

The EZ-B Niche is located off Gallery 04 between GM20 and GM25. It is located in the shaly facies and locally the mean bedding dips at 147/45° (dip direction ranges from 140-155° and dip angle 38 to 50°). Its excavation was the subject of a detailed characterization.

#### 4.3.2 Excavation

Prior to excavation seven boreholes (BEZ-B1-7 see Tab. 4-10) were drilled from Gallery 04 for observation and pore pressure measurements. The niche was excavated using a pneumatic hammer in seven steps over a period of 12 days. The main body of the niche was excavated in the first six steps and the invert in the final step. Each step began with excavation near the invert and finished with partial excavation of BEZ-B1 which ran along the east wall of the niche.

Construction started with removal of the Gallery 04 shotcrete and excavation of a small opening on the first day (09/12/04) and creation of the cross-section on the second day. Fibre-reinforced shotcrete of 150 mm nominal thickness was applied to the entrance surfaces. Roof support was installed as four overlapping steel meshes and 24 steel anchors. The anchors were 50 cm long and embedded with epoxy resin. A 300 mm thick concrete floor was emplaced in the invert with a central contraction joint. A second set of boreholes: two planes of radial boreholes and two boreholes into the niche face were drilled soon after excavation.

Tab. 4-10: Monitoring boreholes around EZ-B Niche.

Borehole	Function
BEZ-B1,2,3	Observation boreholes (100 mm). Drilled from GA04 prior to excavation
BEZ-B4,5,6,7	Pore pressure measurement (20 mm)
BEZ-B8,9,10,11,12,13	Plane #1 of radial boreholes orthogonal to niche
BEZ-B14,15,16,17	Plane #2 of radial boreholes orthogonal to niche
BEZ-B18,19	Into the niche face

#### 4.3.3 Excavation response

An extensive programme of geological, geophysical and geodetic measurements was made during excavation:

- Geological mapping of walls, floor, roof and face;
- Core and optical televiewer logging of boreholes;
- Continuous digital video recording;
- Laser scanning of the niche face (point cloud);
- Total station measurements of displacements;
- Tunnel, single and cross-hole seismics;
- Pore pressure monitoring.

Yong et al. (2006) and Yong (2008) provide an integrated characterization of the rock mass response. Excavation response was monitored in the four monitoring piezometers. Pore pressure rose in BEZ-B7 during excavation and fell quickly in two steps as the face passed (Fig 4-21). Pore pressure in BEZ-B4, 5 and 6 became sub-atmospheric after excavation (sensor response verified during opening in March 2006). Pore-pressure in BEZ-B6 was affected by sensor problems during the initial part of the excavation.

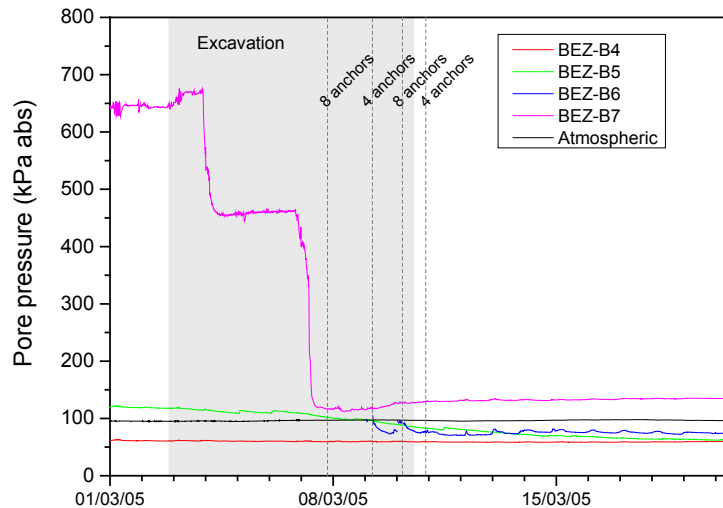


Fig. 4-21: Pore pressures and atmospheric pressure (from nearby niche) from the EZ-B Niche.

Monitoring of displacements used a total station with 27 measurements on four 6-point sections (10x, 20x, 30x, 40x) and at the face (501-503). Prior to invert excavation the largest displacements ( $\sim 10$  mm) were measured in the upper walls at Section 400 (near the end of the excavation). The displacements mostly occurred within 24 hours of excavation. Movement was downward and sub-parallel to bedding. All other displacements were small ( $\sim 3$  mm) and typically upwards (in three points normal to bedding).

After the concreting of the invert, the largest displacement occurred in the upper east wall (Point 202, 11-12 mm downwards and orthogonal to the niche axis). The largest convergences were 9 – 12 mm along Point 202-Point 204 and Point 202-Point 206 and other convergences did not exceed 2 mm. The displacements measured in the last reported survey, 8 months after excavation, again showed the highest values at Point 202 with movement downward and roughly normal to axis (dipping  $\sim 22^\circ$ ). Other displacements were mainly upward and less than 5 mm. Displacements at the face were concentrated near the floor (Point 503) with the largest displacement of 5 – 6 mm upwards and roughly normal to bedding, measured in the 28/10/05 survey (Tab. 4-11).

Tab. 4-11: Summary of maximum displacement magnitude in mm for the different sections of the EZ-B Niche excavation.

Date	Time after excavation	10x	20x	30x	40x	50x
13/03/05	2 days after niche body	2.2	2.5	1	10.9	1.6
17/03/05	2-3 days after invert excavation and concreting	2	11.2	1.2	1.8	1.5
28/10/05	32-33 weeks after completion	2	11.6	4.9	4.2	5.9

#### 4.3.4 Long-term response

The long-term convergence is shown in Fig. 4-22. The data shows little horizontal closure with  $\sim 15$  mm of vertical closure since the first measurement approximately a year after excavation. The vertical deformation is roughly log-linear. A very similar deformation was measured from the base of the excavation to the mid-point of the north-west wall, suggesting that much of the deformation is occurring in the floor.

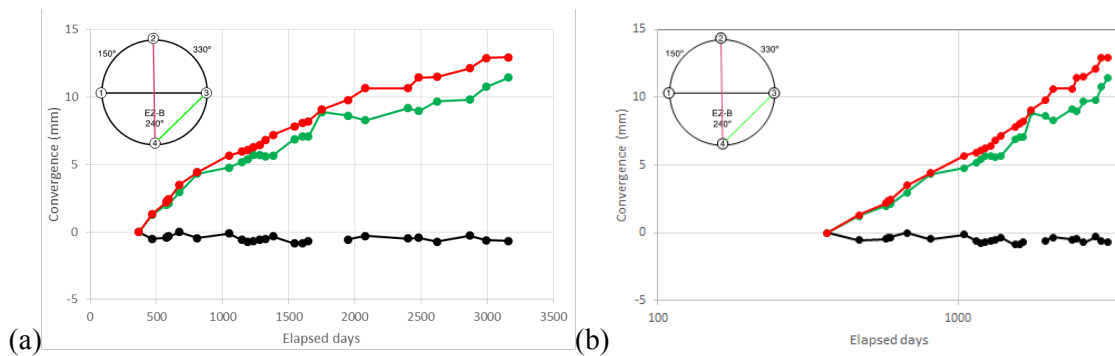


Fig. 4-22: Long-term convergence measured in EZ-B Niche.

#### 4.3.5 Summary of results

##### EDZ extent

The EZ-B Niche provided information on the EDZ in the north wall of Gallery 04 (locally heading  $262^\circ$ ) and around the niche itself. Mapping of the niche walls showed a dense fracture network of induced fractures up to about 1 m from the Gallery 04 walls (Fig. 4-23). In the next 1.5 m isolated clusters of EDZ fractures, sometimes related to the pre-existing bedding-parallel faults, were identified on both walls. Beyond this a lower density of induced fractures were mapped in the middle of the ENE side-wall, but typically not elsewhere. Core logging of BEZ-B1-3, showed unloading features to 1.3 m in BEZ-B1. No similar features were mapped in B2 or B3 where only tectonic (bedding-parallel tectonic shears: labelled as sst in mapping) or artificial features were recorded. In BED-B3, Yong (2008) associated the intersecting of the bedding-parallel shears with reductions in seismic amplitude and velocity suggesting local damage. These measurements were made approximately 4 months after excavation of the relevant section of Gallery 04.

Using a combination of core and geophysical logging in radial boreholes and boreholes drilled into the face, Yong (2008) suggested a narrow zone of induced fracturing up to 0.3 m thick with a larger perturbed zone up to 0.7 m thick as shown in Fig. 4-24. Ahead of the face the fractured zone extended to 0.5 m and the perturbed zone to 1 m. These estimates all relate to short-term observations of the EDZ around the niche. The evidence of sub-atmospheric pore pressures together with ongoing long-term deformation suggests that there may have been a subsequent longer-term evolution.

An example of the integrated analysis for borehole BEZ-B3 is shown in Fig.4-25.

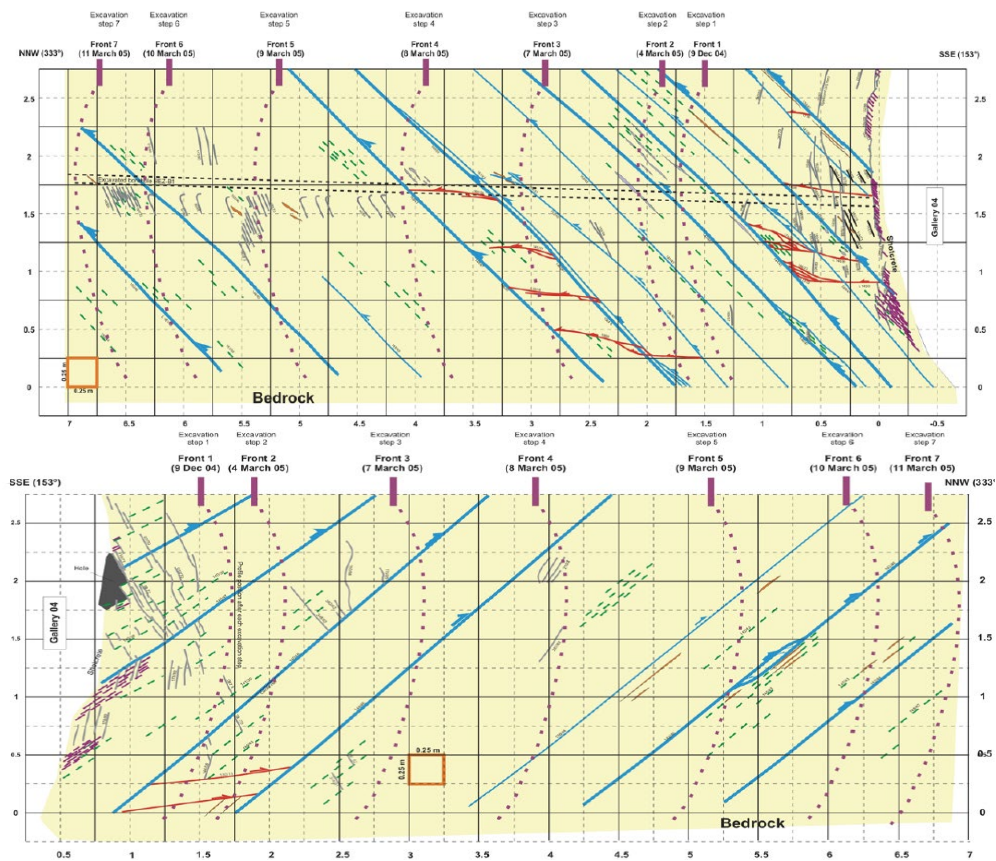


Fig. 4-23: Structural mapping of EZ-B Niche walls. Note dense network of EDZ fractures in sidewall of Gallery 04 from (Yong 2008).

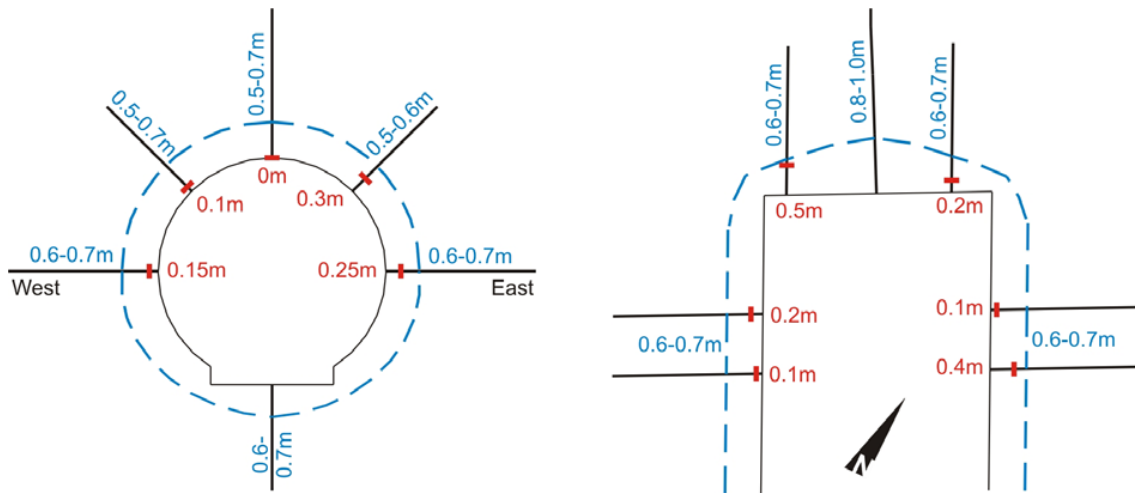


Fig. 4-24: Extent of fractured (red marker) and perturbed zone around EZ-B Niche from (Yong 2008).

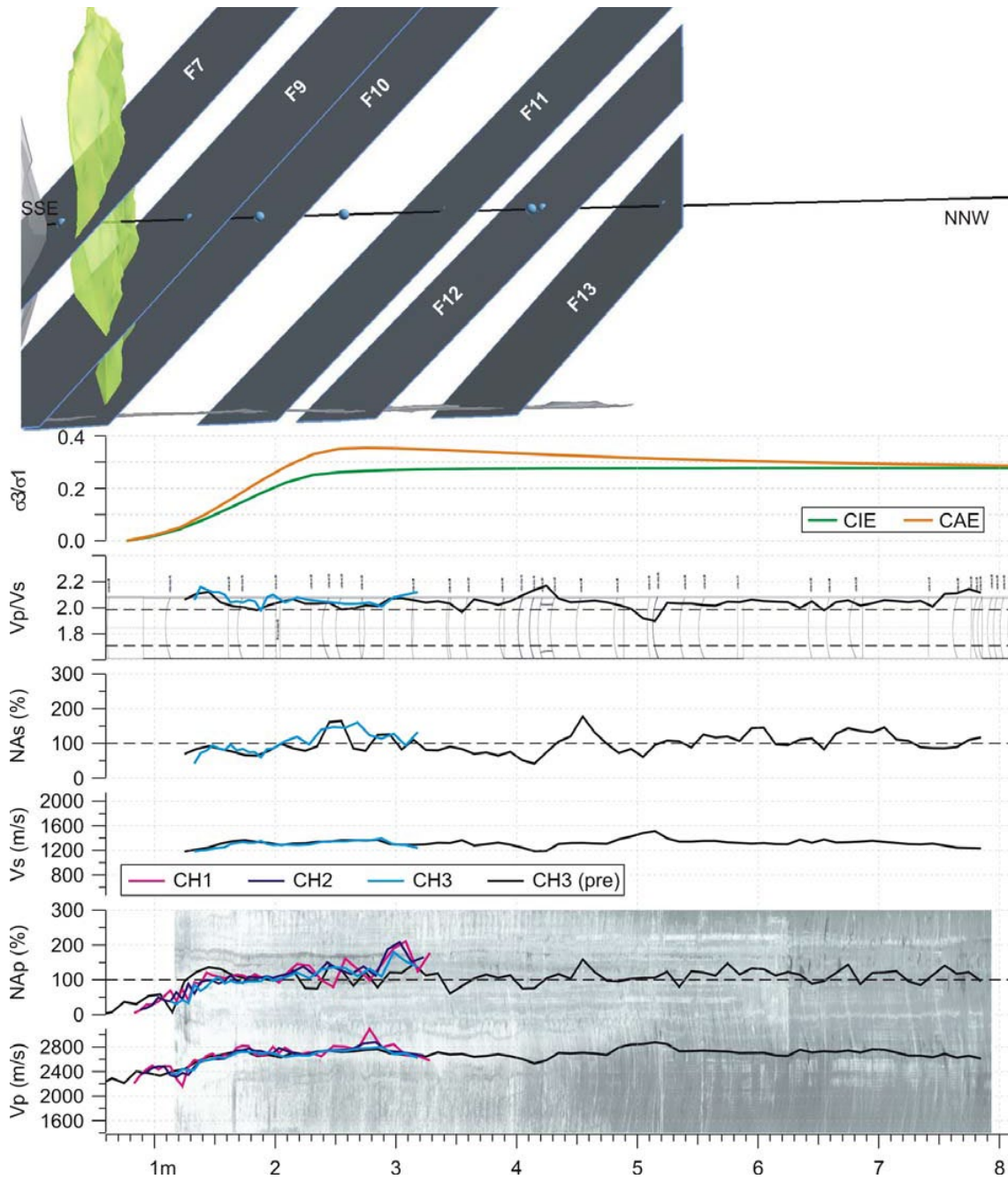


Fig. 4-25: Integrated analysis of BEZ-B3 drilled prior to excavation of EZ-B Niche. Intersections of mapped bedding-parallel shears with BEZ-B3 (blue spheres) and the advancing niche face are shown in the longitudinal-section (top). Lower plots show modelled stress ratios, DOPTV imaging, and seismic parameters derived from logging (from Yong 2008).

- $\sigma_3/\sigma_1$ : Ratio of minimum to maximum stress from modelling.
- CAE: Continuum, anisotropic, and elastic numerical model
- CIE: Continuum, isotropic, and elastic numerical model.
- $V_p/V_s$ : Ratio of P-S wave velocity.
- $V_p, N_{Ap}$ : Velocity and normalized amplitude of P-wave. (Channels 1-4)
- $V_s, N_{As}$ : Velocity and normalized amplitude of S-wave.

## Understanding of failure mechanisms

Analysis by Yong (2008) and Yong et al. (2008, 2010) showed that the pattern of EDZ fracturing was related to the pre-existing shear structures. These features are dominantly parallel to bedding and were well-defined in the niche. Yong (2008) suggested that the observed EDZ structures are best understood by assuming that these structures are significantly less stiff (3D elastic model used  $k_n = 4$ ,  $k_s = 1.5$  GPa/m) than the matrix. Comparison of simulations with (isotropic and anisotropic continua) and without such low stiffness features demonstrated their influence on EDZ fracturing. Feature stiffness was estimated using the approach of Barton (1972) based on inferred rock mass modulus (Hoek et al. 2002) and the measured intact rock modulus, resulting in a 50% reduction in the intact modulus. Compartmentalization of EDZ-induced fracturing has been observed in mapping of the excavation walls in several locations at Mont Terri.

## Pore pressure monitoring

Only one piezometer showed a clear breakdown and the pore pressure data was not analysed to derive an estimate on undrained shear strength. Pore pressures were typically low – near atmospheric (probably due to the proximity to Gallery 04) but the observed pattern of pore pressure response with increases and a subsequent reduction is consistent with other observations at the URL.

## Diametral strains

Yong (2008) reported total convergences determined from geodetic surveys on three arrays. The largest convergence ~ 8 months after excavation (28/10/05) was 12 – 13 mm, approximately 0.3% diametral strain. A horizontal convergence of 18 – 19 mm (0.4%) was reported in a survey on 13/05/05. Long-term measurements show approximately 15 mm of vertical closure from a year after excavation (0.3%).

Tab. 4-12: Summary of observations for EZ-B Niche excavation.

	Summary	Comment
Cross-section	Circular 3.8 m diameter, 6.5 m long	
Orientation	150° roughly normal to bedding strike and parallel to $\sigma_2$ .	Off Gallery 04 heading 262°
Local bedding	Shaly facies Bedding 147/45° (140-155/38-50°)	Shears trend 146/46° with average spacing ~ 1 m Yong (2008).
Method	Pneumatic hammer	Road header used to break out of Gallery 04
Support	Very limited – roof mesh and anchors. 150 mm shotcrete around entrance.	Limited support due to favourable orientation
EDZ	0.3 m-thick fractured region around tunnel.	Integrated assessment of core and geophysics of short-term development (Yong. 2008). Limited observations in floor and roof.
Diametral Strain	0.5% or less	Three arrays derived from geodetic measurements.
Pore pressure monitoring	One piezometer shows clear response to excavation. Sub-atmospheric pressure observed in another piezometer.	

## 4.4 HG-A Microtunnel

### 4.4.1 Location and local geological setting

The HG-A Microtunnel was drilled horizontally from the HG-A Niche, off Gallery 04, towards southwest (N238.5°) into the shaly facies of the Opalinus Clay. In this area, the shaly facies are composed of marly shales with numerous lenses of grey/white sandy limestones and weakly cemented fine grained brownish layers made of siderite. The HG-A Microtunnel was excavated along bedding strike. In this area of the URL bedding dips at approximately 48° towards SSE (see Fig. 4-26). The microtunnel is intersected by two differently oriented fault systems:

- SSE-dipping fault system, sub-parallel to the bedding, and
- Low angle to flat lying S to SW-dipping fault system.

The strike direction of SSE-dipping fault planes is sub-parallel to the microtunnel axis (ca. N240°) and the dip angle amounts to about 50°. Therefore, SSE-dipping fault planes are tangent to the microtunnel circumference at about 10:30 o'clock (see Fig. 4-26).

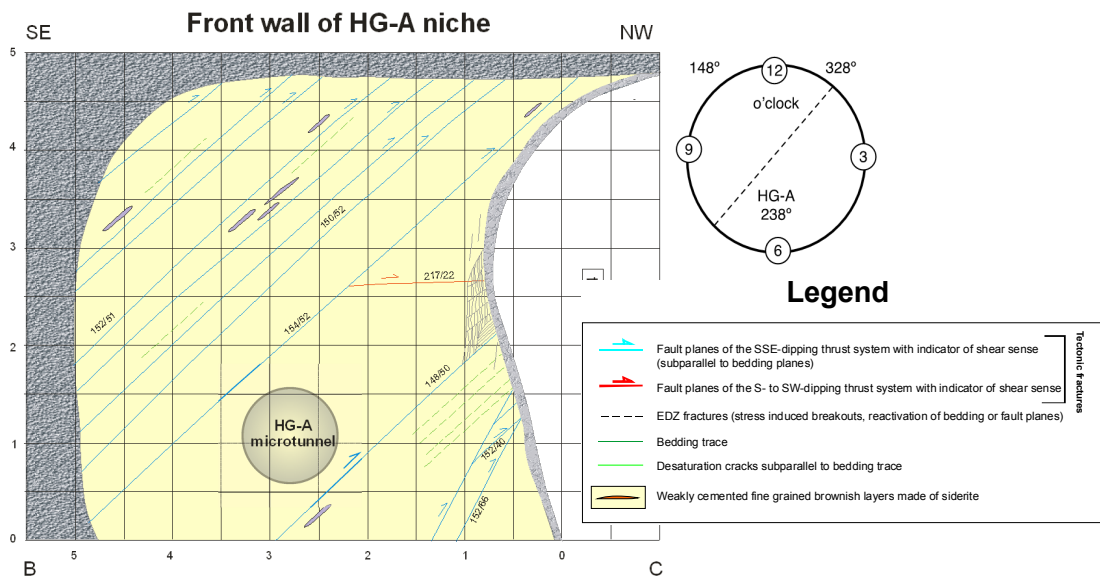


Fig. 4-26: Mapping of front wall of HG-A Niche showing relationship between bedding-parallel faulting and microtunnel.

The proximity of the microtunnel to Gallery 04 and the influence of the enlarged niche area suggest that stresses around the microtunnel will be affected by the larger excavations (especially close to the start of the tunnel). The seal zone is over 5 m (~ 1 tunnel diameter) from the wall of Gallery 04 suggesting that stresses should be approaching the undisturbed values.

#### 4.4.2 Excavation

The planned microtunnel cross-section was circular with a diameter of 1.036 m. The planned microtunnel was 13.1 m long and ran along the pilot-hole BHG-A00 (14.1 m). The microtunnel (BHG-A1) was drilled with a steel augur. Prior to augur-drilling, the pilot hole BHG-A00 (diameter 101 mm) was drilled to allow passage of the augur head stem-guide. After installation of the drilling machine (~ 2 days), drilling was performed between 17/02/05 and 24/02/05. The drilling rate was approximately 1.5 m/hour. The original plan allowed for 5 days drilling although the microtunnel could have been drilled in two: it was decided to slow the drilling for experimental reasons.

A steel liner was installed along the first 6 m of the microtunnel immediately after the end of excavation. Subsequently a cement grout was injected behind the liner, although this probably did not create a seal behind the liner. An open steel mesh was initially installed from 7-13 m to provide some protection for working (mapping and subsequent instrumentation) in the microtunnel. The mesh was removed to allow acquisition of the 3D profile by FLOTRON and reinstalled from 9.5 m on. The excavation schedule is given in Tab. 4-13.

Breakouts continued to develop over time and to limit further development in the section where the Megapacker seal would be emplaced, epoxy resin was applied to the interval between TM6 and TM9.5. The microtunnel remained open for approximately a year prior to instrumentation, backfill and sealing (see Marschall et al. 2008; Lanyon et al. 2009, 2014).

Tab. 4-13: HG-A excavation timetable.

Start Date	End Date	Event
17/02/2005 11:00	17/02/2005 11:20	Excavation 0.00-0.50 m
17/02/2005 16:00	17/02/2005 18:40	Excavation 0.50-4.50 m
21/02/2005 16:00	21/02/2005 17:10	Excavation 4.50-6.25 m
22/02/2005 12:00	22/02/2005 14:00	Excavation 6.25-9.25 m
23/02/2005 08:00	23/02/2005 09:20	Excavation 9.25-11.25 m
24/02/2005 09:50	24/02/2005 11:00	Excavation 11.25-13.00 m
25/02/2005 13:00	25/02/2005 17:00	Excavation liner installation
28/02/2005 09:00	28/02/2005 13:00	Excavation mesh installation
04/03 and 07/03/2005		Excavation mapping
09/03/2005 09:00	09/03/2005 17:00	Excavation FLOTRON 3D profile
10/03/05		Resin coating of seal section wall 6 – 9 m
27/01 and 03/02/2006		Repeat excavation mapping

Fig 4-27 shows the geosphere and microtunnel instrumentation. Much of the microtunnel instrumentation relates to the monitoring of the sealing and test sections during resaturation and gas injection (for discussion see Lanyon et al. 2014). Here we will concentrate on the response to excavation prior to sealing..

Pore pressure and packer pressure responses initially related to changes in volumetric strain induced by excavation: as the face reached the monitoring interval near field instrumentation may have responded to induced fracturing and the proximity of the atmospheric boundary condition – subsequently longer-term pore pressure responses related to dissipation of the induced pressures. Not all boreholes were drilled and instrumented prior to excavation. Tab. 4-14 lists the sensor installation and data acquisition system (DAS) connection dates for the main sensors. Borehole locations are shown in Fig. 4-27a, locations of sensors emplaced in the microtunnel are illustrated in Fig. 4-27b.

Tab. 4-14: HG-A excavation monitoring instrumentation.

Measurement	Instrument	Boreholes/sensors	Installation	
			Date	Days after excavation
Pore pressure	Multi-packer piezometers	B-A02, B-A03	18/02/05	1
Pore pressure	Mini-piezometers	B-A08-A13, B-A24, B-A25	02/03/05	13
Deformation	Deflectometer	B-A04, B-A06	19/02/05	2
Deformation	Clinochain	B-A05, B-A07		
Deformation	Stress-meter (3-axis strain)	B-A21, B-A22, B-A23	13/10/05	238
Sensors within microtunnel				
Deformation	Extensometers	E-H, E-V	13/07/05	146
Deformation	Strain gauges	SG1-SG22 circumferential array		
Pore pressure	Piezometers	Pore pressure in Seal Section S1,2,3 and Test Section see Fig. 4-27b		
Stress	Total Pressure Cells	Seal Section S1,2 – see Fig. 4-27b		
Water content	Time Domain Reflectometers	Within test Section see Fig. 4-27b		

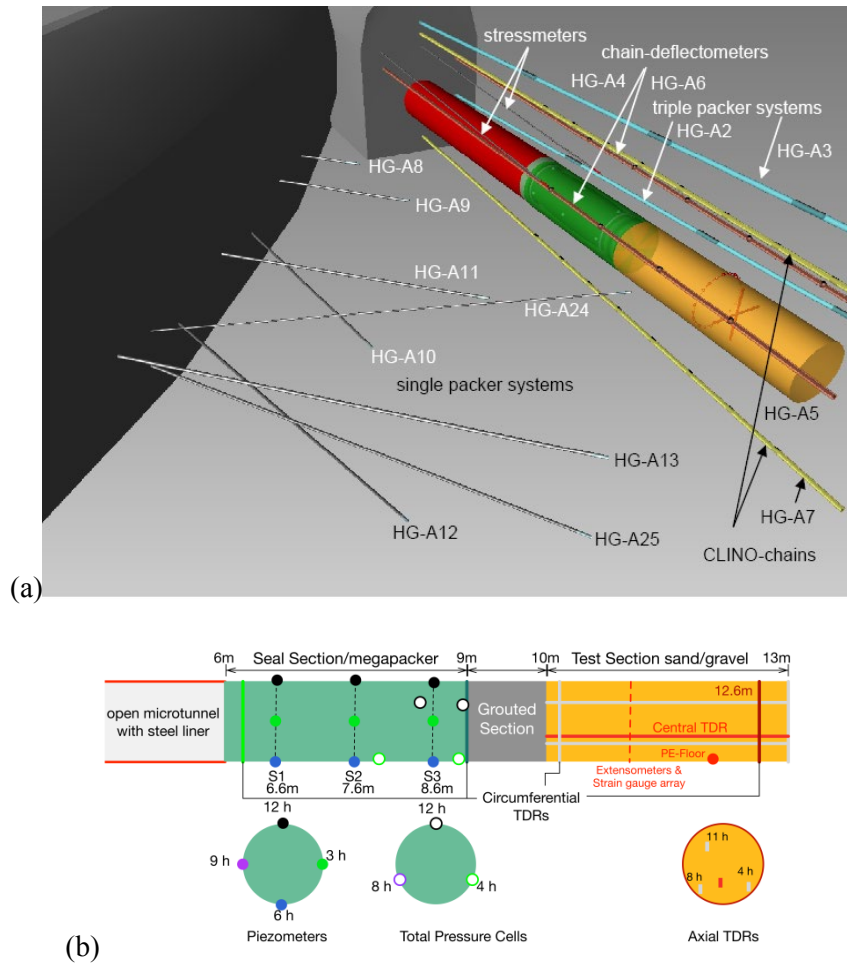


Fig. 4-27: Schematic drawing of the microtunnel and the site instrumentation.

(a) layout and borehole instrumentation (red = steel liner, green = seal section, orange = backfilled test section); (b) seal section and test section instrumentation.

#### 4.4.3 Excavation response

##### Observations during excavation

Shortly after drilling a laser survey was performed to image the as-constructed profile as shown in Fig. 4-28. The overbreak is clearly seen running along the microtunnel wall at approximately 3 o'clock and 11 o'clock. The zone at 3 o'clock is typically narrower than that at 11 o'clock as shown in Fig. 4-29.

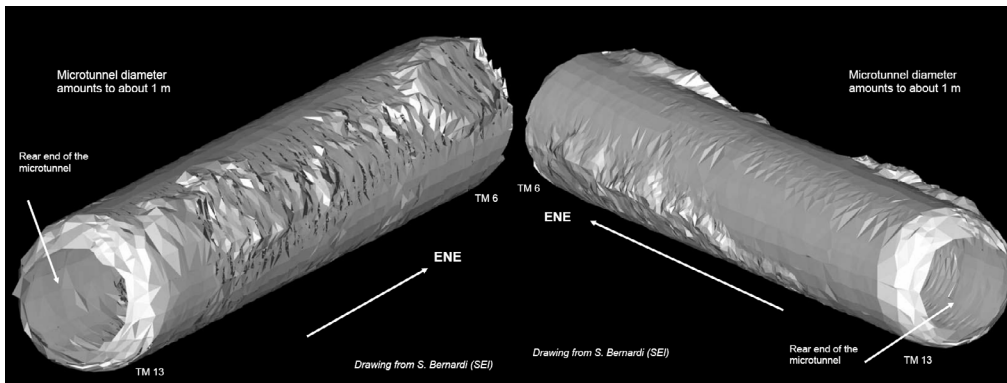


Fig. 4-28: Laser scans of un-lined portion of the microtunnel TM6-TM13.

Spatial resolution: 3 mm radial, 10 cm axial, azimuth 5-10°. Scan performed 09/03/2005 approximately 10 days after end of drilling.

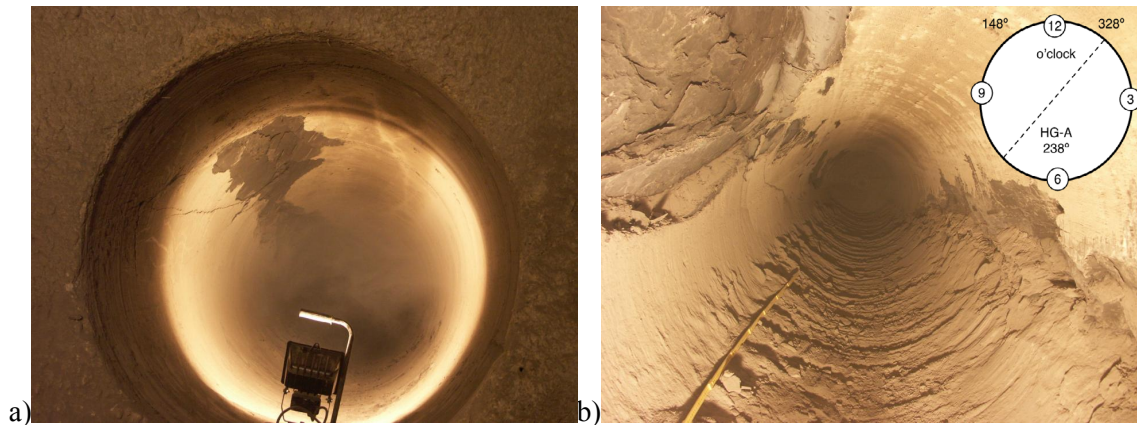


Fig. 4-29: View towards end of microtunnel showing development of breakout zones at a) TM0-TM3 and b)TM6-TM9.

Detailed structural mapping of the tunnel walls from TM6-TM13 was performed approximately 8 days (04/03/05) after excavation as shown in Fig. 4-30a. A breakout zone is visible towards the end of the tunnel between 9 and 11 o'clock (looking toward tunnel end). The minor zone at approximately 3 o'clock seen in Fig. 4-29b is not yet visible in the mapping.

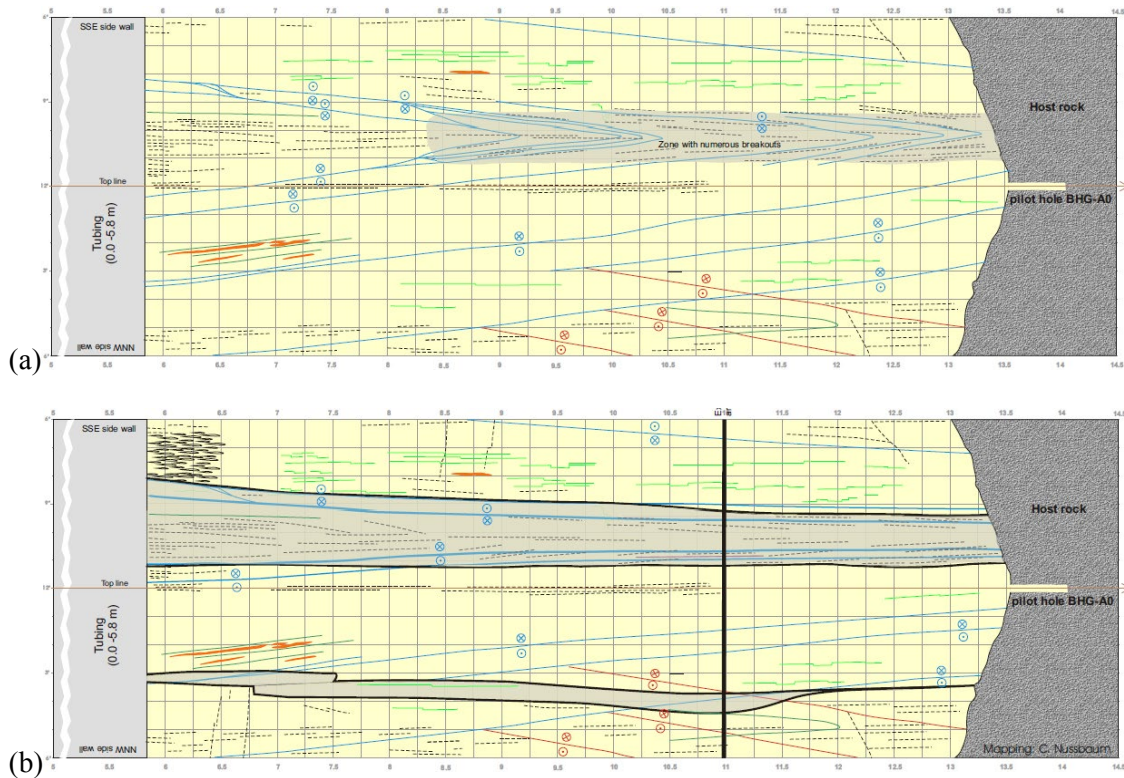


Fig. 4-30: Structural mapping of microtunnel TM6-TM13 (a) March 2005; (b) February 2006 (Nussbaum et al. 2005a, b; Nussbaum & Bossart 2006).

### Pore and packer pressures

Only boreholes B-A02 and B-A03 monitored pore pressures during excavation. Each was equipped with a triple packer system with three monitoring intervals (see Tab. 4-15). The boreholes run approximately parallel to the microtunnel at 2-2.2 m above (B-A02) and 1.4-2 m to the ENE side of (B-A03) the tunnel axis.

Tab. 4-15: Monitoring and packer intervals B-A02 and B-A03 TM coordinates.

	Packer 3	I3	Packer 2	I2	Packer 1	I1
B-A02	4.69-5.19	5.19-8.69	8.69-9.19	9.19-11.69	11.69-12.19	12.19-13.69
B-A03	4.54-5.04	5.04-8.52	8.52-9.02	9.02-11.51	11.51-12.01	12.01-13.53

Although only very limited time was available for pressure equilibration, the measured pressures in the intervals and packers were steady prior to excavation from TM4.5 onwards and showed a very distinct response (Fig. 4-31). Pressures rose in B-A03 and typically fell slightly in B-A02. The pressure responses correlated with the excavation steps. Responses were of larger amplitude in B-A03 which is somewhat closer to the microtunnel than B-A02. The largest response was observed in B-A03-PA3 approximately 1.4 m from the microtunnel wall. There was no clear breakdown and pressures typically continued to rise after the end of excavation suggesting ongoing deformation (the packer pressure in BA03-PA3 was reduced on 12/05).

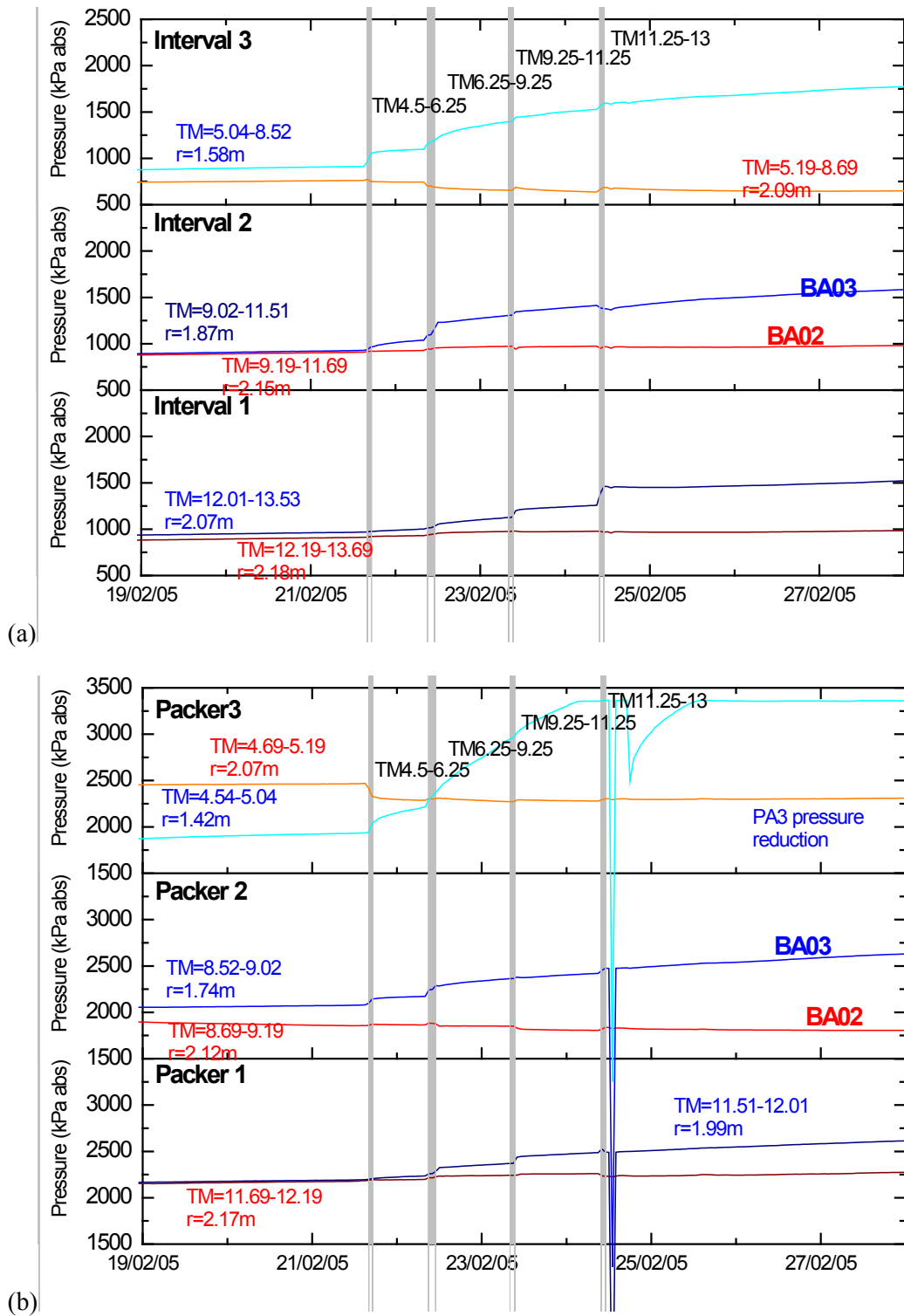


Fig. 4-31: Response during microtunnel excavation in BA02 and BA03: (a) piezometer interval pressure; (b) packer pressure.

## Deformations

Deformations in the geosphere during excavation were measured using the clinochains and deflectometers shown in Fig. 4-27. The tunnel meterage and radius of the mid-points of the deflectometer (B-A04, B-A06) and clinochain elements are given in Tab. 4-16.

Tab. 4-16: Deflectometer and clinochain element locations as tunnel meterage (TM) and radial distance from centre line.

	B-A04		B-A06			B-A05		B-A07	
	TM	Radius (m)	TM	Radius (m)		TM	Radius (m)	TM	Radius (m)
DX2	11.75	1.29	11.07	1.26	DE1	12.99	1.53	13.04	1.76
DX3	10.25	1.30	10.22	1.28	DE2	11.99	1.54	12.04	1.70
DX4	9.40	1.31	8.08	1.34	DE3	10.99	1.56	11.05	1.65
DX5	7.25	1.33	6.58	1.38	DE4	9.99	1.58	10.05	1.59
DX6	5.75	1.35			DE5	8.99	1.59	9.05	1.54
					DE6	7.99	1.61	8.05	1.48
					DE7	6.99	1.62	7.05	1.43
					DE8	5.99	1.64	6.05	1.37

The element deflections measured during excavation were typically small ( $< 0.5$  mm) as shown in Fig. 4-32, indicating relatively small strains. Deflectometer responses (Fig. 4-32a) occur at the excavation steps, while there is some indication of continuing deformation, especially at DE1, from the clinochain measurements (Fig. 4-32b) perhaps due to the higher resolution measurements.

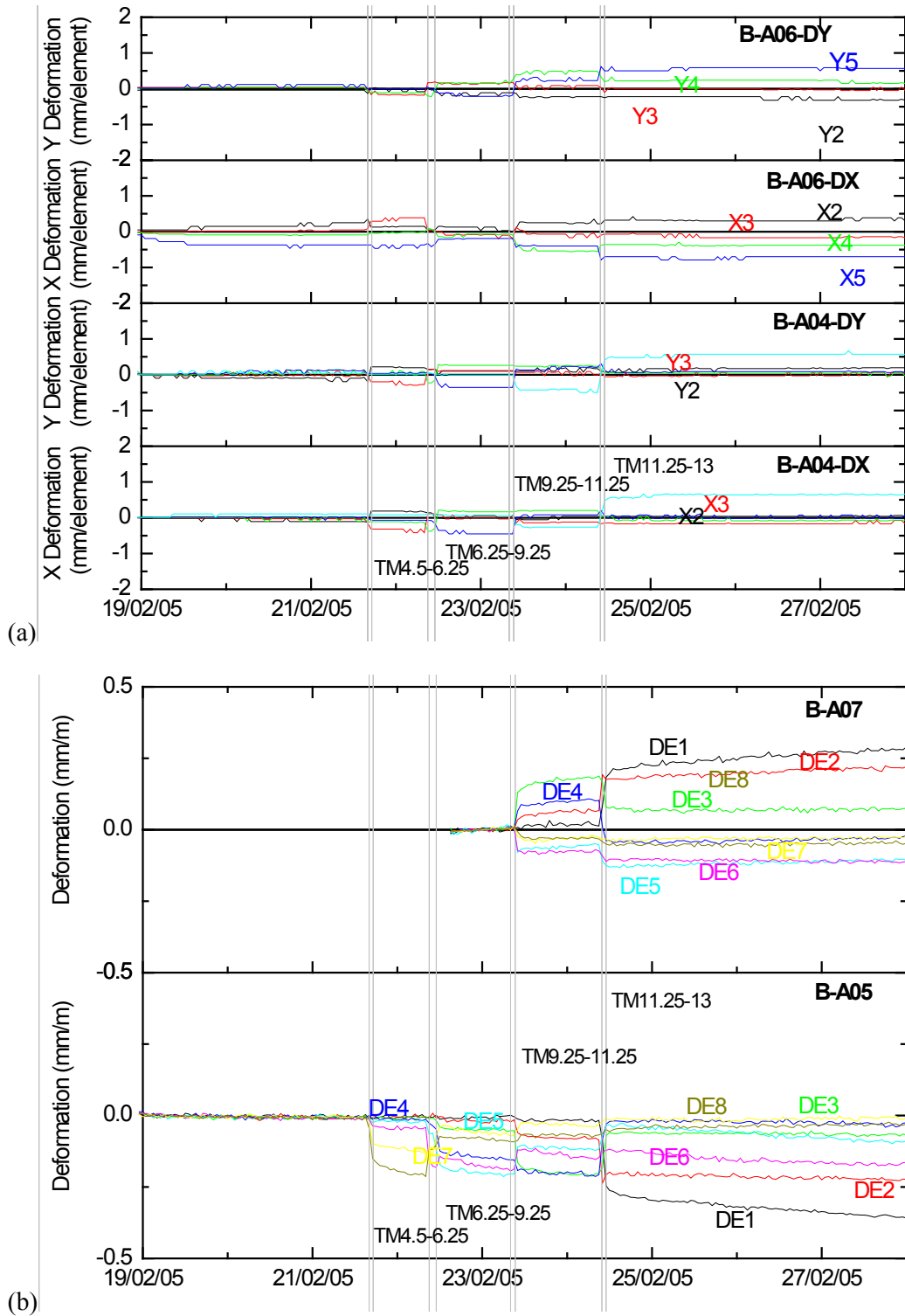


Fig. 4-32: Response during microtunnel excavation in B-A04, B-A05, B-A06 and B-A07. (a) deflectometers, (b) clinochains.

#### 4.4.4 Long-term response

In this section we discuss the longer-term response over approximately eighteen months between excavation and installing of the Megapacker on 29/06/06. During this time, the microtunnel was open although no forced ventilation was applied. Construction work and sensor installation for the test and seal sections started on 23/06/06 and continued until Megapacker emplacement. This resulted in some disruption to the existing sensors. The section between the Megapacker and the retaining wall, TM9-TM10 was grouted with resin on 13/07/06 and further grouting was performed 22/08/06. The test section saturation began on 09/10/06.

Structural mapping of the microtunnel was performed in early 2006, 11 months after excavation as shown in Fig. 4-30b. Since the previous mapping (Fig. 4-30a) the breakout zone at 9-11 o'clock had developed along the complete length of the open tunnel and has widened. A second narrow zone had developed on the opposite side of the tunnel at 3 o'clock.

#### Pore and packer pressures

Interval pressures peaked between 10 and 13/03/05 approximately 2 weeks after the end of excavation (Fig. 4-33). They then declined slowly to about 110-120 kPa in Intervals 2 and 3 and to higher pressures (300-400 kPa) in Interval 1. Sharp responses seen in B-A02 were due to hydrotesting. Peak pressures in the B-A03 intervals were I1: 2180 kPa, I2: 1880 kPa and I3: 1760 kPa. No breakdown was observed and it is assumed that pressures reduced slowly over time due to the small hydraulic diffusivity of the rock. Packer pressures showed a different trend continuing to rise in B-A03 and remaining steady in B-A02. A small peak pressure event can be seen in Packer 2 on 30/12/05 which was apparently unrelated to any field activities. Packer pressure in Packer 3 reached 7250 kPa (although note sensor change) and Packer 2 reached 6000 kPa by the end of June 2006. Pressure in Packer 1 was significantly lower at 3100 kPa.

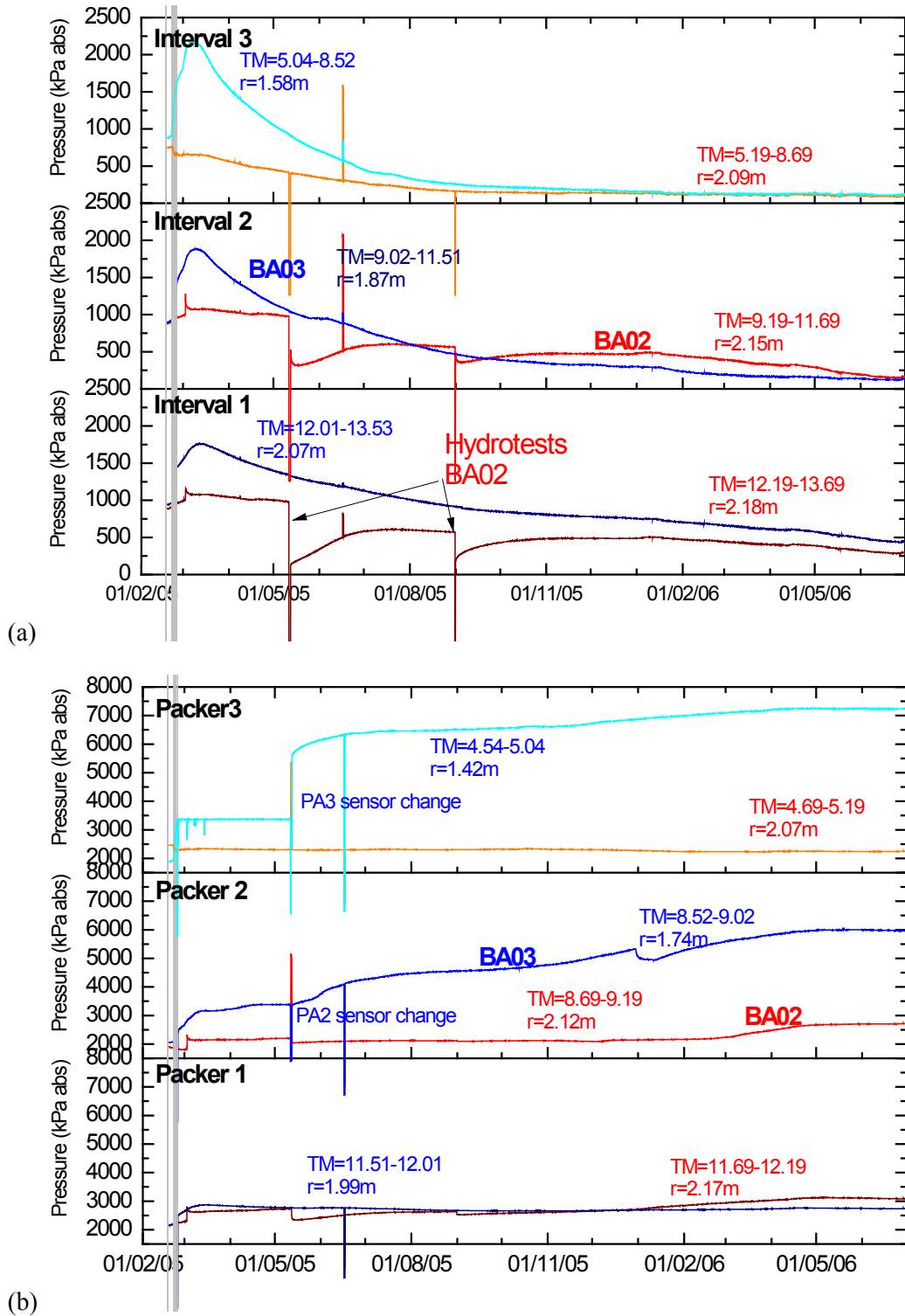


Fig. 4-33: Response during microtunnel excavation in B-A02 and B-A03. (a) piezometer interval pressure, (b) packer pressure.

## Deformations

Following excavation of the microtunnel additional instrumentation was installed in preparation for the resaturation and gas-leakoff tests. There was however no monitoring of convergence. Horizontal (E-H) and vertical (E-V) extensometers and a circumferential strain gauge array were installed in the microtunnel at TM11.09 and TM11.03 on 13/07/05 about five months after excavation and a year before Megapacker emplacement. The extensometers inside the microtunnel both showed a reduction (closure) prior to removal on 23/03/06 (Fig. 4-34). The horizontal extensometer reduced by 1.8 mm (0.2%) while the vertical extensometer reduced by 1 mm (0.1%) with increased deformation from November and December onwards. After reinstatement there was a static offset and a more noisy response, probably due to increased activity in the microtunnel. There was a sharp reduction on 16/05/06 after backfilling on 05/05/06.

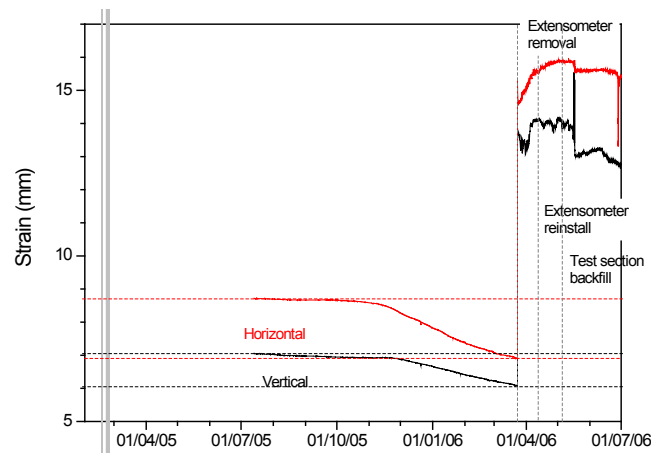


Fig. 4-34: Response after HG-A microtunnel excavation in horizontal and vertical extensometers.

The responses of individual elements of the 22-element circumferential array are shown in Fig. 4-35.

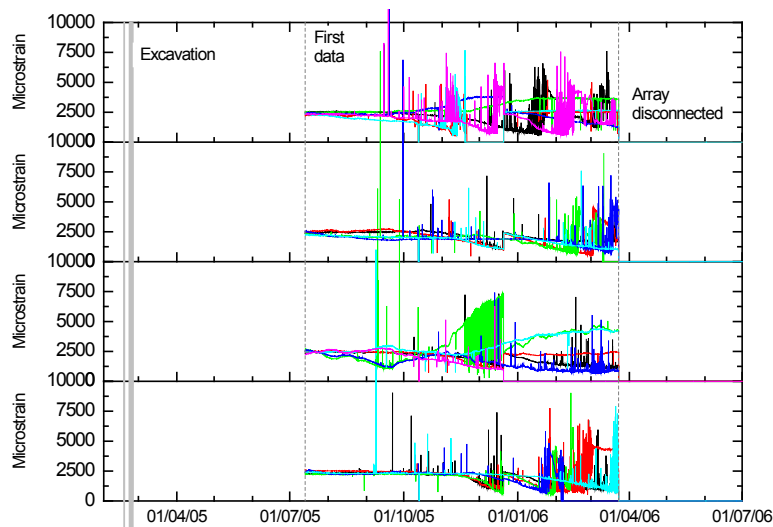


Fig. 4-35: Response after microtunnel excavation in strain gauge array within HG-A microtunnel.

Deformations in the geosphere continued to be monitored and increased to about 2 mm at each element. The clinochains showed a roughly continuous increase during the period (see Fig. 4-36).

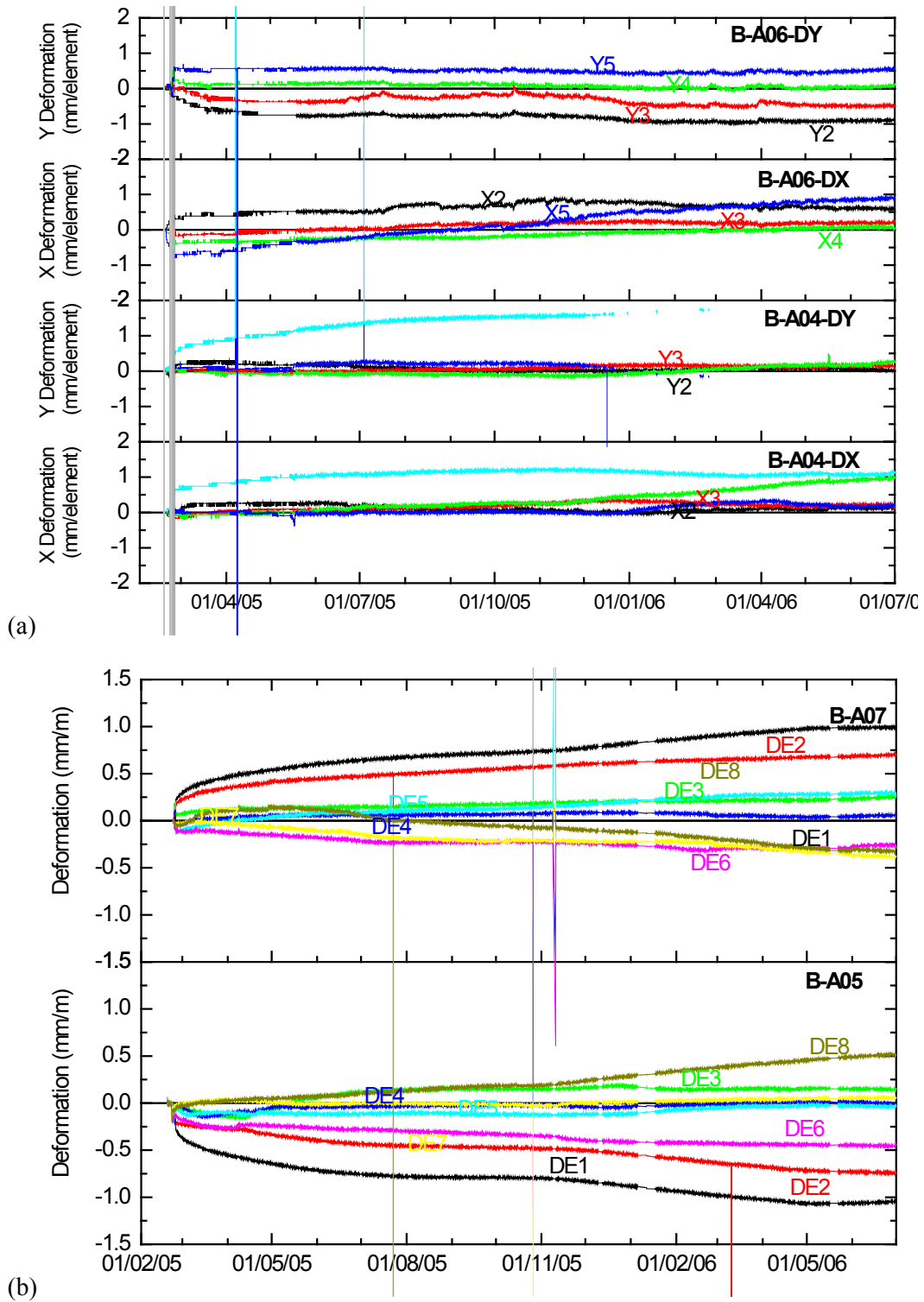


Fig. 4-36: Response after HG-A microtunnel excavation in boreholes B-A04, B-A05, B-A06 and B-A07: (a) deflectometers, (b) clinochains.

In addition to the deflectometers and clinochains three borehole stressmeters were installed. These sensors included three vibrating wire strain gauges installed orthogonal to the borehole axis at 60° angles. The raw data from the strain gauges is plotted in Fig. 4-37.

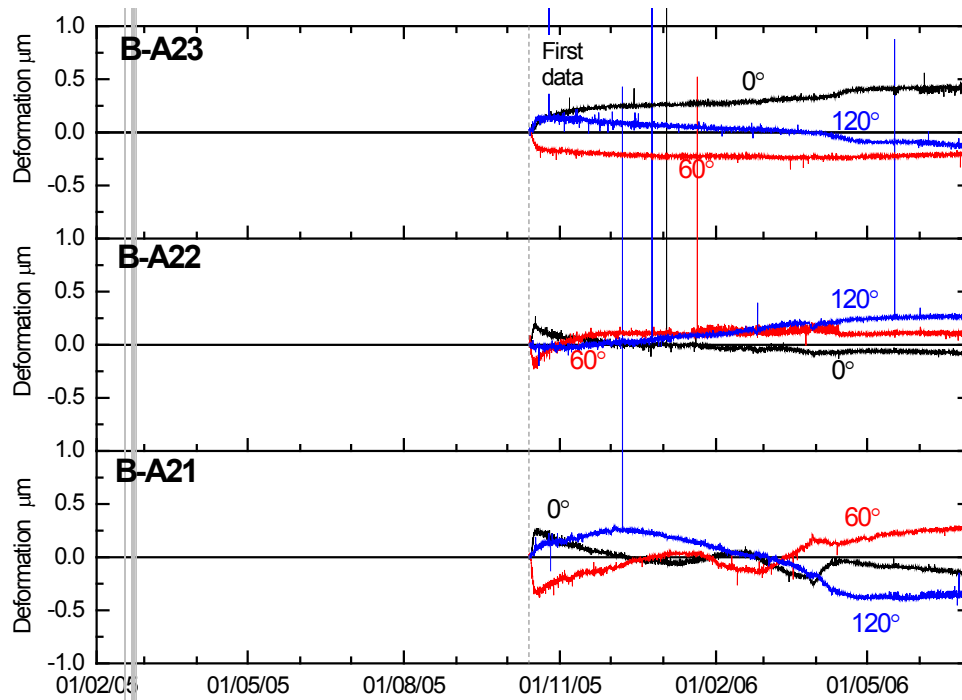


Fig. 4-37: Response after HG-A microtunnel excavation in borehole stressmeter (triple strain gauges).

#### 4.4.5 Summary of results

##### Understanding of failure mechanisms

The excavation and monitoring of the HG-A Microtunnel has provided useful information and concepts (see Chapter 3.4) in relation to the structure of the EDZ around an excavation intermediate in scale between boreholes and large tunnels. The mechanisms are similar to those identified in Martin & Lanyon (2003a) and relate to:

- slip and buckling along bedding planes or other planes of weakness largely controlled by material anisotropy.
- Extension failure due to stress anisotropy.

There are unambiguous indications of ongoing deformation after excavation. This is seen clearly in the monitored pressure and deformation responses together with the repeated structural mapping. The measured peak pressures occurred 10-15 days after the end of excavation.

### Diametral strain

Tunnel convergence measurements were not made after excavation although extensometer data show continued deformation with 0.1 – 0.2% closure being measured between 5 and 18 months after excavation.

### Evidence of EDZ extent

While the structural mapping clearly showed the spatial distribution and development of an EDZ with an overbreak depth of ~ cms., the installed geosphere sensors – typically 0.5 – 1.5 m (1-3a) from the microtunnel wall showed no distinct influence of fracturing events. Modelling showed the development of plastic zones with increased porosity (Levasseur, et al. 2013, Alcoverro et al. 2013) or zones of extension and shear failure (Viator et al. 2006). Levasseur, et al. (2013) estimate that an elliptic EDZ (semi-major axis 1.05 m) based on a Plasticity Indicator can be used to explain the observed response if the Young's modulus of this zone is significantly reduced and permeability significantly increased.

### Pore pressure monitoring

No clear breakdown in pore pressure was observed that would indicate fracturing or significant deformation around the monitoring intervals. The pressure rise continued for some time after the end of excavation possibly due to ongoing failure and enlargement (overbreak) of the unlined microtunnel. The observed reductions in pressures support a diffusive pressure response albeit with a potentially enhanced permeability.

Tab. 4-17: Summary of observations for HG-A Microtunnel excavation.

	Summary	Comment
Cross-section	Circular 1.04 m diameter, 13.1 m long	Significant overbreaks developed
Orientation	238.5° roughly normal to bedding strike and parallel to $\sigma_2$ .	From Gallery 04 HG-A Niche°
Local bedding	Bedding 147/45°	(140-155/38-50°)
Method	Augur	Road header used to excavated HG-A Niche
Support	Steel liner 0-6 m - roof mesh 6-13 m to facilitate working. Resin applied over seal section 6-9 m	Tunnel was open for ~ 18 months
EDZ	Breakouts observed in open micro-tunnel. No evidence of fracturing from monitoring holes. < 0.4 m -thick fractured region around tunnel.	Interpretation of Marschall et al. (2006). Suggests EDZ thickness < 40 cm
Diametral Strain	Initial closure not measured until six months after excavation ~ 0.1% further closure prior to sealing.	Derived from measurements at extensometer installation
Pore pressure monitoring	No clear breakdown observed in near field monitoring intervals.	Pressure peak about 2 weeks after end of excavation

## 4.5 Gallery 08

### 4.5.1 Location and local geological setting

Gallery 08 passes through the three main facies present in the URL:

- The shaly facies in the lower part of the formation (argillaceous and marly shales with micas and nodular, bioturbated layers of marls or with mm-thick layers of sandstones).
- The sandy facies in the middle and upper part of the formation (marly shales with layers of sandstones and bioturbated limestones, or with lenses of grey, sandy limestones and mm-thick layers of white sandstones with pyrite).
- The thin carbonate-rich, sandy facies in the middle of the formation (calcareous sandstones intercalated with bioturbated limestone beds, the latter showing a high detrital quartz content).

The tectonic faults intersected by Gallery 08 belong to the three previously identified fault systems:

1. SSE dipping faults (mainly formed by bedding-parallel slip);
2. low angle SW dipping fault planes and flat-lying SSE to S dipping fault planes and
3. N to NNE trending steeply inclined sinistral strike-slip faults.

Gallery 08 is mainly cut by SSE-dipping faults generally sub-parallel to bedding. The faults are heterogeneously distributed along the gallery with frequency ranging from 1 to 5 faults per 10 metres. In the section between GM52 and GM62, no tectonic faults were identified.

Sub-horizontal faults were also identified. A major fault intersects the tunnel roof between GM90 to GM110. This fault has a visible extent of at least 20 m along the gallery but is certainly larger. The flat structure, located in the ceiling, could have produced severe stability problems during excavation without immediate application of the lining.



Fig. 4-38: The main fault in the side wall and invert of Gallery 08.

The main geological structure intersected by Gallery 08 is the Main Fault which outcrops between GM110 and GM116 (Fig. 4-38). This is a 3 m thick thrust zone with complex geometry. The internal structure is heterogeneously composed of undeformed blocks embedded by strongly tectonized parts, locally as fault gouges. The upper part of the Main Fault is intensively folded. By contrast, the Main Fault intersecting Gallery 98, 50 m distant is only 1 m thick suggesting strong lateral variability. A second tectonized zone outcrops between GM67 and GM68. Mapping revealed a 1 m thick thrust zone dipping to the SE, abruptly cut by a steep inclined fault at GM70 (Nussbaum et al. 2010).

It is expected that the pre-excavation stress-state around Gallery 08 is reasonably well described by the stress tensor suggested by Martin & Lanyon (2003a). Although there will be some influence of the existing galleries over the first few metres, there are no other significant nearby excavations for the majority of the length.

#### 4.5.2 Excavation

Gallery 08 was excavated with a roadheader: hydraulic drum cutter Erkat ER 600 mounted on an excavator machine. Standard roadheaders were too small for a total-profile excavation. The Erkat ER 600 was suitable, but reached its limits when the uniaxial compressive strength of rock exceeded 20 MPa. The overall excavation schedule is given in Tab. 4-18.

Tab. 4-18: Overall schedule of Gallery 08 excavation.

Section	Start (GM)	End (GM)	Start	End	Duration
DI extension			29/10/07	06/11/07	
North	0	50	07/11/07	20/12/07	4
A	50	69.8	31/01/08	19/02/08	14
Break A			20/02/08	26/02/08	
B	69.8	94.5	29/02/08	27/03/08	18
C	94.5	121.5	31/03/08	15/04/08	16
Concrete invert			15/04/08	21/04/08	
South	121.5	159.1	29/05/08	11/07/08	
Lower profile excavation			11/07/08	13/08/08	
Break EZ-G			14/07/08	28/07/08	
EZ-G	159.1	167.2			
Niche 1 (DR-A) ,4 (TT)					
Niche 2 (Mine-By)			13/10/08	07/11/08	18
Niche 3					

#### 4.5.3 Excavation response

Six convergences profiles were installed along Gallery 08, labelled GM14, GM56, GM75, GM88.5, GM117 and GM160 (Burrus et al. 2010). A further four profiles were measured in the niches: the profile locations are listed in Tab. 4-19. Convergence measurements were made roughly every day for the first 7 days and then every week for days 7 – 100 and every two weeks after that.

Tab. 4-19: Convergence profiles monitoring of excavation of Gallery 08 and summary of observations.

Profile	GM	Install	Heading (approx.)	Summary of Observations
GM14	14.36	28/11/07	240°	Displacements wire 5-2: 5 mm and 55 mm for 4-3. Since concreting, stable and the displacements < 5 mm in a year.
GM56	54.33	02/02/08	150°	Largest displacement 4-3 ~ 38 mm. Increased stability after concreting. Some influence of Niche 1 excavation.
GM75	75.25	03/08	150°	Displacements 12 mm for 4-2 to 37 mm for 5-1 in first month until concreting of invert. Since concreting displacements a few mm. Niche 1 caused some small displacements.
GM88.5	88.76	14/03/08	150°	Displacements of 15 – 20 mm stabilized after the concreting of the invert on 17/04/08. Strong wall displacements due to Niche 2/MB not stabilized as of 12/12/08.
GM117	118.45	27/05/08	150°	Close to Main Fault Displacements ranged from 7 mm for 5-2 to 23 mm for 5-3. Minor influence of shotcrete. Strong influence of Niche 3 excavation.
GM160	160.73	04/08/08	140°	Sandy facies Considerable disturbance due to excavation. Displacements stabilize after concreting of invert.
Niche 1 DR-A	GM4	18/09/08	240	Maximum displacement of 5 mm was observed for the distance 4-3 over 3 months. Some movement after concreting of invert.
Niche 2	NM4.5	17/10/08	240	Maximum displacement > 60 mm on 5-1. Ongoing movement after concreting of invert.
	NM12	17/10/08	240	Maximum displacement ~ 70 mm on 5-1. Ongoing movement after concreting of invert.
Niche 4 TT		22/11/08	230	Sandy facies Displacements in Niche 4 were between 5 and 13 mm.

Fig. 4-39 shows the measured convergences in Gallery 08 up to 100 days after excavation. Note that the array at GM14 faces at almost 90° to the other arrays in Gallery 08, that the array at GM117 is located close to the main fault and that the array at GM160 is located within the sandy facies.

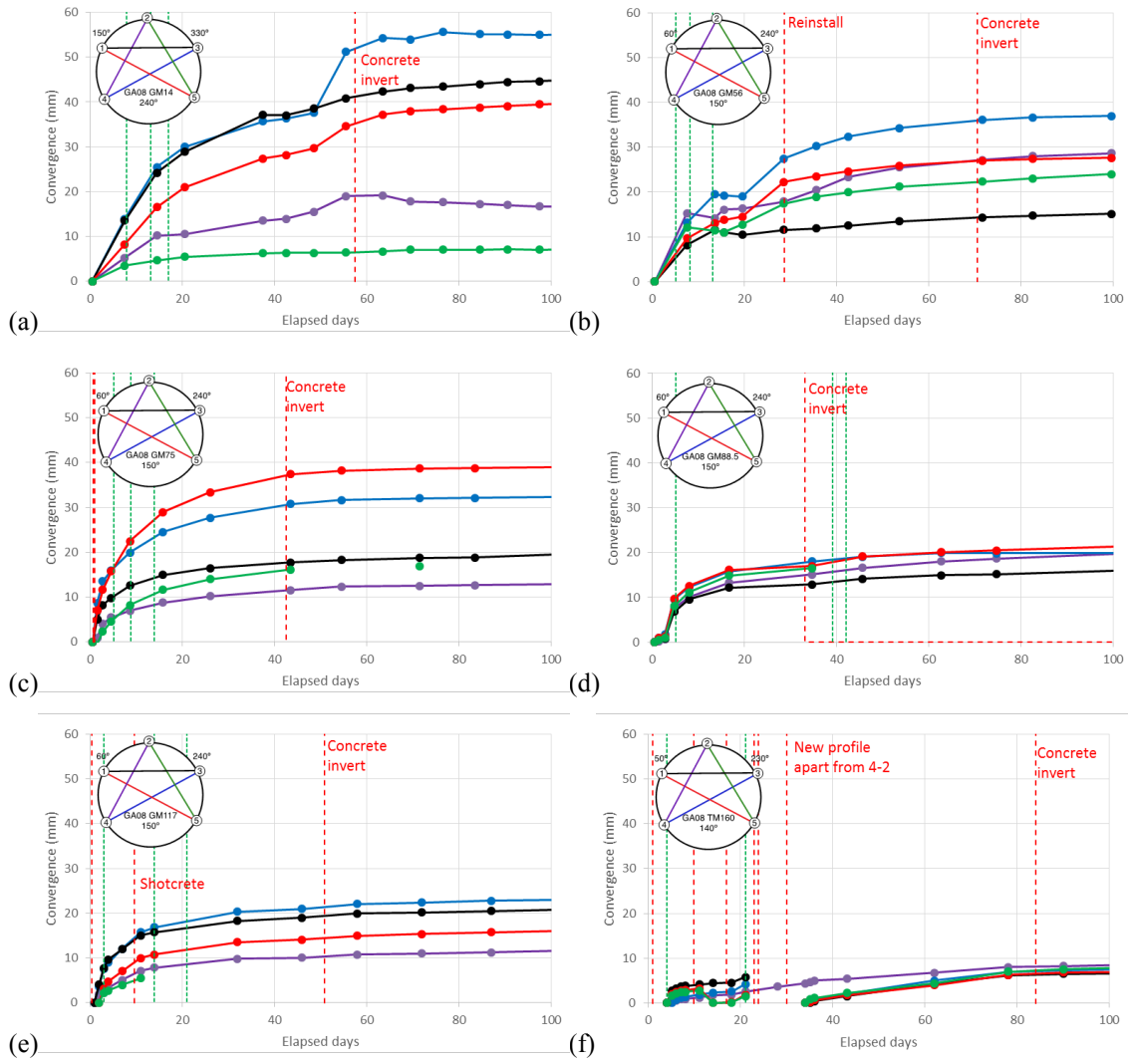


Fig. 4-39: Measured short-term (100 days) convergences in Gallery 08.

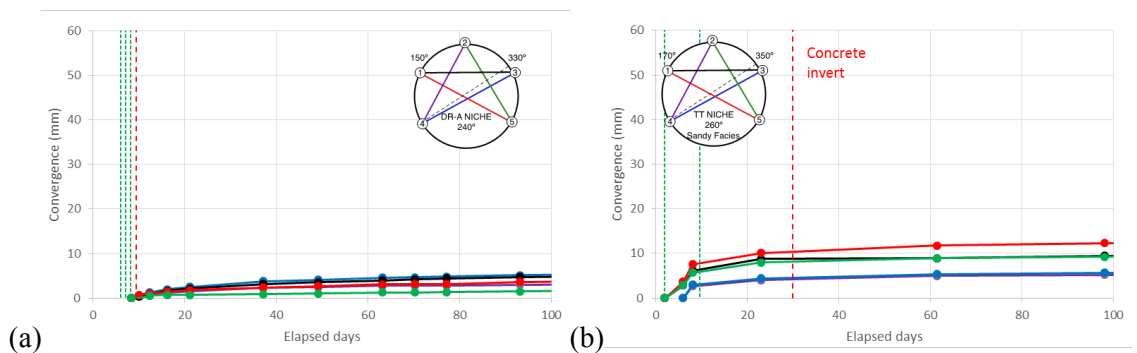


Fig. 4-40: Measured short-term convergences in Gallery 08: (a) DR-A Niche (Niche 1) and (b) TT Niche (Niche 4).

Fig. 4-40 shows the convergences from the DR-A Niche (Niche 1) and TT Niche (Niche 4). The measurements from MB Niche (Niche 2) are discussed in the next section. Convergences were small in both niches – although the exact location was not recorded and so there may be some initial convergence not shown in Fig. 4-40.

The largest short-term convergences in the gallery were measured at GM14 where the gallery is heading roughly along bedding strike. Significantly smaller convergences were measured close to the main fault and in the sandy facies at GM160 and in the TT Niche.

The excavation of Gallery 08 was also monitored in the distometer profile in Gallery 04 (GM68) located in the extension of the Gallery 08 tunnel. Convergences increased by a few mm during excavation of Gallery 08.

In addition to the convergence profiles discussed above a total of 21 5-point 3D convergence sections were installed. The profiles were installed immediately after excavation approximately 80 cm from the face. The accuracy of each point was calculated by multiple measurements and did not exceed  $\pm 1$  mm. The largest deformations took place during the first 30 days after the zero reading. Between GM8 and GM95, transverse deformations of 2-4 cm were observed. From GM110 to GM170 the deformations were  $< 1$  cm. Ceiling settlements were similar to the transverse deformations. Measurements were made at 2-day intervals in the first week, reducing to every 40 days after the 8<sup>th</sup> month.

Tab. 4-20: Convergence profiles monitoring of excavation of Gallery 08.

Survey point	Tunnel Metre	Survey point	Tunnel Metre	Survey point	Tunnel Metre
GM1	8.57	GM68	68.00	GM123	123.00
GM5	5.00	GM75	75.00	GM132	132.00
GM15	15.00	GM81	81.00	GM141	141.00
GM25	25.00	GM85	85.00	GM152	152.00
GM36	36.00	GM93	93.00	GM162	162.00
GM49	49.50	GM110	110.00	GM167	167.00
GM55	55.00	GM115	115.00	NM16	15.90

The largest settlements of up to 3 cm were between GM49 and GM93. The values in the remaining part of the gallery were smaller than 2 cm. The largest transverse deformations were between GM5 and GM25. In the remaining part of the gallery, the values were smaller than 2 cm. The influence of the subsequent excavation periods remained until 2-3 months after the first excavation in a particular section. The results are largely consistent with the data from the convergence profiles with larger convergence when the tunnel is heading close to bedding strike and comparable values.

#### 4.5.4 Long-term response

Longer-term responses are shown in Fig. 4-41 and Fig. 4-42. In general the convergence stabilized after  $\sim 100$  days (after concreting invert) apart from disturbances caused by nearby excavation work.

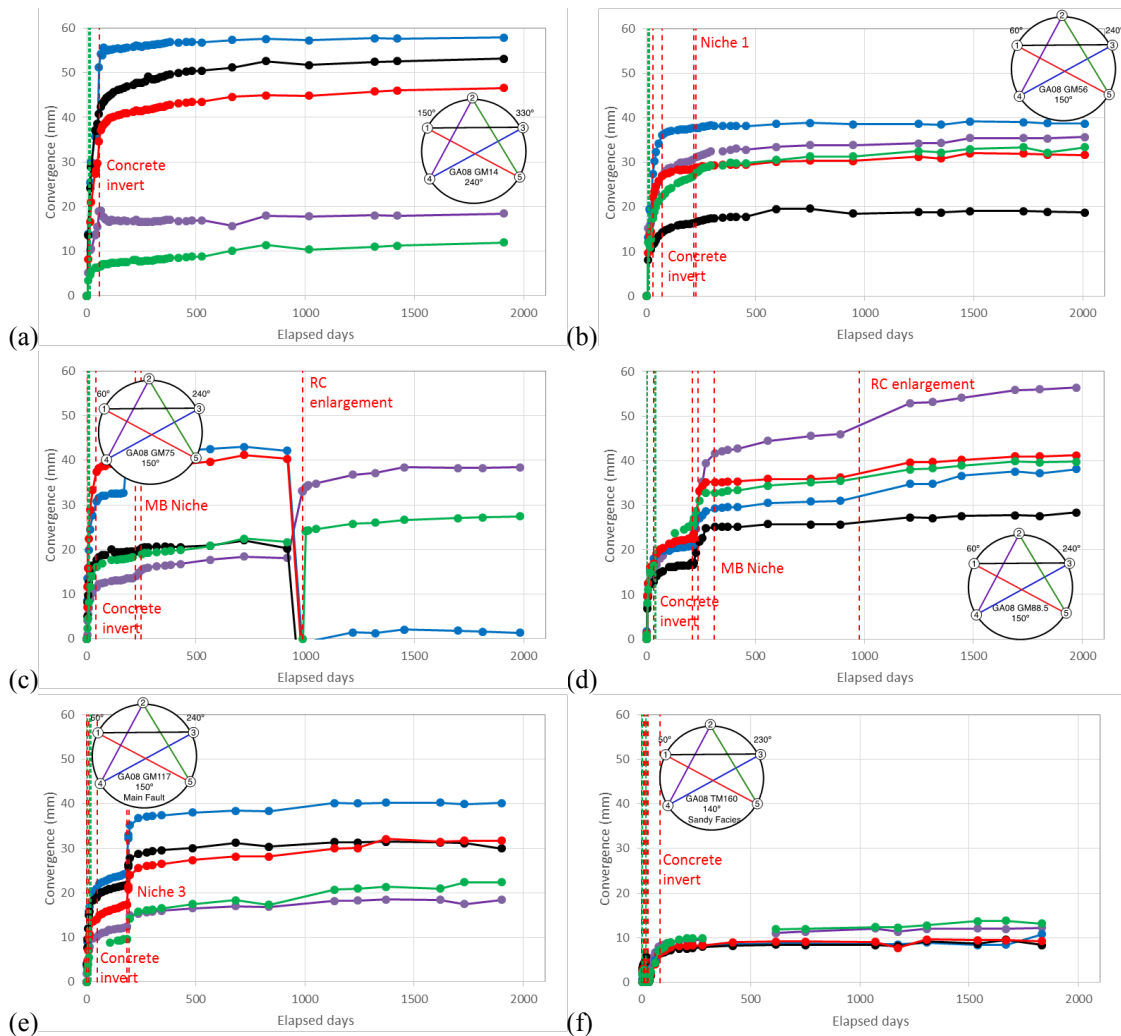


Fig. 4-41: Long-term measured convergences in Gallery 08.

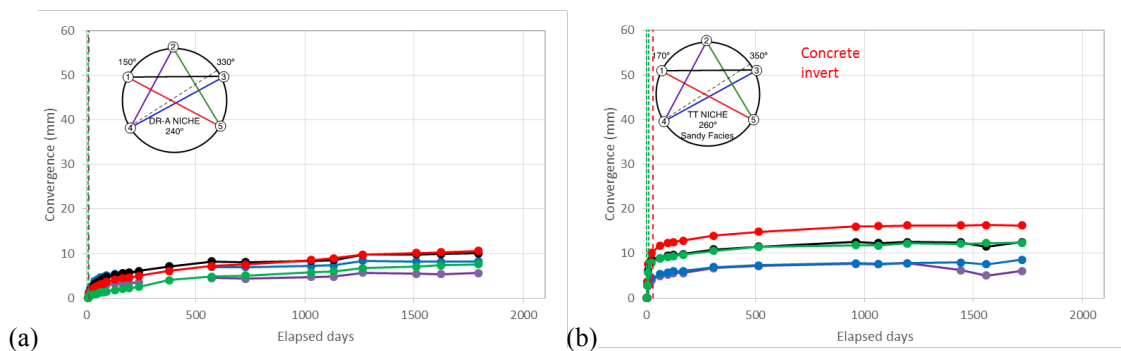


Fig. 4-42: Long-term measured convergences in Gallery 08: (a) DR-A Niche (Niche 1) and (b) TT Niche (Niche 4).

The excavation was also monitored by a magneto-extensometer in borehole BGa08-02 drilled normal to dip (+55°) at GM13 in Gallery 08 close to the GM14 convergence profile. This was in preparation for the Mine-By Experiment. The instrument was installed on 04/01/08 (42 days after excavation 23/11/07). The system failed on 25/02/08. Cumulative displacements amounted

to around 6 mm after about 50 days of monitoring. An increase in deformation (about 4 mm) was recorded immediately after the excavation of the invert on 21/01/08. A Trivec TRD was also emplaced in a vertical borehole in the middle of the new Gallery 08 which has been integrated into the geodetic system.

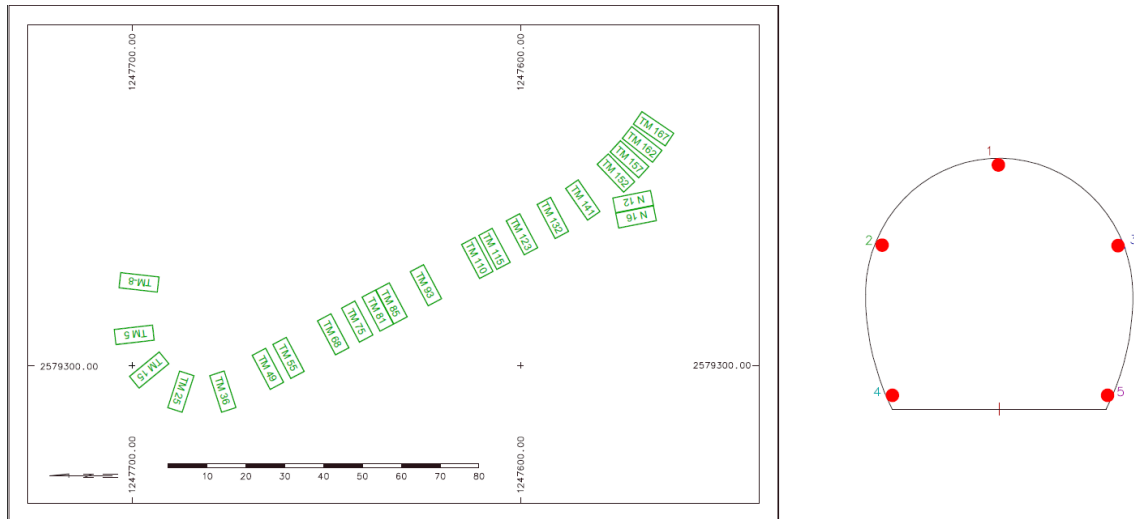


Fig. 4-43: Geodetic measurement sections and point locations.

Swisstopo also installed a new geodetic network to provide highly accurate coordinates everywhere in the laboratory. At the same time, survey points were established to monitor possible deformations in the security tunnel and the experimental area. More than 40 survey points were installed directly in the rock or the concrete of the tunnel floor in the security tunnel as well as the laboratory (Fig. 4-44). A series of geodetic measurement campaigns were performed:

- 1st campaign 0801: 16 – 18/04/08 Gallery 98 – Gallery 08 (as far as the excavation allowed);
- 2nd campaign 0802: 06 – 08/05/08 Gallery 98 – Gallery 08 (as far as the excavation allowed);
- 3rd campaign 0803: 24 – 26/06/08 Gallery 98 – Gallery 08 (as far as the excavation allowed);
- 1st pre-campaign 0804: 03 – 05/11/08 first measurement through Gallery 08;
- 2nd campaign 0901: 26/01 – 05/02/09 complete network including security tunnel, laboratory and Gallery 08.

Significant heaves of the floor of Gallery 08 around the main fault were measured in the order of 20 mm with a resolution of 0.1 mm and an absolute accuracy better than  $\pm 1$  mm (level of significance 95%). In Gallery 98, the vertical displacements were in the order of a maximum of 2.0 mm (Fig. 4-45). No significant movements in position could be detected in Gallery 08 or in Gallery 98.

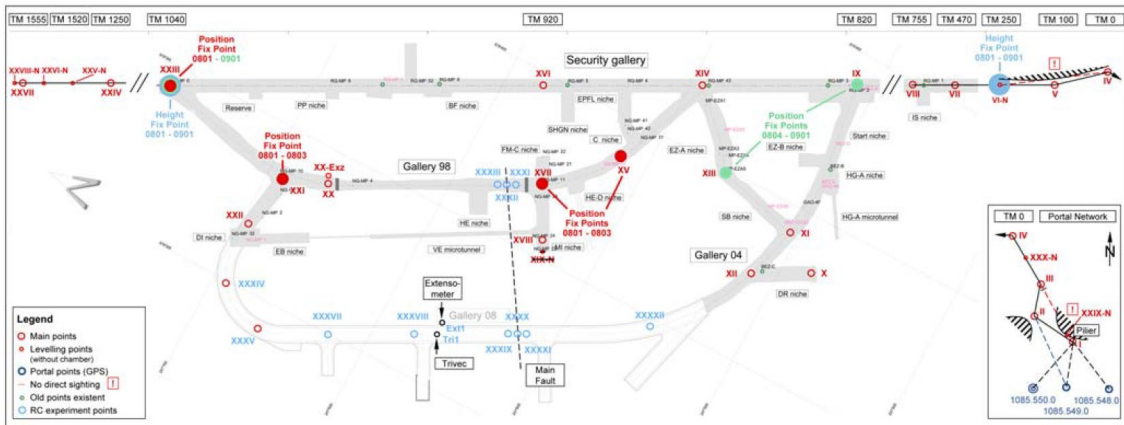


Fig. 4-44: Survey marks in different galleries of the laboratory with the selected fix-points. The fix-points along the main fault in Galleries 98 and 08 are schematically shown.

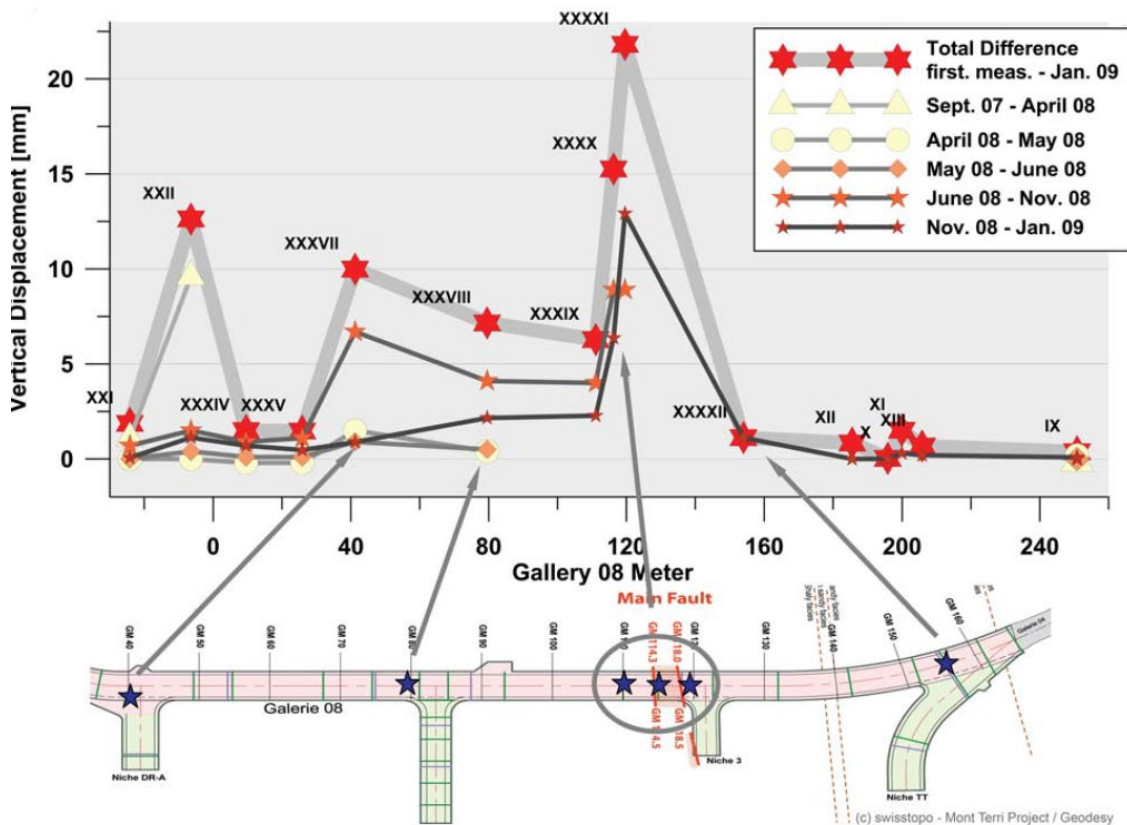


Fig. 4-45: Uplifts in Gallery 08 from September 2007 to January 2009.

## **EZ-G Experiment**

The EZ-G experiment investigated the EDZ ahead of the tunnel face in an 8 m long region at the junction of Gallery 04 and 08. The region is located at the transition between the shaly and sandy facies (the first 2 m from end of Gallery 04 is in the shaly facies and the remaining 6 m in the sandy facies). EDZ characterization methods included: coring and mapping, geo-electrical surveys (Nicollin et al. 2010), resin injection, acoustic imaging and micro-seismic monitoring (Le Gonidec et al. 2012), noble gas sampling and Spontaneous Potential measurements (Maineult et al. 2013). The experiment considered the EDZ caused by excavation of Gallery 04, approximately 4 years prior to the investigation and the EDZ ahead of the face of the advancing Gallery 08.

Analysis of cross-hole acoustics performed around the face of Gallery 04 showed consistent frequency attenuation corresponding to feature spacing  $\sim 0.1$  m and anisotropy consistent with the local bedding-plane orientation. Micro-seismic events (MSEs) as monitored during the excavation of Gallery 08 as it approached the end of Gallery 04, were clustered close to the face and within the rock-mass. The features within the rock mass may relate to the reactivation of a SE-dipping (bedding-parallel) fault (Le Gonidec et al. 2012). After excavation MSEs appeared to be concentrated on a single fault (Le Gonidec et al. 2012) about 5 m from the front of Gallery 04.

Maineult et al. (2013) reported noble gas and Spontaneous Potential (SP) surveys around the end of Gallery 04. Noble gas data suggested a connected EDZ up to 2 m from the excavation face -possibly focused on a single tectonic fault. Geo-electrical surveys (Nicollin et al. 2010) showed a pattern of high resistivity associated with the fault and that the fault acted to delimit high and low resistivity domains in the excavation face. Resin injection experiments also showed that faults acted as preferential flowpaths in the EDZ. They commented that extension fractures were rare and that pre-existing tectonic features appear to have dominated the EDZ at this location.

### **4.5.5 Summary of results**

#### **Understanding of failure mechanisms**

The spatial distribution of the EDZ fractures was heterogeneous along the gallery, influenced both by tectonic faulting and lithology. In sections with few pre-existing faults, the EDZ fracture network is well developed.

Macroscopic EDZ fractures were identified only in the shaly facies and were not identified in the sandy or carbonate-rich, sandy facies. Analysis of a limited number of resin-impregnated cores from the EZ-G experiment did not identify any microscopic EDZ fractures in the sandy facies (Maineult et al. 2013). In the shaly facies, the following types of EDZ fractures were observed:

- Extensional fractures (mode I) often associated with plumose structures. These fractures are sub-parallel to the gallery side walls and front walls;
- Shear fractures (mode II) observed in the front wall, having the same azimuth as the bedding planes (see below) but dip at higher angles.
- Reactivated bedding and fault planes.

Detailed mapping of the front walls identified non-tectonic shear fracture planes. Some were clearly associated with excavation-induced fractures. These shear planes have the same azimuth as bedding planes but dip more steeply. The bedding planes in the Gallery 08 dip from 30° increasing to 40° southwards. The EDZ shear fractures dip from 40° to 80°, with a mean value between 40° and 60°. The shear fracture planes were associated with down-dip lineations indicating normal displacement along the plane. The mapping showed that these EDZ shear fractures developed in the lower half part of the front wall, some extending to several metres. They were not observed on a level above 2.5 – 3.0 metres in the front wall. Some fractures cut across the complete face of Gallery 08. By contrast, the extent of EDZ extensional fractures identified in the front wall was limited to 10s of centimetres, rarely extending over a metre. These extensional fractures are typically parallel to the front walls and dip at over 70°.

Reactivation of pre-existing faults as normal faults was observed to develop during excavation. Nussbaum et al. (2010) reported an offset of over 2 cm developing along a pre-existing fault within 24 hrs of excavation.

Mapping of the side-walls and invert of the niches showed a typically well-developed EDZ (fracture density of  $\sim 10 \text{ m}^{-1}$  at DR-A and MB Niche) often delineated/limited by pre-existing faults. Previously Martin & Lanyon (2003a) noted the influence of main galleries on the EDZ in the niches with a clear decrease in extension fracturing after the first few metres. The pattern was less clear for Gallery 08 where the entrance to Niche 3 showed a clear influence of Gallery 08 while the DR-A and MB Niches showed heterogeneous clustered extensional fractures normal to the niche axis along the length. These fractures were typically delineated by pre-existing features.

### Diametral strain

The short-term convergence profiles showed a relatively consistent pattern influenced by tunnel orientation and lithology. Convergence appeared to be significantly smaller in the sandy facies and close to the main fault. Convergence was largest at the profile measured where the tunnel was heading along bedding strike (over 50 mm (1.1%)). This is consistent with the 3D convergence measurements where transverse deformations  $\sim 60 \text{ mm}$  (1.2%) were observed in the section between GM 5- 25. Values are tabulated in Tab. 4-21.

Tab. 4-21: Summary of convergence data from Gallery 08.

Gallery 08 GM	Heading	Geology	At 100 days			Most recent data (8,9/08/13)		
			Min.	Avg.	Max.	Min.	Avg	Max.
GM14.5	240°	Along strike	0.1%	0.7%	1.1%	0.2%	0.8%	1.2%
GM56	150°		0.3%	0.5%	0.7%	0.4%	0.6%	0.8%
GM75	150°		0.2%	0.5%	0.8%	-0.3%	0.2%	0.8%
GM117	150°	Main Fault	0.2%	0.4%	0.5%	0.4%	0.6%	0.8%
GM160	150°	Sandy facies	0.1%	0.1%	0.2%	0.2%	0.2%	0.3%

### Evidence of EDZ extent

Nussbaum et al. (2010) noted that the EDZ fractures were more strongly developed in regions where tectonic faults are sparse (see Fig. 4-46).

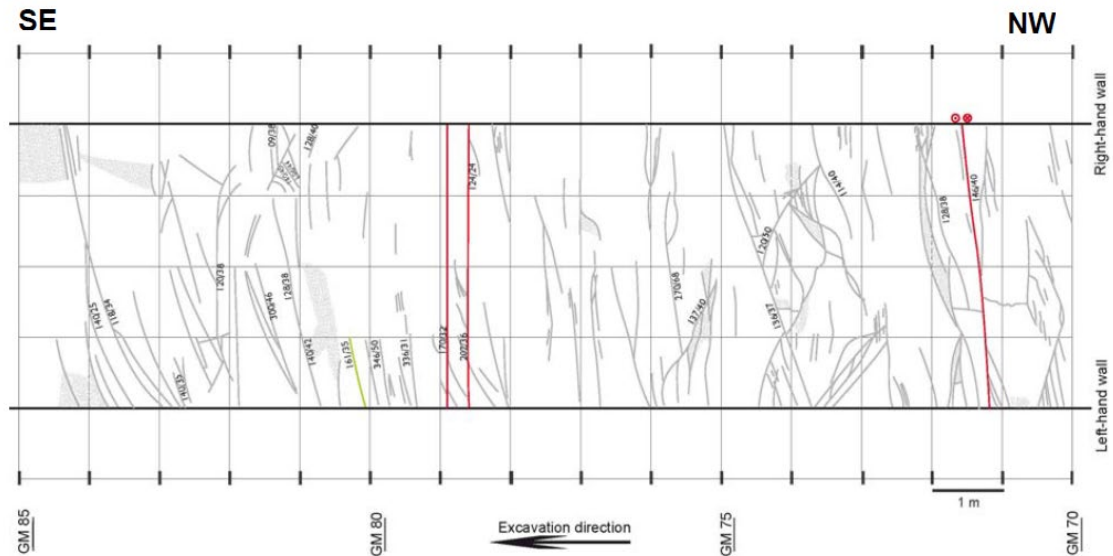


Fig. 4-46: Geological map of the invert between GM 70 and GM 85 (from Nussbaum et al. 2010). Note the very low frequency of pre-existing tectonic faults (in red) and by contrast the well-developed EDZ fracture network (in grey).

Mapping of the niches excavated in the shaly facies parallel to bedding strike to the west of Gallery 08 showed a somewhat different pattern to that normally observed. There is no clear boundary to the EDZ associated with the Gallery 08 side-wall. EDZ fractures were mapped along the length of the niches although they were typically bounded by the traces of the bedding-parallel faults (for example see Fig 4-47).

Within the sandy facies the EDZ appeared to be significantly smaller with no mapped features – convergence measurements were also significantly smaller (see next section).

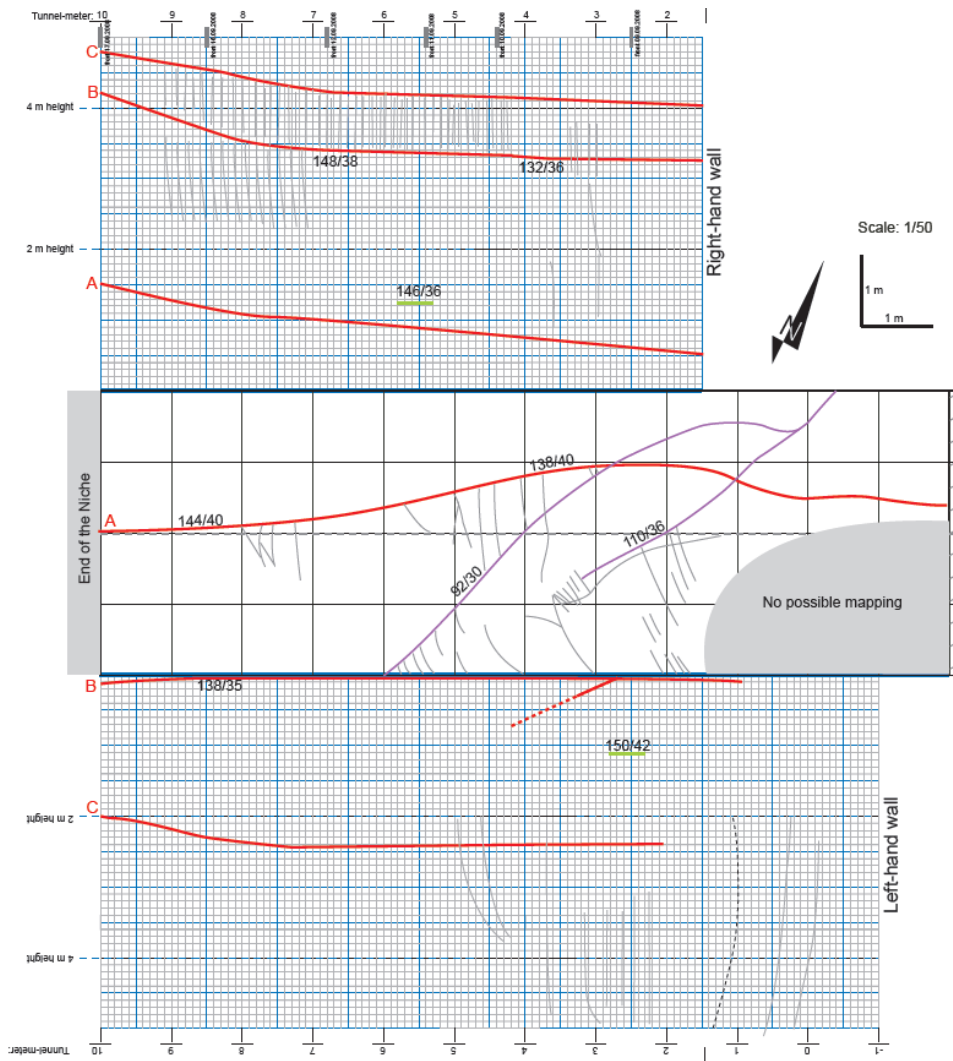


Fig. 4-47: Geological and structural map of DR-A Niche.

**Pore pressure monitoring**

No nearfield piezometer measurements were made for Gallery 08. Emphasis within the monitoring was largely on convergence.

Tab. 4-22: Summary of observations for Gallery 08 excavation.

	Summary	Comment
Geometry	Rounded horseshoe, horizontal diameter 5 m. Height 4.6 m. Start Niche 20 m long. Total length 167 m + 70 m niches.	Dimensions at rock wall horizontal 5.3 m diameter, 5 m high.
Orientation	Gallery 08 starts before heading 270° before turning to 150° parallel to Gallery 04 and Gallery 98.	
Geology	Passes through the three facies and the "Main Fault". Carbonate-rich sandy facies: GM 140.7-143.5. Sandy facies: GM 143.5- 166	
Method	Roadheader	Hydraulic drum cutter Erkat ER 600
Support	3 m anchors 15 cm of fibre-reinforced shotcrete. 30 cm concrete invert.	
EDZ extent	Some areas showed well connected fracture network to 1 m and isolated EDZ fractures to 2 m. Elsewhere difficult to identify EDZ extent in side-walls.	Tectonic features observed to limit extent. Evidence for EDZ heterogeneity due to density of tectonic faults and influence of lithology.
Diametral Strain	0-100 days: 0-1.1% 8,9/0-8/13: 0-1.2%	
Pore pressure monitoring	No near field pressure monitoring	

## 4.6 Mine-By Experiment

### 4.6.1 Location and local geological setting

The Mine-By (MB) Experiment is fully described in Martin et al. (2014a) and the results are interpreted in Martin et al. (2014b). Much of the discussion here summarizes the material presented in Martin et al. (2014b). The MB Experiment was performed to investigate the deformation and coupled hydromechanical behaviour of the Opalinus Clay around bedding-parallel excavations. The Mine-By Experiment was performed in a niche off Gallery 08, later used as access to the FE tunnel (see next section). The tunnel lies within the shaly facies of the Opalinus Clay. The Mine-By Tunnel is oriented along-bedding strike. The bedding dips with an average of 33° and with a dip direction of 150° (average of 72 measurements).

It is expected that the pre-excavation stress-state around the Mine-By Niche is reasonably well described by the stress tensor suggested by Martin & Lanyon (2003a). Although there will be some influence of Gallery 08 over the first few metres, there were no other significant excavations close by. The maximum principal stress 6.5 MPa is assumed to be roughly vertical and equivalent to an overburden of 250 – 300 m. The minimum horizontal stress is taken as 2.2 MPa and is approximately parallel to the niche. The maximum horizontal stress is 4 MPa and is oriented roughly parallel to Gallery 08.

#### 4.6.2 Excavation

The niche is 24.6 m long with a 4.5 m diameter circular cross section (Fig. 4-48). The tunnel axis is  $242^\circ$  and dips from the entrance at slightly less than 1%. The niche was excavated with a roadheader in 0.6-1.9 m/day (plan 1.3 m/day) using a vertical cut. The tunnel was excavated with only limited support to maximise the ability to monitor rock mass behaviour. Six anchors were installed 0.8 m behind the face with 100 m wire mesh and two layers of shotcrete. The first layer of 50 mm was placed immediately after excavation and a second 100 mm layer was placed at completion of the MB. Anchors were typically 22 mm steel installed in 30 mm diameter pilot holes with an epoxy resin. The first two sets of anchors were 3 m in length after which 2 m anchors were used. Volume calculations indicate that 1.3 m of each anchor would be fully bonded to the rock. Anchors were installed in the crown and floor and normal and oblique to bedding. The exact angle varied over the length (see Martin et al. 2014a).

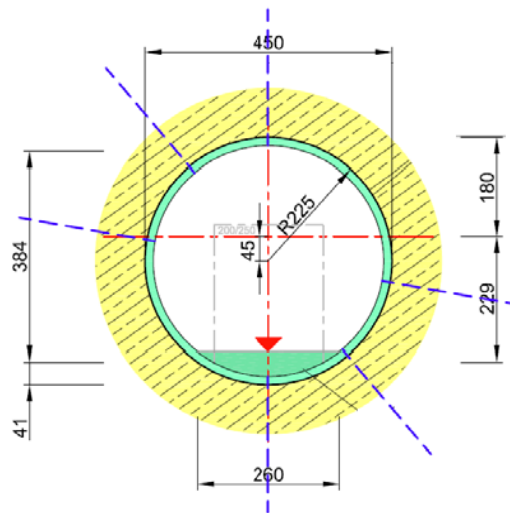


Fig. 4-48: Geometry of Mine-By Niche and associated support (anchors and shotcrete).

After shotcreting of the final excavation face the invert was cleaned, shotcreted and then concreted. The Mine-By Niche excavation commenced on 13/10/08 and ended on 07/11/08. The sequence is illustrated in Fig. 4-49.

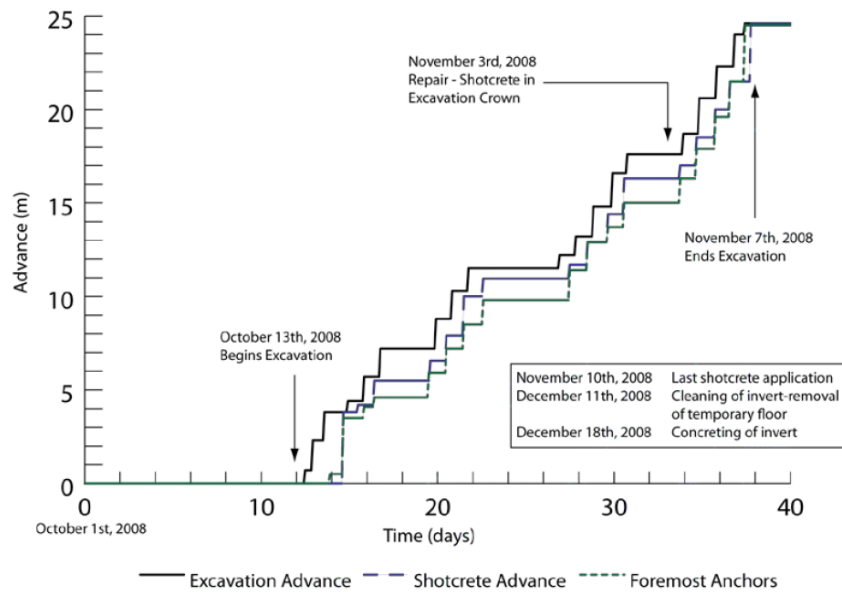


Fig. 4-49: Excavation sequence and support installation.

Excavation was monitored with an array of instruments installed in boreholes and within the niche listed in Tab. 4-23.

Tab. 4-23: Monitoring instruments for the Mine-By Experiment.

Measurement	Description	Borehole	
Convergence	Five Q2-Q6 m, total displacement arrays (P1-P5)		
Pore pressure	Five piezometer intervals installed using multi-packer systems in two boreholes.	BMB-15, BMB-16	
Deformation	Radial extensometers	Normal to bedding	BMB-30 (8 m)
		Parallel to bedding	BMB-28 (8 m)
		Crossing bedding	BMB-29(8 m), BMB-31(5 m)
	Face extensometer (centre-line)		BMB-13
	Magnetic extensometers		BMB-17, BMB-18
	Chain inclinometers		BMB-19, BMB-20

### 4.6.3 Excavation response

Convergence (total displacement) was measured at five locations in the MB Niche using five-pin arrays. Non-radial displacement was found to be minor. Convergences were highly variable ranging at the end of excavation from 3-102 mm (see Tab. 4-24). Many of the highest measurements were recorded at P5; the pin in the floor monitoring displacement approximately normal to bedding. The time-dependent component was typically greater than the instantaneous displacement (Martin et al. 2014b). The discussion here is based on the analysis of Martin et al. (2014b). Data from the two convergence profiles at NM 4.5 and NM 12.1 were not used in the

analysis but are largely comparable to the data from the relevant Q array. Deformations are typically largest for the 5-1 chord – equivalent to the P2+P5 radial displacements.

Tab. 4-24: Measured convergence (mm) in Mine-By Niche (taken from Martin et al. 2014b).

Array	TM	P1	P2	P3	P4	P5
Q2	4.8	23.24	16.52	25.91	2.93	35.54
Q3	10.2	16.63	2.74	16.47	7.57	40.29
Q4	12.1	23.62	17.19	12.28	15.35	37.01
Q5	17.8	13.3	10.31	9.66	7.56	102.18
Q6	22.9	0.21	2.91	2.64	0.74	1.78
End of monitoring						
Q2	4.8	37.3	21.13	27.84	6.68	55.25
Q3	10.2	37.87	2.74	21.21	11.39	67.23
Q4	12.1	32.49	24	16.53	33.21	58.3
Q5	17.8	18.94	14.05	9.66	10.11	105.74
Q6	22.9	7.88	12.47	20.94	9.53	14.94

Radial extensometers were installed at TM10 in the Mine-By Niche in four boreholes (BMB-28 to BMB-31). Measurements from BMB-29 (crossing bedding) and BMB-30 (normal) showed a characteristic response with increasing displacement near the tunnel wall. Measurements from BMB-28 (parallel) and BMB-31 (crossing) indicated either block movement, localized slip or malfunction. Anchors were placed at 8 (except BMB-31), 5, 2 and 1 m from the borehole mouth.

Time-dependent deformation dominated the measured response extending to the full depth of the sensors (5-8 m). The magnitude of total deformation was similar (11-14 mm) for all four boreholes and was typically smaller and more uniform than the convergence measurements. In particular, the measured P5 convergence at end of excavation in Q3 (nearest to TM10) was 40.3 mm and 67.2 mm at the end of monitoring.

Martin et al. (2014b) suggest that the majority of movement is excavation-induced and that the rock mass continues to yield/creep after excavation has stopped. It is not possible to estimate the depth of the yield surface because the extensometers do not extend sufficiently far from the tunnel.

Analysis of the data from an extensometer installed in BMB-13 suggested that the deformations ahead of the face were relatively small at 0.5-1 diameter ahead of the face (0.1-0.76 mm). At 0.5-1 m ahead of the face deformations ranged from 2.5-5 mm with a significant time-dependent component (only seen until the next excavation step).

Two magnetic extensometers were installed in boreholes (BMB-17, BMB-18) drilled roughly parallel to the MB Niche. The measuring points were between 3 and 6 m from the tunnel wall. The measured response followed the expected elastic response during the early stages of excavation when the sensors were at larger distances from the excavation face.

In BMB-17 there was a clear deviation from the elastic response from the point when the face had advanced to TM11.5 with an inflexion point in the deformations at about TM12.5 m. This face position corresponds to a sensor point at 5 m radial distance from the tunnel axis.

In BMB-18 there was a clear deviation from the elastic response from TM10.3 with an inflexion point in the deformations between 11 and 12 m. This face position corresponds to a point at 5.1 m radial distance from the tunnel axis. The effect of assuming a fixed reference anchor is visible in the later data for both boreholes.

Two chain inclinometers were installed in boreholes (BMB-19, BMB-20) drilled obliquely across the tunnel direction. Interpretation of the data was complicated by the borehole trajectories but a consistent pattern of deformation was observed: Time dependent deformations became greater than the instantaneous deformation after the face advanced past the sensor. The boundary between elastic/inelastic response was about 2-3 m ahead of the face.

The deformations in BMB-20 (below the tunnel) were smaller and more erratic than those in BMB-19 (above the tunnel) suggesting some gravitational influence. All sensors were within 6 m radial distance of the tunnel axis so no clear radial extent of the yielding zone can be determined.

Two boreholes (BMB-15, BMB-16) were equipped with multipacker systems to monitor pore pressure response to excavation, with five measuring intervals in each borehole, all within 5 m radial distance of the tunnel axis. The piezometers showed a typical increase in pressure as the face advanced followed by a drop in pressure to close to atmospheric, indicating significant drainage of the intervals as EDZ-related fracturing or microfracturing created sufficient permeability for water movement.

The open screen intervals were 200 mm in length giving a high spatial resolution. Piezometer pressure started to rise in the nearest interval about 10 m ahead of the face and to drop 2-3 m ahead of the face. Pressure in the intervals farthest from the tunnel (5 m radial distance) dropped more gradually (in BMB-15 after the face had passed) indicating an initial lack of direct fracture connection to the face.

### **Post excavation radial boreholes**

Radial boreholes drilled from the Mine-By Niche (Jaeggi et al. 2012a, b, c) investigated the presence of open fractures to a maximum depth of 2.5 m (although one borehole, BMB-42, was 5 m long, only the first 2.5 m of rock was targeted for resin injection). The investigations identified an interconnected EDZ fracture system to 1.1 m depth with the deepest impregnated feature at 2 m into the rock. Several orientations of fractures were identified:

- A set of tunnel surface-parallel (onion-skin) fractures;
- A set sub-parallel to bedding dipping 30-50°. This set extends to at least 2 m into the rock;
- A sub-vertical set striking parallel to the tunnel typically found close to the tunnel wall.

Tectonic fractures were found to have been reactivated and impregnated in some locations, but also acted as boundaries to EDZ fracturing. In BMB-37 the first 0.25 m of core was lost and in BMB-41 low core quality between 0.4-1 m suggests the presence of a dense EDZ network.

All identified impregnated features were found within the first 1.2 m. This suggests that although it is not possible to identify an outer limit to open EDZ fracturing/reactivation, open feature frequency is likely to be low beyond 1.5 m radial distance.

Three hydrotest campaigns were performed in boreholes BMB-15 and BMB-16 which were equipped with multi-packer systems (Tab 4-25, 4-26). The campaigns were performed in:

- 14/07/08-24/07/08: Prior to excavation of the niche;
- 17/02/09-24/02/09: After excavation;
- 24/08/10-29/09/10: Approximately 1.5 years after the excavation.

All intervals showed a significant increase in transmissivity immediately after excavation of the niche (Tab. 4-25). The magnitude of increase in some intervals and near-atmospheric pressure suggests direct connection to the EDZ fracture network (Tab. 4-26). There is significant variation in transmissivity along the boreholes with the location of highest transmissivity intervals typically located at about 4 m from the tunnel axis (1.5 m into the rock). In the third campaign most intervals show a reduction of 1-2 orders of magnitude in transmissivity suggesting self-sealing over time (Fig. 4-50).

Tab. 4-25: Best estimate of near field effective hydraulic conductivity (m/s) from hydrotesting campaigns in BMB-15 and BMB-16 (Achtziger et al. 2011).

	<b>BMB-15i1</b>	<b>BMB-15i2</b>	<b>BMB-15i3</b>	<b>BMB-15i4</b>	<b>BMB-15i5</b>
Radial distance midpoint(m)	3.91	4.03	4.34	4.64	5.00
Campaign 1	$1.8 \times 10^{-13}$	$6.5 \times 10^{-13}$	$2.6 \times 10^{-13}$	$5.6 \times 10^{-13}$	$6.4 \times 10^{-13}$
Campaign 2	$11000 \times 10^{-13}$	$77 \times 10^{-13}$	$150 \times 10^{-13}$	$120 \times 10^{-13}$	$63 \times 10^{-13}$
Campaign 3	$560 \times 10^{-13}$	$7.2 \times 10^{-13}$	$110 \times 10^{-13}$	$1.2 \times 10^{-13}$	$4.1 \times 10^{-13}$
	<b>BMB-16i1</b>	<b>BMB-16i2</b>	<b>BMB-16i3</b>	<b>BMB-16i4</b>	<b>BMB-16i5</b>
Radial distance midpoint(m)	3.08	3.40	3.83	4.34	4.90
Campaign 1	$6.2 \times 10^{-13}$	$1.4 \times 10^{-13}$	$1.4 \times 10^{-13}$	$2.1 \times 10^{-13}$	$4.7 \times 10^{-13}$
Campaign 2	$50 \times 10^{-13}$	$160 \times 10^{-13}$	$6300 \times 10^{-13}$	$6600 \times 10^{-13}$	$20 \times 10^{-13}$
Campaign 3	$1.5 \times 10^{-13}$	$5.2 \times 10^{-13}$	$2300 \times 10^{-13}$	$200 \times 10^{-13}$	$0.9 \times 10^{-13}$

Tab. 4-26: Initial interval pressure (kPa) from hydrotesting campaigns in BMB-15 and BMB-16.

	<b>BMB-15i1</b>	<b>BMB-15i2</b>	<b>BMB-15i3</b>	<b>BMB-15i4</b>	<b>BMB-15i5</b>
Campaign 1	2061	2099	2191	2219	2247
Campaign 2	99		86	135	185
Campaign 3	84.2	99.5	71.6	145.6	172.8
	<b>BMB-16i1</b>	<b>BMB-16i2</b>	<b>BMB-16i3</b>	<b>BMB-16i4</b>	<b>BMB-16i5</b>
Campaign 1	2064	2003	1972	2051	2081
Campaign 2	137		105	105	101
Campaign 3	177.5	81.1	166.9	105.5	107.4

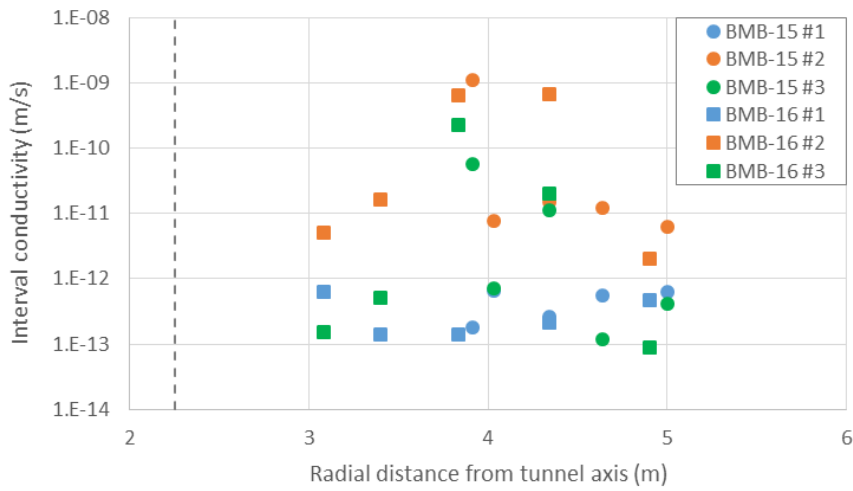


Fig. 4-50: Best estimate interval conductivity (m/s) versus radial distance from tunnel axis for the three hydrotesting campaigns in BMB-15 and BMB-16.

#### 4.6.4 Long-term response

Fig. 4-51 shows the measured convergences for the two arrays in the Mine-By Niche. After ~ 100 days, convergences had typically stabilized. The largest measured convergence was ~ 70 mm (diametral strain of 1.6%) on the 5-1 chord, prior to concreting of the invert. This is consistent with the observations of the Q arrays discussed in Martin et al. (2014b) where deformation is dominantly focussed on the P5 pin (see Tab.4-24). There was a small response to concreting of the invert (~ 740 days) and maximum convergence was 83 mm (less than 2% diametral strain). Prior to concreting the invert convergence on all chords showed a roughly linear increase with log time.

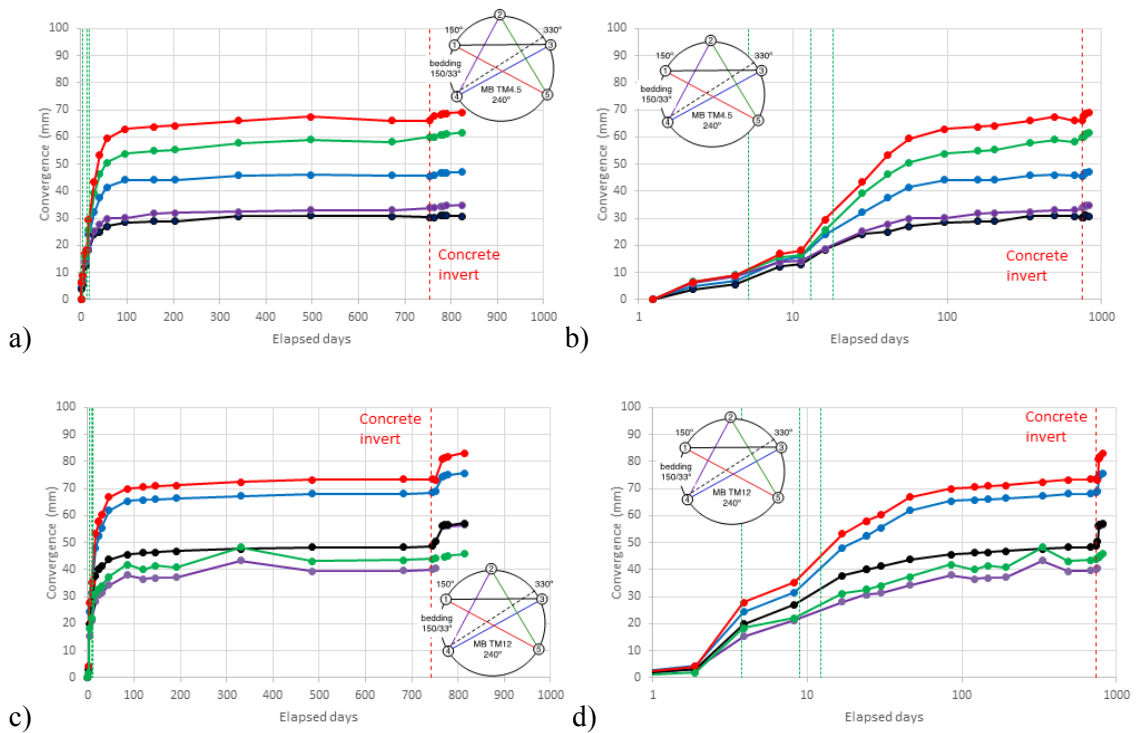


Fig. 4-51: Long-term measured convergences in Mine-By Niche.

### 4.6.5 Summary of results

#### EDZ extent

The resin injection measurements showed an interconnected network of open (impregnated) fractures to a radial depth of about 1.2 m of rock (1.5a from the tunnel axis). It is possible that further open fractures extend beyond this as the maximum depth of investigation into the rock was 2.5 m. This was the only open fracture network detected in the 6.18 m of core taken beyond 1.25 m, however, suggesting that the density of such features is likely to be low ( $\sim 0.75 \text{ m}^{-1}$  or less). Locations of different sensors around the tunnel are shown in Fig. 4-52.

Inelastic yielding was indicated by deformation measurements (clinometer and extensometers) up to 6 m from the tunnel axis (2.7a) while the radial extensometers suggested that such yielding may extend to 8 m (3.5a). It is however not possible to determine the boundary of such a zone because the sensors did not extend sufficiently far to delineate the region of elastic deformation. The majority of the deformation was observed closer to the tunnel wall in regions where fractures were observed in resin injection boreholes.

Piezometer data suggested fracturing and connection to the EDZ to about 5 m from the tunnel axis with the highest transmissivity at about 4 m radial distance.

Fractures identified in the resin injection boreholes are: dominantly N-S striking sub-vertical fractures; bedding-parallel reactivated faults or fractures; or sub-vertical fractures parallel to the tunnel axis.

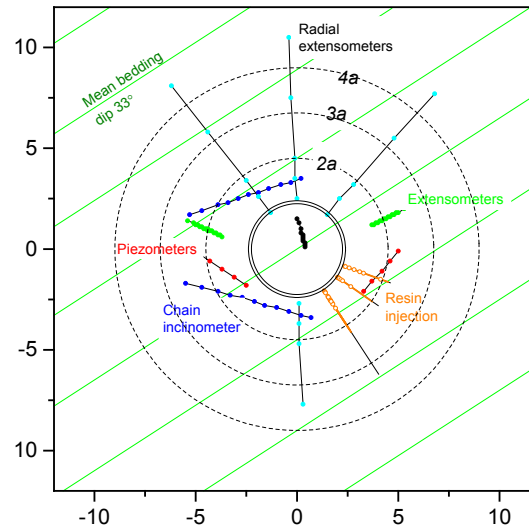


Fig. 4-52: Location of sensors and resin injection boreholes around Mine-By Niche.

A set of tunnel-normal fractures were identified in the side-walls of Gallery 08 (Madritsch & Vietor 2010) similar fractures were observed parallel to the face of the Mine-By Niche. The extent of such fractures is uncertain and radial boreholes would be biased against intersecting such fractures.

### Pore pressure response

Martin et al. (2012b) calculated the elastic stress at the piezometer interval mid-points for a series of positions during face advance. The pressure in the interval was estimated from the change in mean stress in the rock at the midpoint (Skempton's coefficient  $B = 1$ ). As the face approached the interval the predicted pore-pressure followed the measured trend until a sharp pressure drop assumed to relate to fracturing/yielding of the rock. The calculated peak elastic stress at the point of pressure was then used as an estimate of the peak in situ yield. These in situ strength estimates were close to the laboratory undrained strength for samples inclined to bedding (Lux et al. 2007) as shown in Fig. 4-53. This suggests that the excavation response was an undrained response. This is consistent with the expected low permeability ( $\sim 10^{-21} \text{ m}^2$ ) of the intact Opalinus Clay.

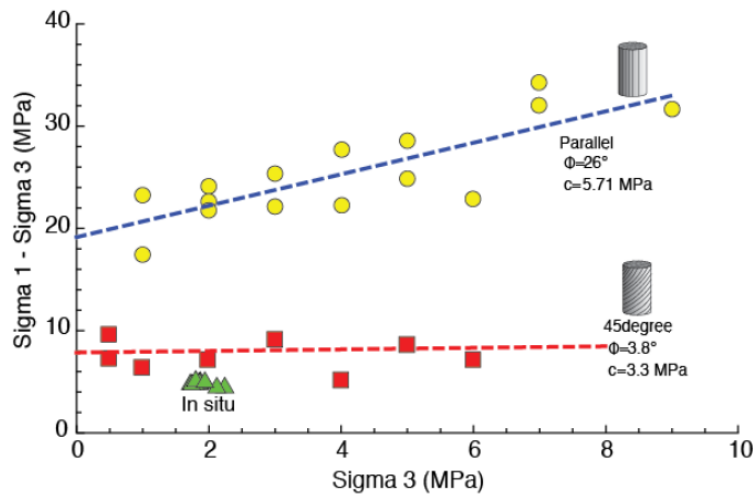


Fig. 4-53: The peak yield stress state (in situ) at the location of piezometers when the piezometers showed the rapid pore-pressure drop.

The laboratory peak strength envelopes for samples with bedding parallel and inclined (45 degree) to the direction of loading are also shown.

**Diametral strains**

Measured convergences at the end of excavation were typically in the range 0.1-1.2% (excluding the arrays near the end of the niche). Long-term monitoring (to 08/01/09) convergences ranged from 0.1-3% for all but one pin which showed a displacement of 4.7% in the floor of the niche at TM17.8.

Martin et al. (2014b) considered the convergence anisotropy based on the total convergence between the 10 different pairs from each of the five sets of five pins. At the end of excavation 45 showed convergence and 4 showed divergence. Diametral strain varied from 0.2 to 3% with a higher average conductance normal to bedding suggesting significantly greater displacement normal to bedding (despite the expected stress anisotropy). The time-dependent convergence showed a similar anisotropy to that at the end of excavation.

Tab. 4-27: Summary of observations for MB Niche excavation.

	Summary	Comment
Cross-section	Circular cross-section diameter 4.5 m	
Orientation	244°	Slightly oblique to bedding strike at 240°
Geology	Shaly facies running sub-parallel to fault structure	
Method	Roadheader vertical cut	
Support	6 anchors 2/3 m located at 0.8 m behind face. 15 cm shotcrete and 10 mm wire mesh	
EDZ	Fracturing and significant permeability increase out to 5 m (2.2a) from the tunnel axis. Possible yielding and deformation to beyond 8 m (3.5a)	Resin injection, hydrotesting and piezometers showing atmospheric pressure behind face. Extensometer at 8 m from tunnel wall showed smaller deformation than measured convergence
Diametral Strain	100 days: 0.6-1.4% 19/01/11: 0.9-1.7%	Profiles at TM4.5 and TM12 Higher radial strains seen on individual pins in floor (Martin 2014b)
Constraint on undrained strength	Estimated undrained shear strength from MB and FE piezometers 2.5 MPa	From analysis of piezometer response

#### 4.7 FE Gallery

The Full-scale Emplacement (FE) Experiment is a full-scale heater experiment based on the current Swiss HLW disposal concept (Fig. 4-54). The experiment is long-term in that it does not include artificial saturation and will instead use natural saturation from the rock. The main aim is to investigate repository induced coupled THM effects in the host rock.

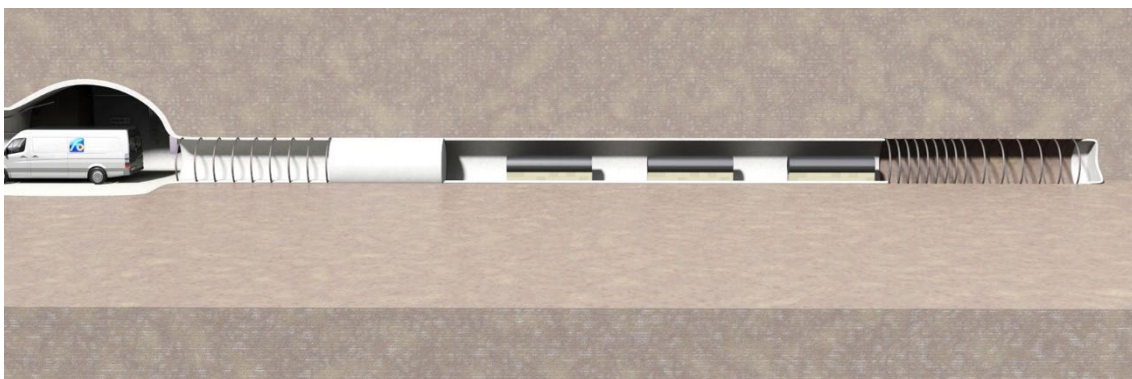


Fig. 4-54: Visualization of FE Experiment.

#### 4.7.1 Location and local geological setting

The experiment is located in an extension of the Mine-By Niche and is excavated towards 244° roughly parallel to bedding strike about 240°. The FE Start Niche (Niche FE-A) was excavated in 2011 (Jaeggi, Müller et al. 2012) and the FE tunnel was excavated between 26/04/12 and 10/07/12.

The tunnel lies within the shaly facies of the Opalinus Clay and passes through a bedding-parallel fault zone. Bedding dip was approximately 35° – 40°, slightly more than that observed in the Mine-By Niche. The bedding was tectonically affected showing visible sheared fractures (split / open bedding) with a normal separation of about 0.4 m. These features were forming slip surfaces and slicken-sides. Secondary fracture sets were also observed but with low frequency (Jaeggi, Lisjak et al. 2012).

A well-developed fault zone is present from GM14.5 to the end of the gallery. The fault shows three zones along the gallery (Jaeggi, Lisjak et al. 2012):

- GM12-GM14.5: The fault zone is located entirely below the invert at shallow depth. During the renovation of the tunnel invert geological mapping identified destabilized rock at 5 o'clock due to the shallow fault zone.
- GM14.5-GM32.5: The fault zone is visible at the invert. The slight oblique orientation with respect to the tunnel axis results in an upward trend to the fault trace. The orientation of the zone is ~ 130° with dip between 40 – 50°, somewhat steeper than the bedding.
- GM32.5-GM50: At GM32.5 the lower boundary of the zone rises out of the invert and wanders upwards. At around GM35 the orientation becomes parallel to the tunnel axis (~ 150°) until the end of the gallery (see Fig. 4-55).

It is expected that the pre-excavation stress-state around the FE tunnel is very similar to that around the Mine-By Niche and is reasonably well described by the stress tensor suggested by Martin & Lanyon (2003a). The maximum principal stress 6.5 MPa is assumed to be roughly vertical and equivalent to an overburden of 250-300 m. The minimum horizontal stress is taken as 2.2 MPa and is approximately parallel to the tunnel. The maximum horizontal stress is 4 MPa and is oriented roughly parallel to Gallery 08. The presence of the fault may indicate some local deviation from this stress field.

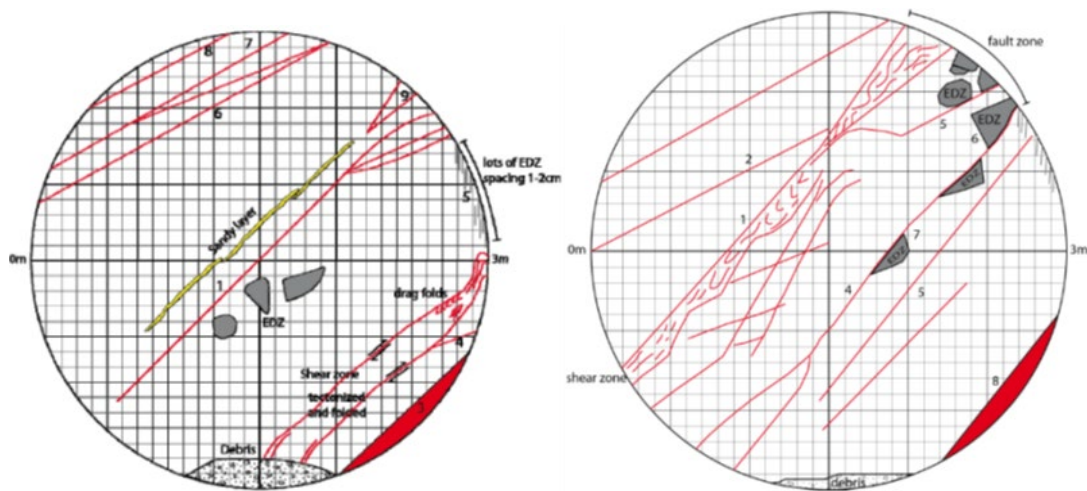


Fig. 4-55: Face mapping from FE Gallery at GM26.5 (left) and at GM43.5 (right).

Red features are pre-existing bedding-parallel tectonic structures – potentially reactivated by excavation.

#### 4.7.2 Excavation

During the excavation of the FE-A Niche cracks in the shotcrete liner of the Mine-By Niche were observed. Fresh shotcrete and additional rock bolts were installed and further displacements minimized.



Fig. 4-56: Initial excavation of FE Gallery from FE-A Niche.

The gallery was designed with a 3 m diameter circular cross-section and 50 m length. It was excavated with pneumatic hammer and roadheader. Initially, a pneumatic hammer was used to break out of the FE-A Niche (Fig. 4-56). Subsequently, a roadheader was used to adjust the profile. The accuracy of the circular profile was low and the invert was excavated as flat section rather than the original circular section. Support was varied along the gallery as listed in Tab. 4-28, with "shotcrete only" and "arches only" sections.

Tab. 4-28: Support used in excavation of FE Gallery.

Section	Support	Section	Anchors
GM0-9	Shotcrete thickness 19 cm & Steel arches (1 m spacing)		
GM9-18	Shotcrete thickness 24 cm	GM12.30-18.3	2.5 m GRP rock bolts, axial spacing 1.5 m
GM18-38	Shotcrete thickness 16 cm	GM19.8-37.8	7.5 m steel rock bolts, axial spacing 1.5 m
GM38-50	No shotcrete only steel arches and mesh		

Problems with cracks and large displacements in the shotcrete section led to the application of an additional 8 cm shotcrete layer from GM9-GM18 together with steel rock bolts. The shotcrete showed some local deformations and ovality and the floor was subsequently replaced between GM9-GM38. No significant problems were encountered in the sealing (steel arch only section). Breakout disturbance was observed located at about 2-3 o'clock and persisting along the gallery. The overall excavation speed was about 1 m/day where steel arches were installed and about 1.5 m/day in regions without arches.

The far-field monitoring instrumentation (Fig. 4-57) included:

- Six boreholes with multi-packer piezometer systems each with six intervals;
- Two boreholes with single packer pressure and temperature monitoring systems;
- Two boreholes with 40-segment two-axis inclinometer chains;
- 360 m fibre-optic cable for temperature measurement (Raman effect).

Within the tunnel, instrumentation included:

- Load cells within the shotcrete;
- Continuous deformation monitoring using 60 reflectors in twelve 5-point sections;
- Boreholes drilled from the tunnel were used for 4-point extensometers and mini-multi packer systems.

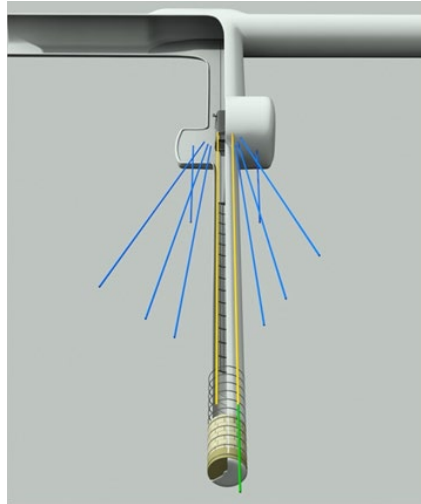


Fig. 4-57: Visualization of FE far-field monitoring borehole array.

#### 4.7.3 Excavation response

Pore pressures were monitored in six boreholes BFEA0002-7 drilled from the FE Niche. Each borehole was equipped with a multipacker system with six monitoring intervals. The geometry of the boreholes (see Fig. 4-57) is such that the i6 intervals are closest to the FE Gallery wall and the i1 interval furthest from the gallery wall. The intervals are arranged roughly on planes along the gallery such that all intervals with the same number are within 1 m of the same distance along the gallery. The arrangement of the intervals is shown in Fig. 4-58. It can be seen that all the BFEA002 and BFEA005 intervals are within two diameters of the tunnel axis, while BFEA004 and BFEA007 are beyond three diameters.

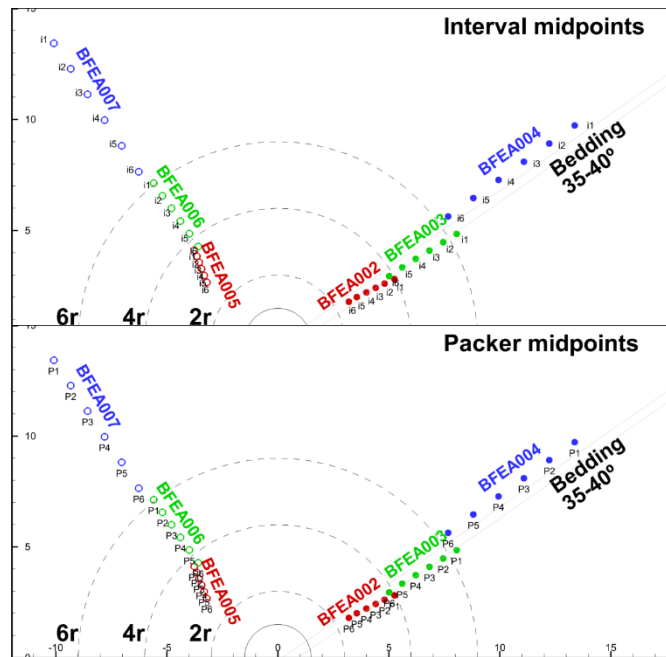


Fig. 4-58: Location in plane normal to excavation of piezometer interval and packer midpoints around FE Gallery.

Fig. 4-59 shows the pore pressure response in the six boreholes. The influence of the open FE Niche can be seen in the data from intervals 4-6 with a range of pre-excitation pressure. Almost all intervals show a pressure rise as the face approaches followed by a subsequent pressure fall and recovery.

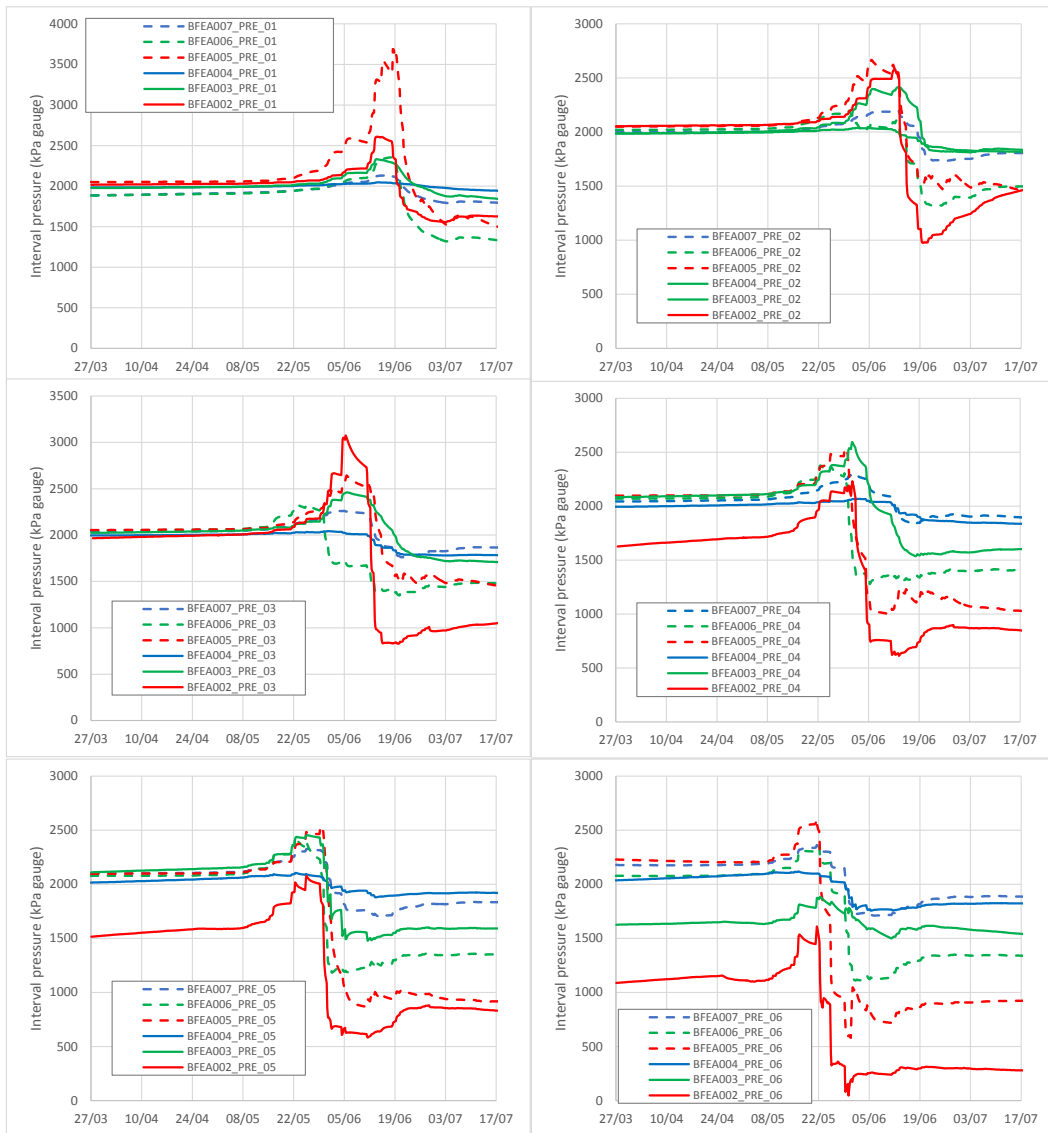


Fig. 4-59: Pore pressure response to FE Gallery excavation in monitoring borehole array.

The delta pressure calculated as the difference from the pre-excavation pressure is plotted against distance ahead of the face in Fig. 4-60. The magnitude of pressure change roughly follows the radial distance from the excavation as would be expected. Pressure typically starts to rise 10-20 m ahead of the face and peaks about 2 m ahead of the face.

Such pore pressure responses can be expected in low-permeability rock where volumetric strain changes induced by excavation result in pore pressure change which is essentially undrained due to the very low hydraulic diffusivity of the intact rock. In addition to this poro-elastic response to excavation, any yield or micro-fracturing may result in dilation (and consequent pore pressure change) or in the case of macro-scale fracturing, possible connection and drainage to the excavation. In order to discriminate such responses it is necessary to compare with the expected elastic response. The spatial distribution of peak pressure change and its location relative to the face are shown in Fig. 4-61.

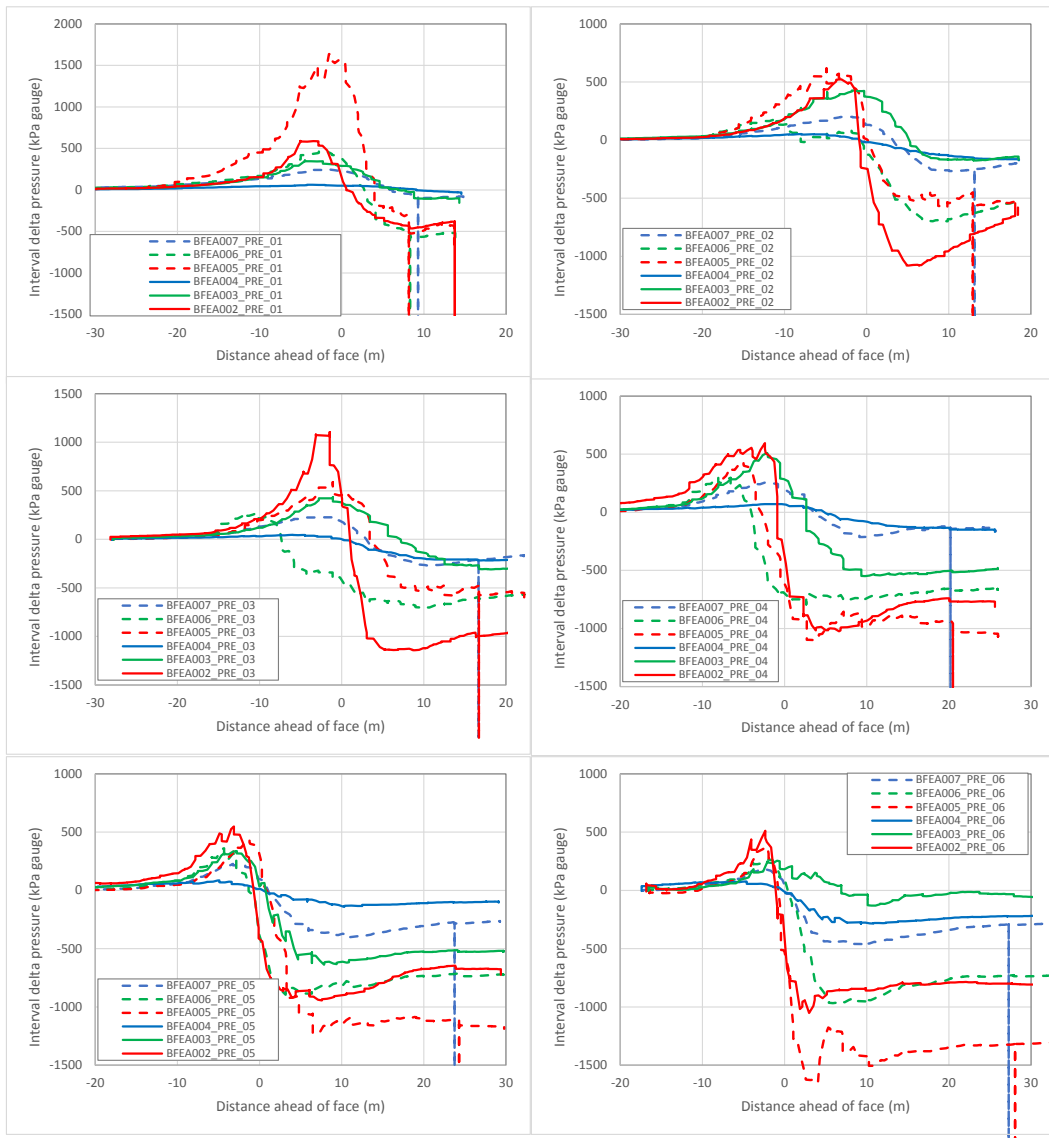


Fig. 4-60: Delta pore pressure as a function of distance ahead of the FE Gallery excavation face.

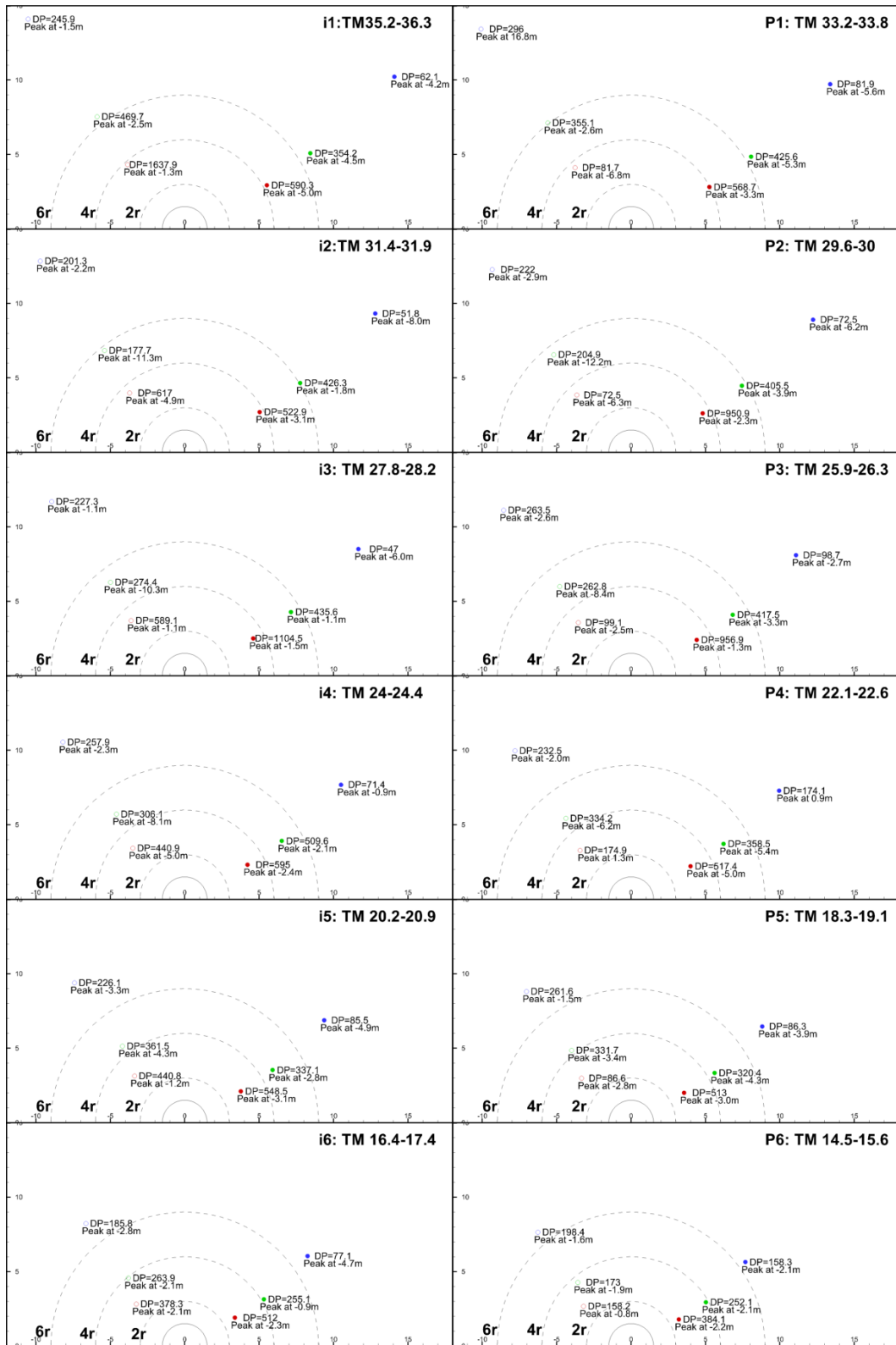


Fig. 4-61: FE Gallery far-field piezometer and packer response. Peak change in pressure (DP) and location relative to the face when it occurred.

The FE Gallery was equipped with both convergence arrays and extensometers installed in radial boreholes (arrangement shown in Fig.4-62). There were nine total convergence sections (see Tab. 4-29) and two radial extensometer sections (Tab. 4-32). Each convergence section contained either five or seven targets located at standardized positions around the tunnel profiles. The radial extensometers included four measurement anchors at 1, 2, 3 and 6 m from the tunnel wall (Eiholzer 2012).

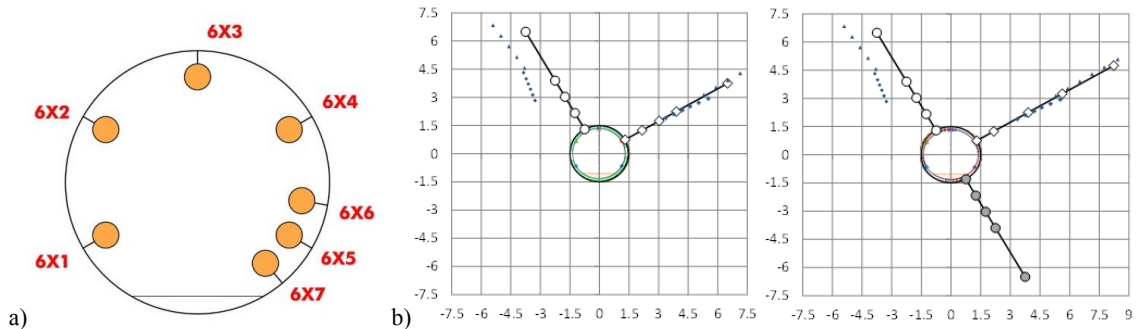


Fig. 4-62: Geometry of FE Gallery convergence sections and extensometer sections.

Tab. 4-29: Convergence sections in FE Gallery.

Section	GM	Support	Pins	Install
C0	5.1	19 cm shotcrete + steel arches	601-605	09/05/2012 05:00
C1	10.6	24 cm shotcrete	611-615	15/05/2012 19:00
C2	14.3	24 cm shotcrete	621-625	22/05/2012 04:30
C3	21.8	16 cm shotcrete	631-635	31/05/2012 15:40
C4	27.6	16 cm shotcrete	641-645	11/06/2012 22:00
C5	34.3	16 cm shotcrete	651-657	18/06/2012 22:10
C6	43.6	Steel arches+mesh	661-667	29/06/2012 20:00
C7	44.2	Steel arches+mesh	671-677	28/06/2012 22:10
C8	48.5	Steel arches+mesh	681-687	09/07/2012 22:10
C9	49.3	Steel arches+mesh	691-697	09/07/2012 22:10

The measured radial convergence for each pin against distance behind the face is shown in Fig. 4-63. The largest convergence was measured at P5 in the "shotcrete only" section (C1-C5). It is also noticeable that convergences continued to develop after the face was beyond 15 m from the pin (5 diameters). The P5 pin is located near the invert at the base of the north-east wall in a region where disturbed tectonic fault planes were observed. These fault planes are associated with a fault zone present from 14.5 m onwards in the gallery. Convergences in the "arches only" section (C6-C9) were heterogeneous with displacements being focused between the arches (e.g. C7). The convergences one month after the end of excavation (08/08/12) are presented in Tab. 4-30 and as normalised strains in Tab. 4-31. The high strains at P5 in the "shotcrete only" section range from 2.4 to 4%. Tunnel face maps along the FE Gallery are shown in Fig. 4-64.

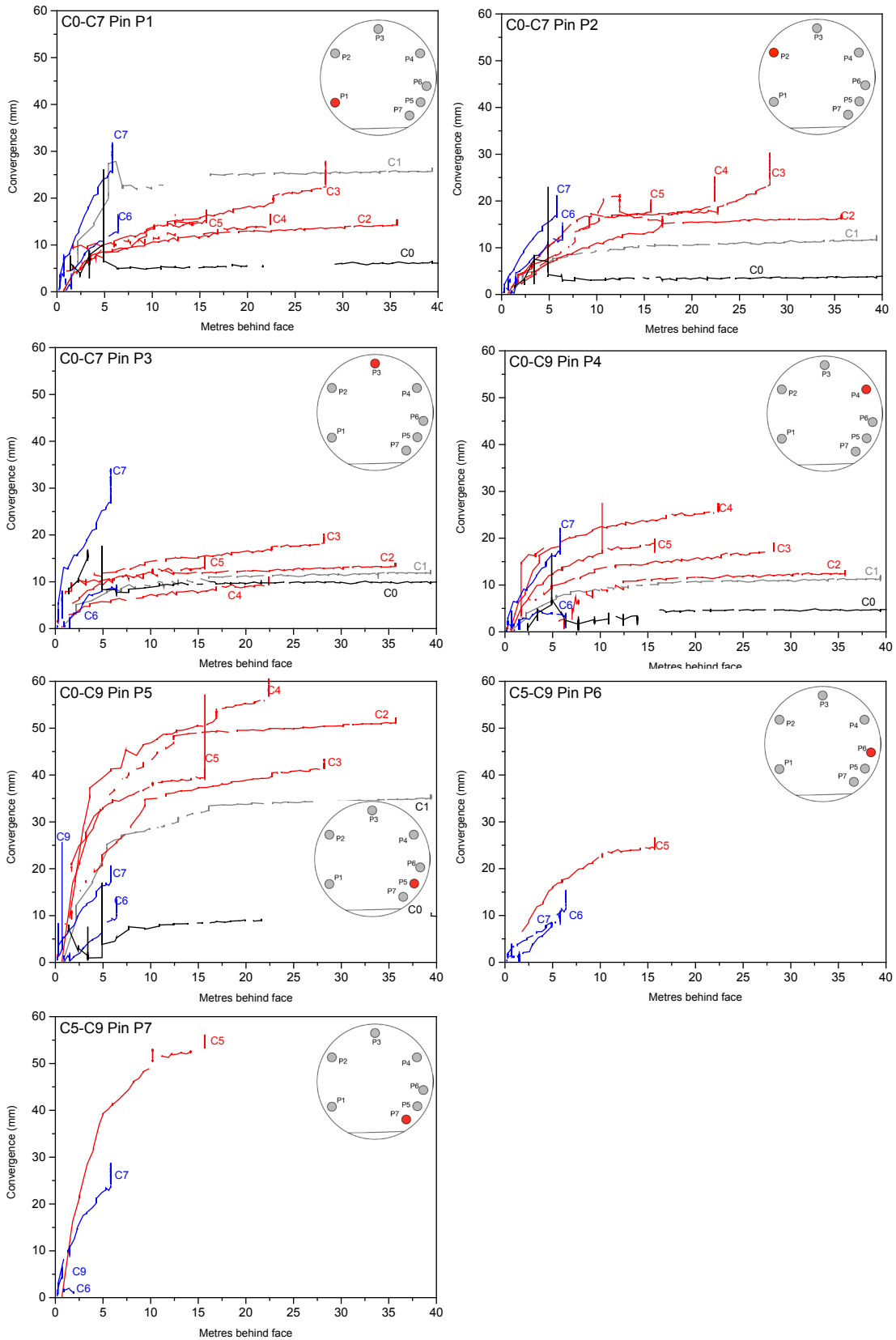


Fig. 4-63: FE Gallery Convergence measurements versus distance behind excavation face for P1-P7.

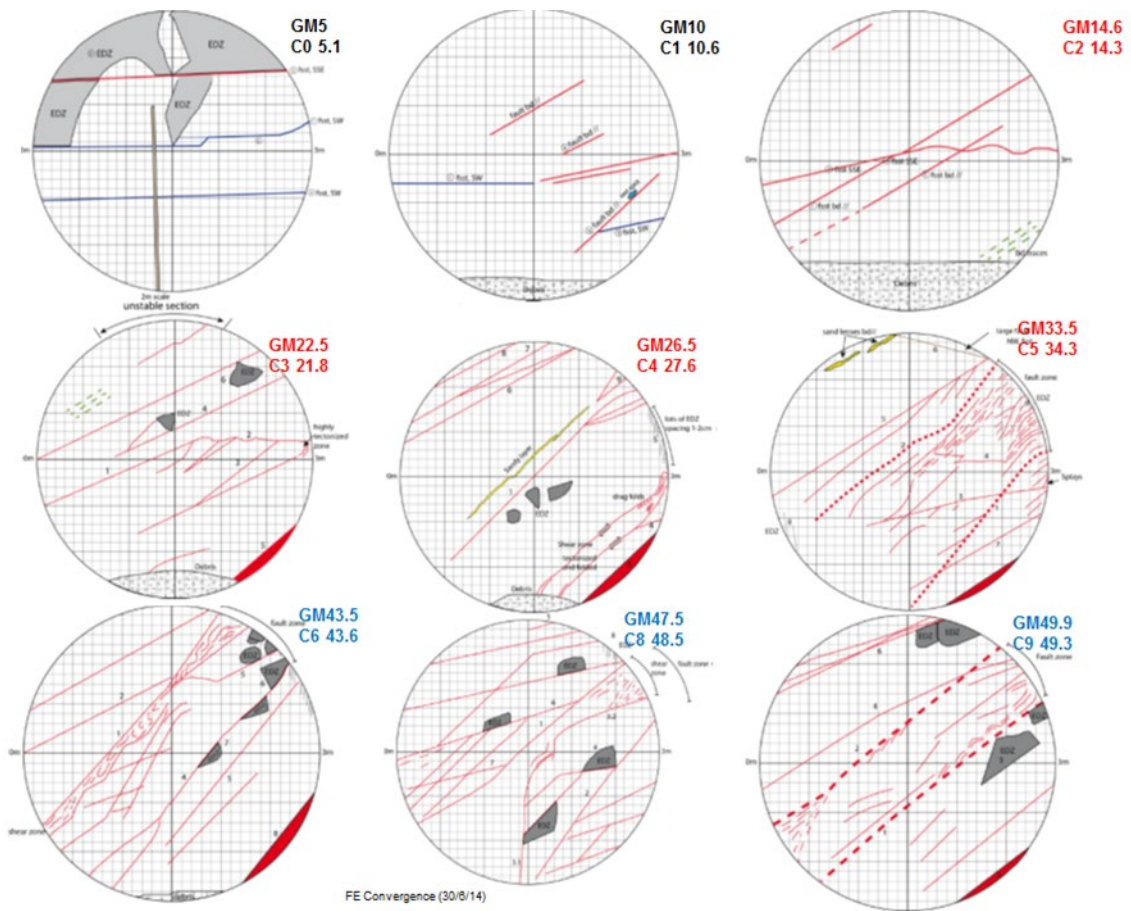


Fig. 4-64: Geological mapping of excavation face of FE Gallery at approximate locations of convergence sections (from Jaeggi, Lisjak et al. 2012).

Tab. 4-30: Measured convergences in FE Gallery approximately one month after excavation.

Convergence section			Days after Excavation	Behind face (m)	P1 (mm)	P2 (mm)	P3 (mm)	P4 (mm)	P5 (mm)	P6 (mm)	P7 (mm)
C0	5.1	08/08/2012	92.08	44.90	6.51	4.25	10.07	4.80	10.25		
C1	10.6	08/08/2012	85.17	39.40	11.79	26.23	12.30	11.89	35.56		
C2	14.3	08/08/2012	78.97	35.70	16.65	15.06	13.74	12.96	51.93		
C3	21.8	08/08/2012	68.97	28.20	29.25	26.64	19.83	18.55	42.90		
C4	27.6	08/08/2012	58.08	22.40	23.76	16.06	10.70	27.01	59.45		
C5	34.3	08/08/2012	51.10	15.70	18.98	16.41	14.53	18.64	40.68	25.98	55.09
C6	43.6	08/08/2012	41.29	6.40	13.59	14.95	7.64	1.50		14.36	
C7	44.2	08/08/2012	41.04	5.80	19.63	30.55	33.17	21.21	19.65	10.22	27.81
C8	48.5	08/08/2012	30.33	1.50	3.18	2.26	1.81	2.50	1.58	1.63	9.50
C9	49.3	08/08/2012	30.00	0.70	1.84	6.58	7.14	3.99	4.85	3.27	5.50

Tab. 4-31: Measured strain normalised to gallery radius.

	Gallery Support	P1	P2	P3	P4	P5	P6	P7
C0	Shotcrete + arches	0.4%	0.3%	0.7%	0.3%	0.7%		
C1	Shotcrete only	0.8%	1.7%	0.8%	0.8%	2.4%		
C2		1.1%	1.0%	0.9%	0.9%	3.5%		
C3		1.9%	1.8%	1.3%	1.2%	2.9%		
C4		1.6%	1.1%	0.7%	1.8%	4.0%		
C5		1.3%	1.1%	1.0%	1.2%	2.7%	1.7%	3.7%
C6	Arches only	0.9%	1.0%	0.5%	0.1%		1.0%	
C7		1.3%	2.0%	2.2%	1.4%	1.3%	0.7%	1.9%
C8		0.2%	0.2%	0.1%	0.2%	0.1%	0.1%	0.6%
C9		0.1%	0.4%	0.5%	0.3%	0.3%	0.2%	0.4%

Radial extensometers were installed in five boreholes located in two sections: E1 at GM 14.6 (BFEC001, 2) in the "shotcrete only" section and E2 at GM 43.1 (BFEC003, 4, 5) in the "arches only" section. Each extensometer was equipped with four sections and installed to 6 or 8 m into the rock. The calculated strains are plotted in Fig. 4-65.

Tab. 4-32: Extensometer sections in FE Gallery.

Section	Boreholes			Pin	Interpretation
E1 GM 14.6 Shotcrete only	BFEC001	6 m	⊥	C2P4	Significant displacement beyond 6 m
	BFEC002	6 m	∥	C2P3	Extensometer consistent with convergence. No significant displacement beyond 6 m
E2 GM 43.1 Arches only	BFEC003	8 m	∥	C6P4	Significant displacement beyond 8 m
	BFEC004	6 m	⊥	C6P7	Significant displacement beyond 6 m
	BFEC005	6 m	⊥	C6P3	Significant displacement beyond 6 m
E2 GM 43.1 Arches only	BFEC003	8 m	∥	C7P4	Significant displacement beyond 8 m
	BFEC004	6 m	⊥	C7P7	Significant displacement beyond 6 m
	BFEC005	6 m	⊥	C7P3	Significant displacement beyond 6 m

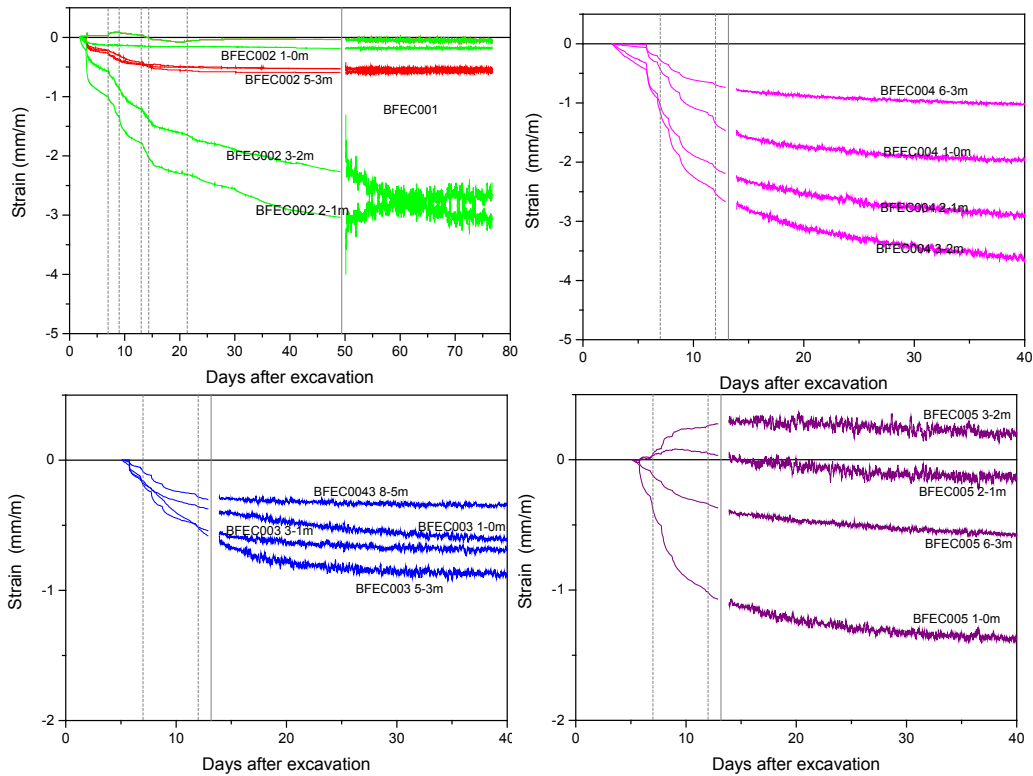


Fig. 4-65: Measured strains versus days after excavation for extensometers at E1 and E2 sections of FE Gallery.

At E1 the largest strains were measured in BFEC002 (normal to bedding) between 1-3 m. Strains continued to increase during excavation. At E2 strains were largest in BFEC004 (normal to bedding) between 1-3 m into the floor.

Strain profiles from the extensometer data (at 06/08/12) show a significant difference between the normal to bedding direction (BFEC002, BFEC004, BFEC005) and the along bedding direction (BFEC001, BFEC003). The strain normal to bedding appears to be strongly localized in a high strain zone (0.2 – 0.4%) close to the tunnel wall while strain along bedding shows a more uniform distribution (~ 0.05 – 0.1%) potentially extending further from the tunnel wall. The profile for BFEC004, also normal to bedding, shows a rather different distribution (see Fig. 4-66) which may indicate significant heterogeneity in the strain profile.

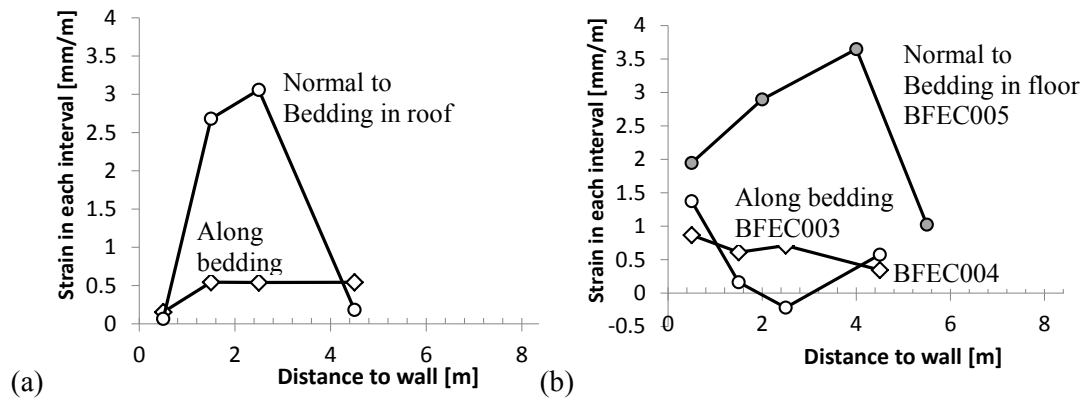


Fig. 4-66: Strain profiles in tunnel wall at (a) E1 (GM 14.6 shotcrete only) and (b) E2 (GM 43.1 arches only) on 06/08/12.

Differences between the response of the radial extensometers and convergence measurements can be due to:

- Deformation beyond the end of the extensometer (E1, E2);
- Differences in installation date (E1);
- Localized greater convergence between arches (section E2);
- Measurement of total rather than radial convergence.

In the E1 section (shotcrete-only) comparison was straightforward indicating good agreement for the displacement parallel to bedding but significantly greater displacement in the convergence data than the extensometer normal to bedding - suggesting displacement beyond the end of the extensometer (see Fig. 4-67).

In the E2 section (arches only) comparison is more difficult because displacements were typically small on the arches (section C6) but much greater between the arches (C7). How these heterogeneous displacements at the tunnel wall are redistributed within the rock is likely to be complex. Arches are placed at 1 m intervals and the extensometer section E2 is located 0.5 m from C6 (on the arch). If we compare the extensometer data with convergence data from C7 (between arches) then there appear to be significant displacements beyond the ends of the extensometers. If we compare with C6 data (on the arch) the two sets of displacements are comparable.

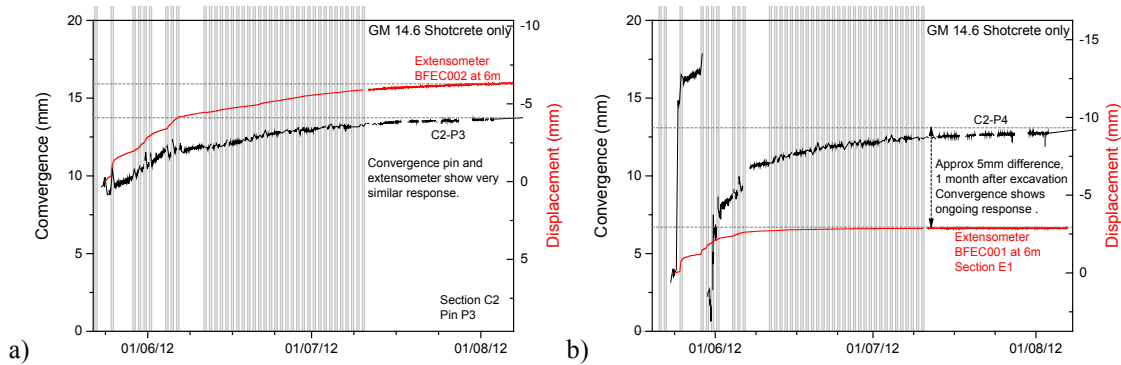


Fig. 4-67: Comparison of convergence and extensometer response, parallel to bedding (left) and normal to bedding (right) for FE Gallery.

#### 4.7.4 Long-term response

Fig. 4-68 shows linear and log-linear plots of the measured convergences at C4 and C7. Convergences were in the range 10-40 mm up to about day 100 in both sections for all but P5 at C4. After concreting of the invert convergence increased sharply at C4 (shotcrete only) and then quickly stabilized with almost stable deformations after this. At C7 (steel arches only) deformations continued with a roughly log-linear increase.

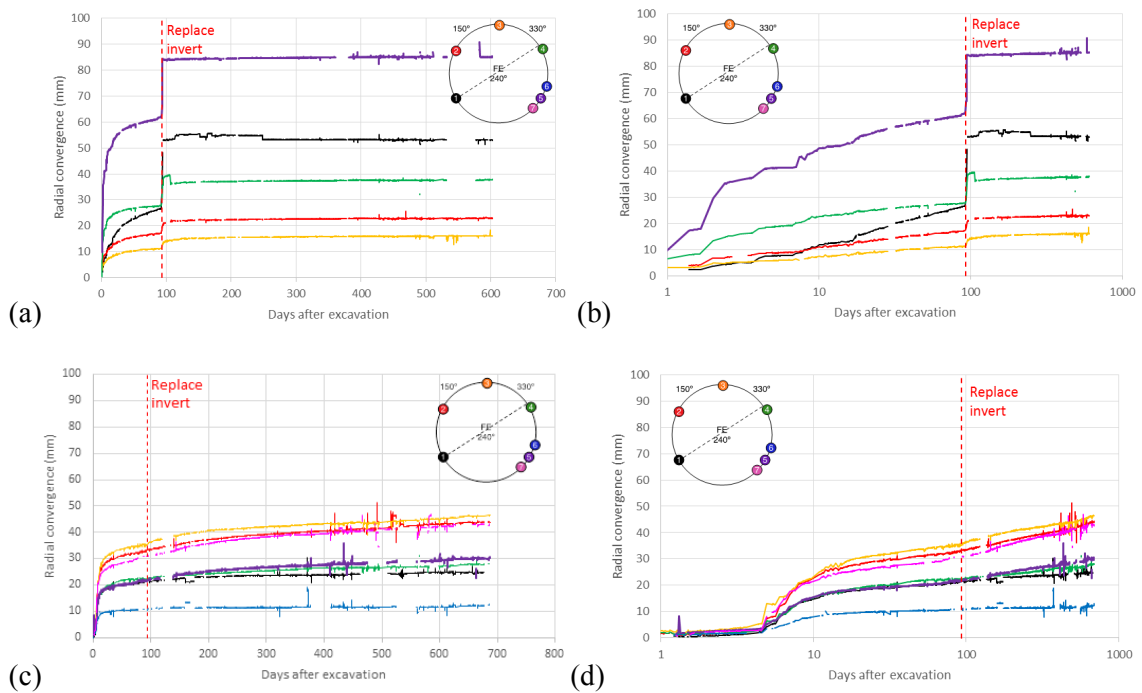


Fig. 4-68: Linear and log-linear plots of total convergence measured at FE Gallery: (a), (b) C4 (GM 27.6 shotcrete only) and (c), (d) C7 (GM 44.2 – steel arches only) sections.

#### 4.7.5 Summary of results

##### **Understanding of failure mechanisms**

Failure mechanisms are likely to be similar to those identified in the MB tunnel although the influence of the fault running along the FE Gallery may have had a significant effect in focusing deformation on pre-existing features.

##### **Diametral strain**

Radial extensometers typically showed smaller displacements than observed in the convergence measurements. In part this may be due to heterogeneity of displacements – especially in the "arches only" section, but probably indicates displacements beyond the extensometers.

Large strains  $\sim 3 - 4\%$  were observed at P5 in the "shotcrete only" section and are associated with bedding-normal deformation in the damage zone which can be seen in the excavation face. Convergences at other points around the excavation in the "shotcrete only" section were typically smaller (1 – 2%).

Strains in the "arches only" sections were heterogeneous with deformation focused between the arches (1 – 2%) while the convergences near the arches themselves were very limited.

The influence of the different support methods is clearly seen in the radial convergence data (Fig. 4-68) with deformations stabilizing in the shotcrete section after concreting of the invert while continuing to increase in the arches section.

##### **Pore pressure monitoring**

Piezometers out to 6 m from the tunnel axis (4a) showed a sustained drop in pressure indicating either anisotropic elastic pore pressure response, possible yielding or, when pressure drops to atmospheric, fracturing and connection to the tunnel.

Only BFEA002-i6 at 2.2 m from the tunnel axis (1.5a) showed a drop to atmospheric indicating a connected EDZ fracture network. However many of the piezometers showed larger pressure drops than indicated by the elastic models indicating possible yielding.

Tab. 4-33: Summary of observations for FE Tunnel excavation.

	Summary	Comment
Cross-section	Circular cross-section with flattened invert diameter 3 m	Originally circular cross-section
Orientation	244°	Slightly oblique to bedding strike at 240°
Geology	Shaly facies running sub-parallel to fault structure	
Method	Pneumatic hammer and roadheader	Initially pneumatic hammer, roadheader used subsequently
Support	GM0-GM9: Shotcrete+arches GM9-GM38: Shotcrete only GM38-GM50: Arches only	Anchors installed at 1.5 m spacing in shotcrete section
EDZ	Piezometer response indicated fracturing up to 1.5a from axis and yielding up to 4a?	Mapping showed disturbance in face and identified EDZ extensional and shear features
Diametral Strain	Excavation: large convergences at P5 in floor; 3 – 4% strain in shotcrete only section. Convergence heterogeneous in "arches only" section Long-term: ongoing time-dependent deformation in arches only section (C7) 3 – 5 mm/ln(day). Higher rates in bedding normal direction.	Radial extensometers typically show smaller displacements Long-term convergence rates smaller in shotcrete only section (C4).
Pore pressure monitoring	Only one piezometer showed possible fracturing	

## 4.8 Other relevant experience from Mont Terri

### EDZ fracture density

Yong (2008) reported a comparison of fracture density in boreholes around tunnels and niches at Mont Terri using data from over 100 boreholes (see Fig. 4-69). All structures other than those clearly related to tectonic features or drill core handling were counted over 0.5 m intervals. Almost 75% of the boreholes were drilled into the side-walls and data has been normalised per borehole to reduce the bias. Fracture count in the first 0.5 m was as high as 10 (mean spacing 5 cm) around some excavations but typically reduced to less than 2 at 3 m from the tunnel wall. Detailed investigation of macro fracturing around the EZ-B Niche suggested a much narrower zone of macro-fracturing ~ 20 cm in thickness with an outer zone extending to 70 cm of reduced seismic velocity. Almost all excavations showed the highest density close to the tunnel wall and significant drop in fracture frequency beyond 2 m.

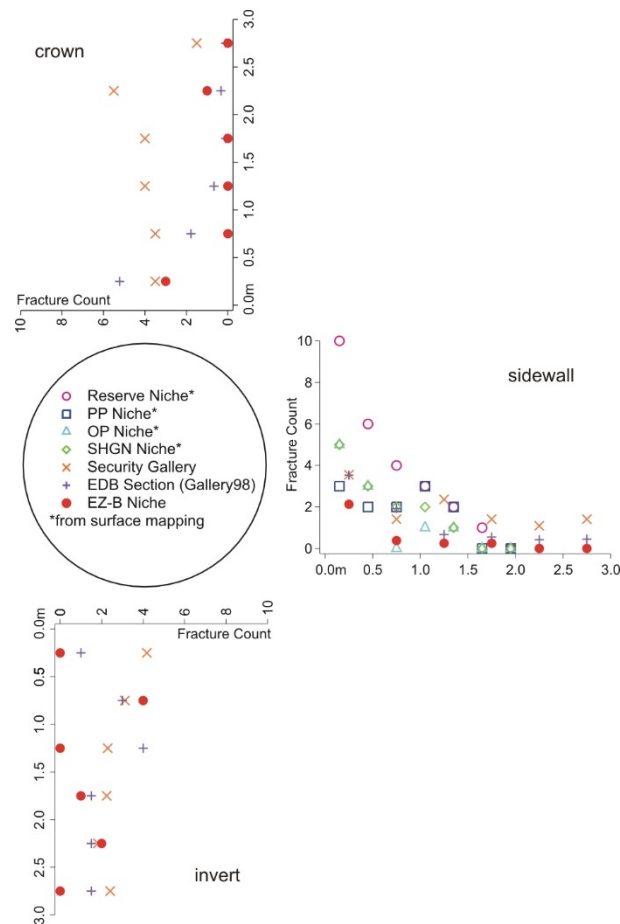


Fig. 4-69: Fracture counts in 0.5 m borehole intervals from around the EZ-B Niche and previous sub-parallel excavations (from Yong 2008).

### Borehole Damage Zone (BDZ)

Borehole breakouts and the damage zone around boreholes have been used as a proxy for the EDZ in several studies (Wermeille & Bossart 1999; Martin & Lanyon 2003a; Vietor et al. 2006; Blümling et al. 2007; Labouise & Vietor 2014). Fig. 4-70 illustrates the observed borehole geometry for different directions from Wermeille & Bossart (1999). Similarities between the failure structures were identified and have been integrated into the conceptual models.

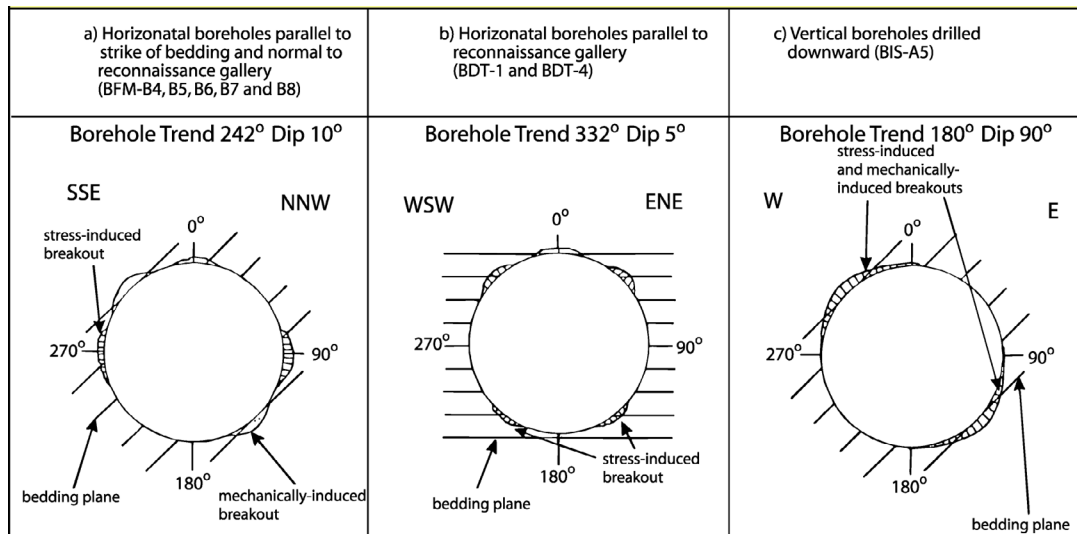


Fig. 4-70: Breakout observations from Wermeille & Bossart (1999).

Note that in these observations both stress-induced yielding and weakening and softening are superimposed.

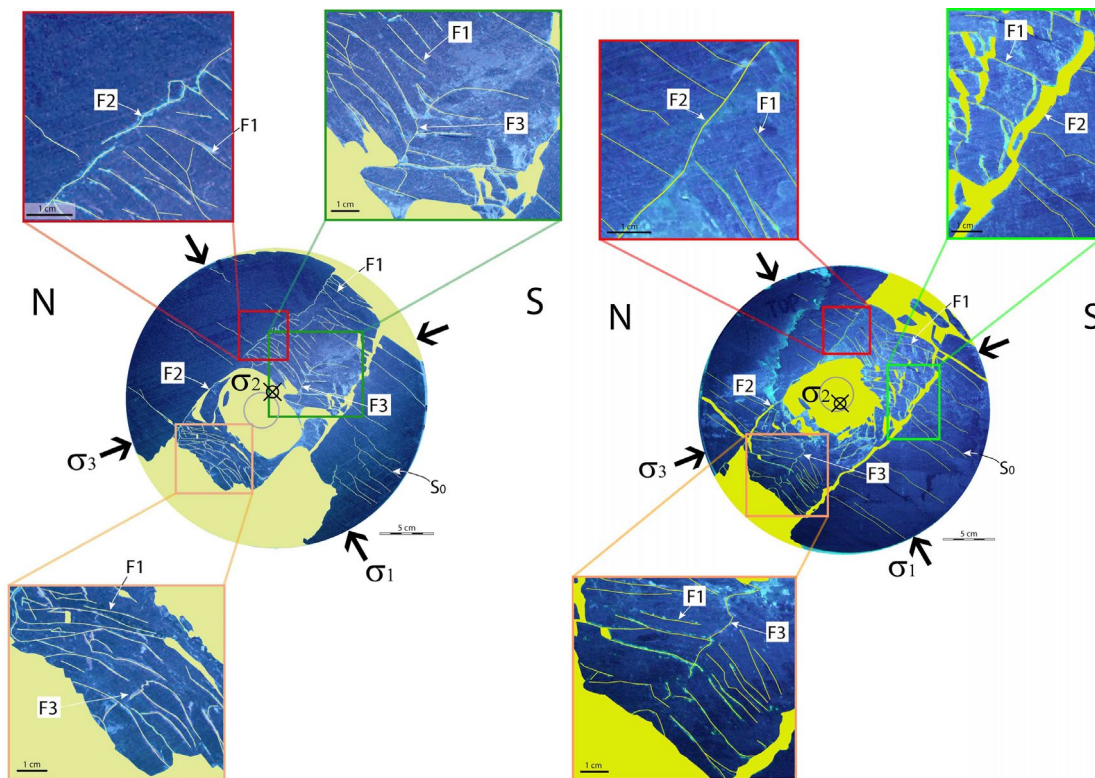


Fig. 4-71: Vertical sections of the overcore at two depths, showing details of failure mechanisms.

The original borehole was sub-horizontal and is now seen as the central oval opening. Bedding dips to the right. Figure from Badertscher (2008).

Labouise & Vietor (2014) compared laboratory excavation simulations with a resin-impregnated overcore from a sub-horizontal 101 mm borehole used for a 3 year-long dilatometer test. Sections corresponding to the test and packer section showed similar fracture patterns indicating that the mechanisms leading to borehole collapse were similar and independent of the testing history. Further, the collapse must have occurred after the dilatometer was withdrawn and the borehole was open. During this period the rock would have been fully resaturated. The sub-vertical buckling failure zones extended beyond the overcore (in excess of a borehole diameter).

Labouise & Vietor (2014) summarize the failure mechanism as:

1. Excessive shear loading along the bedding planes in the tangential orientations to the borehole leads to shear failure initiation. The shear failure has a sub-vertical orientation (sub-parallel to the local maximum stress) and forms an acute angle with bedding.
2. The shear fracture curves into the a bedding-parallel orientation and form a first detached segment that starts to move along the bedding plane and the shear fracture and thus rotates into the existing borehole.
3. As the shearing motion along the shear fracture progresses the stresses are redistributed away from the failed bedding fragment on the intact rock further from the borehole. When the strength of the next flake is exceeded a second fracture is formed at low angle to bedding, curves into a bedding plane parallel orientation and the next fragment starts to move and rotate.

4. The rotation of the fragments leads to cracking where rotation is inhibited by the confining stress farther away from the borehole.

The conditions during testing and after collapse are illustrated in Fig. 4-72.

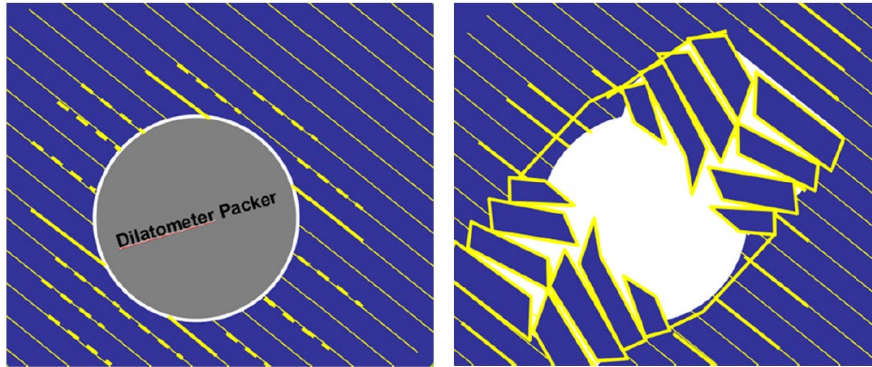


Fig. 4-72: BDZ status during long-term hydrotesting (left) and after collapse (right).

### Ventilation test

Garitte et al. (2013) reported modelling within the DECOVALEX Project of ventilation testing of a 10 m section of the 1.3 m diameter VE microtunnel bored perpendicular to bedding strike. The VE Tunnel is unlined and unsupported and has been open since 1999. The modelling covered a 12 year period from excavation to 2011. The extent of the EDZ was estimated by geophysical means to be 5–25 cm ( $0.1-0.4a$ ) in the bedding plane direction and 10 cm in the perpendicular direction ( $0.2a$ ). No significant changes were induced by ventilation and the EDZ was assumed to be solely related to stress redistribution during the excavation. Neither rock failures nor far-reaching cracking were observed on the walls during testing (Mayor et al. 2007a, Mayor & Velasco 2008) and it was assumed that there was no significant EDZ development during the drying and wetting cycles. Garitte et al. (2013) *inter alia* conclude that:

- Anisotropic rock properties (permeability and stiffness) were shown to explain some second order phenomena.
- The good agreement between measurements and simulation results using a permeability value that does not vary with damage indicates that permeability increase in the EDZ may be neglected in experiments involving a similar diameter tunnel.

## **5 The EDZ in the Opalinus Clay – derivation of a generalised conceptual framework**

### **5.1 Overview**

The development of a generalised conceptual framework for the description of the EDZ around excavations is motivated by the needs of the engineering and safety assessment teams in the framework of SGT Stage 2. A traceable workflow is presented for the derivation of a conceptual framework, which is needed for the simulation of the EDZ around underground structures in the Opalinus Clay with numerical models. The workflow comprises:

- A synopsis of empirical and experimental evidence from Mont Terri, allowing for an integrated interpretation of the EDZ-related databases from different experimental sites;
- A conceptual framework for modelling of the EDZ, comprising the inventory of relevant structural features, constitutive relationships and the effective stress framework applicable to partially saturated Opalinus Clay.

The workflow is a prerequisite for transferring the site specific knowledge about the EDZ from Mont Terri to the geological conditions in the candidate siting regions in Northern Switzerland (Chapter 6).

### **5.2 Results of EDZ-related data analyses at Mont Terri**

In this section the key results from Mont Terri are presented including an inventory of EDZ-related structural features, together with typical measured convergence, pore pressure response and deformation. Further processes and interactions such as the response to ventilation are also discussed.

#### **5.2.1 Identification and classification of excavation-induced features**

In the Opalinus Clay, the EDZ is formed by a complex network of brittle structures of variable extent and orientation, originating from the interaction of various deformation mechanisms and superimposed by pre-existing structures associated with the prevailing tectonic setting. Process couplings in conjunction with the excavation process and impacts during the operational phase may increase the complexity of the structure of the EDZ. It is therefore a priority objective to identify and classify the key structural features of the EDZ according to their supposed origin. Thus, a characteristic inventory of excavation-induced features can be assigned to a given tunnel configuration, addressing not only the impact of the geological setting (litho-stratigraphic and tectonic features, stress orientation, pore pressure), but also the effects associated with the engineering design (excavation procedure, support measures, ventilation).

#### **EDZ-related failure mechanisms and influencing factors**

The results from previous EDZ studies at Mont Terri (Martin & Lanyon 2003a; Bossart et al. 2002, 2004; Yong 2008 and Nussbaum et al. 2011), together with the more recent work presented in Chapter 4 support a consistent description of excavation-related failure mechanisms at Mont Terri. These are:

- Extensional fracturing;
- Bedding and bedding-parallel slip;
- Buckling and kink failures;
- Reactivation of tectonic features;
- Slip-induced tensile and shear fracturing ahead of the face;
- Tensile cracks caused by drying running parallel to excavation.

In addition to these processes in response to the excavation process, the effect of humidity or wetting can result in significant weakening of the rock.

The distribution of the different EDZ feature types varies according to:

- Orientation of the excavation with regard to stress and bedding;
- Excavation geometry;
- Excavation and support methods;
- The rock facies (shaly, sandy or carbonate-rich);
- The presence of pre-existing tectonic features.

The major influence considered here is the excavation orientation. Two cases are considered:

- excavations normal to bedding strike (sub-parallel  $\sigma_{hmax}$ );
- excavations along bedding strike (sub-parallel  $\sigma_{hmin}$ ).

The influence of stress versus material anisotropy (in strength and modulus) is complex. This interaction is further complicated by local variations in tectonic setting (e.g. faulting in FE Gallery) and bedding orientation together with uncertainty on stress direction.

### **Influence of excavation method**

Some dependence on excavation method has been observed in previous studies (FP experiment) where there is evidence that excavation using blasting results in greater EDZ-related fracturing (Bossart et al. 2002, 2004). It was also noted that the frequency of unloading fractures decreased with time since excavation, with the lowest density being recorded in the two holes drilled in the Reconnaissance Gallery some 9 years after excavation.

### **Influence of excavation support**

Most excavations have been supported with fibre-reinforced shotcrete applied in one or two layers to a total thickness of 15-25cm. In addition anchors (typically 2-3 m in length) have been used in the roof or in locations where bedding/faulting is adversely oriented to the tunnel. A summary of the different support levels for excavations normal and parallel to bedding strike is given in Tab. 5-1.

Tab. 5-1: Excavation support for different excavation orientations.

Support	Excavation direction	
	Bedding-strike normal	Bedding-strike parallel
Unlined	VE microtunnel: stable excavation open for several years	HG-A microtunnel: significant overbreak developed, but test section remained open ~ 1 year. Steel mesh used to protect instrumentation work prior to sealing.
Shotcrete (10-20 mm) + anchors	Typical short-term convergence < 1%. Generally long-term stable. Some problems near junctions require local repair or installation of steel arches.	Shotcrete typically applied at end of each day. Measured short-term convergence ~ 1.5%, but larger in FE Gallery (fault zone). Local shotcrete damage requires repair and additional anchors. Significant rockfalls if adverse fault geometry (low angle).
Steel arches		FE section: Heterogeneous convergence around arches showing ongoing deformation

### Influence of rock facies

No EDZ-related features have been identified in the sandy facies which, combined with notably smaller measured deformations, suggests that excavation response in this facies may be significantly different from that observed in the shaly facies. The database for excavations is limited to a short section through the main galleries and the TT-Niche, however, and for this reason we do not provide a separate description of the EDZ in the sandy facies. Further studies would be useful to confirm these observations and determine any constraints on stress or material properties that might follow from them.

### Hydraulic properties of excavation-induced fractures

The development of excavation-induced fractures has been confirmed by coring/resin impregnation (FP, EZ-A, MB) and pneumatic and hydraulic testing (EH, ED-B, EZ-A, EZ-B, HG-A MB). Subsequent sealing of such features on resaturation has also been observed (EH/SELFRAC, EZ-A, MB, HG-A). Initial tests typically showed high transmissivity ( $\sim 10^{-7} \text{ m}^2/\text{s}$ ) which reduced significantly on resaturation. Higher transmissivity has been measured at the EZ-A site during pneumatic tests in the tunnel-floor EDZ where the rock had been extensively disturbed by removal of the concrete invert using pneumatic hammers. However even these highly transmissive features showed subsequent significant transmissivity reduction on resaturation.

### Description of EDZ in excavations normal to bedding strike (sub-parallel $\sigma_{\text{hmax}}$ )

A conceptual model of the EDZ for excavations normal to bedding strike incorporating extensional fracturing and zones of bedding slip was proposed by Martin & Lanyon (2003a). Since that time the importance of tectonic features (Yong 2008; Nussbaum et al. 2011) and the generation of shear structures (Nussbaum et al. 2011) ahead of the face have been identified. The different feature types are listed in Tab. 5-2 and a revised version of the conceptual model is presented in Fig. 5-1.

Tab. 5-2: Inventory of EDZ-related structural features for excavations normal to bedding strike.

Feature type	Location	Remarks
Extension fractures/ unloading joints	In side walls. Can be compartmentalized by tectonic features resulting in isolated clusters controlled by spacing of tectonic features (~ m) Limited by differential stress contour	Dense connected fracture network within 0.5a. Isolated fractures and clusters to 1a
Reactivated tectonic features	Potential formed ahead of the face locally may be reactivated in side walls and within buckling zones	
Bedding-parallel buckling and kink zones	In roof and floor	Complex zones of bedding shear and through-going shears created connected network
Slip-induced failure generated ahead of the face	Formed ahead of the face	Single shear structures connected to reactivated tectonic features
Drying cracks	Present near open tunnel surfaces may open/close according to ventilation.	Isolated longitudinal features.

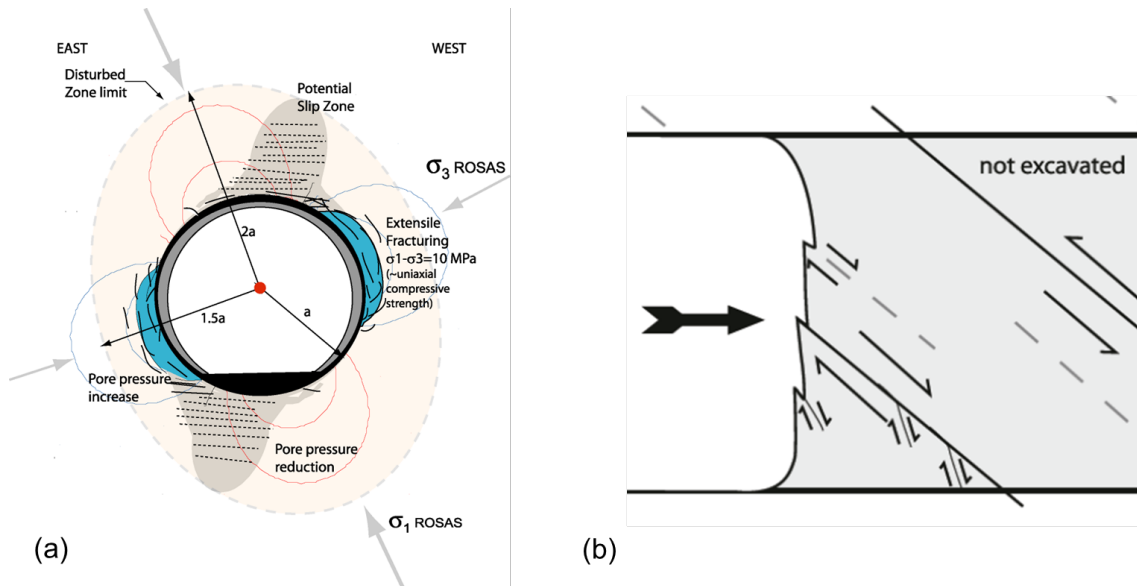


Fig. 5-1: Conceptual model of the EDZ fracture network for excavations normal to bedding strike at Mont Terri.

(a) Cross-section for ED-B experiment from Martin & Lanyon (2003a); (b) ahead of the face shear due to slip on bedding-parallel faults (from Nussbaum et al. 2011).

### Description of EDZ in excavations along bedding strike (sub-parallel $\sigma_{hmin}$ )

Recent studies of excavation response have concentrated on characterizing the EDZ around excavations parallel to bedding strike (HG-A, MB Niche, FE-A Niche, FE Gallery). While the expected stress anisotropy is less severe in this direction, the effects of strength and stiffness anisotropy typically result in greater deformation.

A schematic model of the EDZ around the unlined HG-A microtunnel based on structural mapping is presented by Marschall et al. (2006). The model identifies both stress and structurally controlled features. While this model illustrates the main fracture mechanisms, bedding is steeper at HG-A than in the MB Niche and FE Gallery; sliding on bedding may be more prominent at HG-A. It is also at a relatively small scale here where individual bedding-parallel faults may control much of the response. At larger scales (e.g. MB Niche and FE Gallery) the influence of multiple sub-parallel faults becomes significant. In larger, possibly more tectonically disturbed excavations (MB Niche, FE-A Niche, FE Gallery) reactivation and slip on faults ahead of the face results in the creation of "onion-skin" fractures curving around the excavation face. These EDZ fractures are delimited by the tectonic features and visible as a "band" of sub-parallel fractures intersecting the side-walls at a steep angle as shown in the mapping of the DR-A Niche. A conceptual model of the EDZ around such an excavation is illustrated in Fig. 5-2 and Fig. 5-3. In the southern part of the URL where bedding is steeper, gravity sliding mechanisms as illustrated in Fig. 3-4 will be more important. Tab. 5-3 provides an inventory of the different features within the EDZ for excavations parallel to bedding strike.

Tab. 5-3: Inventory of EDZ-related structural features for excavations parallel to bedding strike.

Feature type	Location	Remarks
Extension fractures/unloading joints	In side-walls and face in regions of high deviatoric stress sub-parallel to excavation surface. Also formed in response to slip along tectonic structures (typically bedding-parallel) resulting in fractures normal to and confined by slip structures.	Fractures form connected fracture network within 0.5a of excavation. Isolated fractures may extend to 1.5a. Fractures often terminate on tectonic features.
Reactivated tectonic features	May occur ahead of the face and around excavations to a distance of ~ 1.5 a.	May be difficult to identify reactivation from core due to drilling disturbance. Can be observed in resin injection studies to 1.1a. Limited data suggest reactivation could extend further from the excavation.
Bedding-parallel buckling and kink zones	Where bedding is tangential to tunnel wall. Upper SSE wall (9-12 o'clock looking 240°) and lower NNW wall (3-6 o'clock).	Extent of buckling zone dependent on confinement. Where confinement fails extensive caving can occur (EZ-A Niche).
Slip-induced failure generated ahead of the face	Slip on faults ahead of the face results in tensile fractures wrapped around excavation face (onion-skin) typically confined between tectonic features. Visible in side walls as bands of parallel fractures oriented with normal close to tunnel heading.	Fractures form ahead of face in onion-skin orientation and fractured band extends ~ 1 m (a/2) into side wall.
Drying cracks	Present near open tunnel surfaces; may open/close according to ventilation.	Isolated longitudinal features.

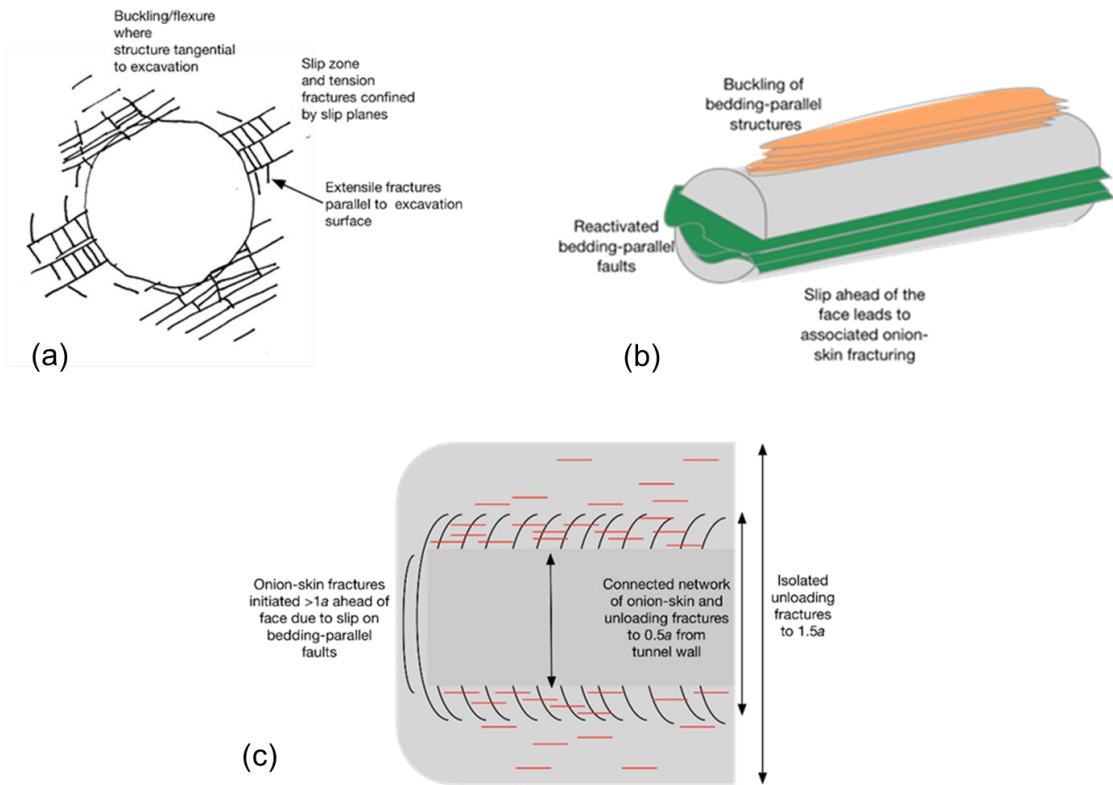


Fig. 5-2: Conceptual model of the EDZ fracture network for excavations parallel to bedding strike (MB Niche, FE Gallery) at Mont Terri:

(a) cross-section illustrating fracturing mechanisms; (b) sketch illustrating slip on tectonic faults ahead-of the face and associated band of fracturing in side-wall; (c) cross-section parallel to bedding.

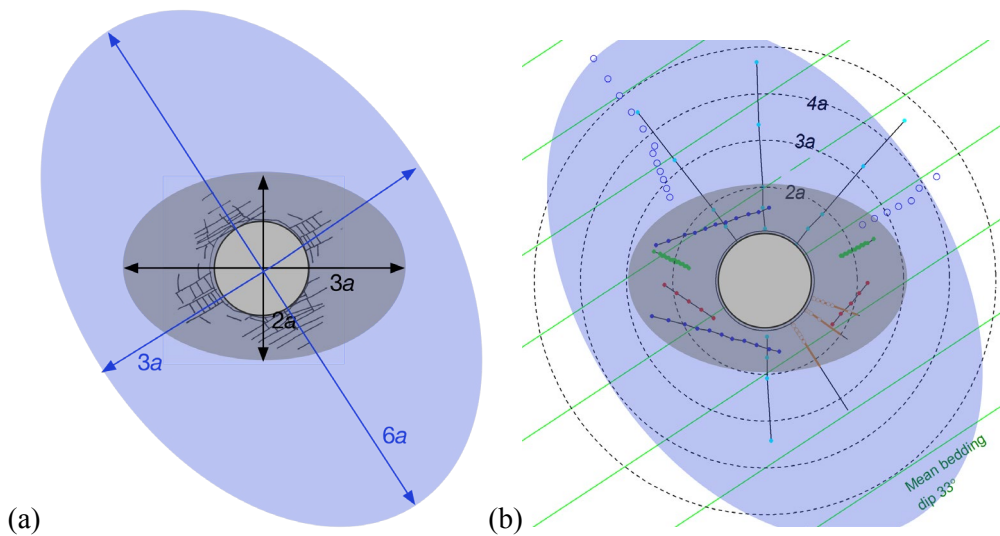


Fig. 5-3: Dimensions of EDZ envelope and pore pressure disturbed zone.

a) schematic sketch; b) comparison with location of MB Experiment and FE sensors indicating fracturing and extent of anisotropic pore pressure disturbance.

Observations of pore pressure change from the FE experiment suggest a more extensive zone of yielding/dilation shown in Fig. 5.3.

In excavations parallel to bedding strike at Mont Terri, fracturing mechanisms and short-term deformation are strongly related to structure. Much of the observed fracturing is related to slip on tectonic faults and is consequently delineated by them. Short-term deformation is also largest in the direction normal to bedding and the dominant bedding-parallel faults.

### **5.2.2 EDZ related phenomena and processes**

The creation and evolution of the EDZ is controlled by a variety of thermo-hydromechanical phenomena and processes together with the prevailing environmental conditions (stress, pore pressure, saturation, temperature). A detailed analysis of the development of excavation-induced damage in terms of loci of initiation, failure mechanisms and failure propagation requires well defined experimental set-ups and adequate hydromechanical site instrumentation, providing the appropriate indicators for the evolution of the state of stress, strain and pore pressure during and after the excavation process. Relevant observational variables as indicators for the deformation behaviour of the rock mass around an excavated cavity are:

- Tunnel convergence;
- Pore pressure response;
- Extent of plastified zone.

The subsequent paragraphs are dedicated to a detailed analysis of excavation-induced damage in the rock mass in terms of loci of initiation, failure mechanisms and failure propagation.

#### **Tunnel convergence**

Convergence profiles have been installed at multiple locations at Mont Terri. Measurements of long-term diametral strain are available from 16 convergence arrays listed in Tab. 5-4. The profiles were generally installed soon after excavation and have been routinely monitored since. Locations are shown in Fig. 5-4. The most recent data used here are measurements made on 8-9/08/13 (compilation by Jaeggi 2014). The longest monitoring periods are therefore about 3500 days.

The profile data have been used here as the basis for analysis as the profiles provide a consistent measurement method applied to a range of excavation locations and orientations. Radial convergence data from the MB Niche and FE Gallery are also available with high time resolution and have been discussed in Chapter 4.

Convergence is likely to be a function of excavation size, orientation, procedure, and support. Further it will be influenced by lithology (facies) and local structure (faults). Within this study the short-term response has been characterized by the measured convergence at 100 days after excavation, by which time the excavation has typically been completed and lined. There is inevitably a time-lag between excavation and installation of a particular sensor; early measurements show short-term responses stabilizing after the excavation face has passed several diameters beyond the measuring instrument. Long-term time-dependent deformations due to visco-plastic effects (creep), hydromechanical processes (consolidation and pore pressure equilibration) and seasonal effects (variation in humidity) continue after excavation. The time-dependent response has been characterized by late-time behaviour during undisturbed periods

(no nearby excavation). A more detailed separation of short-term and time-dependent responses was used in the Mine-By Experiment analysis by Martin et al. (2014b).

Tab. 5-4: Long-term monitoring convergence profiles at Mont Terri.

Location	Heading°	Geology	Diameter (m)	Excavation	First data	Monitoring period days
EZ-A TM6	195	Shaly facies	5	29/01/04	04/02/04	3479
Start Niche	260	Shaly facies	5	02/03/04	05/03/04	3446
Ga04 GM30	260	Shaly facies	5	02/09/04	24/03/05	3262
Ga04 GM40	275	Shaly facies	5	13/09/04	13/09/04	3251
Ga04 GM68	290	Shaly facies	5	07/10/04	22/10/04	3227
EZ-B Niche	330	Shaly facies	5	10/12/04	12/12/05	3162
Ga08 GM14.5	240	Shaly facies	5	27/11/07	28/11/07	2082
Ga08 GM56	150	Shaly facies	5	06/02/08	07/02/08	2011
Ga08 GM75	150	Shaly facies	5	05/03/08	06/03/08	1983
Ga08 GM88.5	150	Shaly facies	5	14/03/08	14/03/08	1974
Ga08 GM117	150	Main fault	5	26/05/08	27/05/08	1900
Ga08 GM160	140	Sandy facies	5	31/07/08	04/08/08	1834
DR-A Niche	240	Sandy facies	5	10/09/08	18/09/08	1794
Ga08 MB TM4.5	240	Shaly facies	4.5	16/10/08	17/10/08	825
Ga08 MB TM12	240	Shaly facies	4.5	27/10/08	28/10/08	813
Ga08 TT TM18	230	Sandy facies	5	18/11/08	20/11/08	1723



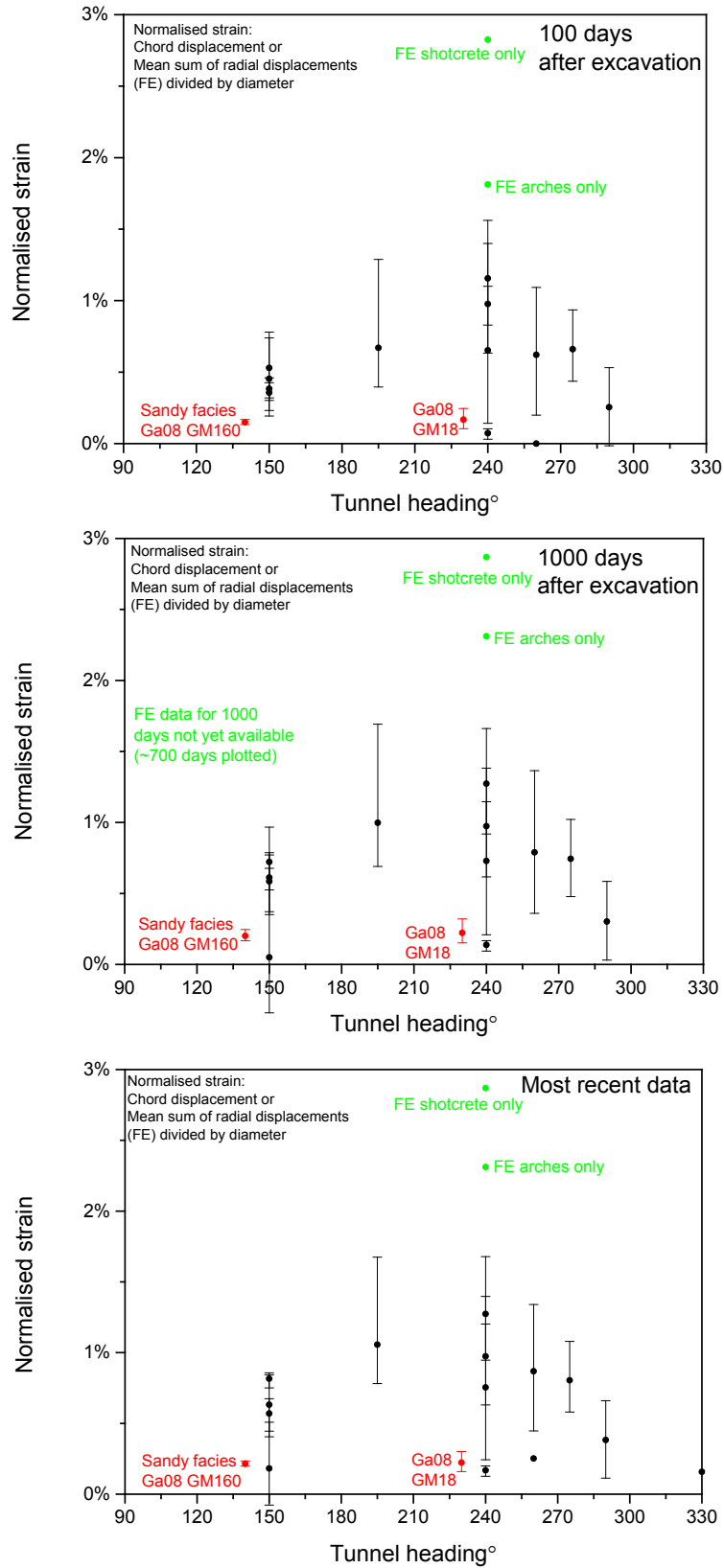


Fig. 5-5: Diametral strain against tunnel heading. (a) at 100 days after excavation; (b) at 1000 days; (c) most recent data. Excavations in sandy facies shown in red.

Fig. 5-5 shows the diametral strain (convergence/diameter) against tunnel heading at a) 100 days after excavation, b) at 1000 days after excavation and c) the most recent data. Excavations parallel to bedding strike in the shaly facies clearly show the largest deformations, while excavations normal to bedding show significantly smaller convergence and excavations in the sandy facies show the smallest. The largest strains are measured in the Mine-By Niche where support was relatively light and convergence arrays were emplaced quickly after excavation.

Statistics for short-term convergence for selected convergence profiles and excavations normal and parallel to bedding strike are given below (Tab. 5-6 and 5-8). Only profiles in the shaly facies (away from the Main Fault) which were installed immediately after excavation have been considered.

Long-term time-dependent responses shown in Fig. 5-6 exhibit a typical log-linear increase in convergence with time (Egger 2000). The log-linear trend is disturbed by nearby excavations or other operational events. The maximum calculated late-time slope for each profile is tabulated in Tab. 5-5. Maximum slopes vary from 1.7 – 7.5 mm/ln(day). Slopes are smallest in the sandy facies, but there is no clear trend with orientation. Most slopes are in the range 2-4 mm/ln (day). Higher slopes are typically associated with small measured convergences in profiles installed significantly after excavation (Ga04 GM30, EZ-B Niche) or where a response to additional excavation is observed (Ga04 GM68 close to join with Gallery 08).

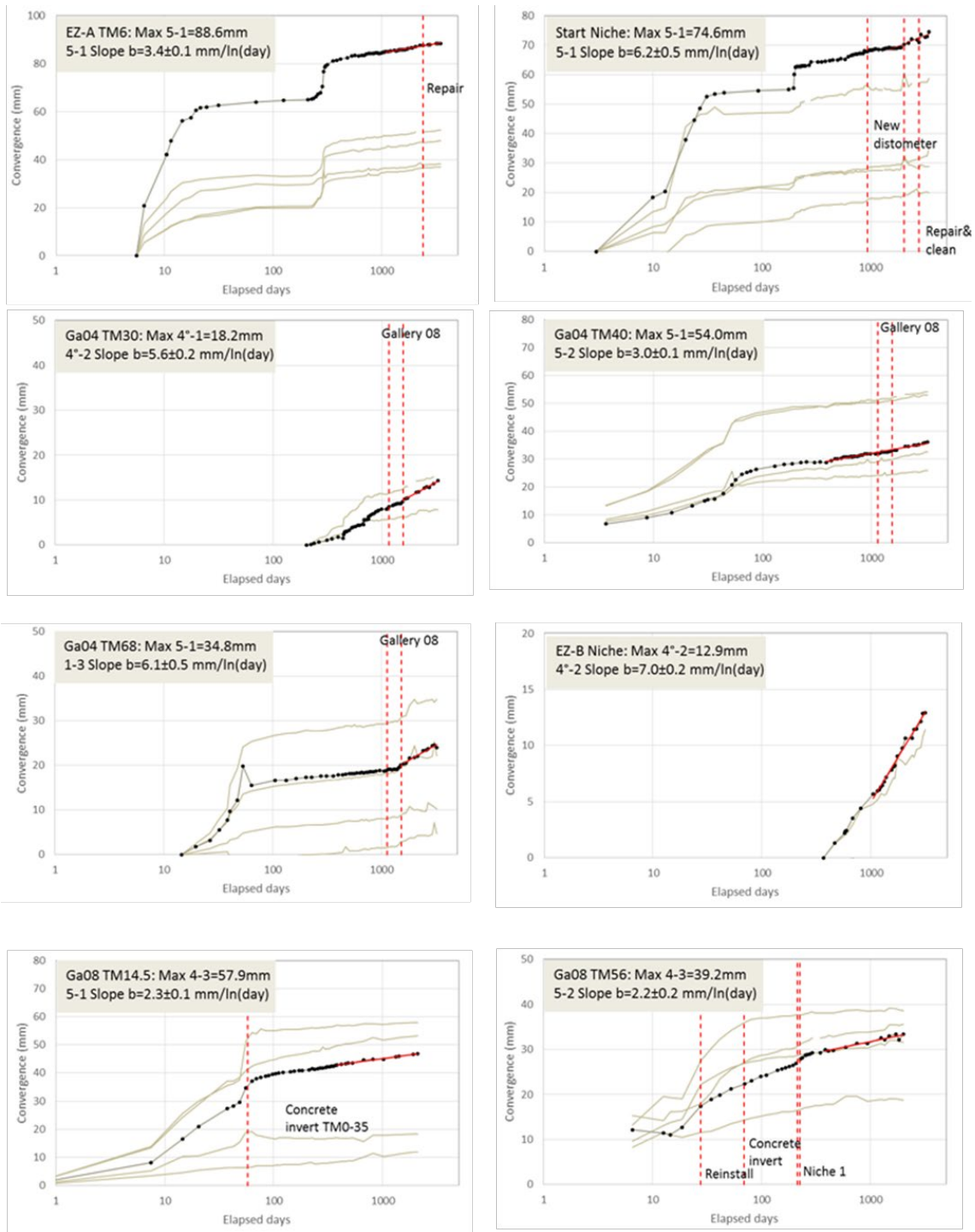
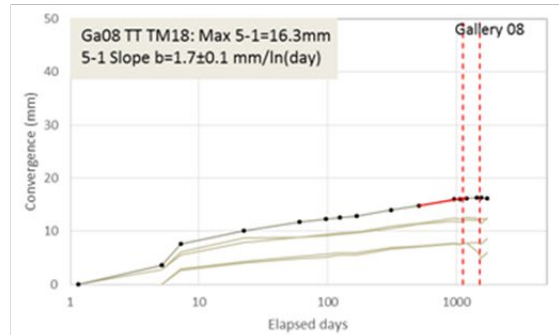
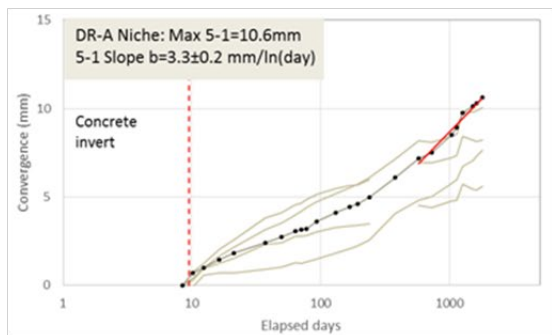
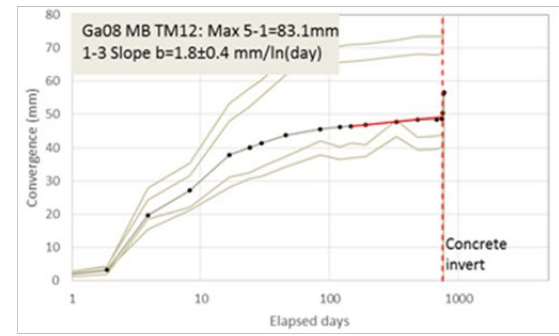
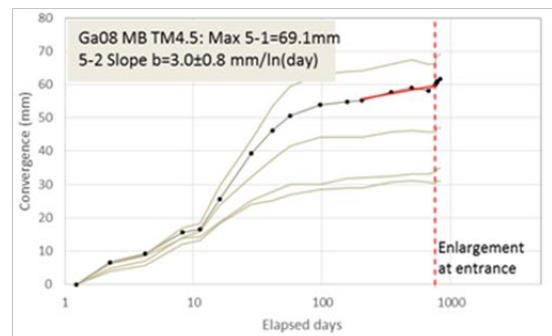
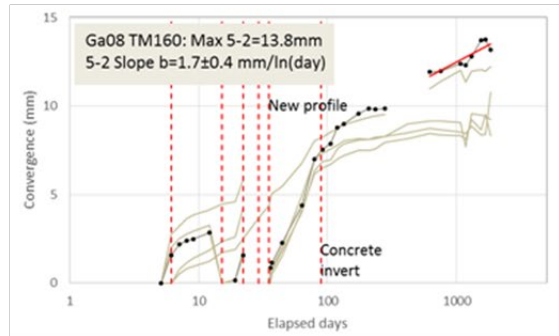
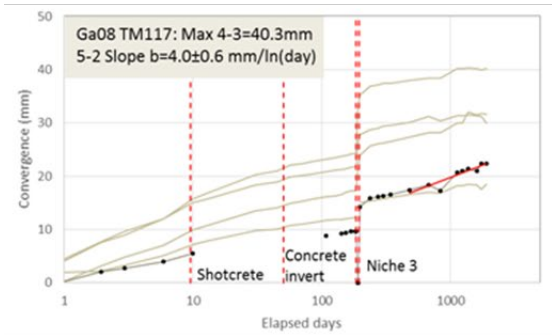
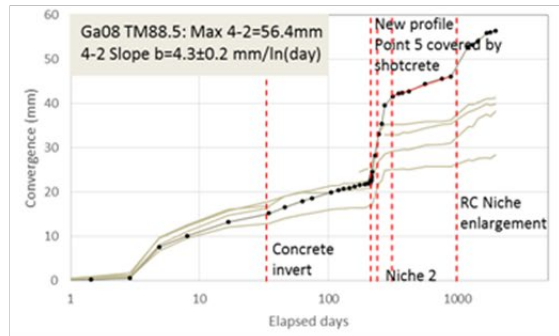
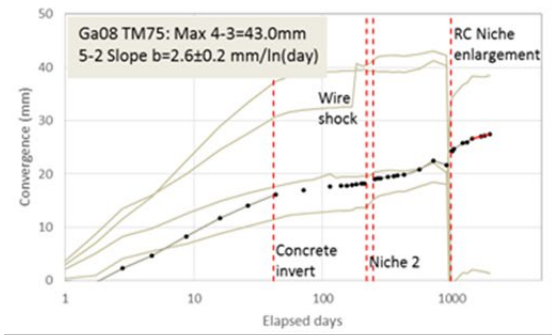


Fig. 5-6: Convergence versus time since excavation (log scale). Fitted maximum log-linear long-term slope shown as red line.



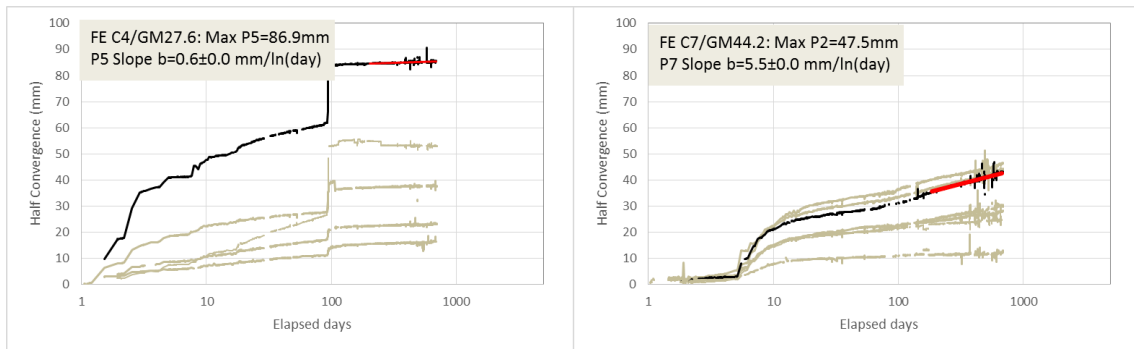


Fig. 5-6 cont<sup>d</sup>: Convergence versus time since excavation (log scale). Fitted maximum log-linear long-term slope shown as red line.

Tab. 5-5: Largest long-term slope (mm/ln(day)) for each convergence profile. Trend lines for slopes larger than 5 mm/ln (day) shown in **bold** in Fig. 5-6.

	Head- ing	Diam- eter (m)	Lithology	Chord	Slope	Error	R <sup>2</sup>	Start	End
EZ-A TM6	195	5	Shaly facies	5-1	3.4	0.1	1.0	1093	3479
Start Niche	260	5	Shaly facies	<b>5-1</b>	<b>6.2</b>	<b>0.5</b>	<b>0.9</b>	<b>1473</b>	<b>3446</b>
Ga04 GM30	260	5	Shaly facies	<b>4-2</b>	<b>5.6</b>	<b>0.2</b>	<b>1.0</b>	<b>1644</b>	<b>3262</b>
Ga04 GM40	275	5	Shaly facies	5-2	3.0	0.1	1.0	385	3251
Ga04 GM68	290	5	Shaly facies	<b>1-3</b>	<b>6.1</b>	<b>0.5</b>	<b>1.0</b>	<b>1609</b>	<b>3227</b>
EZ-B Niche	330	5	Shaly facies	<b>4-2</b>	<b>7.0</b>	<b>0.2</b>	<b>1.0</b>	<b>1049</b>	<b>3162</b>
Ga08 GM14.5	240	5	Shaly facies	5-1	2.3	0.1	1.0	381	2082
Ga08 GM56	150	5	Shaly facies	5-2	2.2	0.2	0.9	384	2010
Ga08 GM75	150	5	Shaly facies	5-2	2.6	0.2	1.0	1454	1983
Ga08 GM88.5	150	5	Shaly facies	4-2	4.3	0.2	1.0	314	889
Ga08 GM117	150	5	Main fault	5-2	4.0	0.6	0.9	483	1899
Ga08 GM160	140	5	Sandy facies	5-2	1.7	0.4	0.8	617	1835
DR-A Niche	240	5	Shaly facies	5-1	3.3	0.2	1.0	575	1794
Ga08 MB TM4.5	240	4.5	Shaly facies	5-2	3.0	0.8	0.8	203	755
Ga08 MB TM12	240	4.5	Shaly facies	1-3	1.8	0.4	0.8	146	751
Ga08 TT TM18	230	5	Sandy facies	5-1	1.7	0.1	1.0	513	1195
Sample FE Convergence – calculation for radial displacement at pin rather than chord length									
FE C4 GM27.6	240	3	Shaly facies	P5	0.6	0.0	0.6	204	689
FE C7 GM44.2	240	3	Shaly facies	<b>P7</b>	<b>5.5</b>	<b>0.0</b>	<b>0.9</b>	<b>187</b>	<b>672</b>



### Tunnel convergence in excavations normal to bedding strike (sub-parallel $\sigma_{hmax}$ )

Short-term diametral strains for these excavations are typically small ( $\sim 0.5\%$ ) with the largest 0.8%. Convergence is also relatively isotropic. Long-term strains are less than 1.1%.

Tab. 5-6: Short-term (100 days) diametral strain from selected convergence arrays for excavations heading  $150^\circ$  normal to bedding strike.

Excavation TM	Dia-meter	Excavation	First data	Diametral strain %							
				4-2	4-3	1-3	5-1	5-2	Min	Mean	Max
Ga08 85	5	14/03/08	14/03/08	0.4	0.4	0.3	0.4	0.0	0.3	0.4	0.4
Ga08 75	5	05/03/08	06/03/08	0.3	0.6	0.4	0.8	0.2	0.2	0.5	0.8
Ga08 54	5	06/02/08	07/02/08	0.6	0.7	0.3	0.6	0.5	0.3	0.5	0.7

Tab. 5-7: Long-term (most recent data 08/08/13) diametral strain from selected convergence arrays for excavations heading  $150^\circ$  normal to bedding strike.

Excavation TM	Dia-meter	Excavation	First data	Diametral strain %							
				4-2	4-3	1-3	5-1	5-2	Min	Mean	Max
Ga08 85	5	14/03/08	14/03/08	1.1	0.8	0.6	0.8	0.8	0.6	0.8	1.1
Ga08 75	5	05/03/08	06/03/08	0.8	0.0	-0.3	-0.1	0.5	-0.3	0.2	0.8
Ga08 54	5	06/02/08	07/02/08	0.7	0.8	0.4	0.6	0.7	0.4	0.6	0.8

Time-dependent convergence rates for excavations normal to bedding strike are in the range 2 - 5 mm / ln(day).

### Tunnel convergence in excavations along bedding strike (sub-parallel $\sigma_{hmin}$ )

Short-term diametral strains for these excavations are larger along bedding strike ( $\sim 1\%$ ) with the largest 1.6%. Convergence is typically greatest normal to bedding (5-1 chord). Long-term convergences show further increases (max 1.7%).

Tab. 5-8: Short-term (100 days) diametral strain from selected convergence arrays for excavations heading  $240^\circ$  along to bedding strike.

Excavation TM	Dia-meter	Excavation	First data	Diametral strain %							
				4-2	4-3	1-3	5-1	5-2	Min	Mean	Max
MB 12	4.5	27/10/08	28/10/08	0.8	1.5	1.0	1.6	0.9	0.7	1.0	1.6
MB 4.5	4.5	16/10/08	17/10/08	0.7	1.0	0.6	1.4	1.2	0.6	0.9	1.3
Ga08 14.5	5	27/11/07	28/11/07	0.3	1.1	0.9	0.8	0.1	0.1	0.7	1.1
Ga04 40	5	13/09/04	13/09/04	0.5	0.9	0.4	0.9	0.5	0.4	0.7	0.9

Tab. 5-9: Long-term (most recent data 08/08/13) diametral strain from selected convergence arrays for excavations heading 150° normal to bedding strike.

Excavation TM	Dia-meter	Excavation	First data	Diametral strain %							
				4-2	4-3	1-3	5-1	5-2	Min	Mean	Max
MB 12	4.5	27/10/08	28/10/08	1.3	1.7	1.3	1.8	1.0	0.9	1.3	1.7
MB 4.5	4.5	16/10/08	17/10/08	0.8	1.0	0.7	1.5	1.4	0.6	1.0	1.4
Ga08 14.5	5	27/11/07	28/11/07	0.4	1.2	1.1	0.9	0.2	0.2	0.8	1.2
Ga04 40	5	13/09/04	13/09/04	0.6	1.1	0.5	1.1	0.7	0.5	0.8	1.1

Time-dependent convergence rates for excavations parallel to bedding strike are in the range 2 - 6 mm / ln (day).

### Measured pore pressure response

Near-field measurements of pore pressures close to advancing excavations have been consistently identified in experiments at Mont Terri (ED-B, EZ-B, HG-A, MB and FE). The measurements show:

- Systematic rise or fall of pore pressure according to location around the tunnel (relationship to stress field) due to coupled poro-elastic effects;
- Rapid pressure drop to atmospheric pressure in intervals connected to the open tunnel wall via the EDZ fracture network (MB, ED-B, FE);
- Pressure rise/drop and subsequent attenuation indicative of enhanced post-excavation permeability due to microfracturing/yielding, isolated fracturing or deformation of pre-existing features;
- Sustained sub-atmospheric pressure at EZ-B indicating partial saturation probably caused by dilation of the rock.

In the Mine-By Experiment almost all piezometer responses indicated that they are within the connected EDZ fracture network. In FE only one piezometer (the closest BFEA002-i6) showed this response while more distant piezometers remained above atmospheric pressure. The extent of the connected EDZ fracture network derived from the MB and FE responses is largely consistent with that derived from geological observations discussed in previous sections.

After excavation around the FE Gallery piezometers beyond 6 radii from the tunnel axis showed roughly constant pressure with only a small reduction from the undisturbed pore pressure observed prior to excavation (Fig. 5-8). Between radii 4 and 6 pressures were higher in BFE-A03 suggesting an anisotropic response. Between radii 3 and 4 there was no clear anisotropy between boreholes BFE-A02 and BFE-A05.

Many of the FE piezometer intervals located between 2 and 6 radii showed a deviation from the elastic models which may indicate yielding. Alternatively this may be due to some inadequacy in the elastic model due to a mismatch in the representation of anisotropy in stress or material properties.

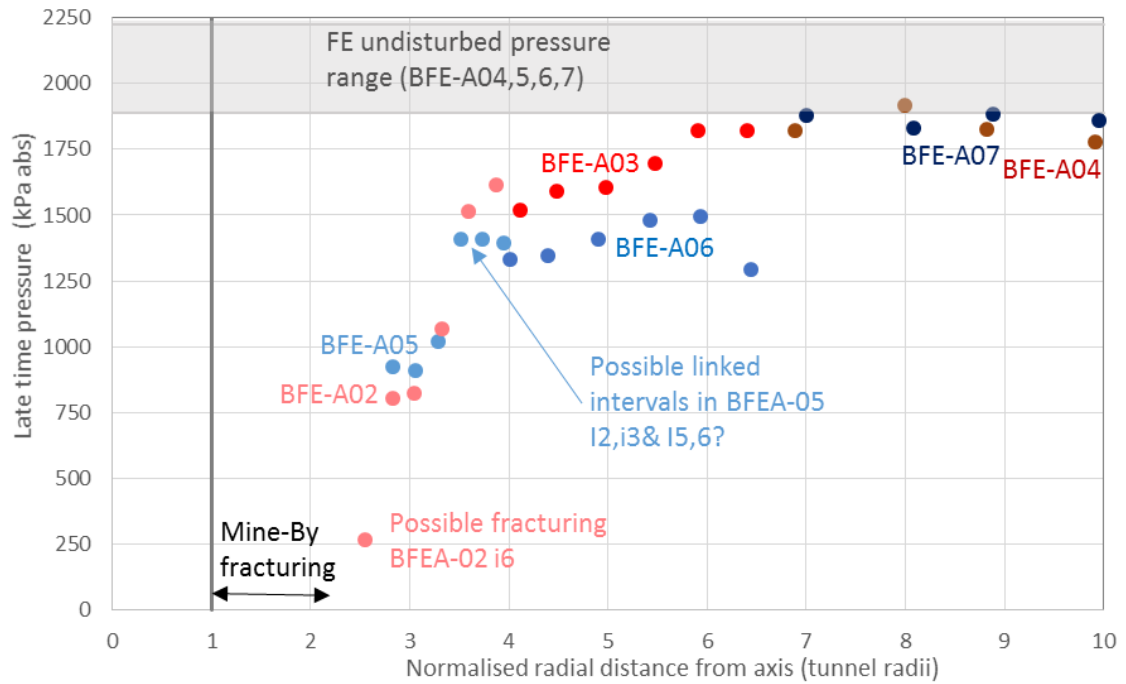


Fig. 5-8: Piezometer pressure (after excavation) as a function of normalised radial distance from the excavation axis.

**Extent of plastified zone**

Additional monitoring of deformation beyond convergence measurements has focused on the excavations parallel to bedding strike (EZ-A Niche, HG-A, MB Niche and FE Gallery). Measurements in the MB Niche and FE Gallery indicate that inelastic deformations are initiated within  $1-2a$  ahead of the face. Fig. 5-9 shows the normalised convergence from the Mine-By Experiment and comparison with an anisotropic elastic model (Martin et al. 2014b).

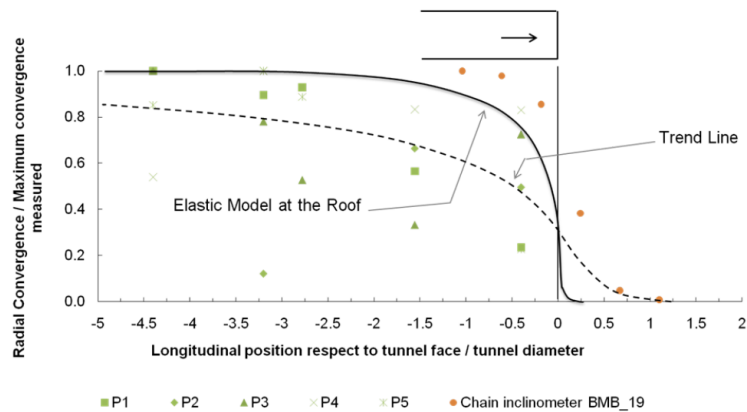


Fig. 5-9: Radial convergence normalised to maximum convergence. The data is compiled from all the instruments and only provides a trend.

Around the excavations, deformation measurements indicate yield to at least  $\sim 3 a$  from the tunnel wall while comparison of radial extensometers with the measured convergence indicates that the deformation field may extend beyond the length of the extensometers ( $MB \sim 3.5 a$ ). Short-term deformations are anisotropic with the strongest deformation around the tunnel occurring normal to bedding.

The pore pressure response around the FE Gallery also provides some constraint on the extent of inelastic deformation. There is no indication of significant yielding beyond  $6a$  (see Fig. 5-5) while piezometers in the direction normal to bedding showed lower pressures (and greater pressure drop) between  $4 - 6 a$ . Anisotropic elastic responses may also result in volume change and consequent pore pressure changes, so the extent of the zone of pore pressure reduction can provide only an upper limit to the yielding zone.

### 5.2.3 Further processes and phenomena during operations period

In the operations period of the Mont Terri URL, the prevailing ventilation conditions and the gravity driven pore water drainage towards the tunnel system have exhibited a significant impact on the development of the EDZ. Desiccation cracks are phenomena typically related to low humidity of the tunnel atmosphere and high ventilation rates (Fig. 5-10b). Cyclic deformation of the tunnel surface due to seasonal variations of humidity and temperature may lead to progressive degradation of the EDZ. Furthermore, activities during the operations phase may have enhanced the EDZ in the long-term (e.g., water uptake due to drilling programmes and/or during borehole instrumentation). EDZ-related phenomena during the operations phase are shown in Fig. 5-10. These phenomena are further discussed in subsequent paragraphs.

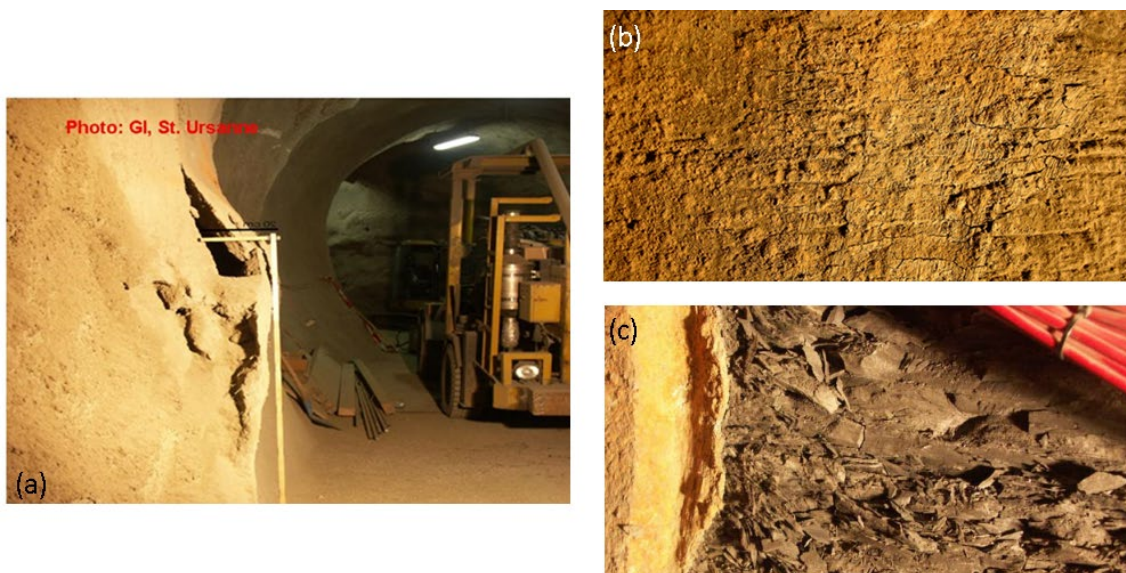


Fig. 5-10: EDZ-related phenomena in the Opalinus Clay during the operations phase of the Mont Terri URL.

(a) damage of the shotcrete liner caused by swelling and creep processes (Bossart & Thury 2007); (b) desiccation cracks at the tunnel wall of the HG-A microtunnel; (c) degradation of the Opalinus Clay caused by water uptake at the contact zone between liner and rock (HG-A microtunnel).

## Influence of ventilation

Martin & Lanyon (2003a) discuss:

- the response of a 600 mm vertical borehole that showed no evidence of breakouts (stress-induced yielding) until the borehole was closed and ventilation ceased which allowed the humidity to increase with associated weakening and softening.
- Possible variations in deformation (convergence measurements) due to seasonal changes in humidity.

Unlined small diameter excavations have demonstrated relatively long-term stability at the VE (normal to bedding strike) and HG-A (parallel to bedding strike) micro-tunnels (Mayor & Velasco 2008). The development and maintenance of a partially saturated zone around the tunnels appears to stabilize the rock.

Isolated drying cracks and other fractures have also been observed to open and close according to seasonal variations in tunnel ventilation as shown in Fig. 5-11. Geophysical monitoring of Gallery 04 (Lesparre et al. 2013) and EZ-B (Möri et al. 2012) also identified possible seasonal increases in resistivity but it was not possible to distinguish between competing processes to identify the mechanisms.

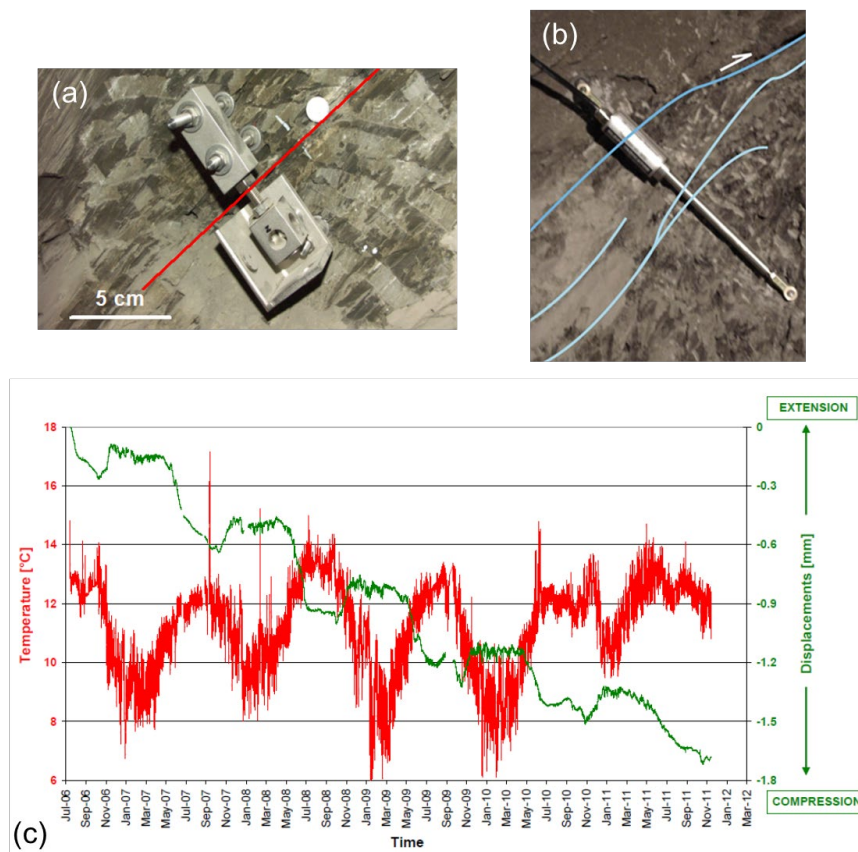


Fig. 5-11: Cyclic deformation experiment in the EZ-B Niche (Möri et al. 2012).

Monitoring of deformation at the tunnel wall with (a) a 3D jointmeter and (b) a crackmeter. (c) Variations of the relative humidity and fracture displacement (opening/extension and closing/compression) measured in the niche EZ-B.

In this context, Peron et al. (2010) developed a conceptual framework, addressing the damage induced by desiccation (i.e. drying, shrinkage and cracking). An advanced constitutive model was used, which relies on multi-mechanism hardening plasticity and on the notion of effective stress in partially saturated media. The results of numerical simulations clearly show the penetration of a drying front in response to the ventilation process. Stress path analyses of the tunnel near field during the simulated ventilation period lead to a possible tensile failure criterion with respect to suction.

### Self-sealing of EDZ fractures

A consistent pattern of self-sealing (Bock et al. 2010) has been observed during the resaturation of the fractured EDZ at Mont Terri:

- HG-A: long-term resaturation and hydraulic testing showed that the effective axial conductance of the EDZ reduced by several orders of magnitude over a period of three years (Lanyon et al. 2014).
- Mine-By Experiment: Repeat hydrotesting in boreholes close to the tunnel showed a significant increase in interval transmissivity immediately after excavation of the tunnel followed by a decrease of 0.5-2 orders of magnitude when testing was repeated 1.5 years later.
- EH Experiment: Repeat testing of the EDZ fracture network in the side-wall of Gallery 98 at GM84.5 showed that fracture transmissivities reduced by about two orders of magnitude over a period of two years and were continuing to do so (Meier et al. 2002; Bossart et al. 2004; Nussbaum et al. 2011). Further reduction due to loading was subsequently observed (Bernier et al. 2007a).
- Comparison between pneumatic and hydraulic tests performed using an MMPS system in the New Gallery as part of the EZ-A experiment (NG 151,154) showed significantly lower permeability to water than air (Fisch,2004; Lanyon 2005) with reductions between 1 and 3 orders of magnitude. Within the EZ-A experiment 10 short boreholes ( $\sim 2$  m) were drilled into the EDZ in the floor of the tunnel after injection tests using Pearson water traced with fluorescein. The cores showed a high density ( $\sim 10$  m<sup>-1</sup>) of induced or reactivated features in the first 40cm of rock. The surfaces of artificial fractures were notably wet and mapping identified self-sealing features as shown in Fig 5-12.

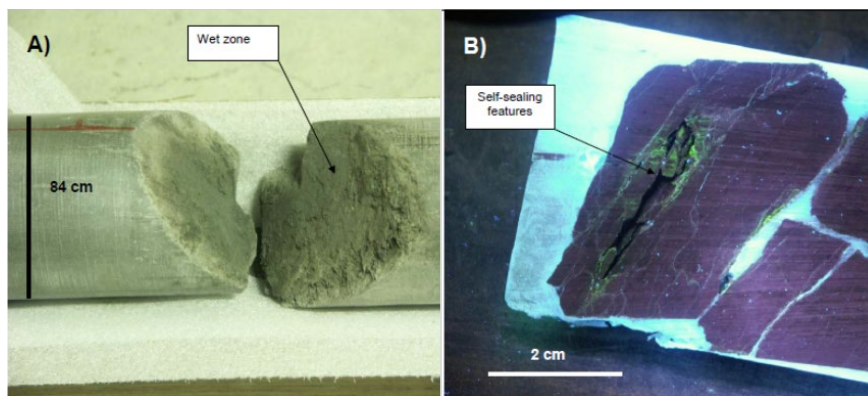


Fig. 5-12: Sample core from EZ-A boreholes.  
 (a) core showing wet zone along fracture; (b) self-sealing feature showing fluorescein dye from previous injection tests.

Alcolea et al. (2014) discuss the self-sealing process further and present an approach to simulating the resaturation and sealing of the EDZ around repository tunnels.

### Chemico-osmotic processes in the EDZ

Chemical processes occurring in the unsaturated EDZ are largely associated with salt precipitation (Mayor et al. 2007b) and development of an oxidation front (Vinsot et al. 2014) in the EDZ due to access to the atmosphere. Salt precipitation gives rise to osmotic suction when the EDZ re-saturates, although the impacts were found to be marginal. Migration of the oxidation front is controlled by the connected EDZ fracture system. Key indicators are gypsum precipitation (Bossart et al. 2004) and oxidised pyrite minerals as shown in Fig. 5-13 (from Mayor & Velasco 2008). Vinsot et al. (2014) comment that at Tournemire "Oxidation was not observed within the rock matrix at more than a few centimetres from a surface exposed to atmospheric air, even after more than 100 years of exposure."

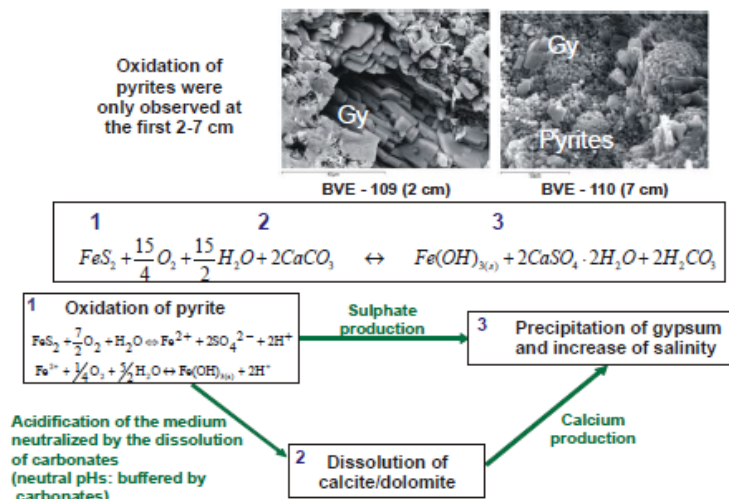


Fig. 5-13: Geochemical processes near the microtunnel wall from Mayor & Velasco (2008).

### 5.2.4 Synopsis of empirical and experimental evidence from Mont Terri

Empirical and experimental evidence from various experimental sites in the Mont Terri URL was compiled and subjected to an integrated interpretation, aimed at developing a conceptual model of the creation of the EDZ in response to the excavation process and its evolution during operations phase. The main findings are:

- Excavation-related failure is associated with brittle fracture processes and slip on pre-existing structures (Amann et al. 2011a, b). The observed EDZ fracture patterns are anisotropic and affected by bedding orientation and stress direction.
- Significant convergence has been observed in response to excavation. Convergence is typically larger for tunnels oriented parallel to bedding strike and  $\sigma_h$ . This is likely to be due to failure mechanisms associated with the rock mass anisotropy rather than stress anisotropy as stress anisotropy is expected to be greater in the direction parallel to  $\sigma_H$ .

- Significant pore pressure responses to excavation have been observed (where monitored) and are to be expected given the very low permeability of the rock. Short-term responses around small diameter excavations are strongly anisotropic (side-wall vs roof) due to stress anisotropy (HG-A). Longer term large-scale responses show weaker anisotropy probably affected by both rock mass permeability and stiffness anisotropy.
- There is evidence for extensive (greater than a diameter) yield zones around excavations and boreholes parallel to bedding strike. In the Mine-By Niche it was possible to identify the onset of plastic yield about 1 tunnel radius ahead of the face, but it was not possible to determine the extent of the yield zone around the excavation due to the limited length of radial extensometers. Further comparison of tunnel convergence with data from radial extensometers typically suggests that the radial extensometers do not capture all the inelastic deformation.
- The influence of ventilation (matric suction) and chemico-osmotic phenomena (osmotic suction) on long-term stability has been previously identified (Martin & Lanyon 2003a; Blümling et al. 2007; Ferrari et al. 2014) for boreholes and micro-tunnels. This supports the need to address processes associated with partial saturation and pore water chemistry and to consider a suitable effective stress framework.

### 5.3 Conceptual framework for modelling the excavation response

Modelling of the excavation response of the rock mass at Mont Terri has been performed as an integrated part of many experiments. Modelling objectives have typically related to the specific goals of each experiment. In addition collaborative modelling has been performed within a range of international projects such as NF-PRO (Aranyossy et al. 2008), DECOVALEX, SELFRAC / TIMODAZ (Bernier et al. 2007a) and FORGE (Harrington 2014). A range of modelling codes has been used from isotropic elastic boundary element codes to anisotropic HM coupled continuum elasto-plastic and FEMDEM codes (Lisjak et al. 2014).

In this study, the focus of model analyses is on the transferability of the excavation response of the Opalinus Clay from Mont Terri to the geological conditions in the candidate siting regions of Northern Switzerland. For the assessment of the engineering feasibility of a deep geological repository in Northern Switzerland, an aspect of special significance is the estimation of the extent and shape of the EDZ around the underground structures in the Opalinus Clay at a repository depth of 700 m and more. In the transferability approach presented in Chapter 6, site specific aspects such as the local pore pressure and stress conditions in the siting regions at repository level have to be defined by site specific boundary and initial conditions, respectively. On the other hand, rock specific characteristics of the Opalinus Clay such as the general rock fabric, constitutive behaviour and the pore pressure coupling can be transferred from Mont Terri to the geological conditions in Northern Switzerland.

#### 5.3.1 Conceptualization of the rock fabric

The fabric of the Opalinus Clay includes structural elements at a range of scales, associated with both sedimentary and tectonic processes. Sedimentary features depend on the depositional environment and provide information on the geological conditions at the time of deposition. Tectonic features provide information on the orientation and magnitude of the strains that have affected the rock in the course of its tectonic history. At Mont Terri, the sedimentary and tectonic features have been characterized in great detail in terms of spatial variability and anisotropy (Fig. 5-14). A brief summary of the inventory of structural features is given in the following sections.

The fabric of the Opalinus Clay at Mont Terri shows significant variability at a range of scales:

- Millimetre-scale: layering of silts and bioclasts due to flocculation and bioturbation;
- Centimetre-scale: silty quartz-rich lenses and diagenetic siderite concretions (Wenk & Voltolini 2008);
- Metre-scale: tectonic features associated with the anticlinal deformation with spacing from ~ 0.05-5 m: depending on location and facies. These features are typically sealed and show no hydraulic influence but are likely to vary in stiffness and strength from the undisturbed rock. The dominant set is SE-dipping bedding-parallel (Nussbaum et al. 2011);
- At 10s of metres: variation in rock facies due to changes in sedimentary environment and the influence of larger scale tectonic structures (Main Fault).

It is likely that core-scale investigations will only capture the effect of variability at the smallest (sub metric) scales.

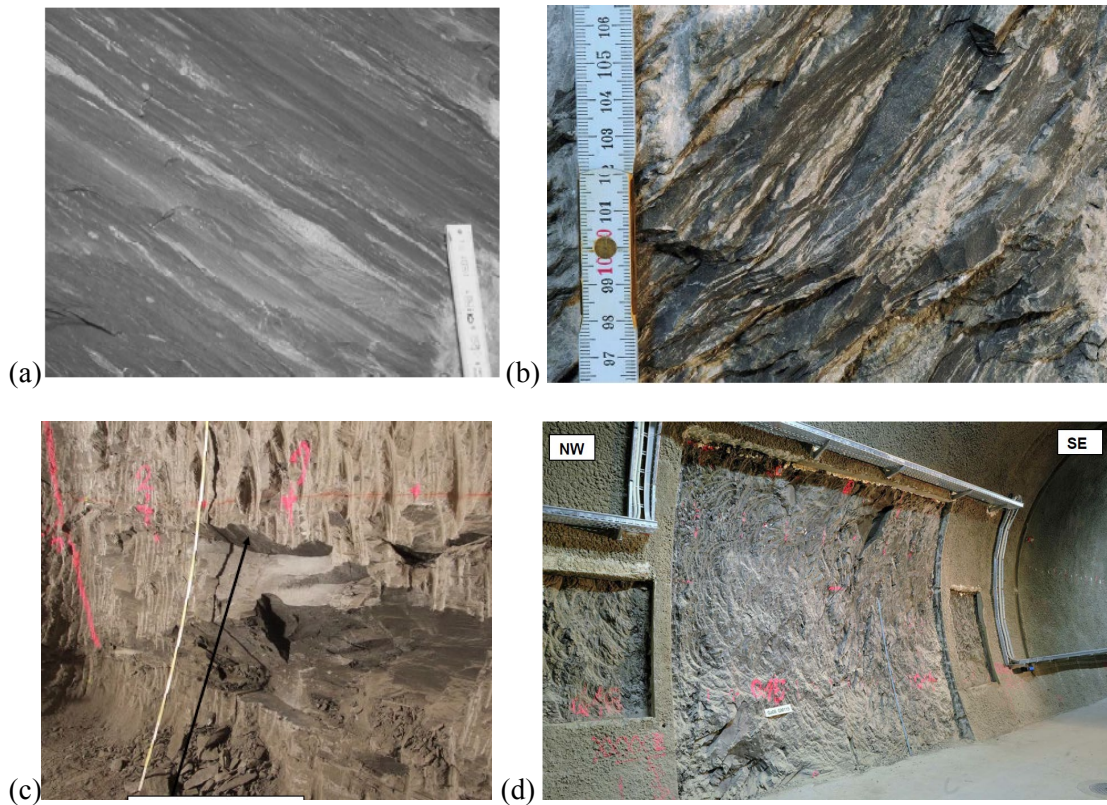


Fig. 5-14: Heterogeneity and anisotropy in the Opalinus Clay at Mont Terri:

a) millimetre-scale: interstratified sandy lenses (Yong 2008); b) layering in the sandy facies Gallery 08; c) SE dipping fault bedding-parallel planes in the face of Gallery 08; d) the Main Fault intersecting Gallery 08 in window through shotcrete (Nussbaum et al. 2011).

Given the aforementioned scale-dependent categories of structural features, it is evident that the classification of the rock fabric in terms of heterogeneity and anisotropy is a matter of scale. In the context of tunnel near field studies, the relevant scales range between decimeters and decameters.

The inventory of sedimentary features in the Opalinus Clay at Mont Terri contains three facies (sandy, shaly, carbon-rich sandy), exhibiting on the scale of interest a somewhat homogeneous fabric with distinct transversal isotropy normal to bedding. The mechanical and hydraulic properties of the sandy and clay-rich sequences are mainly controlled by their mineral composition and their grain size distribution, classifying the rock in the transition between sandy-silty claystone and clay-rich siltstone with moderate strength and low to moderate plasticity (Giger & Marschall 2014).

The inventory of tectonic structures may be classified as inhomogeneous (e.g., distinct clustering of shear planes along the Main Fault) and orthotropic. The three directions of anisotropy are given by the SSE-dipping fault planes, sub-parallel to bedding planes; the low angle to flat lying S- to SW-dipping fault planes and the W- to WNW-dipping fault planes.

Fig. 5-15 displays a schematic sketch representing possible abstractions of the fabric of the Opalinus Clay, which can be implemented in numerical models. Notably, the abstraction process is a critical step in the model set-up, because it affects the formulation of the constitutive behaviour of the rock. Consequently, the abstraction of the fabric is associated with significant conceptual uncertainties related to the sub-scale deformation behaviour of the rock (e.g., strain localization, pore pressure dissipation). With regard to the transferability of modelling results from Mont Terri to the candidate siting regions in Northern Switzerland, an inadequate representation of the fabric could lead to biased conclusions. Hence, an adequate spectrum of possible fabric abstractions of the Opalinus Clay should be considered, representative of the inventory of structural features expected in the siting regions in Northern Switzerland.

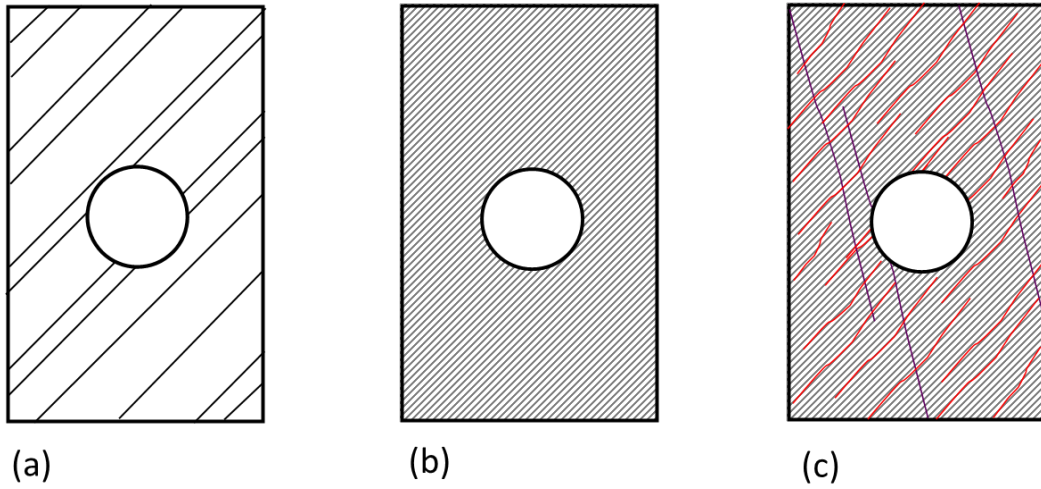


Fig. 5-15: Complementary examples for the abstraction of the rock fabric of the Opalinus Clay at the tunnel scale.

(a) The inclined sandy and clay-rich layers of the 3 facies display a rather uniform mineral content; the layer boundaries are associated with discontinuities of mechanical (and hydraulic) properties. (b) The sandy and clay-rich beds of the sedimentary structures are represented by a homogeneous transversal isotropic continuum. (c) Composite model, consisting of several orthotropic families of tectonic structures, superimposing the stratified rock matrix (represented as a transversal isotropic continuum). The fracture systems are described in stochastic or deterministic frameworks.

### 5.3.2 Conceptualization of deformation behaviour

#### Elastic response

Understanding of the elastic response of the rock mass is of paramount importance for the interpretation of the excavation-induced phenomena and processes at Mont Terri as discussed in Chapter 5.2 (tunnel convergence, pore pressure perturbation, far-reaching strain increments). In this context, the effect of anisotropic stiffness is worth investigating in depth.

After Graham & Houlsby (1983) the transversal isotropy can be expressed in terms of 5 independent elastic variables, namely Young’s modulus  $E_v$  and  $E_h$  parallel and normal to bedding and the directional Poisson’s ratios  $\nu_{hh}$  and  $\nu_{vh}$  and the component  $G_{vh}$  of the directional shear modulus (see also Nagra 2014b / Dossier IV).

Thus, the compliance matrix describing the volumetric strain  $\epsilon_v$  and the shear strain  $\epsilon_s$  in response to the stress components  $p'$  and  $q$ , can be written as:

$$\begin{Bmatrix} \epsilon_v \\ \epsilon_s \end{Bmatrix} = \begin{bmatrix} 1/K & -1/J \\ -1/J & 1/3G \end{bmatrix} \begin{Bmatrix} p' \\ q \end{Bmatrix} \tag{5-1}$$

where

$$\frac{1}{K} = 2 \frac{1 - \nu_{hh}}{E_h} + \frac{1 - 4\nu_{vh}}{E_v} \tag{5-2}$$

$$\frac{1}{J} = \frac{2}{3} \left( \frac{1 - \nu_{hh}}{E_h} - \frac{1 - \nu_{vh}}{E_v} \right) \quad (5-3)$$

$$\frac{1}{G} = \frac{2}{3} \left( \frac{1 - \nu_{hh}}{E_h} + 2 \frac{1 + 2\nu_{vh}}{E_v} \right) \quad (5-4)$$

Correspondingly, the stiffness matrix describes the mean effective stress  $p'$ , and the deviator stress in response to volumetric strains and shear strains:

$$\begin{Bmatrix} p' \\ q \end{Bmatrix} = \begin{bmatrix} K^* & -J^* \\ -J^* & 3G^* \end{bmatrix} \begin{Bmatrix} \varepsilon_v \\ \varepsilon_s \end{Bmatrix} \quad (5-5a)$$

where

$$K^* = \frac{1}{3GD}; G^* = \frac{1}{3KD}; \quad J^* = -\frac{1}{JD}; \quad D = \frac{1}{3GK} - \frac{1}{J^2} \quad (5-5b)$$

In this context the anisotropy factor A is defined as:

$$A = \sqrt{E_h/E_v} \quad (5-6)$$

The high significance of anisotropic stiffness to the creation and evolution of the EDZ can easily be deduced from Equations 5-1 and 5-6. Thus, a strong elastic anisotropy, expressed in terms of a high magnitude of the cross-coupling parameter J, gives rise to high effective stresses and pore pressures respectively, as a consequence of elastic shear strains around the newly excavated tunnel. Far-reaching zones of increased pore pressure may develop, associated with a reduction of effective stress. Progressive failure occurs in the over-pressurized zones when the shear stresses exceed the undrained strength of the rock. The reach of the over-pressurized zone is controlled by the magnitude of the cross-coupling parameter J.

The elastic behaviour of unfractured intact Opalinus Clay samples from Mont Terri has been characterized using undrained triaxial tests and drained compression tests. Drawing on a diagnostic analysis of the available databases from Mont Terri and from other sites, Giger & Marschall (2014) conclude:

- Young's modulus increases with increasing mean effective stress;
- Samples from Mont Terri exhibit E-values which are lower by a factor of 2 than those from core samples from the geothermal well Schlattigen-1 (recovered from a depth of more than 800 m);
- Elastic properties exhibit a clear anisotropic behaviour. The magnitude of the E-modulus parallel to bedding is two times higher than parallel to bedding.

An unequivocal dependence of the elastic properties with the mineralogical composition could not be derived due to the limited amount of reliable data from the sandy facies. Nevertheless, the available evidence seems to confirm that the sandy facies is generally stiffer than the shaly facies. Reference values of the anisotropic Young's modulus and Poisson ratio derived from laboratory tests on core samples from Mont Terri and Schlattingen are given in Tab. 5-10.

Tab. 5-10: Reference values of the anisotropic Young's modulus and Poisson's ratio (after Giger & Marschall 2014).

Derived from Opalinus Clay samples from Mont Terri and from the geothermal well Schlattingen-1. The table is complemented with the corresponding parameters A, K\*, G\* and S of the transversal isotropic stiffness tensor according to Graham & Housby (1983).

Parameter	Mont Terri		Benken/Schlattingen	
	Value $\parallel$	Value $\perp$	Value $\parallel$	Value $\perp$
Young's modulus [GPa]	$E_h = 8$	$E_v = 4$	$E_h = 18$	$E_v = 9$
Poisson ratio $\nu$ [-]	$\nu_{hh} = 0.35$	$\nu_{hv} = 0.25$ $\nu_{vh} = 0.125$	$\nu_{hh} = 0.27$	$\nu_{hv} = 0.27$ $\nu_{vh} = 0.135$
Elastic anisotropy $A = \sqrt{E_h / E_v}$ [-]	$\sqrt{2}$		$\sqrt{2}$	
Effective bulk modulus K* [GPa]	4.37		9.0	
Effective shear modulus G* [GPa]	2.93		6.10	
Cross-coupling coefficient J [GPa]	2.80		5.12	

Despite the fact that the intact matrix of the Opalinus Clay exhibits a certain degree of elastic anisotropy, the estimated magnitude of the cross-coupling coefficient J seems to be too low to explain the far-reaching damage zones in the MB Experiment, reported in Chapter 4. For Mont Terri, the magnitude of the J-value is around 2 GPa, corresponding to about half of the bulk modulus. Accordingly, the pore pressure effect of elastic shear strains is expected to be lower than the corresponding impact of volumetric strains.

The composite rock mass, comprising the intact matrix and the orthotropic network of fractures, can add a significant additional component of elastic anisotropy. In a fractured rock with high fracture density and low fracture stiffness, the elastic behaviour of the fractures dominates the rock mass stiffness. Fig. 5-16 depicts three typical stiffness models, aimed at describing the elastic behaviour of a fractured rock with infinitesimal and finite joint thickness, respectively. Typical values of normal stiffness in the order of 8 GPa/m have been reported for the Opalinus Clay at Mont Terri. Assuming a mean joint spacing of 0.2 – 0.25 m, the infinitesimal joint thickness model (Fig. 5-16a) would suggest an effective Young's modulus  $E_{RM}$  perpendicular to bedding in the order of 0.6 – 0.8 GPa, corresponding to an anisotropy coefficient of around 2.5 according to Equation 5-6.

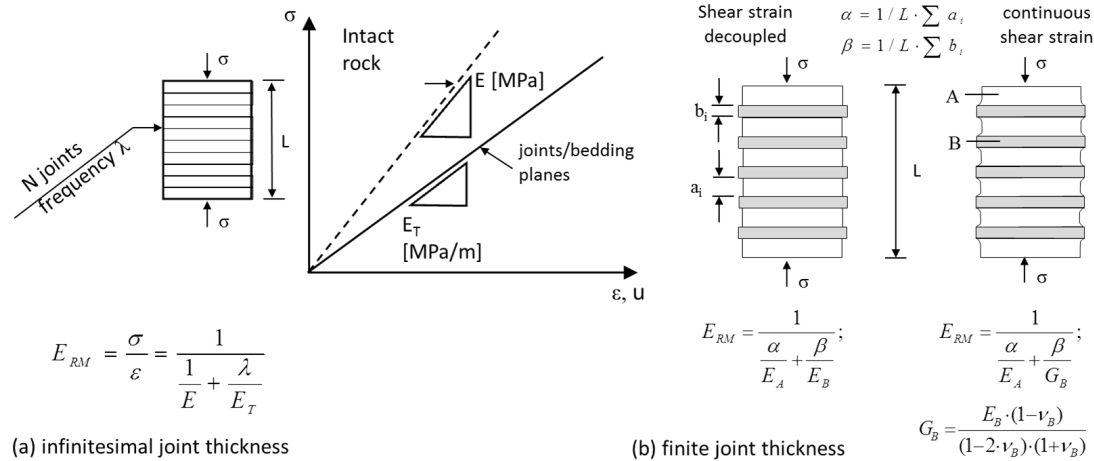


Fig. 5-16: Complementary stiffness models of a fractured rock mass.

(a) effective Young’s modulus  $E_{RM}$  normal to the fracture orientation, assuming an infinitesimal joint thickness; (b) effective  $E_{RM}$  modulus of a rock mass with finite fracture thickness. Two complementary strain conditions may apply perpendicular to the joint planes: detachment of the joint surfaces and continuity of shear strain.

**Plastic response**

The transition from elastic (reversible) to plastic (irreversible) deformation in response to external stresses is associated with significant changes in the hydraulic and mechanical properties of the rock. Constitutive laws are formulated to predict the evolution of the hydromechanical rock properties when yielding. A constitutive framework, which is based on the "critical state concept" (e.g. Azizi 1999), has been applied successfully to describe the elasto-plastic deformation behaviour of the Opalinus Clay both in the normally and overconsolidated state for a wide range of stress paths (Giger & Marschall 2014). Simplified constitutive models, drawing on the Mohr-Coulomb failure criterion were deduced for modelling shear and tensile failure of the Opalinus Clay in the overconsolidated state (Hvorslev yield surface). Thus, in the overconsolidated state, the (peak) strength of the Opalinus Clay can be expressed by a linear equation, which relates the shear stress at failure  $\tau_f$  to the normal stress  $\sigma_n'$ , acting on a potential failure plane:

$$\tau_f = c' + \sigma_n' \cdot \tan \varphi' \tag{5-7}$$

where  $\varphi'$  represents the peak angle of friction and  $c'$  is referred to as apparent cohesion. Note that normal stress, cohesion and friction angle are defined in an effective stress framework.

Drawing on the conceptualization of the rock fabric of the Opalinus Clay according to Chapter 5.3.1, the effect of heterogeneity originating from the sedimentary and tectonic structures can be described in the simplest case by "transverse isotropy", and the shear strength can be described as a function of the angle to bedding as shown in Fig. 5-17. Strength anisotropy is typically associated with failure along planes of weakness, corresponding to specimens oriented at 30-60° to bedding. Fig 5-17 shows the concept and estimated UCS from the Opalinus Clay (Giger & Marschall 2014). Minimum strength is associated with samples at about 30° to bedding. Single plane of weakness theory (Harrison & Hudson 1997) would predict minimum strength to be associated with an angle of  $45 - \varphi/2^\circ$  to bedding. For a discussion of expected failure modes with sample angle see Tang & Hudson (2012).

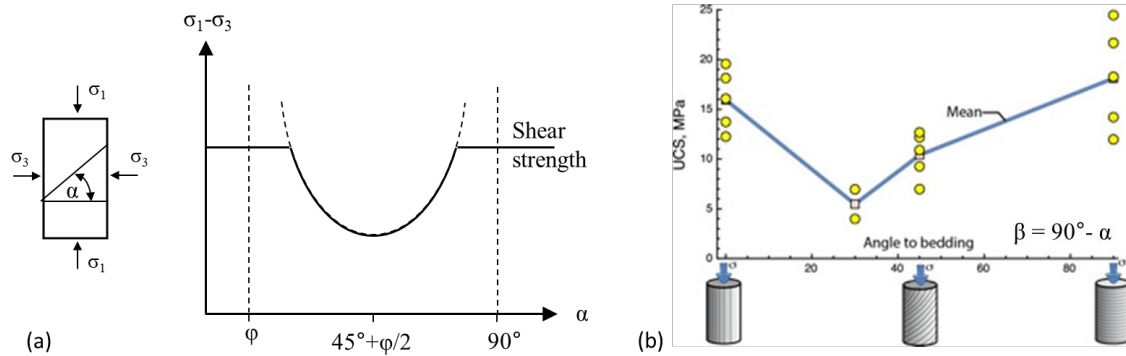


Fig. 5-17: Strength anisotropy caused by bedding and / or sub-parallel fractures. (a) concept; (b) UCS versus sample angle to bedding from the Opalinus Clay.

### 5.3.3 Effective stress framework

Unified formulations of the stress variables of porous materials have been developed through the requirements of numerical modelling. The complexity of the porous medium, which is likely to be fully or partially filled with fluids of a different nature to the skeleton matrix, termed ‘solid phase’, call for an approach for homogenization of the phases in order to obtain an equivalent macroscopic continuum. Thus, the elastic or elastic–plastic deformations are supposed to be directly linked to changes in the macroscopic stress quantity. Effective stress concepts have been widely used and validated in geotechnical applications. In the context of EDZ-related studies, the extension of effective stress concepts to unsaturated behaviour is of special interest, when long-term deformation behaviour during the operational phase is considered. Nuth & Laloui (2008) provide a synopsis of the common conceptual frameworks.

According to Terzaghi the effective stress principle for incompressible geomaterials saturated with (incompressible) water, can be formulated as follows:

- i. All measurable effects of a change of stress of the geomaterial, that is, compression, distortion and change of shearing resistance, are exclusively due to changes in effective stress.
- ii. The effective stress  $\sigma_{i,j}'$  is defined as:

$$\sigma_{i,j}' = \sigma_{i,j} - u_w \cdot \delta_{i,j} \tag{5-8}$$

where  $u_w$  represents the pore water pressure and  $\delta_{i,j}$  the Kroenecker’s operator.

In a strict sense, Terzaghi’s effective stress formulation represents only the particular case of saturated geomaterials with incompressible skeleton and a pore space completely filled with incompressible fluid. Assuming a finite compressibility of the solid constituents  $C_s$  and a drained bulk compressibility of the solid skeleton  $C$ , the effective stress concept can be extended:

$$\sigma_{i,j}' = \sigma_{i,j} - \alpha_w \cdot u_w \cdot \delta_{i,j} \tag{5-9}$$

where the poroelastic coupling coefficient

$$\alpha_w = 1 - \frac{C_s}{C} \quad (5-10)$$

In unsaturated porous media the effective stress has been defined by Bishop as ‘a function of the total stress and the pore pressure which controls the mechanical effects of a change in stress’, the goal being once more to convert a multiphase and multistress medium into a mechanically equivalent single phase and stress state continuum. According to Bishop the effective stress in a partially saturated porous medium is defined as the excess of total stress  $\sigma_{i,j}$  over an equivalent pore pressure  $u^*$ , given as  $\sigma'_{i,j} = \sigma_{i,j} - u^* \cdot \delta_{i,j}$ . The quantity  $u^*$  is considered as that portion of the effective stress in the geomaterial resulting from the pressure of all fluids in the pores. Defining  $u_a$  as the interstitial air pressure in addition to the pore water pressure  $u_w$ , Bishop’s stress takes the peculiar following form:

$$\sigma'_{i,j} = (\sigma_{i,j} - u_a \cdot \delta_{i,j}) + \chi \cdot (u_a - u_w) \cdot \delta_{i,j} \quad (5-11)$$

where  $\chi$  is called the effective stress parameter or Bishop’s parameter. The term

$$s = u_a - u_w \quad (5-12)$$

is called matric suction. Bishop’s effective stress parameter  $\chi$  is a characteristic property of the geomaterial, which depends on the degree of saturation. In the absence of material-specific experimental characterizations, the following identity has been widely accepted as a good estimator of Bishop’s parameter:

$$\chi = S_w \quad (5-13)$$

where  $S_w$  represents the water saturation of the geomaterial. In a partially saturated porous medium, the water saturation is expressed in terms of the gas ( $S_g$ ) or air saturation ( $S_a$ ) by the simple relationship  $S_g = S_a = 1 - S_w$ .

$$\sigma'_{i,j} = \sigma_{i,j} - (S_a \cdot u_a - S_w \cdot u_w) \cdot \delta_{i,j} \quad (5-14)$$

Equation (5-14) presents an elegant formulation of the effective stress of an unsaturated porous medium as total stress minus the sum of the products of saturation multiplied by the pressure of the mobile phases.



## 6 Transferability approach

### 6.1 Motivation and expected deliverables

The evaluation of tunnel stability has been the subject of elaborate repository design studies in the framework of Stage 2 of the Sectoral Plan. Several investigations on engineering feasibility were designed to assess the maximum allowable repository depth for a deep geological repository in the proposed siting regions. In terms of long-term safety assessment, hydraulic significance of the EDZ as a viable release path for radionuclides after repository closure was a major consideration. The engineering and safety requirements led to the specification of a number of EDZ related performance indicators, comprising:

- The allowable *convergence of the cavities* during construction and operational period (Nagra 2014a). In this context, short-term tunnel convergence is significant to the general stability assessment, whereas long-term convergence ("creep") is largely related to the serviceability of the underground structures.
- The *extent and shape of the plastified zone* (EDZ). From a long-term safety perspective, the plastified zone must not decrease the thickness of the intact host rock, such that its safety function as a transport barrier for radionuclides is markedly reduced (Nagra 2014c).
- The *maximum hydraulic conductance* of the EDZ after backfilling of the repository. Safety related simulations (Nagra 2014c) suggest that the radionuclide transport in the EDZ of the backfilled repository structures is not significant when the effective hydraulic conductivity of the EDZ remains below  $1\text{E-}8$  m/s (corresponding to an equivalent thickness of the EDZ of 1 m).

To prove the applicability of the specified performance indicators, a robust and traceable workflow was needed to transfer existing knowledge from Mont Terri and other underground structures in clay-rich formations to the geological conditions in the siting regions of Northern Switzerland. The conceptual framework had to satisfy the following conditions:

- Consistency with in-situ observations at existing underground structures (EDZ-related phenomena, hydromechanical processes, excavation-induced structural features);
- Proof of concept (model validation) by back-analysis of dedicated in situ experiments such as Mine-By tests;
- Demonstration of transferability to the geotechnical conditions in the candidate siting regions.

Drawing on the broad experimental database from the Mont Terri URL, a consistent conceptual framework has been developed in Chapter 5, referring to the key features and phenomena which control the creation and evolution of the EDZ in the Opalinus Clay. The role of anisotropic strength and stiffness of the Opalinus Clay was highlighted. Furthermore, the impact of anisotropic stress conditions and the tectonic setting on the shape and extent of the EDZ was discussed.

This chapter presents an appraisal for transferring the conceptualization of the EDZ to the conditions which are met in the candidate siting regions of Northern Switzerland at a typical repository depth between 500 and 900 m. In this context, transferability concerns the state conditions (pore pressures, stress state), the rock properties and associated anisotropy (strength, stiffness, hydraulic parameters) and the adaptation of the setting of the underground structures (tunnel diameters, shapes of cross-sections, orientations). A simplified 2-D modelling approach has been used, which allows for a wide spectrum of repository settings, simulation of the

convergence strains together with the shape and extent of the yield zone. Based on the model results, nomograms of plastic convergence strain have been developed, which are applicable to the different geological settings in the candidate siting regions.

## 6.2 Geological setting in the siting regions

### 6.2.1 Depth distribution and tectonic regime in Northern Switzerland

Opalinus Clay was proposed as a host rock for L/ILW and HLW in geological siting regions in Northern Switzerland approximately 50 to 100 km east of the Mont Terri URL (Nagra 2008) (Fig. 6-1). The median proposed repository depth in Opalinus Clay in these regions varies between 400 and 800 m (Tab. 6-1), which is significantly deeper than the 250 to 300 m of overburden at the Mont Terri URL.

Tab. 6-1: Overburden depth of the Opalinus Clay in the siting regions of Northern Switzerland (after Nagra 2010).

Siting region	min	max	median
Südranden (SR)	310	410	380
Jura Ost (JO)	300	510	410
Jura-Südfuss (JS)	490	700	560
Zürich Nordost (ZNO)	570	850	700
Nördlich Lägern (NL)	700	910	810

The tectonic history for Opalinus Clay at Mont Terri is somewhat different from its location further to the east in the siting areas of Northern Switzerland. At Mont Terri, maximum burial of Opalinus Clay is thought to have been reached in Cretaceous time with a depth of approximately 1350 m (Nagra 2002). In the siting areas of Northern Switzerland maximum burial was probably only reached in late Tertiary with an estimated depth range of 1500 and 1700 m (Nagra 2002). Comparison between maximum and current burial depth also indicates that the overconsolidation ratio (OCR) of Opalinus Clay at Mont Terri is greater (OCR  $\approx$  3-5) than in the siting regions of Northern Switzerland (OCR  $\approx$  2-4).

Tectonic overprint of Opalinus Clay is also different between Mont Terri and the siting areas of Northern Switzerland, and also between the different geological siting areas (Figs. 6-1 & 6-2). The URL Mont Terri is located in the south-eastern limb of the Mont Terri anticline and tectonically belongs to the Folded Jura of the detached Alpine foreland (Fig. 6-2). The total accommodated shortening by the Mont Terri anticline is estimated to equate to 2km (Nussbaum et al. 2011). Based on restoration of balanced cross sections it can be estimated that Miocene shortening in Northern Switzerland was also of the order of several hundred meters (Nördlich Lägern, Jura Ost) to kilometers (Jura-Südfuss) (Dossier II, Nagra 2014b). However the siting areas are not located within the strongly deformed Folded Jura, but in the (deformed) Tabular Jura and the Subjuristic Zone.

Structural analysis of Opalinus Clay cores also indicate a greater frequency of fractures in wells from the Subjuristic zone (Schafisheim) and partly from the Deformed Tabular Jura (Riniken) than in wells in the Eastern Tabular Jura further to the east (Benken). Although this observation is broadly restricted to the lowermost 10 to 30 m of the broadly 100 m thick Opalinus Clay (cf. Ebert 2014), it must be expected that structural integrity of Opalinus Clay in the geological siting areas of Northern Switzerland is variable.

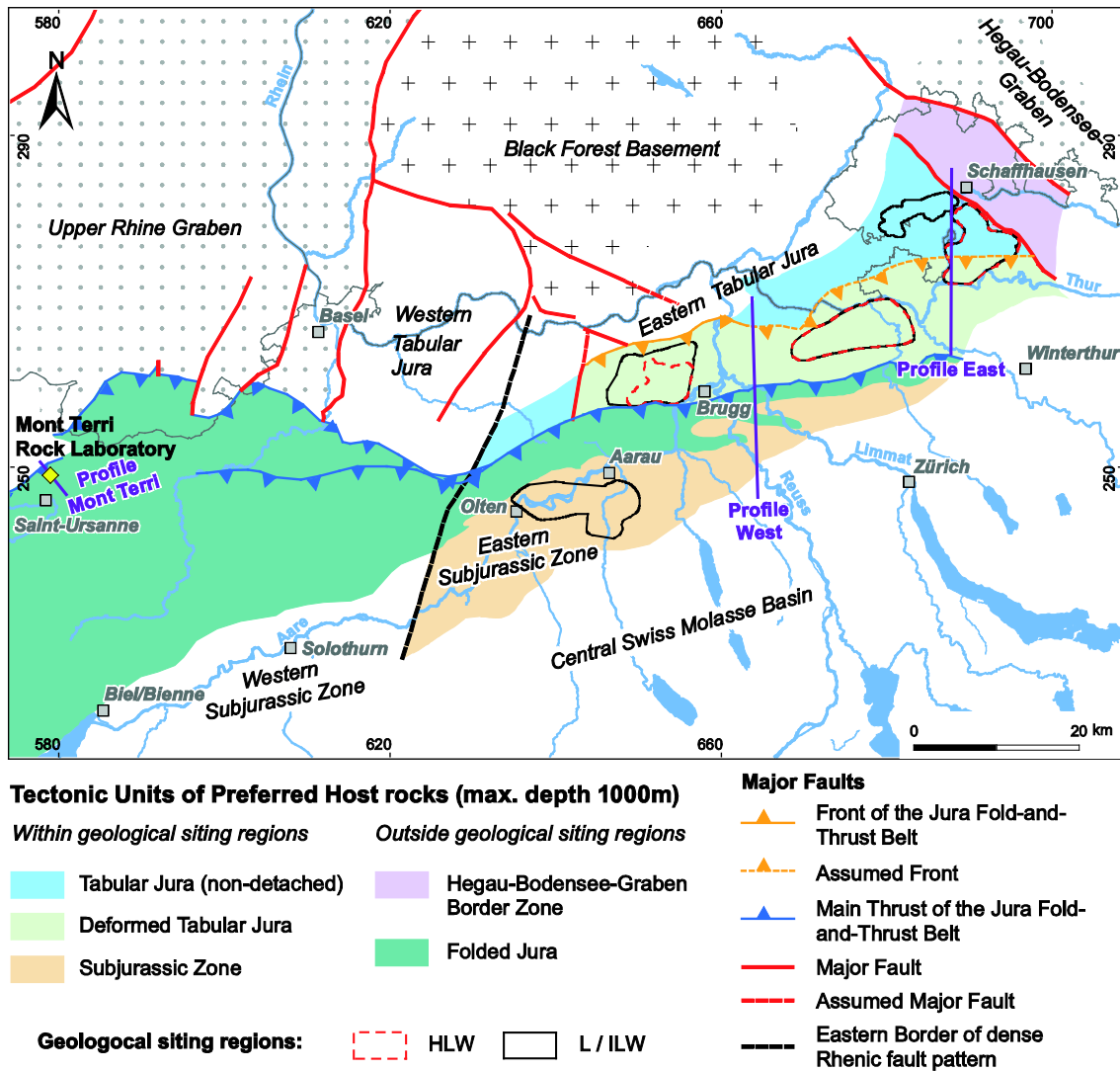


Fig. 6-1: Tectonic units of the proposed geological siting regions in Northern Switzerland. Profile sections are provided in Fig. 6-2.

### **6.2.2 Stress conditions in the siting regions**

Based on analyses of borehole breakouts in deep wells and focal mechanisms of earthquakes, the derived orientation of the maximum horizontal stress magnitude (SH) in Northern Switzerland appears to be fairly consistent in a NNW-SSE direction with a mean azimuth of  $160^{\circ} \pm 21^{\circ}$  (Heidbach & Reinecker 2013) (Fig. 6-3). In Western Switzerland and including the URL Mont Terri, the dominant direction of SH rotates slightly anticlockwise in a NW-SE direction.

Absolute stress magnitude data at greater depth is very scarce for Northern Switzerland (c.f. yellow points in Fig.6-2). Minimum and estimated maximum horizontal stress magnitudes were constrained by hydraulic fracturing at the borehole of Benken in the siting region of Zürich Nordost, and approximately 10km further to the east in a well near the village of Schlattingen (cf. Giger & Marschall 2014 for summary). Finally, hydraulic fracturing for derivation of stress magnitudes was also performed in a well of the geological siting region of Jura Ost, but only to a depth of 340 m b.g. (Klee & Becker 2013). The magnitude data suggest that although the orientation of SH is comparable for Mont Terri and the geological siting regions of Northern Switzerland, the stress regime for the Opalinus Clay varies from transtension in Mont Terri, to strike slip in Benken (Zürich Nordost).

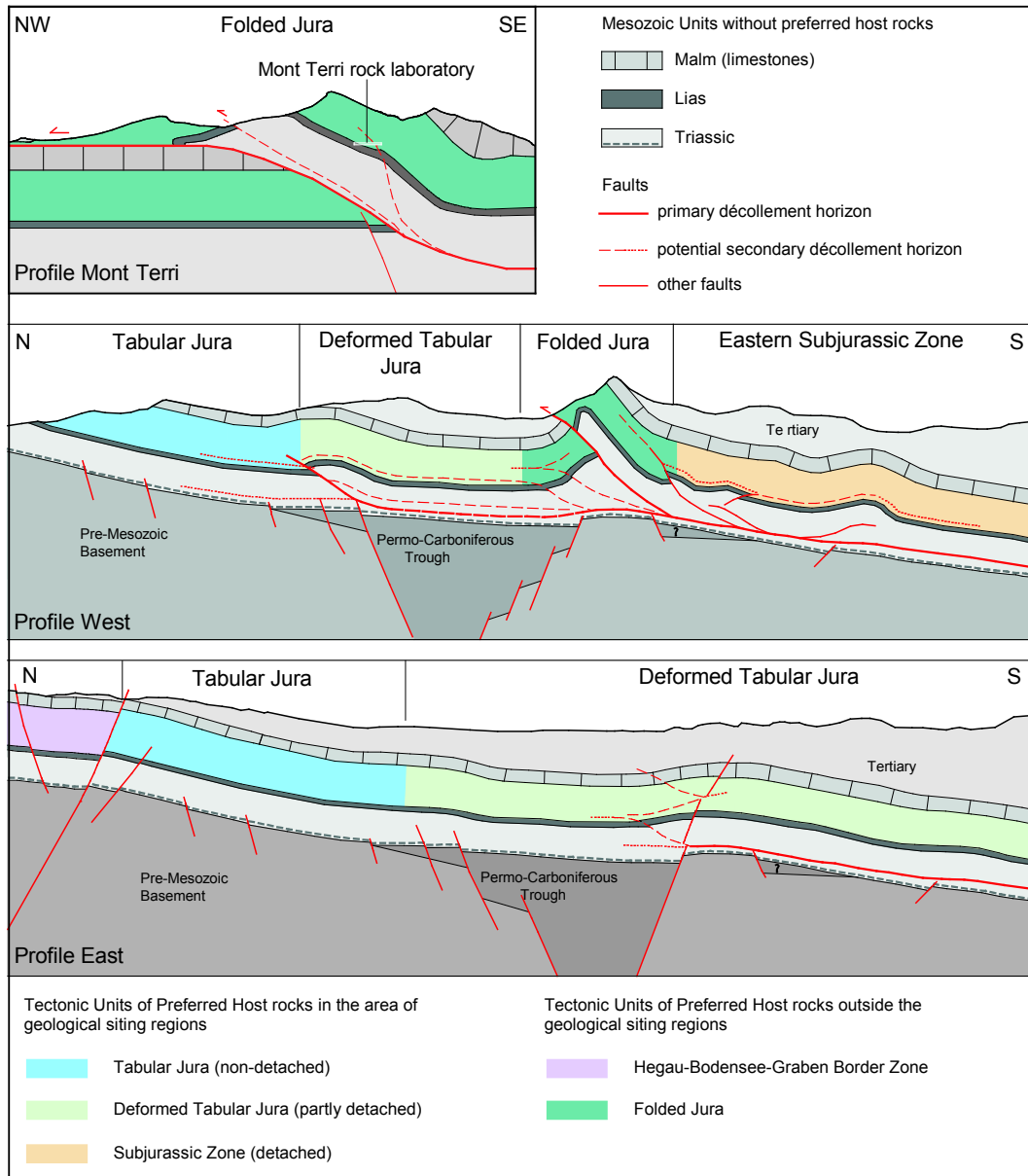


Fig. 6-2: Schematic cross sections through the Mont Terri underground lab and the area of geological siting regions in Northern Switzerland.

Traces of cross-sections are indicated in Fig. 6-1

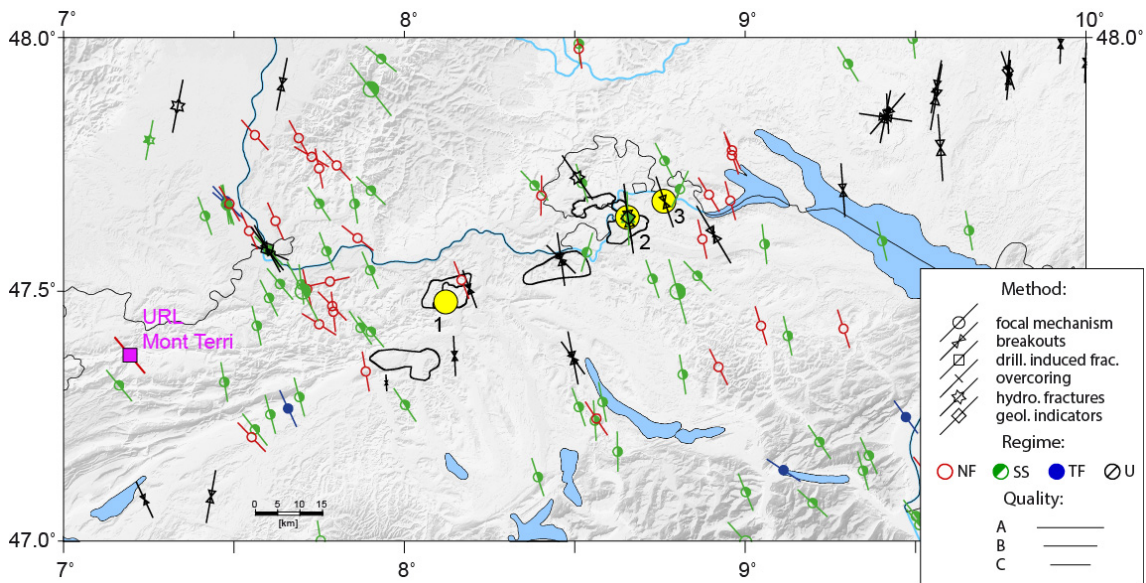


Fig. 6-3: Overview of stress data in Northern Switzerland.

Azimuth of bars depict the orientation of derived maximum horizontal stress magnitude SH, length of bars indicate data quality. Blue, green and red colours refer to the stress regime, i.e. the relative ratios of the maximum stress magnitudes: thrust faulting (TF), strike-slip faulting (SS) and normal faulting (NS). Yellow circles indicate locations with information of stress magnitudes at greater depths (300-1000 m) from hydraulic fracturing: (1) Bözberg B2/13 (Klee & Becker 2013), (2) Benken (Nagra 2001), (3) Schlattingen-1 (Klee 2012). After Heidbach & Reinecker (2013). The bar for the URL Mont Terri was constructed on the basis of Tab. 3-3.

Tab. 6-2: Reference principal total normal stress values as a function of depth.

See also Fig. 6-3 for graphical visualization. After Giger & Marschall (2014).

Parameter	Unit	Any depth	Example at 600m [b.g.]	Comments
<b>Overburden stress Sv (ρ=2500kg/m3)</b>	[MPa]	$= 0.0245 \times z^a$	14.7	
<b>Principal horizontal stress magnitudes</b>				
<i>Reference horizontal stress couple</i>				
minimum horizontal stress (SH <sub>ref</sub> )	[MPa]	$= 0.95 \cdot Sv$	14.2	Moderate horizontal tectonic loading <b>RSR_ref</b>
maximum horizontal stress (SH <sub>ref</sub> )	[MPa]	$= 1.35 \cdot SH_{ref}$	19.1	
K <sub>SH/Sv</sub>	[-]		0.9	
K <sub>SH/Sv</sub>	[-]		1.3	
<i>Low-end alternative horizontal stress couple</i>				
minimum horizontal stress (SH <sub>min</sub> )	[MPa]	$= Sv \cdot \left[ 0.35 \cdot \left( 1 + \frac{300}{z} \right)^{0.42} + 0.4 \right]$	12.2	SH <sub>min</sub> controlled by overconsolidation <b>RSR_min</b>
maximum horizontal stress (SH <sub>min</sub> )	[MPa]	$= 1.35 \cdot SH_{min}$	16.4	
K <sub>SH/Sv</sub>	[-]		0.8	
K <sub>SH/Sv</sub>	[-]		1.1	
<i>High-end alternative horizontal stress couple</i>				
minimum horizontal stress (SH <sub>max</sub> )	[MPa]	$= SH_{max} / 1.35$	20.5	SH <sub>max</sub> limited by residual strength of Opalinus Clay <b>RSR_max</b>
maximum horizontal stress (SH <sub>max</sub> )	[MPa]	$= Sv \times \left[ \frac{1 + \sin(\varphi)}{1 - \sin(\varphi)} \right] + 2C \times \left[ \frac{\cos(\varphi)}{1 - \sin(\varphi)} \right]^b$	27.7	
K <sub>SH/Sv</sub>	[-]		1.4	
K <sub>SH/Sv</sub>	[-]		1.9	

<sup>a</sup>=depth below ground in [m]; <sup>b</sup>with φ=17° and C=0.3 [MPa]

In addition to the derived magnitudes from hydraulic fracturing, semi-empirical relationships and geomechanical numerical modelling at the scale of the geological siting regions were also used to estimate the in situ stress conditions in Northern Switzerland. This led to the formulation of three different stress scenarios, which are considered plausible at the level of the Opalinus Clay (Giger & Marschall 2014) and which could facilitate engineering feasibility assessment (Tab. 6-2 and Fig. 6-3). Simpson (1997) relates all three principal stress magnitudes to each other as a regime stress ratio (RSR), which allows the stress regime to be expressed by a single number. The three stress scenarios are therefore referred to as RSR\_ref, RSR\_min and RSR\_max to express a reference scenario, as well as a lower- and upper bound scenario, respectively (cf. Giger & Marschall 2014 for details).

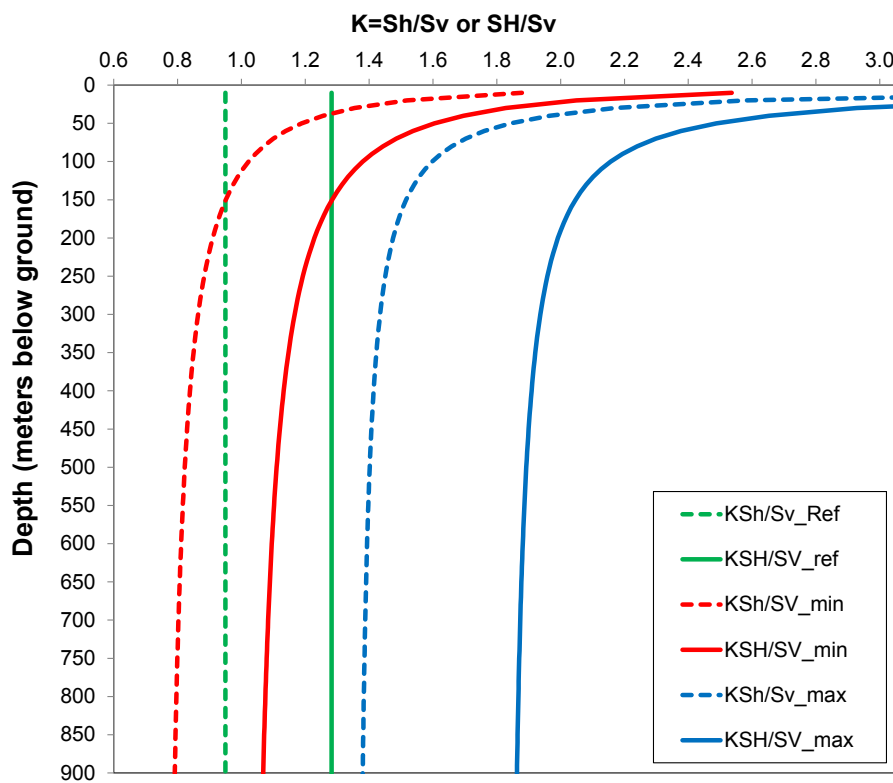


Fig. 6-4: Depth trend of stress scenarios for Opalinus Clay in Northern Switzerland.

Stress ratios expressed with respect to overburden stress ( $S_v$ ). Dashed lines represent minimum ( $Sh$ ), solid lines maximum horizontal stress ( $SH$ ) for each scenario (Tab. 6-2): green = RSR\_ref, red = RSR\_min and blue = RSR\_max. From Giger & Marschall (2014).

### 6.2.3 Rock properties and rock models

Core characterization from deep boreholes and the Mont Terri URL has demonstrated that mineralogy and geotechnical index properties of Opalinus Clay are comparable for different locations across northern Switzerland (Giger & Marschall 2014). In contrast, a fairly systematic positive correlation is recognized for porosity with greater current burial depth or overconsolidation ratio. Importantly, geomechanical testing provides ample evidence that stiffness, swelling and strength parameters are inversely proportional to water content, which is a measure of porosity. Since the average porosity of Opalinus Clay at Mont Terri is greater than

at repository depth in Northern Switzerland, geomechanical properties cannot directly be transferred. Giger & Marschall (2014) derived geomechanical reference data for the undrained shear strength as a function of water content. For this, analyses of triaxial tests from Mont Terri, Benken and Schlattingen were conducted, drawing on the assumption of undrained unconsolidated test conditions (Fig. 6-5). In this case, the undrained shear strength  $S_u$  is defined on the Mohr circle in the  $\sigma$ - $\tau$ -graph as follows (see also Fig. 6-11):

$$S_u = (\sigma_1 - \sigma_3) / 2 = q_f / 2 \tag{6-1}$$

where  $q_f$  is the maximum deviator stress at failure. The data compilation, representing the undrained shear strength of the Opalinus Clay for a wide range of water contents, exhibits a significant scatter. This can be partly attributed to imperfections in test execution and test interpretation. On the other hand, there is strong evidence that the marked variability of the rock strength is also associated to some degree with the mineralogical, lithological and tectonic variability of the rock mass. A distinct strength anisotropy parallel/perpendicular to bedding is another characteristic feature of the compiled  $S_u(w)$  data.

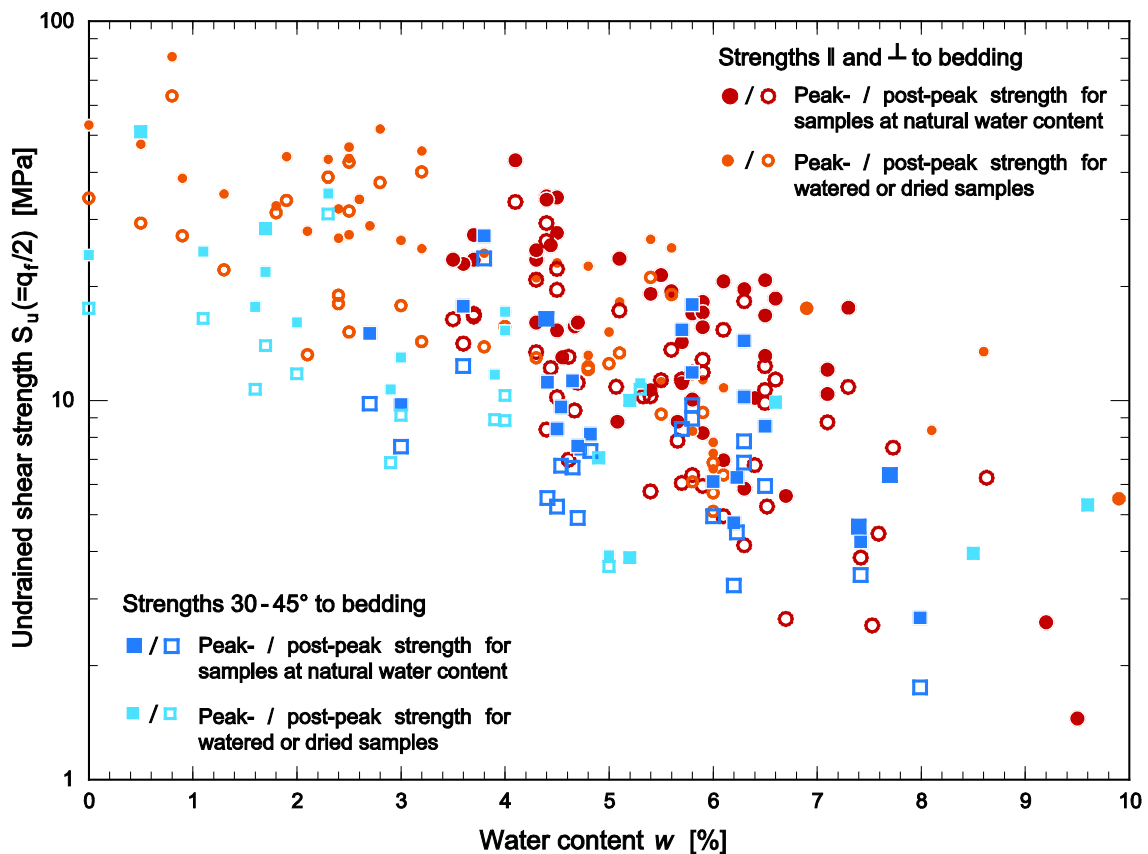


Fig. 6-5: Relationship between undrained shear strength and water content of the Opalinus Clay.

Compilation based on the analysis of triaxial tests by Rummel & Weber (1999, 2004), Jahns (2010, 2013) and Olalla et al. (1999). For further details see Giger & Marschall (2014).

The rock properties discussed here were derived from geomechanical testing of ‘intact’ cores. Although sampling, storage and specimen preparation are likely to damage samples and lead to underestimation of strength, it is reasonable to assume that the measured peak strengths in laboratory testing are representative for ‘intact rock’ at the cavern scale.

Besides excavation-induced discontinuities, tectonic faults and fractures have been described in virtually all caverns at the Mont Terri URL (Chapter 4). The ‘Main Fault’ is the most prominent of these tectonic features, and it is considered to be a splay off the Jura main thrust, which in turn accommodates the bulk part of an estimated 2km of shortening at the Mont Terri anticline (Nussbaum et al. 2011). Fractures and zones of apparent structural disintegration are also present in the Opalinus Clay in the geological siting regions of Northern Switzerland (Ebert 2014), although the frequency of structures in boreholes of Northern Switzerland is generally lower than at Mont Terri, in good agreement with the location of the siting regions with respect to the tectonic units.

It is thus acknowledged that structural discontinuities are present in Opalinus Clay at greater depth (i.e. at repository level) in Northern Switzerland, and that this will impact on the rock mass strength with respect to measured ‘intact’ samples in the laboratory. Addressing the impact of discrete fractures would require a good knowledge of subseismic fracture distribution, however, and such a database does not exist for Opalinus Clay at potential repository depth in Northern Switzerland. It is therefore desirable to address rock mass weakening in Opalinus Clay by a continuum approach.

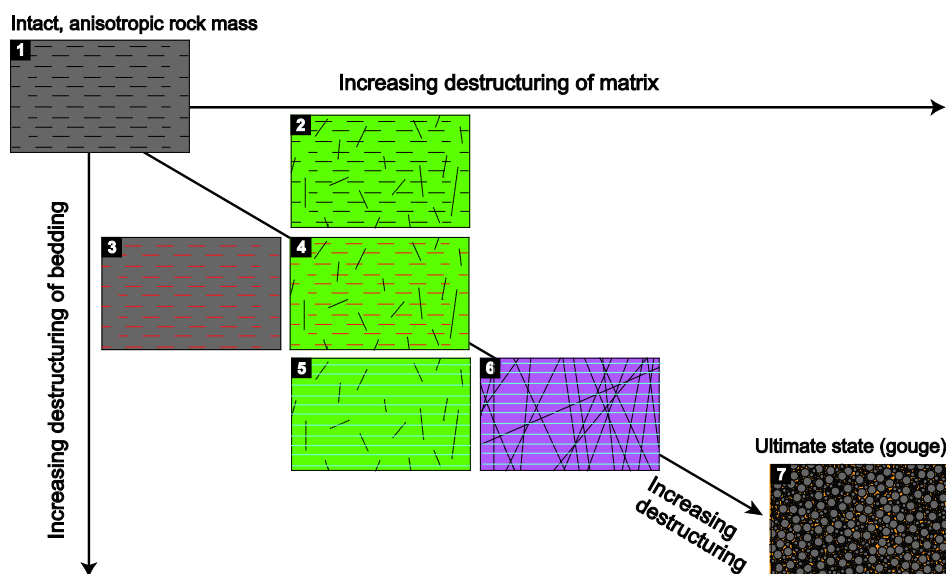


Fig. 6-6: Schematic destructuring of intact, anisotropic Opalinus Clay rock mass.

Numbers indicate rock models ("Gebirgsmodelle"). Background colour refers to values of the ‘matrix’: Grey colour indicates ‘intact’ matrix strength, green colour reduced peak strength (indicated by dotted lines in different orientations), purple colour loss of intact strength and reduction to post-peak strength values measured in the laboratory (i.e. development of through-going fractures). Horizontal lines refer to values of the ‘bedding’: dashed black line indicates schematically the strength anisotropy, red dashed line a reduction of intact strength and blue line a loss of intact strength and reduction to post-peak strength (i.e. development of through-going fracture). At the ultimate state, strength properties are close to isotropic and further reduced with respect to laboratory measurements. From Giger & Marschall (2014).

In an overconsolidated argillite with transversal anisotropic strength properties such as observed in Opalinus Clay, structural weakening can be assumed to occur preferably along the dominant fabric ('bedding planes') or the matrix (i.e. any direction different from the dominant fabric). In contrast to Mont Terri, the dominant fabric orientation in Opalinus Clay of Northern Switzerland is approximately horizontal. Fig. 6-6 illustrates schematically the possible destructuring of intact, anisotropic Opalinus Clay to an essentially isotropic gouge material ("ultimate state" in terms of critical state soil mechanics). The strength reduction can conceptually be linked to laboratory strength measurements (cf. Giger & Marschall 2014). The destructuring with assigned strength values then leads to the formulation of different *rock models* ("*Gebirgsmodelle*") which can be used to estimate the impact of structural overprint on intact rock strength. Giger & Marschall (2014) derived for each rock model a parameter set, representing the drained strength parameters (effective cohesion  $C'_{GMi}$  and friction angle  $\phi'_{GMi}$  for both matrix and bedding) and the corresponding parameter models, representing the undrained shear strength  $S_{u,GMi}$ :

$$S_{u,GMi} = A_{GMi} \cdot \exp(-B_{GMi} \cdot w) \quad (6-2)$$

The correspondence of drained and undrained strength parameters was based on a reference water content, representative for the Opalinus Clay at Benken and Schlattingen, respectively ( $w = 4.5\%$ ). As a further simplification, the slopes  $B_{GMi}$  of the  $\log(S_{u,GMi}(w))$  curves were assumed to be constant for all rock models. Fig. 6-7 shows the graded rock models of undrained shear strength, representative for the matrix and the bedding, respectively. The coefficients  $A_{GMi}$  and  $B_{GMi}$  of the corresponding parameter models are tabulated in Table 6-3.

Tab. 6-3: Reference values of undrained shear strength  $S_{u,GMi}$ , representing the rock models GM1-GM6.

Parameter values  $A_M$ ,  $B_M$  (matrix) and  $A_S$ ,  $B_S$  (bedding) according to Equation (6-2). The units of  $S_u$  given in [MPa] and water content in [%].

Rock model	Parameter model, representing the undrained shear strength of the rock models $S_{u,GMi}$ according to Equation (6-2)					
	Matrix parameters			Bedding parameters		
	$A_M$ [MPa]	$B_M$ [-]	$\lambda_M$ [-]	$A_S$ [MPa]	$B_S$ [-]	$\lambda_S$ [-]
GM 1	61.5	23.5	0.12	42.4	28.9	0.09
GM 2	35.0	23.5	0.12	42.4	28.9	0.09
GM 3	61.5	23.5	0.12	30.0	28.9	0.09
GM 4	35.0	23.5	0.12	30.0	28.9	0.09
GM 5	35.0	23.5	0.12	18.0	28.9	0.09
GM 6	20.0	23.5	0.12	18.0	28.9	0.09

In many geotechnical applications such as limit state analyses, the undrained shear strength is used as a strength indicator for evaluating the short term response of the rock mass on load increments (total stress analyses). Such an application is presented in Chapter 6.3.3, aimed at evaluating the yield zone around an excavated cavity in terms of size and shape (Chapter 6.4.1) and eventually leading to the derivation of nomograms of diametral strain (Chapter 6.4.2).

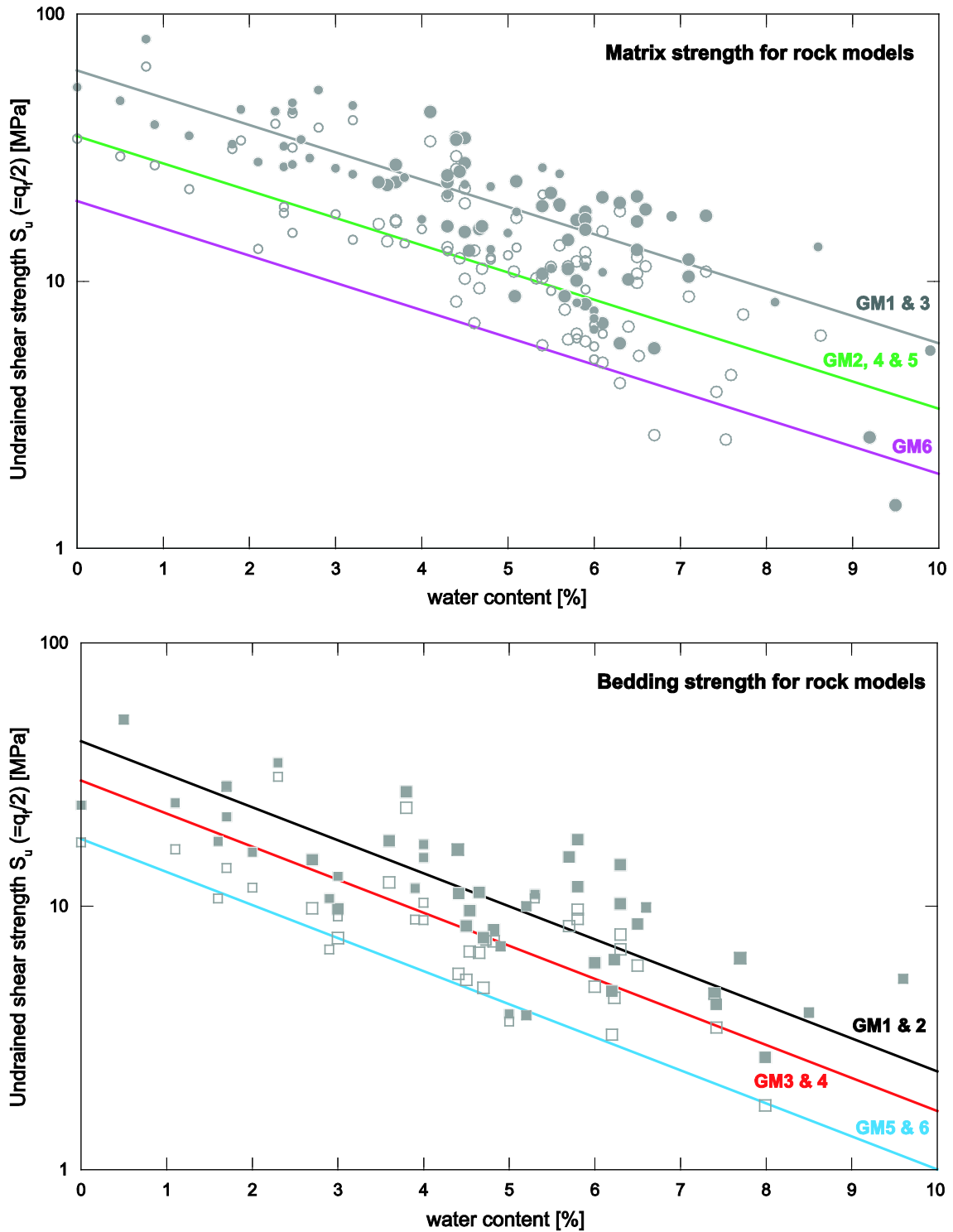


Fig. 6-7: Undrained shear strength ( $S_u$ ), derived for the different rock models GM1 – GM6.

The test results marked in gray colour correspond to Fig. 6-5. The parameter values  $A_{GMi}$  and  $B_{GMi}$  derived by regression of the  $S_u(w)$  data are given in Tab. 6-3. From Giger & Marschall (2014).

### 6.3 Description of the transferability approach

#### 6.3.1 Rationale

With reference to the design indicators described in Section 6.1, the following premises are central to the assessment of maximum repository depth in the candidate siting regions of Northern Switzerland (Nagra 2014a):

- The acceptable range of *convergence strain* of the tunnel cross-section is based on recommendations from Hoek & Marinos (2000), (Fig. 6-8) and represents a range of expected challenges during construction;
- The acceptable vertical extent of the *plastified zone* (Fig. 6-9b), which reduces the thickness of the intact vertical migration path to the upper and lower host rock boundary, is bound by safety assessment requirements;
- The effective hydraulic *conductance* of the horizontal migration path along the backfilled underground structures is determined by the cross-sectional area of the EDZ (Fig. 6-9a), the acceptable extent of which is thus also limited by safety assessment requirements.

For the purpose of tunnel design, deformations are often predicted using ground reaction curves that utilise analytical solutions with rock properties derived from geomechanical laboratory tests. The approach tends to under-predict the deformations when the laboratory properties are applied without consideration of possible weaknesses of the rock mass. For this, Hoek & Marinos (2000) developed a pragmatic scheme by using a numerical plasticity model and calibrating the model to field experience (Fig. 6-8).

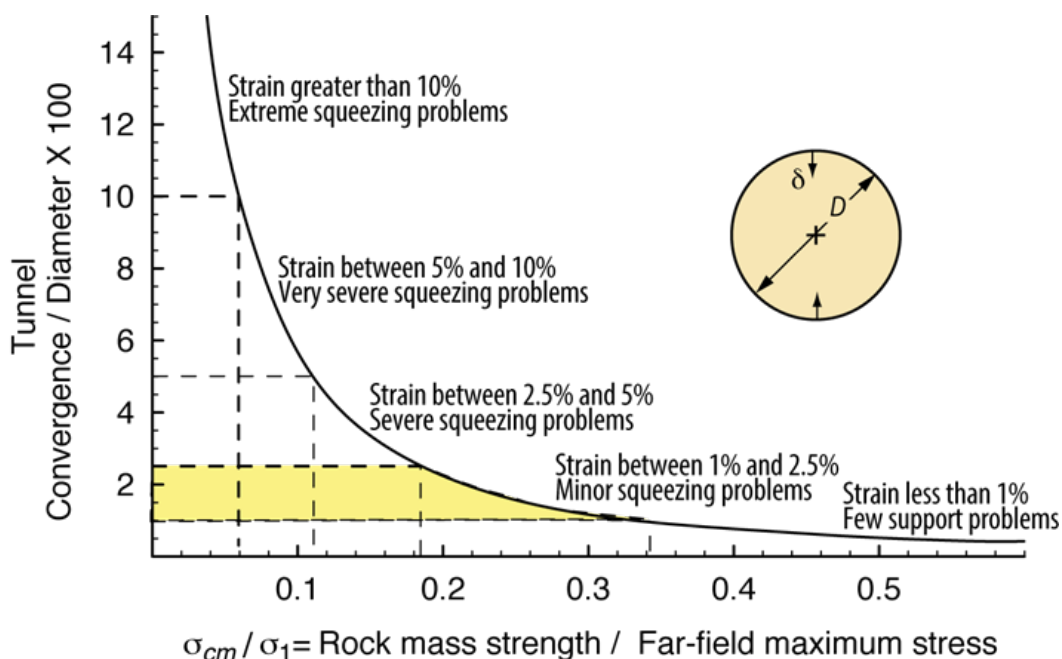


Fig. 6-8: Numerically predicted squeezing convergence normalised to the tunnel diameter versus rock mass strength normalised by the far field maximum stress.

Experience suggests that supporting a tunnel becomes challenging when the squeezing strains range between 2.5% and 5% (from Hoek and Marinos 2000).

They also related the diametral strain (Convergence/Diameter x 100%) to the expected support and suggested that beyond 2.5% strain the support becomes challenging. The description of the support classes associated with Fig. 6-8 is expanded in Tab. 6-4. Note that the strains in Fig. 6-8 assume that no support is installed. In Fig. 6-8 the rock mass strength was determined using the Hoek Brown Geological Strength Index methodology and then normalised to the far-field stress.

Tab. 6-4: Approximate relationship between strain and the degree of difficulty associated with tunnelling through squeezing rock. Note that this curve is for tunnels with no support (from Hoek & Marinos 2000).

Strain $\epsilon$ [%]	Geotechnical issues	Support types
Less than 1	Few stability problems and very simple tunnel support design methods can be used. Tunnel support recommendations based upon rock mass classifications provide an adequate basis for design.	Very simple tunnelling conditions, with rockbolts and shotcrete typically used for support.
1 to 2.5	Convergence confinement methods are used to predict the formation of a 'plastic' zone in the rock mass surrounding a tunnel and of the interaction between the progressive development of this zone and different types of support.	Minor squeezing problems which are generally dealt with by rockbolts and shotcrete; sometimes with light steel sets or lattice girders are added for additional security.
2.5 to 5	Two-dimensional finite element analysis, incorporating support elements and excavation sequence, are normally used for this type of problem. Face stability is generally not a major problem.	Severe squeezing problems requiring rapid installation of support and careful control of construction quality. Heavy steel sets embedded in shotcrete are generally required.
5 to 10	The design of the tunnel is dominated by face stability issues and, while two-dimensional finite analyses are generally carried out, some estimates of the effects of forepoling and face reinforcement are required.	Very severe squeezing and face stability problems. Forepoling and face reinforcement with steel sets embedded in shotcrete are usually necessary.
More than 10	Severe face instability as well as squeezing of the tunnel make this an extremely difficult three-dimensional problem for which no effective design methods are currently available. Most solutions are based on experience.	Extreme squeezing problems. Forepoling and face reinforcement are usually applied and yielding support may be required in extreme cases.

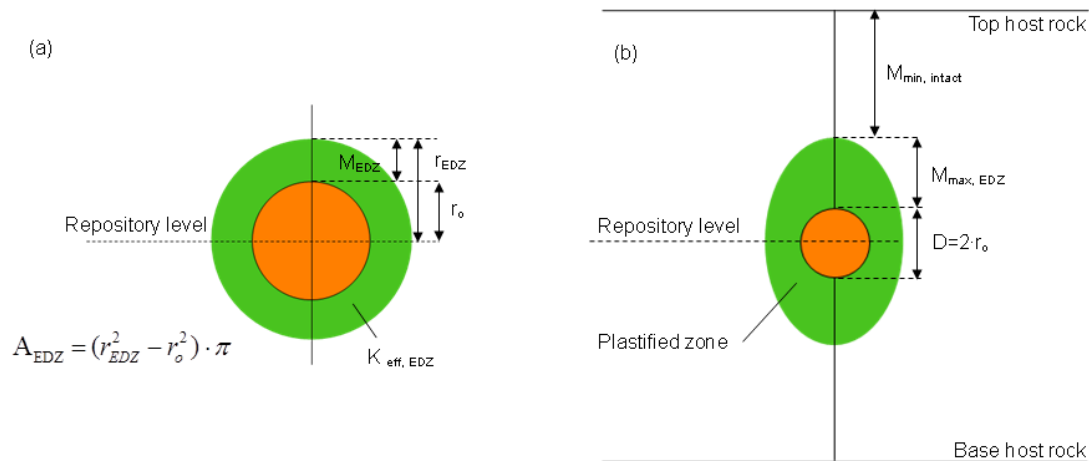


Fig. 6-9: EDZ indicators related to long-term safety:  
 (a) hydraulic conductance of the EDZ and (b) minimum thickness of the intact host rock.

It is well known that the Hoek-Brown approach is not appropriate for estimating the strength of weak rocks such as clay shales. An alternative to the approach in Fig. 6-8 is to establish an empirical relationship using the results from case histories. The x-axis in Fig. 6-8 uses the rock mass strength. This is essentially impossible to establish from borehole data, particularly in sedimentary rocks. A more practical strength parameter is the uniaxial compressive strength (UCS). The other parameter on the x-axis in Fig. 6-8 is the far-field stress. Experience has shown that it is more useful to express the stress as the maximum tangential stress on a circular tunnel boundary ( $\sigma_{max} = 3 \cdot \sigma_1 - \sigma_3$ ). This approach also captures the importance of the direction of the tunnel relative to the stress field, as demonstrated by Armand et al. (2013).

In this way convergence data from Mont Terri and other underground structures in similar argillaceous rocks were compiled (Tab.6-5, Fig. 6-10). All the convergence data were taken at 100 days after excavation<sup>2</sup>. Examples from Mont Terri were chosen from the shaly facies and from galleries for which the axes were approximately parallel (Ga08) or perpendicular (MB, FE) to the maximum horizontal stress magnitude. Due to the steeply dipping bedding of Opalinus Clay at Mont Terri, a UCS value of 17 MPa was selected for galleries perpendicular to bedding strike (Ga08), and a value of 8 MPa was selected for galleries parallel to bedding strike (MB, FE) (cf. Tab.3-2). The in-plane principal stress magnitudes were calculated from the stress tensor of Bossart & Wermeille (2003) (cf. Tab.3-3).

<sup>2</sup> It is noted that for the Boom Clay at Mol/Hades site, Bernier et al. (2007) do not specify a time period but quote the "total convergence related to construction".

Tab. 6-5: Compilation of convergence data in Opalinus Clay at Mont Terri and underground structures with similar argillaceous rocks.

<sup>a</sup>The maximum tangential stress at the tunnel wall is calculated as  $S_{max} = 3\sigma_1 - \sigma_3$ . <sup>b</sup>Little (1989) specifies a UCS value of 6 MPa, but this was later revised to 10 MPa (comment D. Martin).

Location (gallery)	Lithology	UCS [MPa]	In-plane principal stress magnitudes [MPa]		Squeezing index $UCS/\sigma_{max}^a$ [-]	Diametral strain $2\delta/D$ [%]	Reference
			$\sigma_1$	$\sigma_3$			
Mont Terri (Ga08)	Opalinus Clay	17	6.5	2.3	0.99	0.50	Tab.4-21
Mont Terri (Ga08)	Opalinus Clay	17	6.5	2.3	0.99	0.80	Tab.4-21
Mont Terri (MB)	Opalinus Clay	8	6.5	4.2	0.52	1.33	Tab.5-8
Mont Terri (MB)	Opalinus Clay	8	6.5	4.2	0.52	1.56	Tab.5-8 <sup>a</sup>
Mont Terri (FE)	Opalinus Clay	8	6.5	4.2	0.52	2.67	Fig.4-68
Bure (GCR)	Callovo-Oxfordian	21	11.3	11.3	0.93	0.42	Armand et al. (2013)
Bure (GCS)	Callovo-Oxfordian	21	11.3	11.3	0.93	0.83	Armand et al. (2013)
Bure (GED)	Callovo-Oxfordian	21	14.6	11.3	0.64	1.39	Armand et al. (2013)
Bure (GED)	Callovo-Oxfordian	21	14.6	11.3	0.64	2.20	Armand et al. (2013)
Bure (GED)	Callovo-Oxfordian	21	14.6	11.3	0.64	1.39	Armand et al. (2013)
Mol/Hades	Boom Clay	2	4.5	4.5	0.22	1.88	Bernier et al. (2007)
Site C (Test chamber)	Shaftesbury shale	10 <sup>b</sup>	2.6	0.8	1.43	0.07	Little (1989)

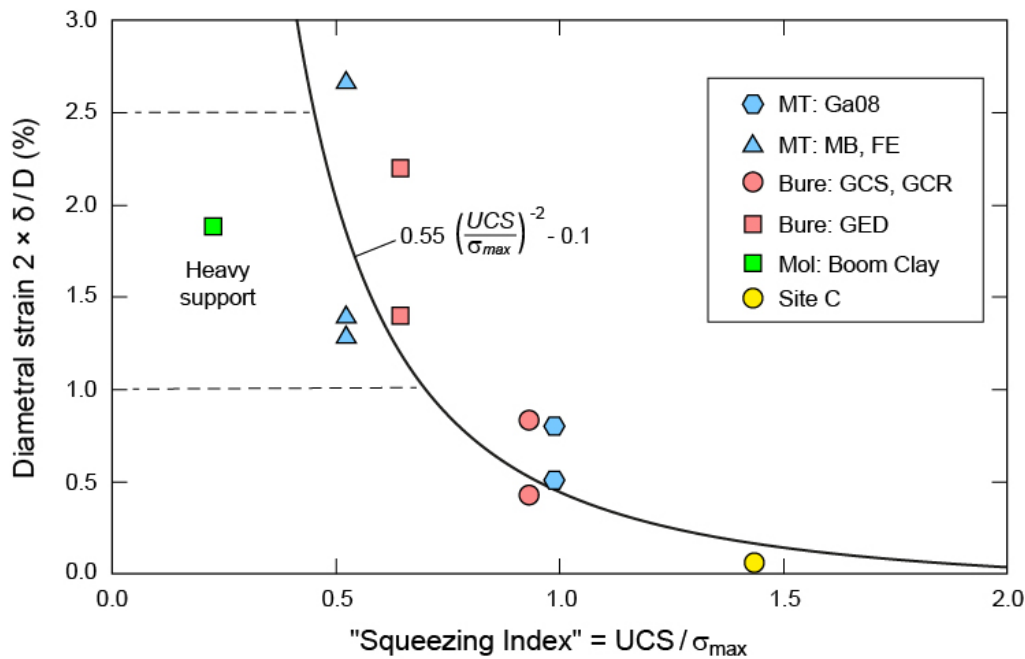


Fig. 6-10: Measured diametral convergence strain in tunnels at Mont Terri versus Squeezing Index.

The Squeezing Index is defined as the maximum tangential stress ( $\sigma_{max} = 3\sigma_1 - \sigma_3$ ) on a circular opening normalised to the uniaxial compressive strength. For reference, the data is compared to the performance of other tunnels in argillaceous rocks. Site C refers to a large diameter test tunnel in the Shaftsbury Shales where the rock mass response was essentially elastic.

### 6.3.2 Applied modelling tools

The distinct tendency of the Opalinus Clay to form brittle fractures (i.e. localization of deformation) in response to tensile and shear stresses is ultimately attributed to microscopic failure processes in the amorphous rock fabric and can therefore be predicted with only limited accuracy using macroscopic modelling concepts. In previous modelling studies and depending on the application, both continuum mechanics approaches and Discrete Element Methods (DEM) were used for modelling the deformation behaviour of Opalinus Clay (Harrington 2014; Geomechanica 2013). The modelling approaches are complementary, since continuum models are particularly suitable for implementing complex THM material laws, while the strength of DEM models is the ability to track the localization of deformation in a realistic manner, provided that the structural variability in the rock fabric is known in sufficient detail.

In Stage 2 of the Sectoral Plan, commercially available geomechanical software tools were used for assessing the maximum repository depth, based on classical continuum mechanics approaches. In this context, comprehensive EDZ related sensitivity studies were conducted with the three-dimensional continuum modelling software FLAC<sup>3D</sup>, using the constitutive model "SUBI" ("Bi-Linear Ubiquitous Joints with Strain Hardening Softening"). The simulations concerned the creation and evolution of the EDZ for the full range of repository depths and stress regimes in the candidate siting regions. Further sensitivity analyses were dedicated to the impact of the geomechanical rock properties, both for 2-D and 3-D geometries of the emplacement rooms (Nagra 2014a). The corresponding numerical simulations turned out to be time consuming, especially when hydromechanical coupled processes were taken into account. In addition, in the constitutive law SUBI the elastic behaviour is assumed to be isotropic, so that

the couplings between shear deformation and pore water pressure, as a consequence of the anisotropic stiffness described in Chapter 5.3, could not be modelled adequately. To overcome these limitations, the commercial two-dimensional finite element program Phase<sup>2</sup> (www.roscience.com) was used as a complementary analysis tool to assess the impact of anisotropic stiffness of the Opalinus Clay.

Phase<sup>2</sup> had been tested successfully in previous modelling exercises in the context of the MB- and FE-experiment (see Chapter 5.3). The sensitivity studies presented in this chapter were performed for simple model geometries (Fig. 6-11 circular tunnel cross-section), simulating the deformation processes in the rock during tunnel excavation with a total stress approach. The total stress approach is justified for the estimation of short-term tunnel convergence immediately after the excavation, since these occur under undrained conditions in very low permeability formations such as the Opalinus Clay. However, the long-term convergence strains are significantly affected by the dissipation of the pore pressure perturbation in response to the excavation process (see Chapter 6.3.3) and hence are not considered in the total stress approach.

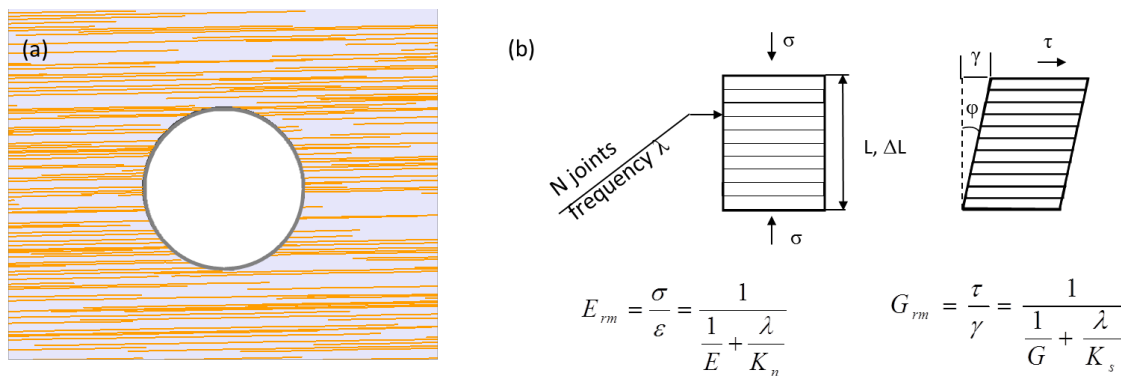


Fig. 6-11: Model analyses addressing the impact of anisotropic stiffness on the size and extent of the EDZ around a circular cavity.

(a) Model implementation in the 2-D Code Phase<sup>2</sup>. The bedding planes are represented as stochastically distributed horizontal elements in the homogeneous rock matrix. (b) The effective Young's modulus of the rock mass normal to bedding,  $E_{rm}$ , is calculated as the harmonic mean of the E-Modulus of the intact rock  $E$  and the normal stiffness of the bedding planes  $K_n$ , where  $\lambda$  is the average number of bedding planes per metre. The effective shear modulus  $G_{rm}$  is derived correspondingly from the shear modulus of the intact rock mass  $G$  and the shear stiffness of the bedding planes  $K_s$  (after Duncan & Goodman 1968).

In the analyses carried out using Phase<sup>2</sup>, the rock is considered as a composite continuum, which consists of a homogeneous and isotropic rock matrix and randomly distributed bedding or fault planes. In the two-dimensional representation (Fig. 6-11a), the discrete bedding/fault elements are represented as lineaments with a given length, orientation and spatial frequency. In the present study, horizontal bedding is assumed, which reflects the conditions in the siting regions in Northern Switzerland. The effective elastic and plastic deformation behaviour of the rock mass is resulting from the interaction between the matrix and bedding. Thus the effective Young's modulus  $E_G$  normal to bedding can be derived in a first approximation of the harmonic mean of the moduli of the intact rock  $E$  and the bedding planes  $E_T$ , where  $\lambda$  is the average number of bedding planes per meter (Fig. 6-11b). The effective Young's modulus parallel to the

bedding, however, is virtually identical to the modulus of the matrix. Hence, the effective anisotropy coefficient of the stiffness tensor can be determined from Equation (5-6) as

$$A = \sqrt{E_G / E} .$$

### 6.3.3 Modelling approach

#### Justification of the total stress analysis and general work flow

When a saturated claystone is subject at its surface to a total stress increment  $\Delta\sigma$ , the volume of the rock mass is expected to change. For that to happen, water must be either expelled from within or absorbed by the clay-bearing rock matrix; in other words a flow rate must be established (drained conditions; e.g. Azizi 1999). However, when a tunnel is excavated in a low-permeability claystone such as the Opalinus Clay, in the short term, the flow of pore water associated with the total stress change is insignificant due to the low permeability of the rock mass. Thus, the rock experiences virtually no volume change in the short term, meaning that the interlocking of the grains forming the solid skeleton of the rock matrix remains unchanged, and so does the effective stress ( $\Delta\sigma' = 0$ ). According to the effective stress principle, in the short term any total stress increase  $\Delta\sigma$  applied at the surface of a saturated clay is transmitted to the pore water, generating an excess pore water pressure  $\Delta u = \Delta\sigma$ .

Accordingly, in the short term, shear failure of a saturated claystone occurs under a constant volume prior to any dissipation of the pore water pressure taking place and thus, before occurrence of any consolidation. The deviator stress at failure  $q_f = (\sigma_1 - \sigma_3)_f$  has a constant value irrespective of the magnitude of the confining pressure (Mohr's circles at failure are displaced along the  $\sigma$ -axis, but have the same diameter as shown in Fig. 6-12a). As such, the behaviour of the rock is referred to as *unconsolidated undrained*. Under these circumstances and assuming the validity of the Mohr-Coulomb failure criterion for heavily overconsolidated claystones (see also Chapter 5.3.2):

$$\tau_f = c' + \sigma' \cdot \tan \phi' \quad (6-3)$$

with the angle of friction  $\phi'$  and the apparent cohesion  $c'$ , the effective stress  $\sigma' = 0$  and the Mohr-Coulomb equation reduces to:

$$\tau_f = \frac{q_f}{2} = S_u \quad (6-4)$$

Where  $S_u$  denotes the undrained shear strength. The undrained shear strength is a fundamental soil design parameter, in that it governs the clay behaviour in the short term (Azizi 1999). Moreover, a log-linear relationship between  $\ln(S_u)$  and water content can be established for saturated normally consolidated clay. It should be borne in mind, however, that the undrained shear strength of stiff clay, measured in the laboratory, often represents an overestimate of the actual value in the field, because small size samples are unlikely to contain slip planes or fissures that characterize a thick stiff clay layer in situ (Simpson et al. 1979).

The procedure for the evaluation of the convergence strains is shown in the schematic sketch in Fig. 6-12c. All simulations are based on the assumption of an unlined tunnel, i.e. the corresponding ground response was determined for the extreme case without support measures ( $p_i = 0$ ). In order to separate elastic and plastic strains, a purely elastic simulation was performed for each calculation case.

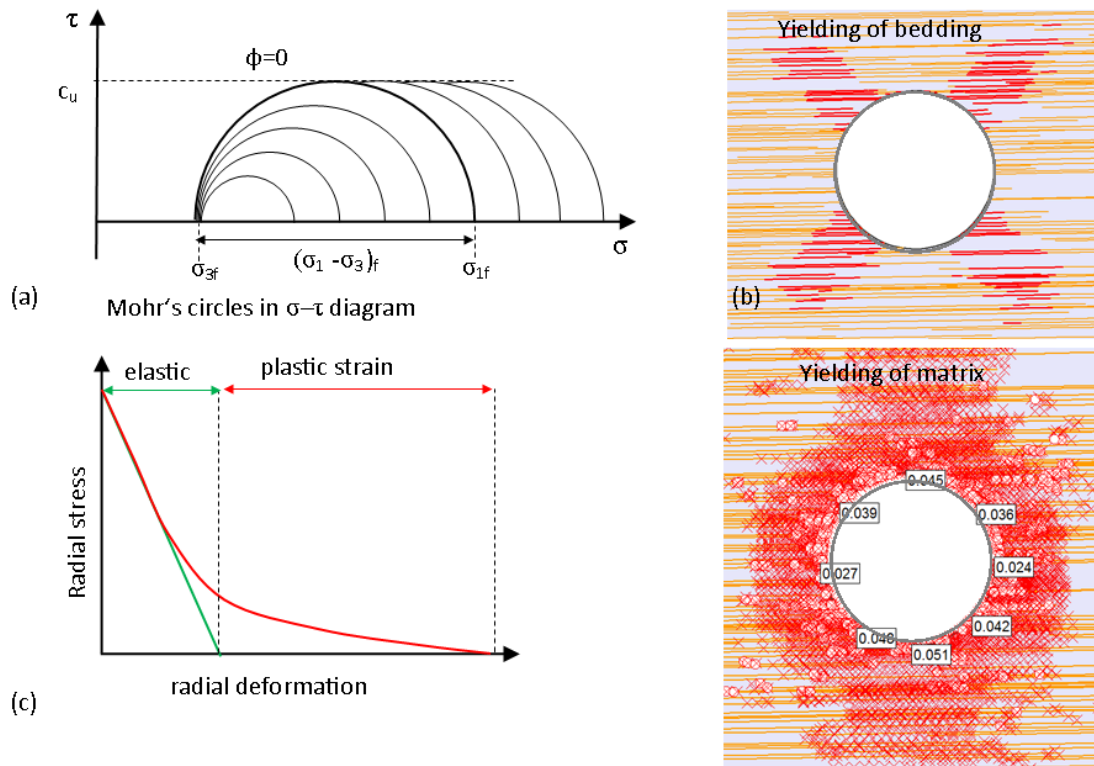


Fig. 6-12: Transferability approach: workflow for the elaboration of the nomograms for the assessment of maximum repository depth.

(a) Mohr's circles in the total stress plane  $\sigma$ - $\tau$ , describing the relationship between deviator stress at failure  $q_f$  and undrained shear strength  $c_u$  in the unconsolidated undrained case. (b) Example of a 2-D simulation of the EDZ around a circular cavity using the code *Phase<sup>2</sup>*. The red symbols indicate plastified zone in the matrix (x - shear, o - tensile) and along bedding. (c) Principle sketch of the ground response curve, indicating the components of elastic and plastic deformation, respectively.

### Model calibration using the Mine-By Tunnel from Mont Terri

All numerical models should be calibrated with field data to gain confidence in the modelling approach. Without this calibration numerical modelling results must be evaluated with caution. The excavations at Mont Terri provide extensive monitoring and observational data that can be used for numerical modelling calibration. The excavation response data at Mont Terri and discussed in the previous sections identified several factors that the numerical modelling must simulate:

- The bedding in the Opalinus Clay plays a major role in controlling the yielding observed around the Mont Terri excavations
- The measured convergence around the excavations in Mont Terri are an order of magnitude greater than the elastic response
- The onset of the large convergence-deformations is coincident with the onset of excavation-advance. In other words the measured deformation/convergence is dominated by plastic yielding.

The Mine-By Niche excavation, which is summarized in Chapter 4.6, was simulated using Phase<sup>2</sup> and the total stress approached discussed above. All input parameters required for the Phase<sup>2</sup> model were taken from Bock (2009). The bedding in the Phase<sup>2</sup> model was simulated as discrete lineaments with variable spacing and trace length (Fig. 6-12).

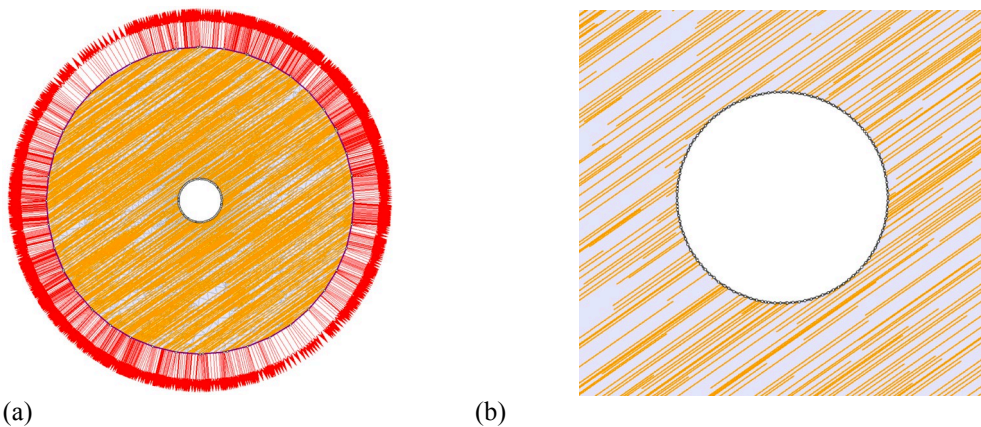


Fig. 6-13: Phase<sup>2</sup> Model with bedding represented by a variable joint network.

The dip of the bedding is set at 36 degrees. (a) Overall Phase 2 model with infinite springs at boundary to reduce model size but capture all the displacement. (b) Bedding represented by discontinuous joints with bedding properties. Bedding spacing varied from 0.005 m to 0.150 m

The unknown in the Phase<sup>2</sup> simulations is the rock mass undrained shear strength, which is assumed to be the same for the bedding and the matrix. A series of Phase<sup>2</sup> analyses were carried out varying only the undrained shear strength. For each simulation the radial convergence was recorded and averaged for the 5 monitoring points. The Phase<sup>2</sup> simulations provide the total convergence<sup>3</sup> while in reality only a portion of the measured convergence can be measured. If the deformation response was entirely elastic only 50%<sup>4</sup> of the total convergence could be measured. Hence for each analysis 50% of the elastic displacements are subtracted from the total displacements. The results from the numerical analyses for the Mine-By tunnel are summarized in Fig. 6-14. The degree of difficulty associated with tunnelling through squeezing rock proposed by Hoek & Merinos (2000) is also shown in Fig. 6-14 and the maximum diametral strain recorded for the Mine-By tunnel (see Chapter 4.6.5). Using the results in

<sup>3</sup> Tunnel advance was modelled by a stiffness reduction technique, which therefore captures also elastic deformation ahead of the tunnel face

<sup>4</sup> The 50% stem from comparison of inclinometer data (FE and MB experiment, see Chapter 4) with elastic deformation in the model runs

Fig. 6-14, the undrained shear strength corresponding to the maximum diametral strain is approximately 2.5 MPa. This magnitude for the operational undrained shear strength was also derived for the Mine-By tunnel using a different approach (see Chapter 4.6.5 and Chapter 5). The results from these analyses suggest that the empirical nomogram in Fig. 6-14 provides a useful link between the laboratory properties for the Opalinus Clay, expected tunnel diametral strain, the degree of difficulty associated with tunnelling through squeezing rock and the undrained shear strength of the rock mass.

As with all numerical models, the output is sensitive to the input. The nomogram in Fig. 6-14 was created using only measured laboratory data for the input to Phase<sup>2</sup>. The diametral strains in the nomogram in Fig. 6-14 are a function of the stiffness of the matrix and the bedding planes. If the bedding plane stiffness is made the same as the rock matrix stiffness, the diametral strains are significantly less than those predicted in Fig. 6-14 for any given undrained shear strength. To obtain the measured diametral strains would require a much lower undrained shear strength, which is not supported by the existing data. If the bedding plane stiffness is less than that used for Fig. 6-14, the diametral strains are significantly greater than those predicted in Fig. 6-14 for any given undrained shear strength. To obtain the measured diametral strains with a lower bedding plane stiffness would require a much higher undrained shear strength, which is not supported by the existing data. Hence while different nomograms can be generated depending on the input, additional information is needed to judge the relevance of the output. This creates uncertainty in the absolute magnitudes obtained from numerical models. Consequently, nomograms such as illustrated in Fig. 6-14 are more useful for comparing the diametral tunnel strain from one site to another.

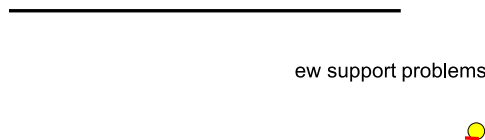


Fig. 6-14: Relationship between undrained shear strength and tunnel strain established using Phase<sup>2</sup> for the Mont Terri Mine-By tunnel.

### Model set-up and simulation cases

The methodology described above to develop the nomograms relating undrained shear strength and diametral tunnel strain for the Mine-By tunnel was used for the potential repository sites. The simulations were conducted with the above-described total stress approach, assigning a constant undrained shear strength  $c_u$  and a friction angle  $\phi = 0$  to the intact rock matrix. As a further simplification, it was assumed that the undrained shear strength is the same for the bedding and the matrix. The elastic behaviour of the rock differs markedly along the principal axes of the stiffness tensor (see Fig. 6-11). In the baseline simulations, an isotropic Young's modulus was assigned to the matrix ( $E = 18$  GPa –cf. Tab. 7-1 of Giger & Marschall 2014), whereas the normal and shear stiffness of the bedding planes ( $K_n = K_s = 8$  GPa) and the average number of bedding planes per meter ( $\lambda$  ranging between 5 and 20  $m^{-1}$ ) were derived from the back analysis of the MB- and FE-experiments.

Baseline simulations were carried out for repository depths of 500 m, 700 m and 900 m for the reference stress scenario RSR\_REF. Additional sensitivity analyses were carried out for stress regimes RSR\_MAX and RSR\_MIN and for the assessment of the impact of bedding plane stiffness. A summary of the input parameters for those cases is provided in Tab. 6-6.

Tab. 6-6: Overview of input parameters for for the development of the nomograms.

	Baseline	Stress regime	Bedding plane stiffness
Matrix and bedding $c_u$ (MPa)	2 – 30	2 - 30	2 – 30
Matrix E (GPa)	18	18	18
Bedding plane stiffness (MPa/m)	$K_n = 8000$ $K_s = 8000$	$K_n = 8000$ $K_s = 8000$	$K_n = 8,000, 800,000$ $K_s = 800$ to 800,000
Stress regime	RSR_REF	RSR_REF, RSR_MIN and RSR_MAX	RSR_REF
Repository depth (m)	500, 700, 900	500**, 700, 900*	700
* sensitivity cases for RSR_MAX only			

## 6.4 Results of the sensitivity analyses

The numerical analyses comprised the simulations for the baseline configuration and the additional sensitivity cases addressing the stress regime and the bedding plane stiffness (Tab. 6-6). The interpretation of modelling results was dedicated to the evaluation of the yield zone in terms of size and shape (Chapter 6.4.1) and to the derivation of nomograms of diametral strain (Chapter 6.4.2 and 6.4.3).

### 6.4.1 Size and shape of the yield zone

The evaluation of the size and shape of the yield zone was conducted for the baseline configuration with repository depths of 500 m, 700 m and 900 m using the reference stress scenario RSR\_REF. For this, the yield zones associated with the matrix and the bedding, respectively, were calculated for  $s_u$  values ranging between 6 and 10 MPa. The width  $W$  and the height  $H$  of the yield zone were derived from graphical representation of the yielded zone in the matrix (Fig. 6-15). The corresponding area of the yield zone  $A_e$  was calculated as the area of the ellipse (minus the tunnel) normalised to the area of the tunnel.

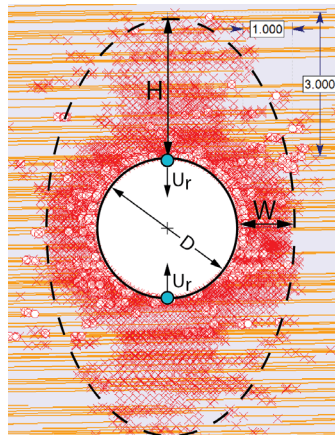


Fig. 6-15: Definitions used for the geometry of the yield zone ( $W$  and  $H$ ) and the associated diametral strain ( $D_e = 2 \cdot U_r / D$  %).

The area of the yield zone ( $A_e$ ) is the area of the ellipse (minus the tunnel) normalised to the area of the tunnel.  $U_r$  represents the convergence strain.

Fig. 6-16 presents examples of the yield zone in the bedding and the matrix, respectively, for three baseline cases. In Fig. 6-16a the assumed repository depth is 500 m and the undrained shear strength is 6 MPa. Yielding of the bedding planes is limited to a narrow zone around the tunnel surface with a thickness of less than a tunnel radius, whereas the yield zone of the matrix exhibits an elliptical shape with a thickness of 0.4 – 1.2 tunnel diameters.

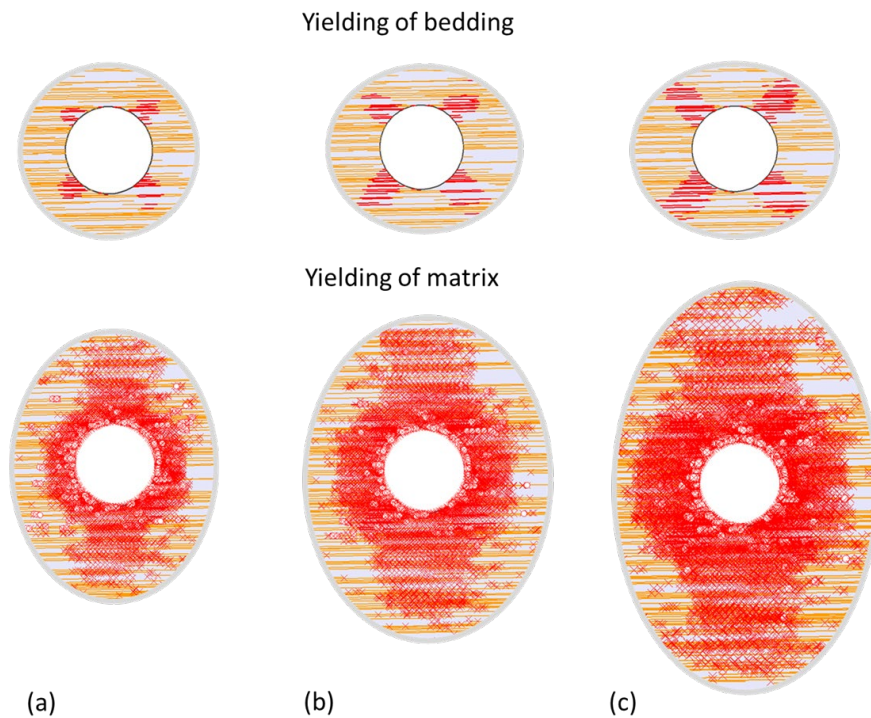


Fig. 6-16: Examples of the geometry of the yield zone for baseline simulations with various undrained shear strengths.

Yield zone of the bedding (top) and of the matrix (bottom): (a) undrained shear strength  $S_u = 6$  MPa, repository depth 500 m; (b)  $S_u = 7$  MPa / 700 m; (c)  $S_u = 8$  MPa / 900 m.

Tab. 6-7: Summary of geometry of the yield zone (W, H in metres) and the associated average diametral strain, (see Fig. 6-15 for definitions).

Depth	Yield Parameters	S <sub>u</sub> 6 MPa	S <sub>u</sub> 7 MPa	S <sub>u</sub> 8 MPa	S <sub>u</sub> 10 MPa
500 m	W = m	1	1	0.9	0.8
	H = m	3	1.8	1.5	0.9
	D <sub>e</sub> = %	1.1	0.82	0.65	0.54
	A <sub>e</sub> =	4	2.7	2.2	1.45
700 m	W = m	2.5	1.8	1.3	1
	H = m	5.5	3.4	3.0	1.8
	D <sub>e</sub> = %	3.7	2.6	1.9	1.3
	A <sub>e</sub> =	11.4	6.2	4.6	2.7
900 m	W = m	4.5	3.3	2.3	1.3
	H = m	11+	6.8	5.1	3.2
	D <sub>e</sub> = %	9.5	6.2	4.3	2.6
	A <sub>e</sub> =	32	16.7	10	4.8

With increasing repository depth, the yield zone increases significantly, even when an increase of the undrained shear strength is taken into account, which can be explained by higher compaction of the Opalinus Clay at greater depth (Fig. 6-16b, c).

The results of the analyses are summarized in Tab. 6-7, providing further evidence for an increasing extension of the yield area (width, height and area) with increasing repository depth. This is highlighted in Fig. 6-16, displaying for the 3 repository depths 500 m, 700 m and 900 m, the relationships between yield area and S<sub>u</sub> (Fig. 6-17a) and average diametral strain (Fig. 6-17b, c).

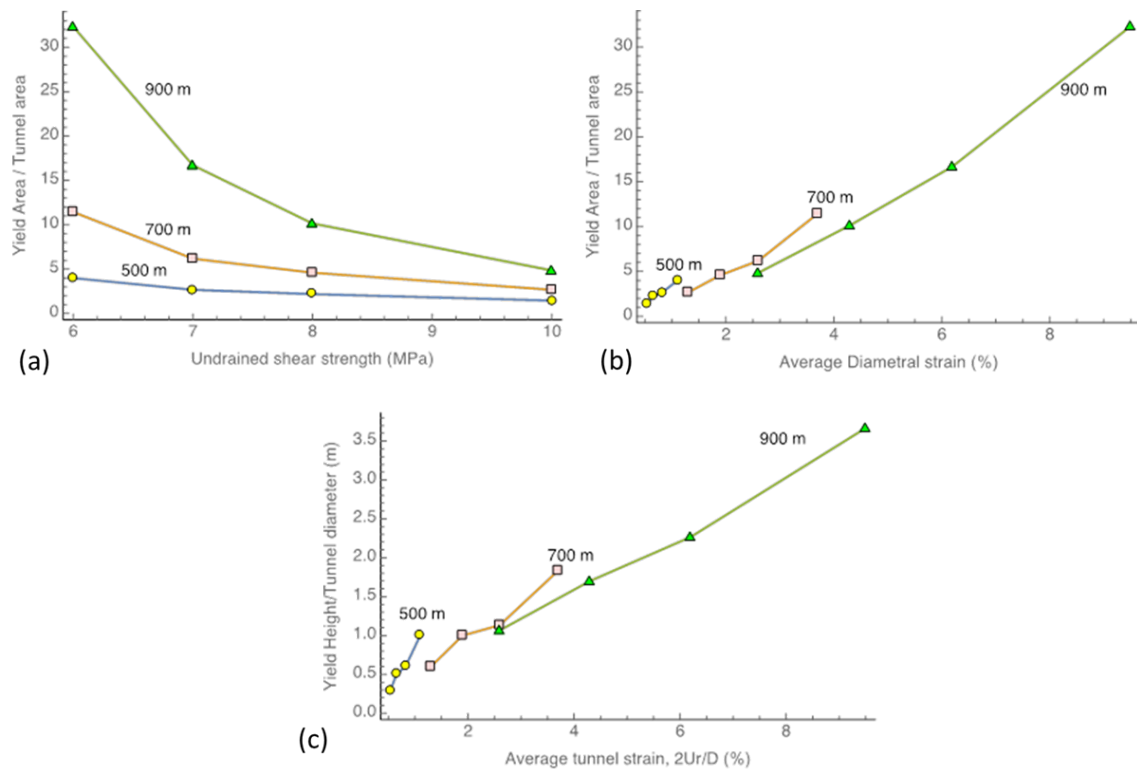


Fig. 6-17: Various relationships between the extent of yielding measured around the tunnel in the Phase<sup>2</sup> models, and the undrained shear strength and tunnel strain.

Derived from baseline simulations for undrained shear strength ranging between 6 and 10 MPa and repository depths of 500 m, 700 m and 900 m: (a) yield area  $A_e$  versus  $S_u$ ; (b) yield area  $A_e$  versus diametral strain; (c) yield height  $H$  versus diametral strain.

#### 6.4.2 Nomograms representing the baseline configuration

The approach described above was used to establish the relationship between diametral tunnel strain and the undrained shear strength for three repository depths: 500 m, 700 m and 900 m. The reference in situ stress ( $RSR_{ref}$ ) for those depths was discussed in Chapter 6.2.2. The analyses are carried out for the case when the tunnels are excavated in the direction of the minimum horizontal stress. The  $RSR_{ref}$  scenario gives the maximum in-plane stress as the horizontal stress with the vertical stress being the minimum in-plane stress. This provides the maximum deviatoric stress on the tunnels and hence will impose the largest amount of yielding. For this stress configuration, the maximum extent of yielding occurs above the roof of the tunnel. When the diametral strains exceed two percent the height of the yielding is approximately equivalent to the diameter of the tunnel (See Fig. 6-17c and Tab. 6.7).

The results from these analyses are provided in Fig. 6-18 and the maximum diametral strain measured at Mont Terri for the Mine-By tunnel is provided for reference. As expected, the amount of diametral strain, for a given undrained shear strength, increases with depth. With increasing undrained shear strength the plastic strains stabilize as the deformations become dominated by the elastic response.

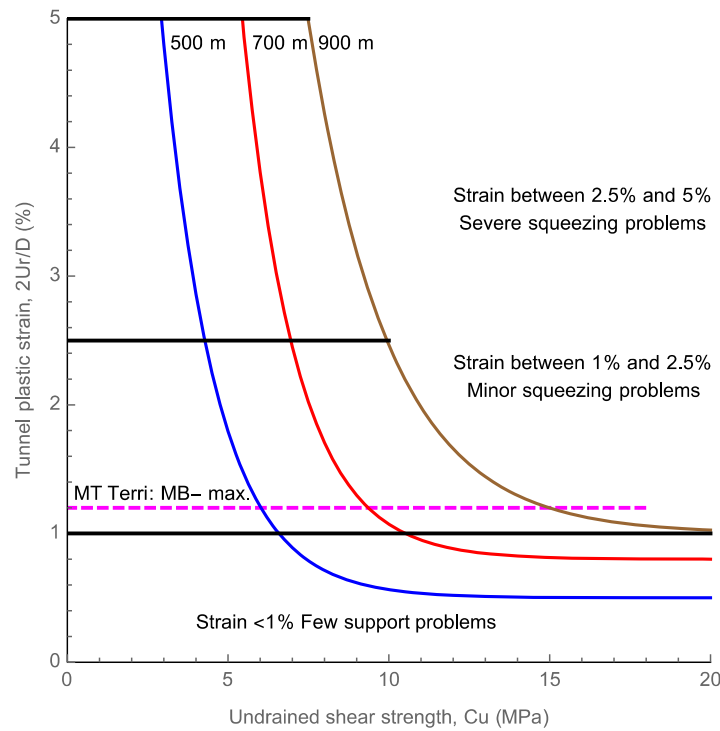


Fig. 6-18: Nomogram of diametral tunnel strains in [%] for repository depths of 500 m, 700 m and 900 m using the reference stress scenario RSR\_ref.

According to Chapter 6.2 the shear strength of the Opalinus Clay in the proposed siting regions in Northern Switzerland does not only depend on the burial depth, but also on the so-called rock model GMi, which represents a measure of the structural integrity of the rock mass prior to the excavation process. In other words, the rock models reflect the degree of destructuring of the intact rock mass, primarily caused by tectonic overprint.

The peculiarity of the nomogram approach is the use of undrained shear strength of the rock mass, representing a normalised excavation response for a wide range of rock models. The corresponding failure criterion is given by the undrained Hvorslev envelope (see Nagra 2014b / Dossier IV)<sup>5</sup>.

Assuming the reference water content  $w_o$  of the rock mass and the corresponding mean effective stress  $p_o'$  at a given depth is known (e.g., in-situ conditions in the center of the Opalinus Clay at Benken), the unloading/reconsolidation line URL defines the reference water content of the rock in the overconsolidated state (for details see Nagra 2014b / Dossier IV):

$$w = w_o + \kappa \cdot \frac{\rho_w}{\rho_s} \cdot \ln \frac{p'}{p_o'} \tag{6-5}$$

<sup>5</sup> In the undrained case the deviator stress at failure  $q_f$  for a given water content  $w_o$  can be expressed as:  
 $q_f = 2 \cdot (1 - h / M) \cdot S_u(w_o) + h \cdot p'$   
 where  $h$  (friction parameter, overconsolidated state) and  $M$  (friction parameter, normally consolidated state) are intrinsic properties of the rock.

In this context  $\kappa$  is the negative slope of the URL line, which can be determined by oedometer tests. For the present study two alternative  $\kappa$ -values (0.04 and 0.01) were specified to cover the range of expectation with regard to the reference water content at repository depth. Assuming  $w_o = 3.4\%$  and  $p_o' = 25$  MPa (cf. Dossier IV, Chapter 5.3.4) this leads to the different water contents at specific depths as documented in Table 6-8.

Tab. 6-8: Water contents used to derive undrained shear strengths for nomograms.

Depth (m b.g.)	500	700	900
$w_{\kappa=0.01}$ (%)	5.2	4.7	4.3
$w_{\kappa=0.04}$ (%)	3.8	3.7	3.6

The undrained shear strength at a given repository depth is then derived from Equation 6-2 and Table 6-3 for each rock model GMi and the corresponding plastic convergence strain can be determined graphically from the nomograms in Fig. 6-18.

Fig. 6-19 displays the ranges of diametral strain, associated with the rock models GM1 – GM6 and separated by results for the matrix (a) and for the bedding (b). Due to the lower  $S_u$  values for the bedding with respect to the matrix, the diametral strains are also greater. Therefore the results in the following are discussed based on the observation of Fig. 6-18b (bedding strength). The nomograms suggest moderate strains of  $< 2\%$  for all rock models at a repository depth of 500 m with the exception of GM6 with high water contents, (i.e.  $w = 5.2\%$  assuming  $\kappa = 0.04$ ). At a depth of 700 m, it must be expected that strains for the destructured rock models GM5 & 6 (corresponding to post-peak strength in triaxial testing, see Fig.6-5 and 6-6) are in excess of 2.5%, which represents the strain level where the onset of severe squeezing problems may be expected (see Fig. 6-8). For a depth of 900 m, significant strains ( $> 2.5\%$ ) must also be expected for rock models GM3&4, which correspond to a tectonically weakly altered rock mass with respect to intact properties.

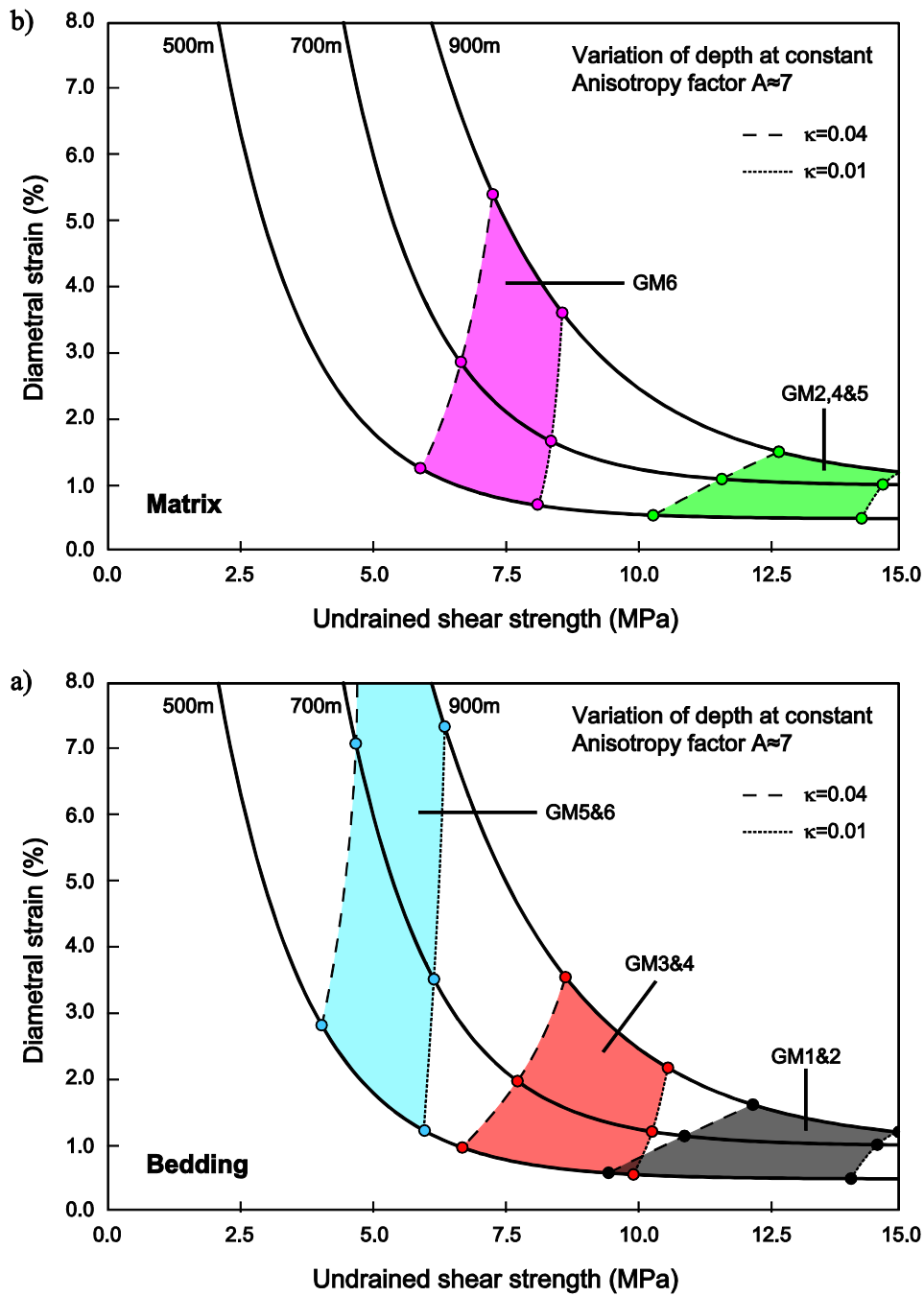


Fig. 6-19: Nomograms of the diametral tunnel strains in [%] for various repository depths.

Reference stress scenario (RSR\_ref) was used to constrain the nomograms at a depth of 500 m, 700 m and 900 m. The undrained shear strengths of the rock models GM1 – GM6 were derived from Equation 6-2 and Tab. 6-3. (a) Results using undrained shear strength values for the matrix. Note that results for GM1 and GM3 would plot further to the right on the x-axis and are not covered in the plot. (b) Results using undrained shear strength values for the bedding.

### **6.4.3 Effect of the stress magnitudes (RSR\_max, RSR\_min)**

Analyses were also carried out to assess the impact of the stress magnitudes on the diametral tunnel strain. The results from the maximum (RSR\_max) and minimum (RSR\_min) stress scenarios are compared to the results for the reference case (RSR\_ref) in Fig. 6.20a and 6-20b, respectively. The increase in the stress magnitudes in the RSR\_max scenario results in larger diametral strains for the same undrained shear strength. However as shown in Fig. 6-20b, there is little change in the diametral strains for the RSR\_min stress scenario.

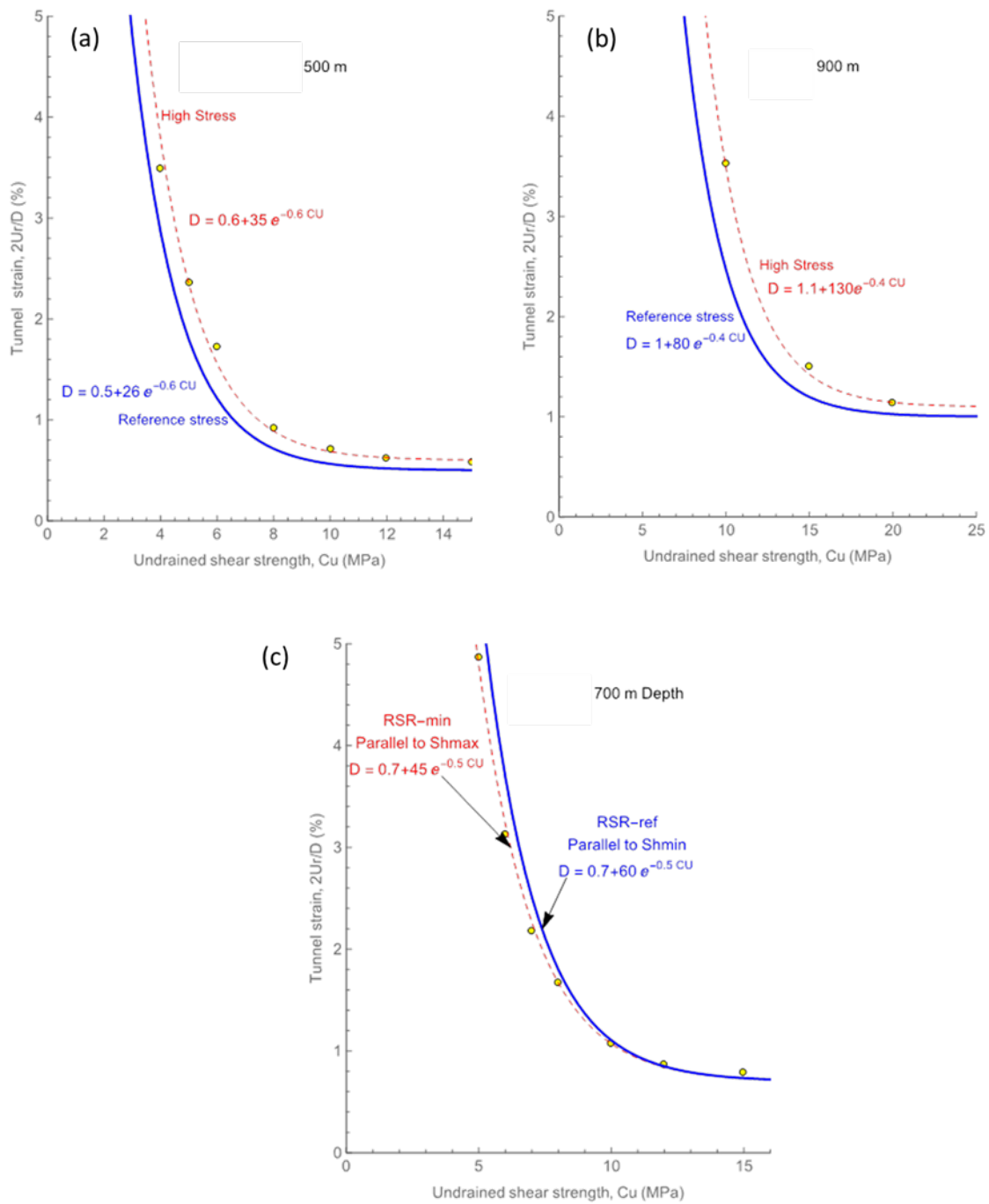


Fig. 6-20: Comparison of the diametral tunnel strain from the reference stress case (RSR\_ref) with the RSR\_max and RSR\_min cases, respectively.

- (a) RSR\_ref versus RSR\_max for 500 m;
- (b) RSR\_ref versus RSR\_max for 900 m depths
- (c) RSR\_ref versus RSR\_min for 700 m.

#### 6.4.4 Effect of bedding plane stiffness

Anisotropic stiffness has a significant impact on the deformation behaviour of the rock mass in response to the excavation process. Thus, in a geomaterial characterized by anisotropic stiffness, shear strains are associated with changes in volumetric strain and pore pressure, respectively. This cross coupling is of relevance for the creation of the EDZ, because shear deformation in response to the drop of radial stress at the tunnel wall could give rise to far-reaching pore pressure anomalies. Such phenomena have been observed at Mont Terri in the context of the MB- and FE-Experiments.

Anisotropic stiffness can be simulated in Phase<sup>2</sup> with the composite model shown in Fig. 6-10a, consisting of stochastically distributed bedding planes in a homogeneous rock matrix. The stiffness of the matrix is characterized by Young's modulus  $E$  and the shear modulus  $G$ , which can be expressed in terms of the Poisson ratio  $\nu$  and Young's modulus<sup>6</sup>. The elastic behaviour of the bedding planes is given by normal stiffness  $K_n$  and shear stiffness  $K_s$ . The elastic deformation behaviour of the composite model with stochastically distributed bedding planes can be described approximately by a transverse isotropic homogeneous continuum, using the Duncan & Goodman (1968) approach (Fig. 6-11b).

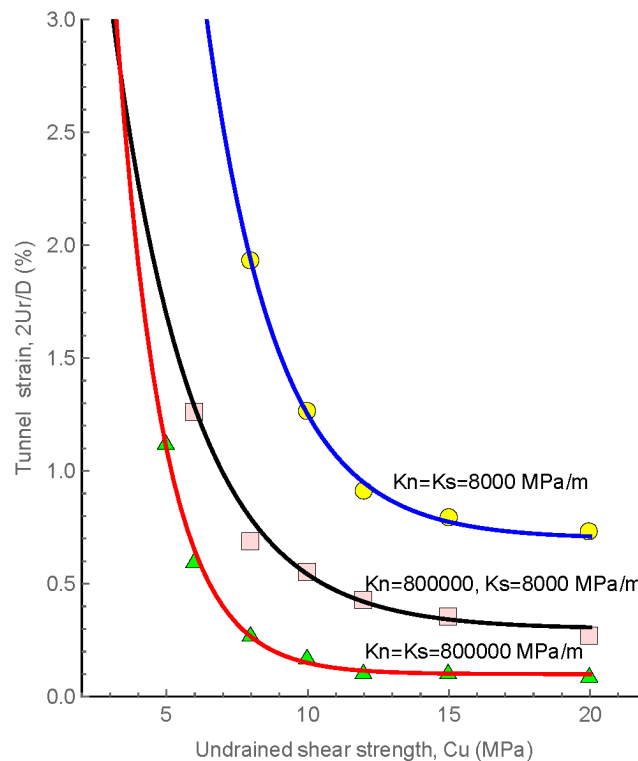


Fig. 6-21: Comparison of the diametral strain at a depth of 700 m with the normal stiffness of the bedding increased from 8000 MPa/m to 800000 MPa/m.

The shear stiffness is  $K_s = 8000$  MPa/m.

<sup>6</sup> Relationship between Young's modulus, Poisson's ratio and shear stiffness:  $G = \frac{E}{2 \cdot (\nu + 1)}$

Sensitivity analyses on bedding plane stiffness were conducted with the input parameters described in Tab. 6-6. Three nomograms, representing the repository depth of 700 m and the stress regime RSR\_ref were established for the bounding cases of a quasi-isotropic medium ( $K_n = K_s = 800,000$  MPa/m), a composite medium dominated by the joint stiffness ( $K_n = 8000$  MPa/m,  $K_s = 8000$  MPa/m) and a medium with high normal stiffness, but low shear stiffness ( $K_n = 800,000$  MPa/m,  $K_s = 8000$  MPa/m). Fig. 6-21 displays marked differences between the three cases, indicating favorable tunnel conditions for quasi-isotropic case (red line) with plastic strains  $< 0.5\%$  when the undrained shear strength  $S_u$  is around 7 MPa. In contrast, the highly anisotropic case is associated with significant strains around 2% for the same undrained shear strength (i.e.,  $S_u = 7$  MPa).

Further simulations were conducted to investigate the impact of shear stiffness. For this, normal stiffness was fixed ( $K_n = 800,000$  MPa/m) and  $K_s$  was varied between 800 and 800'000 MPa/m. The equivalent elastic moduli  $E_{rm}$  (Young's modulus perpendicular to the bedding planes) and  $G_{rm}$  (shear stiffness parallel to bedding) of the corresponding transverse isotropic geomaterial are given in Tab. 6-9. Even though the Duncan & Goodman (1968) approach does not perfectly represent the elastic deformation behaviour of the composite Phase<sup>2</sup> model (mainly due to the stochastic distribution of the bedding planes), it is evident that the "high anisotropy model" ( $K_n = 8000$  MPa/m,  $K_s = 8000$  MPa/m; blue nomogram in Fig. 6-21) is characterized by a very low Young's modulus perpendicular to the bedding planes.

Tab. 6-9: Equivalent elastic moduli of the corresponding transverse isotropic homogeneous continuum.

The composite Phase<sup>2</sup> model, consisting of stochastically distributed bedding planes in a homogeneous rock matrix can be described approximately by a transverse isotropic homogeneous continuum, using the Duncan & Goodman (1968) approach (Fig. 6-10b).

$K_n$	$K_s$	$E_{rm}$ [MPa]	$G_{rm}$ [MPa]
800'000	800'000	1.62E+04	6.6E+03
800'000	80'000	1.62E+04	4.8E+03
800'000	8'000	1.62E+04	1.3E+03
800'000	800	1.62E+04	1.6E+02
8'000	8'000	1.47E+03	1.3E+03

Matrix: Young's modulus  $E = 18$  GPa, Poisson ratio  $\nu = 0.3$   
 Bedding : horizontal layering, stochastic distribution, mean distance:  $\lambda = 0.2$  m

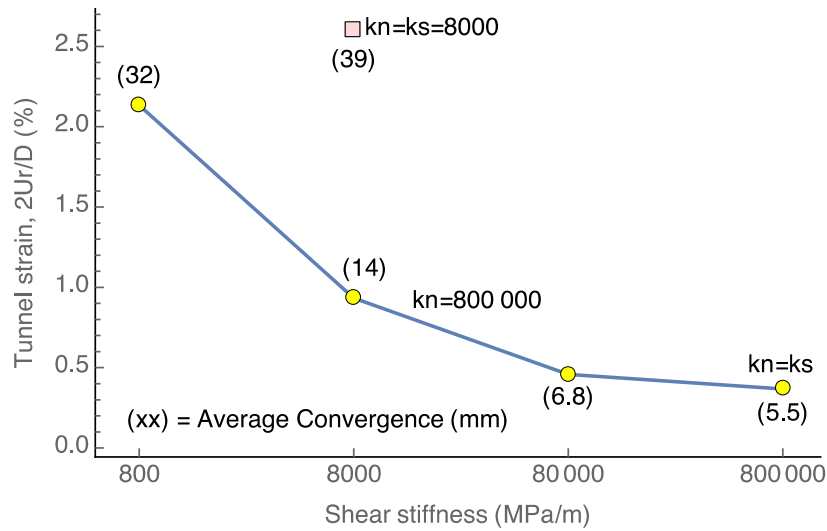


Fig. 6-22: Effect of shear stiffness on diametral tunnel strain, for a depth of 700 m.

The normal stiffness was held constant at  $K_n = 800,000$  MPa/m. The undrained shear strength is 8 MPa. The tunnel strain for  $k_n = k_s = 8000$  MPa/m is shown for reference.

The effect of shear stiffness on plastic tunnel strain is depicted exemplarily in Fig. 6-22 for the case with  $S_u = 8$  MPa. The simulations indicate that plastic strains are very small in the quasi-isotropic case ( $K_n = K_s = 800,000$  MPa/m), whereas a significant increase is observed for decreasing shear stiffness with plastic strains  $> 2\%$  for the anisotropic case with  $K_s = 800$  MPa/m.

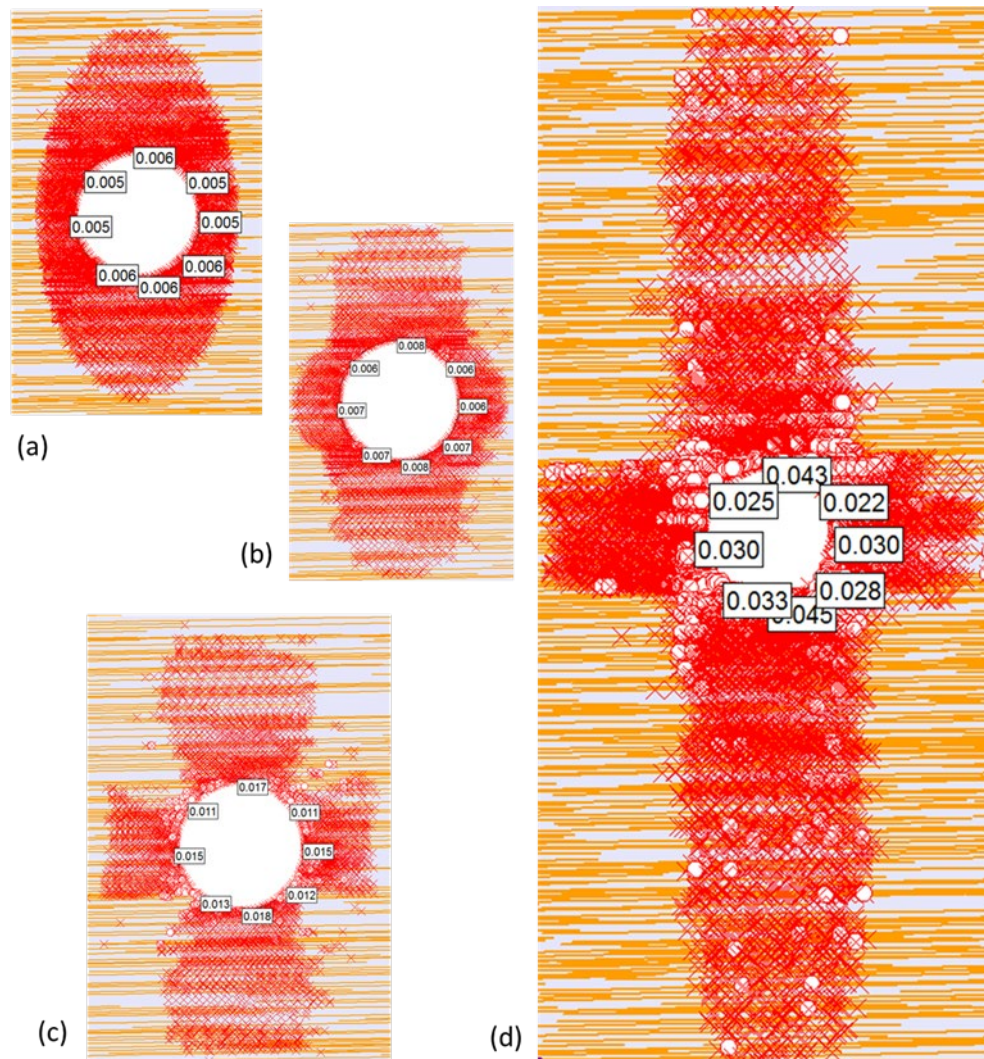


Fig. 6-23: Effect of shear stiffness on diametral tunnel strain, for a depth of 700 m.

The normal stiffness was held constant at  $K_n = 800,000$  MPa/m and  $s_u = 8$  MPa. (a)  $K_s = 800,000$  MPa/m; (b)  $K_s = 80,000$  MPa/m; (c)  $K_s = 8,000$  MPa/m; (d)  $K_s = 800$  MPa/m.

Fig. 6-23 illustrates the distinct impact of shear stiffness on the size and the shape of the yield zone. In the quasi-isotropic case (Fig. 6-23a), the yield zone is mainly controlled by the initial stress field, displaying the characteristic elliptical shape with the major axis oriented in the direction of the minor principal stress. Shear failure is the prevailing failure mechanism and the convergence strains at the tunnel circumference are small. Reduction of the shear stiffness (Fig. 6-23b-d) results in extended yield zones with increasing convergence strains. Furthermore, the onset of tensile failure is observed (Fig. 6-23c-d). The extreme case with  $K_s = 800$  MPa/m is characterized by a vertical extension of the yield zone H, which exceeds 5 tunnel diameters (Fig. 6-23d). This marked chimney effect seems to be triggered by distinct shear strains around the cavity in response to the excavation process, creating high shear stresses and progressive failure of the matrix. Shear failure is the dominant failure mechanism. In addition, tensile failure is observed in the vicinity of the cavity, but surprisingly the loci of tensile failure are extending over the entire yield zone. Tensile failure may be interpreted as progressive buckling of the bedding planes, which has been observed at Mont Terri at various experimental sites.

## 6.5 Summary

The motivation for this chapter was to develop a methodology for comparing the expected performance of tunnels constructed in Opalinus Clay at different depths at repository sites. Recognizing that there is always uncertainty when forecasting tunnel performance based on borehole information, the methodology was first developed and applied to the tunnel observations at Mont Terri Laboratory. The methodology expresses the rock mass strength in terms of the undrained shear strength and using total stresses computes the tunnel diametral strain. These strains are then compared with published tunnelling experience.

The experience from Mont Terri has shown that weak planes in the form of bedding and geological structure play a major role in controlling the performance of the tunnels. The numerical approach used to compute the diametral strains simulates this geological structure as discrete lineaments. The statistical spacing of these lineaments in the numerical model was based on the mapping at Mont Terri. Incorporating discrete weak planes (bedding), captures the anisotropic behaviour of the Opalinus Clay and represents the matrix and bedding as a composite material. Consequently the shape and extent of the EDZ around the tunnel is a function of both yielding of the intact matrix and slip along the bedding.

The results from the numerical modelling are expressed in the form of nomograms to facilitate comparison between different repository depths and stress conditions. All results demonstrate that for a given undrained shear strength the diametral strains at depths of 900 m are likely associated with major squeezing problems. Such strains will challenge the construction and operation of the repository underground openings.



## **7 Acknowledgements**

The discussion in Chapter 4 is based on excavation characterisation studies performed by the Swisstopo geologists at Mont Terri and others. The detailed work of mapping the EDZ and interpreting the excavation response is the basis for understanding of the EDZ.

Thanks are also due to David Jaeggi (Swisstopo), Salina Yong (Mirarco) and Benoit Garitte (Nagra) for provision of data compilations and interpretations.



## 8 References

- Achtziger, P., Trick, T., Kontar, K. & Roesli, U. (2011): FE-A / MB Experiment: Third hydraulic test campaign in BMB-15 and BMB-16 boreholes. Mont Terri Technical Note TN 2011-08.
- Alcolea, A., Kuhlmann, U., Lanyon, G.W. & Marschall, P. (2014): Hydraulic conductance of the EDZ around underground structures of a geological repository for radioactive waste – A sensitivity study for the candidate host rocks in the proposed siting regions in Northern Switzerland. Nagra Arb. Ber. NAB 13-94, Nagra, Wettingen, Schweiz.
- Alcoverro, J., Arnedo, D., Olivella, S. & Alonso, E.E. (2013): Simulation Results of the HG-A Test. FORGE Report D4.23. 75pp.
- Alheid, H.J., Aranyosy, J.F., Blümling, P., Hoteit, N. & Van Geet, M. (2007): EDZ development and evolution – State of the art. NF-PRO. Contract Number F16W-CT-2003-02389.
- Amann, F., Kaiser, P. & Button, E.A. (2011a): Experimental Study of Brittle Behavior of Clay Shale in Rapid Triaxial Compression. *Rock Mechanics and Rock Engineering*, 45(1), 21–33. doi:10.1007/s00603-011-0195-9.
- Amann, F., Button, E.A., Evans, K.F., Gischig, V.S. & Blümel, M. (2011b): Experimental Study of the Brittle Behavior of Clay Shale in Rapid Unconfined Compression. *Rock Mechanics and Rock Engineering*, 44(4), 415–430. doi:10.1007/s00603-011-0156-3.
- Aranyosy, J.F., Mayor, J.C., Marschall, P., Plas, F., Blümling, P., Van Geet, M., Armand, G., Techer, I., Alheid, A.J., Rejeb, A., Pinettes, P., Balland, C., Popp, T., Rothfuchs, T., Matray, J.M., De Craen, M., Wiczorek, K., Pudewills, A., Czaikowski, O., Hou, Z. & Fröhlich, H. (2008): EDZ Development and Evolution (RTDC 4) - Final Synthesis Report (D. 4.5.3). FP6-EURATOM/NF-PRO, F16W-CT-2003-02389.
- Armand, G., LeBon, P., Cruchaudet, M., Rebours, H., Morel, J. & Wileveau, Y. (2007): Characterization of the excavation-damaged zone in the Meuse Haute Marne Underground Research Laboratory. *Clays in Natural and Engineered Barriers for Radioactive Waste Confinement International Meeting September 17-18, 2007*. Lille, France.
- Armand, G., Noiret, A., Zghondi, J. & Seyedi, D.M. (2013): Short- and Long-Term Behaviors of Drifts in the Callovo-Oxfordian Claystone at the Meuse/Haute-Marne Underground Research Laboratory. *Journal of Rock Mechanics and Geotechnical Engineering* 5 (3) (June): 221–230. doi:10.1016/j.jrmge.2013.05.005.
- Armand, G., Leveau, F., Nussbaum, C., Vaissiere, R., Noiret, A., Jaeggi, D. & Righini, C. (2014): Geometry and Properties of the Excavation-Induced Fractures at the Meuse/Haute-Marne URL Drifts. *Rock Mechanics and Rock Engineering*, 47(1), 21–41. doi:10.1007/s00603-012-0339-6.
- Azizi, F. (1999): *Applied analyses in geotechnics*. E & FN Spon, London.
- Badertscher, N., Girardin, C. & Nussbaum, C. (2008): SE-H Experiment: EDZ structural analysis of resin impregnated sections from BSE-3 overcore. Mont Terri Technical Note TN 2008-15, Saint Ursanne, Switzerland.

- Bernier, F., Li, X.L. & Bastiaens, W. (2007): Twenty-Five Years' Geotechnical Observation and Testing in the Tertiary Boom Clay Formation. *Géotechnique* 57 (2) (March 1): 229–237. doi:10.1680/geot.2007.57.2.229
- Bernier, F., Li, X.L., Bastiaens, W., Ortiz, L., Van Geet, M., Wouters, L., Frieg, B., Blümling, P., Desrues, J., Viaggiani, G., Coll, C., Chanchole, S., De Greef, V., Hamza, R., Malinsky, L., Vervoort, A., Vanbrabant, Y., Debecker, B., Verstraelen, J., Govaerts, A., Wevers, M., Labiouse, V., Escoffier, S., Mathier, J.-F., Gastaldo, L. & Bühler, Ch. (2007): Fractures and Self-healing within the Excavation Disturbed Zone in Clays (SELFRAC). Final report, EURATOM, Fifth Framework Programme, Contract No: FIKW-CT2001-00182.
- Blümling, P., Bernier, F., Lebon, P. & Martin, C.D. (2007): The excavation damaged zone in clay formations time-dependent behaviour and influence on performance assessment. *Physics and Chemistry of the Earth* 32(8-14), 588-599.
- Bock, H. (2000): RA experiment - Rock mechanics analyses and synthesis: Data report on rock mechanics. Mont Terri Technical Report TR 2000-02.
- Bock, H. (2009): RA Experiment: updated review of rock mechanics properties of the Opalinus Clay of Mont Terri URL based on laboratory and field testing. Mont Terri Technical Report TR 2008-04.
- Bock, H., Dehandschutter, B., Martin, C.D., Mazurek, M., De Haller, A., Skoczylas, F. & Davy, C. (2010): Self-sealing of Fractures in Argillaceous Formations in the Context of Geological Disposal of Radioactive Waste Review and Synthesis Report. OECD NEA 6184. Waste Management. Paris, France: NEA OECD.
- Bossart, P., Meier, P.M., Moeri, A., Trick, T. & Mayor, J.C. (2002): Geological and hydraulic Characterization of the excavation disturbed zone in the Opalinus Clay of the Mont Terri Rock Laboratory. *Engineering Geology* 66, 19-38.
- Bossart, P., Trick, T., Meierand, P.M. & Mayor, J.C. (2004): Structural and hydrogeological Characterization of the excavation-disturbed zone in the Opalinus Clay (Mont Terri Project, Switzerland). *Applied Clay Science* 26, 429– 448.
- Bossart, P. & Thury, M. (2007): Research in the Mont Terri Rock laboratory: Quo vadis? *Physics and Chemistry of the Earth, Parts A/B/C*, 32(1-7), 19–31. Retrieved from <http://linkinghub.elsevier.com/retrieve/pii/S1474706506002026> .
- Bossart, P. & Wermeille, S. (2003): Derivation of the Primary Stress Field in the Mont Terri Rock Laboratory. Reports of the FOWG (Swiss Federal Office for Water and Geology, Ittigen), Geology Series. No. 4- Bern 2003.
- Burrus, F., Bossart, P. & Nussbaum, C. (2010): Gallery 08: Documentation of the excavation and the convergence measurements. Mont Terri Technical Note TN 2008-10.
- Contrucci, I., Cabrera, J., Klein, E. & Ben-Slimane, K. (2007): EDZ investigations by ultrasonic borehole logging in drifts of different ages excavated in argillaceous formations of the Tournemire experimental station (Aveyron, France). International Meeting, September 17-18, 2007, Lille, France, Clays in Natural and Engineered Barriers for Radioactive Waste Confinement.

- Corkum, A.G., Martin, C.D. (2006): Analysis of tunnel deformations in opalinous clay using a stress-dependent modulus model. In 59th Canadian Geotechnical Conference: Sea to Sky Geotechnique (pp. 461–468).
- Corkum, A.G., Martin, C.D. (2007): Modelling a Mine-By test at the Mont Terri rock laboratory, Switzerland. *International Journal of Rock Mechanics and Mining Sciences*, 44(6), 846–859. doi:10.1016/j.ijrmms.2006.12.003.
- De Craen, M., Van Geet, M., Honty, M., Weetjens, E. & Sillen, X. (2008): Extent of oxidation in Boom Clay as a result of excavation and ventilation of the HADES URF: experimental and modelling assessments. *Physics and Chemistry of the Earth, Parts A/B/C*, 33(Suppl. 1), S350–S362.
- Diederichs, M.S. & Kaiser, P.K. (1999): Stability of large excavations in laminated hard rock masses: the Vousoir analogue revisited. *International Journal of Rock Mechanics and Mining Sciences* 36(1), 97-118.
- Duncan, J.M. & Goodman, R.E. (1968): Finite element analyses of slopes in jointed rock. Contract report 8-68-3. US Army Engineers Waterways Experimental Station, Vicksburg.
- Ebert, A. (2014): *Strukturgeologische Kernaufnahmen der Wirtgesteine aus Tiefbohrungen der Nordschweiz*. Nagra Arbeitsbericht NAB 13-89. Nagra, Wettingen.
- Egger, P. (2000): Design and construction aspects of deep tunnels (with particular emphasis on strain softening rocks). *Tunnelling and Underground Space Technology*, 15(4), 403–408. doi:10.1016/S0886-7798(01)00008-6.
- Eiholzer, L. (2012): FE-C experiment: Geodetic 3D convergence measurements during the excavation of FE Gallery. Mont Terri Technical Note TN 2012-88.
- Einstein, H.H. (1996): Tunnelling in difficult ground—Swelling behaviour and identification of swelling rocks. *Rock Mechanics and Rock Engineering* 29(3), 113-124.
- Einstein, H.H. (2002): Tunnels in Opalinus Clayshale—A Review of Case Histories and New Developments. *Geotechnology Compendium* 1, 177.
- Emsley, S., Olsson, O., Stenberg, L., Alheid, H.-J. & Falls, S. (1997): ZEDEx: A Study of Damage and Disturbance from Tunnel Excavation by Blasting and Tunnel Boring. Svensk Kärnbränslehantering AB/Swedish Nuclear Fuel and Waste Management Co.
- Enachescu, C. (2011): DS (Determination of stress) Experiment: Hydraulic Fracturing Tests in BDS-2 and BDS-4 at the Mt. Terri Underground Research Facility. FMT DS Experiment - Phase 15. Mont Terri Technical Note TN 2010-53.
- Ferrari, A., Favero, V., Marschall, P. & Laloui, L. (2014): Experimental analysis of the water retention behaviour of shales. *Int. J. Rock Mech. & Mining Sci.* 72, 61-70.
- Fisch, H. (2004): EDZ cut-off (EZ-A) experiment, EH site: hydraulic characterisation with modular mini-packer systems (MMPS). Mont Terri Technical Note TN2004-39.

- Garitte, B., Bond, A., Millard, A., Zhang, C., Mcdermott, C., Nakama, S. & Gens, A. (2013): Analysis of hydro-mechanical processes in a ventilated tunnel in an argillaceous rock on the basis of different modelling approaches. *Journal of Rock Mechanics and Geotechnical Engineering*, 5(1), 1–17. doi:10.1016/j.jrmge.2012.09.001
- Geomechanica (2013): Extent and shape of the EDZ around underground structures of a geological repository for radioactive waste – A sensitivity study for the candidate host rocks in the proposed siting regions in Northern Switzerland. Nagra Arb. Ber. NAB 13-78, Nagra, Wettingen, Schweiz.
- Giger, S. & Marschall, P. (2014): Geomechanical properties, rock models and in-situ stress conditions for Opalinus Clay in Northern Switzerland. Nagra Arb. Ber. NAB 14-01, Nagra, Wettingen, Schweiz.
- Graham, J. & Housby, G.T. (1983): Elastic anisotropy of a natural clay. *Géotechnique* 33/2, 165-180.
- Harrington, J.F. (ed) (2014): FORGE Milestone D4.24-R Summary report: Experiments and modelling of excavation damage zone (EDZ) behaviour in argillaceous and crystalline rocks (Work Package 4)1.
- Harrison, J.P. & Hudson, J. (1997): *Engineering rock mechanics-an introduction to the principles*. Elsevier, London.
- Heidbach, O. & Reinecker, J. (2013): Analyse des rezenten Spannungsfeldes der Nordschweiz. Nagra Arbeitsbericht NAB 12-05. Nagra, Wettingen.
- Hoek, E. & Marinos, P. (2000): Predicting tunnel squeezing problems in weak heterogeneous rock masses. *Tunnels and Tunnelling International*, Part 1, 32(11), 45–51; Part 2, 32(12), 33–36.
- Jaeggi, D. (2014): Compilation of convergence data from Mont Terri. Provided as Excel spreadsheet.
- Jaeggi, D., Lisjak, A., Gisiger, J. & Becker, J. (2012): FE-C Experiment: Engineering part of full-scale emplacement experiment Geological and structural mapping of the FE-tunnel including a photogrammetric method. Mont Terri Technical Note TN12-82.
- Jaeggi, D., Müller, P., Dolder, F. & Nussbaum, C. (2012): FE-A Experiment: Site preparation for Full-Scale Emplacement Demonstration Experiment Geological and structural mapping of the FE-A niche (start niche). Mont Terri Technical Note TN11-19.
- Jaeggi, D., Nussbaum, C. & Vietor, T. (2012): MB Experiment: Visualization of EDZ-fractures around the MB niche by using the in-situ resin impregnation technique. Mont Terri Technical Note TN 10-56.
- Kim, Y.S., Peacock, D.C.P. & Sanderson, D.J. (2004): Fault damage zones. *Journal of Structural Geology*, 26(3), 503–517. doi:10.1016/j.jsg.2003.08.002.
- Klee, G. & Becker, F. (2013): SBB Bözbergtunnel Projekt Hydraulic-Fracturing Spannungsmessungen in der Bohrung B2/13. Nagra Arbeitsbericht. NAB 13-082.

- Labiouse, V. & Vietor, T. (2014): Laboratory and In Situ Simulation Tests of the Excavation Damaged Zone Around Galleries in Opalinus Clay. *Rock Mechanics and Rock Engineering*, 47(1), 57–70. doi:10.1007/s00603-013-0389-4.
- Lanyon, G.W. (2005): EZ-A (EDZ cut-off) experiment: Discrete fracture network models of the EDZ in the EH section. Mont Terri Technical Note TN 2005-14.
- Lanyon, G.W. (2011): Excavation Damaged Zones Assessment. Report NWMO DGR-TR-2011-21.
- Lanyon, G.W., Marschall, P; Trick, T; de la Vaissière, R, Shao, H. & Leung, H. (2009): Hydromechanical Evolution And Self-Sealing of Damage Zones Around a Microtunnel In a Claystone Formation of the Swiss Jura Mountains. In 43rd U.S. Rock Mechanics Symposium & 4th U.S. - Canada Rock Mechanics Symposium, June 28 - July 1, 2009 , Asheville, North Carolina, Pages 652-663, paper 09-333.
- Lanyon, G.W., Marschall, P., Trick, T., de la Vaissiere, R., Shao, H. & Leung, H. (2014) : Self-sealing experiments and gas injection tests in a backfilled microtunnel of the Mont Terri URL. Geological Society, London, Special Publications, 400(1), 93–106. doi:10.1144/SP400.8.
- Le Gonidec, Y., Schubnel, A., Wassermann, J., Gibert, D., Nussbaum, C., Kergosien, B., Sarout, J., Maineult, A. & Guéguen, Y. (2012): Field-scale acoustic investigation of a damaged anisotropic shale during a gallery excavation. *International Journal of Rock Mechanics and Mining Sciences*, 51(August 2008), 136–148. doi:10.1016/j.ijrmms.2012.01.018.
- Lesparre, N., Gibert, D., Nicollin, F., Nussbaum, C. & Adler, A. (2013): Monitoring the excavation damaged zone by three-dimensional reconstruction of electrical resistivity. *Geophysical Journal International*, 195(2), 972–984. doi:10.1093/gji/ggt282.
- Levasseur, S., Collin, F. & Charlier, R. (2013): Modelling of lab and field experiments HGA Experiment. FORGE Report D4.22.
- Lisjak, A., Garitte, B., Grasselli, G., Müller, H. & Vietor, T. (2014): The excavation of a circular tunnel in a bedded argillaceous rock (Opalinus Clay): short-term rock mass response and FDEM numerical analysis. *Tunnelling and Underground Space Technology*.
- Little, T. (1989): Construction and performance of a large diameter test chamber in shale. In K.Y. Lo, editor, *Proc. International Congress on Progress and Innovation in Tunnelling*, Toronto, volume II, pages 869– 876, 1989.
- Lux, K.H., Duesterloh, U. & Czaikowski, O. (2007): Laboratory tests on indurated clay. Clausthal University of Technology. Final Report for EDZ long term evolution (WP 4.4). European Commission NF-PRO (Contract Number: FI6W-CT-2003-02389) (D 4.4.13).
- Madritsch, H. & Vietor, T. (2010): Mine By (MB) Experiment:Excavation history of Niche 2 and results of structural geological tunnel mapping. Mont Terri Technical Note TN 2008-87.

- Maineult, A., Thomas, B., Nussbaum, C., Wieczorek, K., Gibert, D., Lavielle, B., Kergosien, B., Nicollin, F., Mahiouz, K. & Lesparre, N. (2013) : Anomalies of noble gases and self-potential associated with fractures and fluid dynamics in a horizontal borehole, Mont Terri Underground Rock Laboratory. *Engineering Geology*, 156, 46–57. doi:10.1016/j.enggeo.2013.01.010.
- Marschall, P., Croisé, J., Schlickerrieder, L., Boisson, J.-Y., Vogel, P. & Yamamoto, S. (2004): Synthesis of Hydrogeological Investigations at the Mont Terri Site (Phases 1 to 5). Heitzmann, P. ed. 2004: Mont Terri Project- Hydrogeological Synthesis, Osmotic Flow. Reports of the Federal Office for Water and Geology, FOWG, Geology Series No. 6.
- Marschall, P., Distinguin, M., Shao, H., Bossart, P., Enachescu C. & Trick, T. (2006): Creation and evolution of damage zones around a microtunnel in a claystone formation of the Swiss Jura Mountains, International Symposium and Exhibition on Formation Damage Control.
- Marschall, P., Trick, T., Lanyon, G.W., Delay J. & Shao, H. (2008): Hydro-Mechanical Evolution of Damaged Zones around a Microtunnel in a Claystone Formation of the Swiss Jura Mountains. ARMA 2008, San Francisco.
- Martin, C.D., Christiansson, R. & Söderhäll, J. (2001): Rock Stability Considerations for Siting and Constructing a KBS-3 Repository. SKB Technical Report TR-01-38.
- Martin, C.D., Kaiser, P.K. & McCreath, D.R. (1999 ): Hoek-Brown Parameters for Predicting the Depth of Brittle Failure Around Tunnels. *Canadian Geotechnical Journal* 36 (1): 136-151.
- Martin, C.D. & Lanyon, G.W. (2003a): EDZ in clay shale: Mont Terri. Mont Terri Techn. Rep.2001, 1. With contributions from P. Bossart and P. Blümling.
- Martin, C.D. & Lanyon, G.W. (2003b): Measurement of in-situ stress in weak rocks at Mont Terri Rock Laboratory, Switzerland. *International Journal of Rock Mechanics and Mining Sciences* 40(7-8), 1077-1088.
- Martin, C.D., Maciotta, R., Elwood, D., Lan, H. & Vietor, T. (2014a): Evaluation of the Mont Terri Mine-By response: Summary of the instrumentation results. Mont Terri Technical Note TN 2009- 02 (in review).
- Martin, C.D., Maciotta, R., Elwood, D., Lan, H. & Vietor, T. (2014b): Evaluation of the Mont Terri Mine-By response: Interpretation of results and observations. Mont Terri Technical Note TN 2009- 02 (in review).
- Matray, J., Savoye, S. & Cabrera, J. (2007): Desaturation and structures relationships around drifts excavated in the well-compacted Tournemire's argillite and their impact on the hydraulic head profiles. *Engineering Geology* 90, 1-16.
- Mayor, J.C., Velasco, M. (2008) Ventilation Test (VE) Experiment: Final activity report for ENRESA, WP 4.3 The Ventilation Experiment Phase II (Synthesis Report). Mont Terri Technical Report TR 2008-01 (also NF-PRO Deliverable D-N°:4.3.18).
- Mayor, J.C., Velasco, M. & García-Siñeriz, J.-L. (2007a): Ventilation experiment in the Mont Terri underground laboratory. *Physics and Chemistry of the Earth, Parts A/B/C*, 32(8-14), 616–628. doi:10.1016/j.pce.2006.04.030.

- Mayor, J.C., García-Siñeriz, J.L., Velasco, M., Gómez- Hernández, J., Lloret, A., Matray, J.-M., Coste, F., Giraud, A., Rothfuchs, T., Marshall, P., Roesli, U. & Mayer, G. (2007b): Ventilation Experiment in Opalinus Clay for the disposal of radioactive waste in underground repositories. –In: Bossart, P. & Nussbaum, C. (Eds.): Mont Terri Project – Heater Experiment, Engineered Barrier Emplacement and Ventilation Experiment (p.188–240). – Rep. Swiss Geol. Surv. 1.
- Meier, P.M., Trick, Th., Blümling, P. & Volckaert, G. (2002): Self healing of fractures within the EDZ at the Mont Terri Rock Laboratory: results after one year of experimental work. In: Hoteit, N., Su, K., Tijani, M. & Shao, J.-F. (Eds.): Hydromechanical and Thermo-hydromechanical Behaviour of Deep Argillaceous Rock. Swets and Zeitlinger, Lisse, pp. 267– 274. ISBN 905809 533 9
- Mellanen, S. (ed.), Koskinen, L., Hellä, P., Löfman, J., Lanyon, G.W., Öhberg, A., Autio, J., Sacklén, N., Saukkonen, K., Saari, J., Lakio, A., Silvast, M., Wiljanen, B., Vuokko, J. & Lyytinen, T. (2008): EDZ Programme, EDZ Studies in ONKALO 2007-2008. Posiva Working Report 2008-66.
- Möri, A., Bossart, P., Matray, J.-M., Müller, H., Frank, H., Ababou, R. & Fatmi, H. (2012): Mont Terri project, cyclic deformations in the Opalinus Clay. Special Issue: Clays in Natural & Engineered Barriers for Radioactive Waste Confinement (4th Internat. Meeting Clays 2010, Nantes, 29 March – 1st April 2010). Journal of Physics & Chemistry of the Earth.
- Nagra (1997): Geosynthese Wellenberg 1996-Ergebnisse der Untersuchungsphasen I und II; Nagra Technical Report NTB 96-01. Wettingen, Switzerland.
- Nagra (2002): Projekt Opalinuston – Synthese der geowissenschaftlichen Untersuchungsergebnisse. Entsorgungsnachweis für abgebrannte Brennelemente, verglaste hochaktive sowie langlebige mittelaktive Abfälle. Nagra Technical Report NTB 02-03. Wettingen, Switzerland.
- Nagra (2010): Beurteilung der geologischen Unterlagen für die provisorischen Sicherheitsanalysen in SGT Etappe 2. Nagra Technischer Bericht NTB 10-01. Nagra, Wettingen, Switzerland.
- Nagra (2014a): Unterlagen zur Anlagenauslegung in Bezug auf maximale Tiefenlage und Platzbedarf: Grundlagen für die Abgrenzung und Bewertung der Lagerperimeter. Nagra Arb. Bericht NAB 14-81.
- Nagra (2014b): Geologische Unterlagen – Dossier IV: Geomechanische Unterlagen und hydro-mechanische Kopplung. Nagra Tech. Ber. NTB 14-02.
- Nagra (2014c): Charakteristische Dosisintervalle und Unterlagen zur Bewertung der Barrierensysteme. Nagra Tech. Ber. NTB 14-03.
- Nicollin, F., Gibert, D., Bossart, P., Nussbaum, C. & Guervilly, C. (2008): Seismic tomography of the Excavation Damaged Zone of the Gallery 04 in the Mont Terri Rock Laboratory. Geophysical Journal International, 172(1), 226–239. doi:10.1111/j.1365-246X.2007.03615.x.

- Nicollin, F., Gibert, D., Lesparre, N. & Nussbaum, C. (2010): Anisotropy of electrical conductivity of the excavation damaged zone in the Mont Terri Underground Rock Laboratory. *Geophysical Journal International*, 181(1), 303–320. doi:10.1111/j.1365-246X.2010.04517.x.
- Nussbaum, C., Armand, G., Meier, O., Badertscher, N. & Bossart, P. (2005a): EZ-A (EDZ cut-off) experiment: Identification of water conducting features and conceptual model of the water flowpaths at the EH section. Mont Terri Technical Note TN 2005-54.
- Nussbaum, C., Badertscher, N., Metille, J., Meier, O. & Bossart, P. (2005b): HG-A experiment: Detailed geological mapping of the microtunnel walls. Mont Terri Technical Note TN 2005-49.
- Nussbaum, C., Bossart, P. (2006): HG-A experiment: Mapping of new breakouts developed in the HG-A microtunnel about 11 months after the excavation. Mont Terri Technical Note TN 2006-31.
- Nussbaum, C., Bossart, P., Amann, F. & Aubourg, C. (2011): Analysis of tectonic structures and excavation induced fractures in the Opalinus Clay, Mont Terri underground rock laboratory (Switzerland). *Swiss Journal of Geosciences*, 104(2), 187–210. doi:10.1007/s00015-011-0070-4.
- Nussbaum, C., Bossart, P., Burrus, F., Badertscher, N., Meier, O. & Nold, A. (2005): Excavation of Gallery 04: General Documentation, Deformation Measurements and Geological Surveys. Mont Terri Technical Note TN 2005-05.
- Nussbaum, C., Bossart, P., Piedevache, M. & Badertscher, N. (2004): EZ-A Experiment: Raw data report of the convergence and extensometer measurements. Mont Terri Technical Note TN 2004-08.
- Nussbaum, C., Girardin, C., Badertscher, N., Risse, V., Veuve, C., Mayoraz, J. & Bossart, P. (2010): Extension of the rock laboratory: Geological documentation of the Gallery 08 and adjacent niches (DR-A, MB, Niche 3 and TT) Mont Terri Technical Note TN 2008-12.
- Nuth, M., Laloui, L. (2008): Effective stress concept in unsaturated soils: Clarification and validation of a unified framework. *Int. J. Numer. Anal. Meth. Geomech.* (32): pp 771-801.
- Peron, H., Eichenberger, J., Laloui, L., Salager, S. & Marschall, P. (2010): Modelling of drying and cracking initiation in a gallery excavated in shale. *European Rock Mechanics Symposium, Eurock 2010* – pp. 771-774.
- Rejeb, A. & Cabrera, J. (2007): Time-dependent evolution of the excavation damaged zone in the argillaceous Tournemire site. *Advances on coupled thermohydro-mechanical-chemical processes in geosystems and engineering. Proceedings International Conference GeoProc 2006, Nanjing, China*, p.648–657.
- Schuster K. & Alheid, H.-J. (2007): EDZ Characterization with ultrasonic interval velocity measurements in the URL Meuse/Haute-Marne – performed between depth of 85 m and 504 m. *International Meeting, Clays in Natural and Engineered Barriers for Radioactive Waste Confinement, September 17-18, 2007, Lille, France.*

- Schuster, K., Alheid, H.J., Böddener, D., Eichhorn, P., Spies, T. & Heidrich, D. (2001): ED-C: Seismic Investigations of the EDZ and Acoustic Emission Measurements in the New Gallery. Mont Terri Technical Note TN 2000-61.
- Schuster, K., Alheid, H.J., Böddener, D., Eichhorn, P., Spies, T. & Heidrich, D. (2002): Geophysical Characterisation of the Excavation Disturbed Zone (ED-C) Experiment: Seismic Investigations of the EDZ and Acoustic Emission Measurements in the New Gallery, Mont Terri Rock Laboratory. Mont Terri Technical Report TN 2000-05.
- Schuster, K., Alheid, H.-J. & Kruschwitz, S. (2004): Observation of an engineered barrier experiment in the Opalinus Clay of the Mont Terri Rock Laboratory with geophysical and hydraulic methods. Proceedings of EURADWASTE '04.
- Swiss Federal Office of Energy (SFOE) (2008): Sectoral Plan for Deep Geological Repositories, Conceptual Part. Swiss Federal Office of Energy, Bern, Switzerland.
- Shao, H., Schuster, K., Sönke, J. & Bräuer, V. (2008): EDZ development in indurated clay formations—In situ borehole measurements and coupled HM modelling. *Physics and Chemistry of the Earth* 33, 388-395.
- Simpson, R.W. (1997): Quantifying Anderson's fault types, *J. Geophys. Res.*, 102, 17909-17919.
- Steiner, W. (1993): Swelling rock in tunnels: rock characterization, effect of horizontal stresses and construction procedures. *International Journal of Rock Mechanics and Mining Sciences and Geomechanics Abstracts*, 361-380.
- Steiner, W. (1996): Tunnelling in squeezing rocks: case histories. *Rock Mechanics and Rock Engineering* 29(4), 211-246.
- Tang, C.A. & Hdon, J.A. (2010). *Rock Failure Mechanisms: Illustrated and Explained*. CRC Press.
- Thury, M. & Bossart, P. (1999): The Mont Terri Rock Laboratory, a New International Research Project in a Mesozoic Shale Formation, in Switzerland, *Engineering Geology* 52, 347-359.
- Tsang, C.F., Bernier, F. & Davies, C. (2005): Geohydromechanical processes in the Excavation Damaged Zone in crystalline rock, rock salt, and indurated and plastic clays—in the context of radioactive waste disposal. *International Journal of Rock Mechanics and Mining Sciences* 42(1), 109-125.
- Vietor, T., Blümling, P. & Armand, G. (2006): Failure mechanisms of the Opalinus Clay around underground excavations. In: *Proc. of Eurock 2006, ISRM reg symp, Liège, Belgium*, 479-484.
- Vinsot, A., Leveau, F., Bouchet, A. & Arnould, A. (2014): Oxidation front and oxygen transfer in the fractured zone surrounding the Meuse/Haute-Marne URL drifts in the Callovian-Oxfordian argillaceous rock. Geological Society, London, Special Publications. doi:10.1144/SP400.37.

- Wenk, H. & Voltolini, M. (2008): Preferred orientations and anisotropy in shales: Callovo-Oxfordian shale (France) and Opalinus Clay (Switzerland). *Clays and Clay Science* 56(3), 285–306. doi:10.1346/CCMN.2008.0560301.
- Wermeille, S & Bossart, P. (1999): In situ stresses in the Mont Terri Region: data compilation. Mont Terri Project: Technical Report 99-02; 1999.
- Wileveau, Y., Cornet, F.H., Desroches, J. & Blumling, P. (2007): Complete in situ stress determination in an argillite sedimentary formation. *Physics and Chemistry of the Earth* 32(8-14), 866-878.
- Wilson, C.R., Witherspoon, P.A., Long, J.C.S., Galbraith, R.M., DuBois A.O. & McPherson, M.J. (1983): Large-scale hydraulic conductivity measurements in fractured granite. *International Journal of Rock Mechanics and Mining Sciences and Geomechanics Abstracts* 20(6), 269-276.
- Yong, S. (2008): A three-dimensional analysis of excavation-induced perturbations in the Opalinus Clay at the Mont Terri Rock Laboratory. PhD Thesis, ETH Zurich.
- Yong, S., Kaiser, P.K., Loew, S. & Corrado, F. (2008): The role of heterogeneity on the development of excavation-induced fractures in the Opalinus Clay. Canadian Geotechnical Conference, Edmonton, Canada.
- Yong, S., Loew, S., Fidelibus, C., Frank, E., Lemy, F. & Schuster, K. (2006): Induced fracturing in the Opalinus Clay: an integrated field experiment, rock mechanics in underground construction: ISRM International Symposium 2006: 4th Asian Rock Mechanics Symposium, 8-10 November 2006, Singapore, p.418.